

**STRUCTURAL BEHAVIOUR OF CONCRETE FILLED  
STEEL TUBES WITH HIGH STRENGTH MATERIALS**

**XIONG DEXIN**

**NATIONAL UNIVERSITY OF SINGAPORE**

**2012**



**STRUCTURAL BEHAVIOUR OF CONCRETE FILLED STEEL  
TUBES WITH HIGH STRENGTH MATERIALS**

**XIONG DEXIN**

(B. Eng. and M. Eng., Huazhong University of Science and Technology)

**A THESIS SUBMITTED  
FOR THE DEGREE OF DOCTOR OF PHILOSOPHY  
DEPARTMENT OF CIVIL AND ENVIRONMENTAL ENGINEERING  
NATIONAL UNIVERSITY OF SINGAPORE**

**2012**





## DECLARATION

I hereby declare that the thesis is my original work and it has been written by me in its entirety. I have duly acknowledged all the sources of information which have been used in the thesis.

This thesis has also not been submitted for any degree in any university previously.

A handwritten signature in black ink, appearing to read 'Xiong Dexin', written over a horizontal line.

Xiong Dexin

13 August 2012



## **Acknowledgements**

I would like to express my deep gratitude to my supervisor, Professor LIEW Jat Yuen, Richard, for his dedicated supervision, invaluable guidance and continuous support during the period of candidature. I have been greatly encouraged by his unending pursuits of excellence and hard work. Without his excellent expertise, this research would not have been progressed.

My sincere appreciation is dedicated to the Department of Civil and Environmental Engineering at the National University of Singapore, for providing necessary facilities for this research project. My thanks also extend to all academic and administrative staff of the Department of Civil and Environmental Engineering. I gratefully acknowledge the kindly assistance from all the staff members of the Structural Engineering Laboratory. Special thanks go to Ms TAN Annie, Mr KOH Yian Kheng, Mr ANG Beng Oon, Mr ISHAK Bin A Rahman, Mr CHOO Peng Kin, Mr KAMSAN Bin Rasman, Mr YIP Kwok Keong, Mr WONG Kah Wai and Mr LIM Huay Bak for their continuous supports during testing.

I also would like to thank all my colleagues and friends from our research group under Prof LIEW for their friendships, companionship and help. I am greatly indebted to Mr XIONG Ming Xiang, Mr WANG Tong Yun, Mr YAN Jia Bao, Mr YU Xin, Dr CHIA Kok Seng and Mr LEE Ning Kit Nicholas for their continuous help and invaluable advice.

## *Acknowledgements*

---

This research project was funded by A\*STAR (SERC Grant No. 092 142 0045) and the research scholarship was provided by the National University of Singapore. The test materials were sponsored by Densit Asia, Yongnam Holdings Ltd and Continental Steel Pte Ltd. All their financial supports are gratefully acknowledged.

Last but not least, I would like to convey my love to my families who often sacrificed their time during the development of my research. Especially, I would like to thank my wife, WANG Ting, and my lovely daughter, XIONG Kai En, for their continuous support, without which this work would not have been possible.

## Table of Contents

<b>Acknowledgements .....</b>	<b>i</b>
<b>Table of Contents .....</b>	<b>iii</b>
<b>Summary.....</b>	<b>viii</b>
<b>List of Tables .....</b>	<b>x</b>
<b>List of Figures.....</b>	<b>xiii</b>
<b>List of Symbols .....</b>	<b>xx</b>
<b>List of Abbreviations .....</b>	<b>xxiii</b>
<b>Chapter 1 Introduction.....</b>	<b>1</b>
1.1 General.....	1
1.2 Background.....	1
1.2.1 Concrete filled steel tubes ( <i>CFSTs</i> ) .....	2
1.2.2 An overview of experimental investigations done on <i>CFSTs</i> .....	4
1.3 Research Motivations .....	5
1.4 Research Objectives and Scope of Work.....	8
1.5 Layout of the Thesis .....	11
<b>Chapter 2 Literature Review .....</b>	<b>19</b>

2.1 General.....	19
2.2 <i>CFSTs</i> with High Strength Concrete .....	19
2.3 <i>CFSTs</i> with High Strength Steel.....	22
2.4 <i>CFSTs</i> with Preload Effect .....	23
2.5 Current Design Guidelines for <i>CFST</i> Columns .....	25
2.5.1 Eurocode 4 .....	25
2.5.2 AISC 360-10 .....	30
2.5.3 Comparison between the two codes.....	33
2.6 Summary.....	34
<b>Chapter 3 Basic Mechanical Properties of Ultra High Strength Concrete .....</b>	<b>37</b>
3.1 General.....	37
3.2 Experimental Investigation .....	37
3.2.1 Basic materials .....	37
3.2.2 Mix proportions .....	38
3.2.3 Specimens .....	39
3.2.4 Workability .....	39
3.2.5 Density .....	41
3.2.6 Compressive properties.....	41
3.2.7 Tensile properties.....	50
3.2.8 Flexural properties .....	51
3.3 Design Recommendations .....	53
3.3.1 Recommendations on compressive strength.....	54
3.3.2 Recommendations on modulus of elasticity .....	54
3.3.3 Recommendations on tensile strength.....	55
3.3.4 Recommendations on flexural tensile strength.....	57

3.4 Summary .....	57
<b>Chapter 4 Stub <i>CFST</i> Columns with High Strength Materials under Concentric Compression .....</b>	<b>85</b>
4.1 General.....	85
4.2 Ductility Requirements .....	86
4.3 Series 1 Tests: Small Scale <i>CFST</i> Columns with <i>UHSC</i> .....	87
4.3.1 Material properties .....	87
4.3.2 Specimens .....	88
4.3.3 Test setup and loading procedure .....	89
4.3.4 Test results and observations .....	90
4.4 Series 2 Tests: Full Scale <i>CFST</i> Columns with both <i>UHSC</i> and <i>NSC</i> .....	93
4.4.1 Material properties .....	94
4.4.2 Specimens .....	96
4.4.3 Test setup and loading procedure .....	97
4.4.4 Test results and observations .....	97
4.5 Series 3 Tests: Coarse Aggregate Effect on <i>CFST</i> Columns with <i>UHSC</i> .....	100
4.5.1 Material properties .....	100
4.5.2 Specimens .....	102
4.5.3 Test setup and loading procedure .....	102
4.5.4 Test results and observations .....	102
4.6 Series 4 Tests: <i>CFST</i> Columns with <i>UHSC</i> and <i>HSS</i> .....	105
4.6.1 Material properties .....	105
4.6.2 Specimens .....	106
4.6.3 Test setup and loading procedure .....	107
4.6.4 Test results and observations .....	107

4.7 Evaluation of Test Results .....	109
4.7.1 Mechanics of composite action between concrete core and steel tube .....	109
4.7.2 Performance of <i>CFST</i> columns on ductility.....	113
4.7.3 Test results of ultimate resistance compared with Eurocode 4 predictions ....	114
4.8 Summary .....	118
<b>Chapter 5 CFST Beams with High Strength Materials under Flexural Moment ...</b>	<b>164</b>
5.1 General.....	164
5.2 Experimental Investigation .....	164
5.2.1 Materials .....	164
5.2.2 Specimens .....	166
5.2.3 Test set-up and loading procedure .....	166
5.2.4 Test results and observations .....	167
5.3 Evaluation of Test Results .....	174
5.3.1 Test values of ultimate resistance compared with Eurocode 4 predictions ....	174
5.3.2 Test values of flexural stiffness compared with Eurocode 4 predictions .....	175
5.4 Summary.....	176
<b>Chapter 6 Slender CFST Beam-Columns with High Strength Materials under Concentric and Eccentric Compression.....</b>	<b>205</b>
6.1 General.....	205
6.2 Experimental Investigation .....	206
6.2.1 Materials .....	206
6.2.2 Specimens .....	207
6.2.3 Test set-up and loading procedure .....	208
6.2.4 Test results and observations .....	209



6.3 Evaluation of Test Results .....	210
6.3.1 Test values of ultimate resistance compared with Eurocode 4 predictions ....	211
6.4 Summary .....	212
<b>Chapter 7 Preload Effect on the axial compressive resistance of CFST columns ...</b>	<b>229</b>
7.1 General.....	229
7.2 Theoretical Analyses.....	230
7.2.1 Overall buckling resistance of steel columns.....	230
7.2.2 Comparison with Eurocode 4 approach .....	232
7.2.3 Preload effect .....	232
7.2.4 Parametric studies .....	234
7.3 Verifications.....	235
7.4 Finite Element Analysis ( <i>FEA</i> ).....	236
7.4.1 Numerical modelling and calibration with test results.....	236
7.4.2 Numerical parametric analysis.....	238
7.5 A Step-by-Step Design Procedure .....	239
7.6 Summary .....	240
<b>Chapter 8 Conclusions.....</b>	<b>251</b>
8.1 Conclusions.....	251
8.2 Recommendations for Future Work .....	255
<b>References.....</b>	<b>259</b>
<b>List of Publications .....</b>	<b>265</b>
<b>Appendix I: Formulae for Calculation of Sectional Properties.....</b>	<b>267</b>

## **Summary**

Concrete filled steel tubes (*CFSTs*) have been widely used in many structures. For high-rise structures, it is better to employ higher strength materials, since smaller section members can be properly adopted and then more workable space can be saved. However, investigations on *CFSTs* with high strength materials are considerably lacking. In addition, a problem of preload effect may present during the construction of *CFST* columns in high-rise structures by fast-track construction method, leading to significant influence on the ultimate resistance. Furthermore, current design guidelines for *CFSTs* are only applicable for normal strength concrete and steel without the preload effect. The aim of this study was to examine the structural behaviour of *CFSTs* employing ultra-high strength concrete (*UHSC*) and high strength steel (*HSS*) under static loading, assess the preload effect on the overall buckling resistance of *CFST* columns under concentric compression, and extend current design codes to *UHSC*, *HSS* and preload effect.

For the design of *CFST* members, generally it only needs to check the cross-sectional resistance of the critical sections and second order effect for slender members. The second order effect can be considered by taking into account member imperfections and amplifying the greatest first-order moment force within the member length as stipulated in Eurocode 4, or it can be considered by taking into account member imperfections and multiplying the cross-sectional compressive resistance by a reduction factor as stipulated

in Eurocode 4 and AISC 360-10. Therefore, this study carried out several series of experimental investigations on materials *UHSC* and *HSS* to examine the basic mechanical material properties, stub *CFST* columns under concentric compression to assess the cross-sectional compressive resistance, *CFST* beams under pure bending to assess the cross-sectional moment resistance, and slender *CFST* beam-columns under concentric and eccentric compression to assess the overall buckling resistance under coupled compression and moment with second-order effect. For evaluation, the test results were compared with Eurocode 4 predictions. It was found that ultra-high resistance could be achieved by employing *UHSC* and *HSS* in *CFST* columns. Therefore, they are most suitable to be applied in high-rise constructions. It was also found that Eurocode 4 limitations on materials can be extended to the *UHSC* and *HSS* with minor modifications.

In addition, this study also investigated preload effect on the overall buckling resistance of *CFST* columns under concentric compression by theoretical analysis, verification with test and *FE* results, and numerical parametric study. Design formulae based on modified Eurocode 4 approach were proposed to consider the preload effect. It was found that a significant reduction in ultimate resistance can be produced under high preload.

In conclusion, this study has made a significant contribution to fill the gap in the research on the structural behaviour of *CFSTs* with *UHSC*, *HSS* and preload effect. The findings provide valuable guidelines for designers to adopt *UHSC* and *HSS* in *CFST* columns and for constructors to use fast-track construction method in *CFST* structures.

## List of Tables

Table 2.1: Maximum values ( $d/t$ ) and ( $h/t$ ) with $f_y$ in MPa as recommended in EC4 .....	35
Table 2.2: Classification for local buckling as recommended in AISC 360-10 .....	35
Table 3.1: Size grading of Ducorit® D4.....	60
Table 3.2: Size grading of coarse aggregates.....	60
Table 3.3: Physical properties of coarse aggregates .....	60
Table 3.4: Mix proportions per cube meter of <i>UHSC</i> .....	61
Table 3.5: Number of specimens tested for each mix proportion design .....	61
Table 3.6: Test values of slump flow spread .....	61
Table 3.7: Test values of density .....	61
Table 3.8: Compressive cylinder strength .....	62
Table 3.9: Compressive cube strength .....	63
Table 3.10: Modulus of elasticity and Poisson's ratio.....	64
Table 3.11: Secant and elastic modulus .....	65
Table 3.12: Compressive cylinder versus cube strength.....	66
Table 3.13: Scale effect on compressive cylinder strength.....	66
Table 3.14: Effect of maximum coarse aggregate size on compressive strength .....	67
Table 3.15: Effect of maximum coarse aggregate size on modulus of elasticity .....	68
Table 3.16: Splitting tensile strength .....	69
Table 3.17: Effect of maximum coarse aggregate size on splitting tensile strength.....	70

*List of Tables*

---

Table 3.18: Flexural tensile strength.....	71
Table 3.19: Effect of maximum coarse aggregate size on flexural tensile strength .....	72
Table 3.20: Summary of basic mechanical properties .....	72
Table 4.1: Basic properties of high tensile strength steel fiber.....	120
Table 4.2: Basic material properties of concrete used in Series 1 .....	120
Table 4.3: Basic properties of steel sections used in Series 1 .....	120
Table 4.4: Specimen configuration details for Series 1 .....	121
Table 4.5: Test values of ultimate and residual resistance for Series 1 .....	121
Table 4.6: Mix proportion design for <i>NSC</i> used in Series 2 .....	122
Table 4.7: Basic material properties of concrete used in Series 2 .....	122
Table 4.8: Basic properties of two additional steel sections used in Series 2.....	122
Table 4.9: Single-tube specimen configuration details for Series 2 .....	123
Table 4.10: Double-tube specimen configuration details for Series 2.....	123
Table 4.11: Test values of ultimate and residual resistance for Series 2 .....	124
Table 4.12: Basic material properties of concrete used in Series 3 .....	125
Table 4.13: Basic properties of one additional steel section used in Series 3 .....	125
Table 4.14: Single-tube specimen configuration details for Series 3 .....	125
Table 4.15: Double-tube specimen configuration details for Series 3.....	125
Table 4.16: Test values of ultimate and residual resistance for Series 3 .....	126
Table 4.17: Basic material properties of concrete used in Series 4 .....	126
Table 4.18: Basic material properties of steel sections used in Series 4.....	126
Table 4.19: Specimen configuration details for Series 4 .....	127
Table 4.20: Test values of ultimate and residual resistance for Series 4 .....	128
Table 4.21: Test results and predictions for hollow steel tube columns.....	129

*List of Tables*

---

Table 4.22: Test results and predictions for <i>NSC</i> filled circular steel tube columns .....	129
Table 4.23: Test results and predictions for <i>UHSC</i> filled circular single-tube .....	130
Table 4.24: Test results and predictions for <i>UHSC</i> filled circular double-tubes .....	131
Table 4.25: Test results and predictions for <i>UHSC</i> filled square single-tube .....	131
Table 4.26: Test results and predictions for <i>UHSC</i> filled square <i>HSS</i> single-tube .....	132
Table 4.27: Test results and predictions for <i>UHSC</i> filled square <i>HSS</i> double-tubes .....	132
Table 5.1: Basic mechanical properties of steel sections .....	178
Table 5.2: Specimen configuration details .....	178
Table 5.3: Flexural stiffness degradation during unload-reload procedure .....	179
Table 5.4: Test values of ultimate resistance and $h_n$ compared with EC4 predictions ....	180
Table 5.5: Test values of elastic and secant flexural stiffness compared with $(EI)_{\text{eff,II}}$ ...	180
Table 6.1: Basic mechanical properties of steel sections .....	213
Table 6.2: Specimen configuration details .....	213
Table 6.3: Test results and EC4 predictions for concentrically loaded specimens .....	214
Table 6.4: Test results and EC4 predictions for eccentrically loaded specimens .....	214
Table 7.1: Test specimen details .....	242
Table 7.2: Comparison of predictions compared with test and FEA results .....	242
Table 7.3: Comparison of predictions with test results from Zha (1996) .....	243
Table 7.4: Comparison of predictions with test results from Han and Yao (2003) .....	243
Table 7.5: Numerical results compared with predictions .....	244
Table 7.6: Proposed modifications to EC4 equations for incorporating preload .....	245

## **List of Figures**

Figure 1.1: Typical cross-sections of <i>CFSTs</i> .....	14
Figure 1.2: Typical fully and partially concrete encased steel sections.....	14
Figure 1.3: Loading cases of axially compressed <i>CFST</i> columns .....	15
Figure 1.4: Tests on <i>CFSTs</i> with different concrete strengths.....	15
Figure 1.5: Tests on <i>CFSTs</i> with different steel strengths .....	16
Figure 1.6: Composite construction of a 50-storey building (Liew, 2004) .....	16
Figure 1.7: Hollow circular steel columns before infilling with concrete (Liew, 2004) ...	17
Figure 1.8: Fast-track construction sequence of a typical composite building.....	18
Figure 2.1: Resistance interaction curve as recommended in EC4.....	36
Figure 2.2: Resistance interaction curve as recommended in AISC 360-10 .....	36
Figure 3.1: Size grading curve for Ducorit® D4 .....	73
Figure 3.2: Sieved Ducorit® D4.....	73
Figure 3.3: Size grading curves for 10mm coarse aggregates .....	74
Figure 3.4: Size grading curves for 20mm coarse aggregates .....	74
Figure 3.5: Slump flow spread curves .....	75
Figure 3.6: Test values of density .....	75
Figure 3.7: Compressive cylinder strength at different curing ages .....	76
Figure 3.8: Compressive cube strength at different curing ages.....	76

*List of Figures*

---

Figure 3.9: Modulus of elasticity at different curing ages .....	77
Figure 3.10: Compressive stress - strain curves.....	77
Figure 3.11: Compressive cylinder strength versus cube strength .....	78
Figure 3.12: Scale effect on compressive cylinder strength .....	78
Figure 3.13: Effect of maximum coarse aggregate size on compressive strength.....	79
Figure 3.14: Effect of maximum coarse aggregate size on modulus of elasticity .....	79
Figure 3.15: Effect of coarse aggregate proportion on compressive strength .....	80
Figure 3.16: Effect of coarse aggregate proportion on modulus of elasticity.....	80
Figure 3.17: Splitting tensile strength at different curing ages.....	81
Figure 3.18: Effect of maximum coarse aggregate size on splitting tensile strength .....	81
Figure 3.19: Effect of coarse aggregate proportion on splitting tensile strength.....	82
Figure 3.20: Flexural tensile strength at different curing ages .....	82
Figure 3.21: Flexural tensile stress - deflection curves.....	83
Figure 3.22: Effect of maximum coarse aggregate size on flexural tensile strength.....	83
Figure 3.23: Effect of coarse aggregate proportion on flexural tensile strength .....	84
Figure 4.1: High tensile strength steel fiber - SF 13/80.....	133
Figure 4.2: Coupon test samples and setup.....	133
Figure 4.3: Coupon test stress-strain curves for CHS114.3mm×3.6mm .....	134
Figure 4.4: Coupon test stress-strain curves for CHS114.3mm×6.3mm .....	134
Figure 4.5: Different loading cases for specimens in Series 1 .....	135
Figure 4.6: Load-shortening curves for S1-1-1(a), S1-1-2(a) and S1-1-2(b) .....	136
Figure 4.7: Load-shortening curves for S1-2-1(a) and S1-2-1(b).....	136
Figure 4.8: Load-shortening curves for S1-3-1(a) and S1-3-1(b).....	137
Figure 4.9: Load-shortening curves for S1-3-2(a) and S1-3-2(b).....	137



*List of Figures*

---

Figure 4.10: Load-shortening curves for S1-3-3(a) and S1-3-3(b).....	138
Figure 4.11: All the tested specimens in Series 1 .....	138
Figure 4.12: Failure modes of <i>UHSC</i> cores in <i>CFST</i> columns .....	139
Figure 4.13: Circular single- and double-tube <i>CFST</i> columns .....	140
Figure 4.14: Failure modes for different types of concrete .....	140
Figure 4.15: Coupon test stress-strain curves for CHS219.1mm×5mm .....	141
Figure 4.16: Coupon test stress-strain curves for CHS219.1mm×10mm .....	141
Figure 4.17: Test setup for specimens in Series 2 .....	142
Figure 4.18: Load-shortening curves for Group S2-1 specimens in Series 2 .....	143
Figure 4.19: Load-shortening curves for Group S2-2 specimens in Series 2 .....	143
Figure 4.20: Load-shortening curves for Group S2-3 specimens in Series 2 .....	144
Figure 4.21: Load-shortening curves for Group S2-4 specimens in Series 2 .....	144
Figure 4.22: All the tested specimens in Series 2 compared with those in Series 1 .....	145
Figure 4.23: Failure modes of <i>UHSC</i> reinforced with coarse aggregates.....	146
Figure 4.24: Coupon test stress-strain curves for CHS219.1mm×6.3mm .....	146
Figure 4.25: Test setup for specimens in Series 3 .....	147
Figure 4.26: Load-shortening curves for single-tube specimens in Series 3 .....	148
Figure 4.27: Load-shortening curves for double-tube specimens in Series 3 .....	148
Figure 4.28: The failure of ordinary coarse aggregates in <i>UHSC</i> .....	149
Figure 4.29: Comparison of single-tube specimens with double-tube specimens.....	149
Figure 4.30: All the specimens before casting and after tested in Series 3 .....	150
Figure 4.31: Coupon test stress-strain curves for 8mm-thick HSS plate.....	151
Figure 4.32: Coupon test stress-strain curves for 12mm-thick HSS plate.....	151
Figure 4.33: Coupon test stress-strain curves for 6mm-thick steel strip.....	152
Figure 4.34: Coupon test stress-strain curves for SHS150mm×12.5mm .....	152

Figure 4.35: Square single-tube specimen without concrete casting.....	153
Figure 4.36: Square double-tube specimen without concrete casting.....	153
Figure 4.37: Dimension details for single-tube specimens.....	154
Figure 4.38: Dimension details for double-tube specimens.....	154
Figure 4.39: Test setup for specimens in Series 4 .....	155
Figure 4.40: Load-shortening curves for Group S4-1 specimens in Series 4 .....	156
Figure 4.41: Load-shortening curves for Group S4-2 specimens in Series 4 .....	156
Figure 4.42: Load-shortening curves for Group S4-3 specimens in Series 4 .....	157
Figure 4.43: Load-shortening curves for Group S4-4 specimens in Series 4 .....	157
Figure 4.44: All the specimens before casting and after tested in Series 4 .....	158
Figure 4.45: Variation of Poisson’s ratio with longitudinal stresses for steel .....	159
Figure 4.46: Variation of Poisson’s ratio with longitudinal stresses for <i>NSC</i> .....	159
Figure 4.47: Variation of Poisson’s ratio with longitudinal stresses for <i>UHSC</i> .....	160
Figure 4.48: A simple model of <i>CFST</i> column under uniaxial compression.....	160
Figure 4.49: Variation of stresses and $\varepsilon_{\theta}/\varepsilon_z$ in <i>CFST</i> columns.....	161
Figure 4.50: Measured strains and loading curves for S2-1-1 and S2-2-1 .....	161
Figure 4.51: Measured strains and loading curves for S2-1-2 and S2-2-2 .....	162
Figure 4.52: Residual resistance ratio for all single-tube <i>CFST</i> columns with <i>UHSC</i> ....	162
Figure 4.53: Test results compared with EC4 predictions without confinement effect...	163
Figure 4.54: Test results compared with EC4 predictions with confinement effect.....	163
Figure 5.1: Casting of <i>UHSC</i> by pumping.....	181
Figure 5.2: Coupon test stress-strain curves for CHS114.3mm×6.3mm .....	181
Figure 5.3: Coupon test stress-strain curves for CHS219.1mm×16mm .....	182
Figure 5.4: Coupon test stress-strain curves for SHS200mm×12.5m.....	182

Figure 5.5: Different types of composite sections .....	183
Figure 5.6: Dimension details of welded square box sections.....	183
Figure 5.7: Test set-up .....	184
Figure 5.8: Test instrumentations .....	185
Figure 5.9: Moment-deflection curves for specimen N1-CS.....	186
Figure 5.10: Moment-deflection curves for specimen N2-CD .....	186
Figure 5.11: Moment-deflection curves for specimen N3-CDH .....	187
Figure 5.12: Moment-deflection curves for specimen N4-SS .....	187
Figure 5.13: Moment-deflection curves for specimen N5-SS .....	188
Figure 5.14: Moment-deflection curves for specimen N6-SS .....	188
Figure 5.15: Moment-deflection curves for specimen N7-SD.....	189
Figure 5.16: Moment-deflection curves for specimen N8-SDH.....	189
Figure 5.17: Comparison of moment-deflection curves .....	190
Figure 5.18: Curvature of the middle region under pure bending .....	191
Figure 5.19: Comparison of moment-curvature curves .....	192
Figure 5.20: Flexural stiffness degradation during un/re-load procedure for N1-CS.....	193
Figure 5.21: Flexural stiffness degradation during un/re-load procedure for N2-CD .....	193
Figure 5.22: Flexural stiffness degradation during un/re-load procedure for N3-CDH ..	194
Figure 5.23: Flexural stiffness degradation at different loading levels .....	194
Figure 5.24: Moment-strain curves for specimen N4-SS .....	195
Figure 5.25: Moment-strain curves for specimen N5-SS .....	195
Figure 5.26: Moment-strain curves for specimen N6-SS .....	196
Figure 5.27: Moment-strain curves for specimen N7-SS .....	196
Figure 5.28: Moment-strain curves for specimen N8-SS .....	197
Figure 5.29: Strain distribution along cross-section height .....	198

Figure 5.30: Variation of neutral axis location .....	199
Figure 5.31: Variation of curvature derived from deflection and strain for N4-SS.....	199
Figure 5.32: Variation of curvature derived from deflection and strain for N5-SS.....	200
Figure 5.33: Variation of curvature derived from deflection and strain for N6-SS.....	200
Figure 5.34: Variation of curvature derived from deflection and strain for N7-SD .....	201
Figure 5.35: Variation of curvature derived from deflection and strain for N8-SDH .....	201
Figure 5.36: Failure modes of test specimens at the maximum deflections .....	202
Figure 5.37: Failure of <i>UHSC</i> infilling .....	203
Figure 5.38: Comparison of test values of ultimate resistance with EC4 predictions .....	204
Figure 6.1: Coupon test stress-strain curves for CHS273mm×10mm .....	215
Figure 6.2: Coupon test stress-strain curves for CHS273mm×16mm .....	215
Figure 6.3: Test set-up and instrumentation .....	216
Figure 6.4: Load-deflection curves for specimen CS-1 .....	216
Figure 6.5: Load-deflection curves for specimen CS-2 .....	217
Figure 6.6: Load-deflection curves for specimen CS-3 .....	217
Figure 6.7: Load-deflection curves for specimen CS-4 .....	218
Figure 6.8: Load-deflection curves for specimen CS-5 .....	218
Figure 6.9: Load-deflection curves for specimen CS-6 .....	219
Figure 6.10: Load-deflection curves for specimen CD-1 .....	219
Figure 6.11: Load-deflection curves for specimen CD-2 .....	220
Figure 6.12: Load-deflection curves for specimen CDH-1 .....	220
Figure 6.13: Load-deflection curves for specimen SS-1 .....	221
Figure 6.14: Load-deflection curves for specimen SS-2 .....	221
Figure 6.15: Load-deflection curves for specimen SS-3 .....	222

Figure 6.16: Load-deflection curves for specimen SD-1 .....	222
Figure 6.17: Load-deflection curves for specimen SDH-1 .....	223
Figure 6.18: Comparison of load-deflection curves for CS-1, CS-2 and CS-3 .....	223
Figure 6.19: Comparison of load-deflection curves for CS-4, CS-5 and CS-6 .....	224
Figure 6.20: Comparison of load-deflection curves for CD-1, CD-2 and CDH-1 .....	224
Figure 6.21: Comparison of load-deflection curves for SS-1, SS-2 and SS-3.....	225
Figure 6.22: Comparison of load-deflection curves for SD-1 and SDH-1 .....	225
Figure 6.23: Failure modes of test specimens at the maximum deflections .....	226
Figure 6.24: Failure of <i>UHSC</i> infilling.....	229
Figure 6.25: Comparison of test results with Eurocode 4 predictions.....	230
Figure 7.1: Design buckling curves of <i>CFST</i> columns with preload effect.....	246
Figure 7.2: Preload reduction factor curves under different preload ratio values .....	246
Figure 7.3: Verification of predictions with test results .....	247
Figure 7.4: Verification of predictions with other published test results.....	247
Figure 7.5: Uniaxial stress-strain relationship for concrete.....	248
Figure 7.6: Uniaxial stress-strain relationship for steel .....	248
Figure 7.7: Geometrical models for steel tube and concrete core with imperfection .....	249
Figure 7.8: Load-displacement curves.....	249
Figure 7.9: Comparison of numerical results with predictions.....	250
Figure 8.1: Contribution of current research in <i>CFST</i> members .....	257
Figure 8.2: Cross-section of stub square <i>HSS</i> double-tube specimens .....	258

## **List of Symbols**

$A$	Total cross-sectional area of column
$A_a$	Cross-sectional area of steel tube
$A_c$	Cross-sectional area of concrete core
$A_s$	Cross-sectional area of reinforcement
$b$	Breadth of square section
$d$	Overall diameter of circular hollow steel section
$E_a$	Modulus of elasticity of structural steel
$E_{cm}$	Secant modulus of elasticity of concrete
$E_s$	Modulus of elasticity of reinforcement
$(EI)_{eff}$	Effective flexural stiffness of composite cross-section
$f_{ck}$	Characteristic cylinder (150mm×300mm) compressive strength of concrete
$f_{ck,100}$	Characteristic cylinder (100mm×200mm) compressive strength of concrete
$f_s$	Nominal yield strength of reinforcement
$f_y$	Nominal yield strength of structural steel
$f_u$	Nominal ultimate tensile strength of structural steel
$I_a$	Second moment of area of structural steel section
$I_c$	Second moment of area of uncracked concrete section
$I_s$	Second moment of area of reinforcement section
$L$	Actual column length

$l_e$	Effective column length
$\Delta L_{lim}$	Limit of axial shortening displacement
$M$	Moment applied on columns
$N$	Axial load applied on columns
$N_{add}$	Superimposed axial load after preload
$N_{a,cr}$	Euler buckling load of steel column, $N_{a,cr} = \pi^2 E_a I_a / l_e^2$
$N_{a,pl,Rk}$	Characteristic cross-sectional plastic resistance of steel column, $N_{a,pl,Rk} = A_a f_y$
$N_{a,u}$	Characteristic buckling resistance of steel column, $N_{a,u} = \chi_a N_{a,pl,Rk}$
$N_{cr}$	Euler buckling load of composite column, $N_{cr} = \pi^2 (EI)_{eff} / l_e^2$
$N_{pl,Rd}$	Design value of composite sectional plastic resistance to compression
$N_{pl,Rk}$	Characteristic value of composite sectional plastic resistance to compression
$N_{pre}$	Axial preload applied to steel tube
$N_{pre,u,d}$	Design buckling load of composite column with preload effect
$N_{pre,u}$	Characteristic buckling load of composite column with preload effect
$N_{test,r}$	Testing values of the residual resistance
$N_{test,u}$	Testing values of the ultimate resistance
$N_{u,d}$	Design overall buckling resistance of axially loaded column
$N_u$	Characteristic overall buckling resistance of axially loaded column
$r$	Radius of gyration for a cross-section
$S$	Elastic section modulus
$t$	Thickness of steel tube
$u_r^p$	The displacement in radial direction at the point "P"
$\alpha$	Imperfection factor
$\beta_a$	Preload ratio, $\beta_a = N_{pre} / N_{a,u}$
$\gamma_a, \gamma_c, \gamma_s$	Partial factor for structural steel, concrete and reinforcement

## *List of Symbols*

---

$\delta$	Steel contribution ratio; deflection
$\varepsilon_r^p, \varepsilon_z^p, \varepsilon_\theta^p$	Strains in radial, longitudinal and circumferential directions respectively at the point ‘‘P’’
$\eta_a, \eta_c$	Factors related to the confinement effect
$\eta_{pre}$	Preload reduction factor, $\eta_{pre} = N_{pre,u}/N_u = \chi_{pre}/\chi$
$\lambda$	Relative slenderness, the same as defined in Eurocode 4
$\nu_a, \nu_c$	Poisson’s ratio of steel and concrete respectively
$\xi_{pre}$	Preload effect factor, $\xi_{pre} = (1 - N_{pre}/N_u)/(1 - N_{pre}/N_{a,u})$
$\sigma_{max}$	Maximum equivalent nominal stress in composite cross-section
$\phi_{lim}$	Deformation limit on axial shortening displacement ratio
$\chi', \chi$	Slenderness reduction factor of composite column
$\chi_a$	Slenderness reduction factor of steel tube
$\chi_{pre}$	Slenderness reduction factor of composite column considering preload effect



## **List of Abbreviations**

CFST	<b>C</b> oncrete <b>F</b> illed <b>S</b> teel <b>T</b> ube
EC4	<b>E</b> urocode 4
FRP	<b>F</b> iberglass- <b>R</b> einforced <b>P</b> lastics
HSC	<b>H</b> igh <b>S</b> trength <b>C</b> oncrete
HSS	<b>H</b> igh <b>S</b> trength <b>S</b> teel
LVDT	<b>L</b> inear <b>V</b> arying <b>D</b> isplacement <b>T</b> ransducer
NSC	<b>N</b> ormal <b>S</b> trength <b>C</b> oncrete
NSS	<b>N</b> ormal <b>S</b> trength <b>S</b> teel
SF	<b>S</b> teel <b>F</b> iber
UHSC	<b>U</b> ltra- <b>H</b> igh <b>S</b> trength <b>C</b> oncrete



## Chapter 1 Introduction

### 1.1 General

This chapter will provide an overview of this thesis on the topic of structural behaviour of concrete filled steel tubes (*CFSTs*) with high strength materials, including the background of the study, research motivations and objectives, and the layout of this thesis.

### 1.2 Background

Steel and concrete are the most important constructional materials with different characteristics. Steel is characterized by high tensile and compressive strengths, perfect ductility and great elastic modulus, resulting in small size sections and long clear span structures where buckling may be the most significant problem as well as fire resistance. Concrete is characterized by relatively high compressive but weak tensile strength, high fire resistance and low economic cost, resulting in massive bulk members where brittle crushing and premature cracking may be the most critical problems.

Steel and concrete can compensate with each other and work together to form composite structural members with expected characteristics. Steel rebar is the most widely used reinforcement in composite members such as reinforced concrete beams, columns and slabs. It is designed to carry tensile stress while the concrete carries the compressive

stress. At the same time, stirrups are usually added together with steel rebar to enhance the ductility and strength of concrete, while the concrete can prevent steel rebar and stirrups from buckling and fire. Structural steel sections such as I-sections and hollow sections can also be used with concrete to form a composite section. The strength and ductility of concrete can be increased by steel sections while steel sections can be prevented from local buckling and fire by concrete.

### 1.2.1 Concrete filled steel tubes (CFSTs)

CFSTs, one type of the most widely used composite members, can take the full advantages of steel and concrete. Conventionally, one of CFSTs comprises a hollow steel tube and a concrete core with or without additional reinforcement. The local buckling of steel tube is delayed or even prevented by the concrete core while the strength and ductility of concrete core is enhanced by the confinement effect provided by the steel tube. Moreover, the steel tube can serve as permanent formwork for concrete casting and thus it eliminates the need of formwork and leads to fast track construction and more economical design.

CFSTs have various composite cross-sections as shown in Figure 1.1. Circular, square and rectangular sections are commonly adopted while polygonal sections may be used in some special cases. Conventionally, only plain concrete is used to fill the hollow steel sections as shown in Figure 1.1(a). In addition, the concrete core can be reinforced by fiberglass-reinforced plastics and steel fiber to improve the strength and ductility of concrete, especially for high strength concrete. It can also be reinforced by steel rebar to enhance the ductility and fire resistance. For convenience, the steel rebar can be replaced

by an internal steel tube which can provide higher confinement effect on the concrete core. Other steel sections, such as solid steel bars and I-sections, can be encased in the concrete core to improve the resistance and reduce section sizes. For members mainly subjected to bending, concrete filled double-tube sections can be used to increase the stiffness but with a relatively smaller volume of materials as shown in Figure 1.1(b).

*CFST* columns have been applied in many constructions due to their plenty of advantages over other types of columns as follows,

(1) Advantages over steel columns

- (a) Higher fire resistance
- (b) The local buckling of steel sections can be delayed or even prevented
- (c) Higher damping ratio
- (d) Almost the same fast track construction

(2) Advantages over reinforced concrete columns

- (a) Higher strength and ductility
- (b) Faster track construction
- (c) Better performance in bending
- (d) No spalling problem of concrete subjected to fire, leading to even higher fire resistance

(3) Advantages over other composite columns without external tubes (Figure 1.2)

- (a) Stronger confinement enhancement on the strength and ductility of concrete
- (b) Faster track construction
- (c) No spalling problem of concrete subjected to fire, leading to even higher fire resistance

*CFST* columns are expected to mainly carry axial compression load and there are two loading cases as shown in Figure 1.3. The first case is that the upper load is transferred to both external steel tube and concrete core simultaneously and the other case is that the upper load is transferred to the concrete core only, leading to different interaction mechanisms between the external steel tube and concrete core. In the first case, the external steel tube and concrete core are compressed simultaneously; therefore, the strength of steel can be fully used. However, in the second case, the concrete core gets compressed first and then transfers a portion of load to steel tube through interfacial friction force; therefore, the concrete core is subjected to stronger confinement stress and its strength and ductility will get highly improved, leading to better seismic performance.

### **1.2.2 An overview of experimental investigations done on *CFSTs***

There are a lot of investigations on *CFSTs* that have been done in the past decades. Figure 1.4 and Figure 1.5 show 1,948 test data samples collected from literature on *CFSTs* (including columns, beams and beam-columns) with non-slender hollow steel sections (at least class 3) subjected to static load, excluding the tests with stainless or aluminum steel tubes (Liew, Yu, Wang, & Xiong, 2012). The test results are compared with Eurocode 4 predictions by simply extending its limitations on material strengths to the test strengths reported in the literature. It can be observed that many tests have been done on *CFSTs* with normal strength materials but only limited investigations have been done on *CFSTs* with high-strength materials. There are 19.10% of the test specimens with concrete strength higher than 60MPa, 8.52% with concrete strength higher than 80MPa, only 1.18% with concrete strength higher than 120MPa, and only 7.49% with steel yield strength

higher than 460MPa. Most of the tests concentrate on *CFSTs* with normal strength materials and there are significant gaps in the range of high strength materials.

### 1.3 Research Motivations

High strength materials have been found to be attractive alternatives to normal strength materials for multi-storey and high-rise constructions. The higher the material strength, the smaller is the member size needed. This will translate to more usable space with less construction materials. However, the problem of buckling may become more severe for high strength steel and the problem of brittleness may become more critical for high strength concrete.

To overcome these problems, the best choice is to apply high strength steel and concrete in *CFSTs* where the local buckling of steel tube can be prevented and the ductility and strength of concrete core can be enhanced. In addition, high strength concrete can be designed to be compatible with high strength steel tubes; otherwise, only a very thin wall thickness is need for high strength steel to work with normal strength concrete, but the local buckling may not be efficiently prevented if the thickness is too thin and thus the strength of high strength steel cannot be fully used. Meanwhile, high strength steel tubes can be designed to be compatible with high strength concrete. To ensure sufficient ductility of *CFSTs*, the steel contribution should keep at a proper level. However, high strength concrete is more brittle than normal strength concrete, leading to an increase in the limit on the minimum steel contribution ratio. As a result, thicker or higher strength steel tube should be used in compatibility with high strength concrete which is used as the

core material. By increasing the thickness, it may become too thick to weld. Therefore, it is a better solution to increase the strength of steel by using high strength steel.

As stated in previous section, most of the existing research focused on *CFSTs* with normal strength materials, and there is a lack of sufficient work done for *CFSTs* with high strength materials, especially for *CFSTs* with ultra high strength concrete (*UHSC*) with compressive strength higher than 120MPa and high strength steel (*HSS*) with yield strength greater than 460MPa. Only several limited investigations have been carried out on *CFSTs* with high strength concrete and *HSS*, which will be reviewed in details in **Chapter 2**. Therefore, more investigations should be carried out to evaluate the performance of *CFSTs* with high strength materials and assess their potential applications in multi-storey and high-rise constructions.

In addition, a problem of preload effect in *CFST* columns may present during the construction of multi-storey and high-rise constructions, leading to significant effect on the resistance of composite columns. In multi-storey construction including *CFSTs*, the external steel tubes, prior to the development of composite action, are often subjected to pre-loading arising from the self-weight and construction imposed loads. The steel tubes are usually installed first and followed by steel beams and metal floor decking forming the steel skeleton structures which are then connected to the vertical bracing system to ensure lateral stability during construction. Figure 1.6 shows a typical multi-storey building with internal core wall providing lateral bracing to the structural steelwork during construction, Figure 1.7 shows the steel tubes at the perimeter of the building before concrete is pumped into them, and Figure 1.8 illustrates a general construction sequence of a multi-storey composite building in which concrete is pumped into the



hollow steel tubes after several floors above them have been constructed. Before the concrete is pumped into the steel tubes, these tubes are subjected to preloads due to the building self-weight and construction imposed loads. These preloads cause initial stresses and deformations in the steel tubes which could affect the resistance of composite columns after construction. Some experimental studies and numerical analyses have been conducted to investigate the preload effect on the behaviour of circular and square *CFST* columns, which will be reviewed in details in **Chapter 2**. Design methods were proposed by various researchers to predict the resistance of *CFST* columns by calibrating them against the test data and numerical results. These studies have shown significant influence of preload on slender *CFST* columns. However, the formulae proposed by different researchers are semi-empirical in nature and the terms and parameters used are rather different from each other. Therefore, it is necessary to provide uniform formulae based on theoretical analyses and experimental calibrations for all sections including circular, square, rectangular, etc.

Furthermore, current design guidelines for *CFSTs* may be only applicable for normal strength concrete and steel, and the preload effect is not considered. For example, Eurocode 4 (2004) only applies to composite columns with normal weight concrete cylinder strength from 20MPa to 50MPa and structural steel yield strength from 235MPa to 460MPa, AISC 360-10 (2010) only applies to composite columns with normal weight concrete cylinder strength from 21MPa to 70MPa, light weight concrete cylinder strength from 21MPa to 42MPa and structural steel yield strength up to 525MPa, and DBJ/T13-51-2010 (2010) only applies to composite columns with normal weight concrete cylinder strength from 25MPa to 65MPa and structural steel yield strength from 235MPa to 430MPa. Therefore, sufficient work should be done to extend current design guidelines or

propose new provisions for composite columns with high strength concrete which is beyond C60/75, especially for *UHSC* which is beyond C120, and for *HSS* which is beyond S460. Besides, current design guidelines should also be extended to cover the preload effect since there may be significant influence on the resistance of *CFST* columns in multi-storey and high-rise constructions where high strength materials are most suitable to be applied.

Besides, the need for sustainable construction in Singapore has been hastened after the recent ban on Indonesia's export of sand and subsequent price hikes on aggregates, followed by the announcement by the Ministry of National Development to reduce concrete consumption by 50% in a 5-years timeframe. Some ways to achieve this goal is to replace the conventional concrete with more sustainable non-concrete alternatives such as steel, or to use higher strength concrete.

#### **1.4 Research Objectives and Scope of Work**

In view of the preceding discussion, this study aims to investigate the structural behaviour of *CFSTs* with high strength materials including *UHSC* and *HSS*, and to assess the preload effect on overall buckling compressive resistance of *CFST* columns. Specific objectives and scope of work are described as follows,

(1) Basic mechanical properties of *UHSC* and *HSS*

Objectives:

- (a) Investigate and evaluate the basic mechanical properties of *UHSC*,
- (b) Investigate and evaluate the basic mechanical properties of *HSS*,

- (c) Propose design recommendations.

Scope:

- (a) Conduct experimental investigations to assess the basic mechanical properties of *UHSC* with different mix proportions at different curing ages,
- (b) Conduct standard coupon tensile tests to assess the basic mechanical properties of *HSS*, including the stress-strain relationship, and the yielding and ultimate strength,
- (c) Check whether current design guidelines can be extended to *UHSC* and *HSS*, any modifications should be made, or new design recommendations should be proposed.

(2) Structural behaviour of stub *CFST* columns with high strength materials

Objectives:

- (a) Investigate and evaluate the structural behaviour of stub *CFST* columns with high strength materials under concentric compression,
- (b) Propose design guidelines.

Scope:

- (a) Conduct experimental investigations on stub *CFSTs* under concentric compression with an *UHSC* of compressive strength in the range from 140MPa to 200MPa and *HSS* of yielding strength up to 780MPa (normal strength concrete and steel are also used for comparison),
- (b) Check whether current design guidelines can be extended to the new composite columns, any modifications should be made, or new design method should be proposed.

(3) Structural behaviour of *CFST* beams with high strength materials

Objectives:

- (a) Investigate and evaluate the structural behaviour of *CFST* beams with high strength materials under pure bending,
- (b) Propose design guidelines.

Scope:

- (a) Conduct experimental investigations on simple *CFST* beams by third-point loading method with an *UHSC* of compressive strength up to 200MPa and *HSS* of yielding strength up to 780MPa (normal strength steel is also used for comparison)
- (b) Check whether current design guidelines can be extended to the new composite beams, any modifications should be made, or new design method should be proposed.

(4) Structural behaviour of slender *CFST* beam-columns with high strength materials

Objectives:

- (a) Investigate and evaluate the behavior of slender *CFST* beam-columns with high strength materials under concentric and eccentric compression,
- (b) Proposed design guidelines.

Scope:

- (a) Carry out experimental investigations on concentrically and eccentrically loaded slender *CFST* beam-columns with an *UHSC* of compressive strength up to 200MPa and *HSS* of yielding strength up to 780MPa (normal strength steel is also used for comparison),

- (b) Check whether current design guidelines can be extended to the new composite beam-columns, any modifications should be made, or new design method should be proposed.

(5) Preload effect on the resistance of *CFST* columns

Objectives:

- (a) Investigate and evaluate the preload effect on cross-sectional resistance,
- (b) Investigate and evaluate the preload effect on overall buckling resistance,
- (c) Propose design guidelines considering preload effect.

Scope:

- (a) Conduct theoretical analyses to provide unified formulae for predictions of the ultimate column strength considering preload effect,
- (b) Verify the theoretical formulae with test results,
- (c) Carry out finite element analyses for parametric study,
- (d) Check whether any modifications should be made to current design guidelines, or new design method should be proposed.

## 1.5 Layout of the Thesis

This thesis reports the outcomes of the study on structural behaviour of *CFSTs* with high strength materials under static loading and preload effect on the overall buckling compressive resistance of *CFST* columns, including eight chapters as follows,

**Chapter 1** has introduced the general background of *CFSTs*, discussed the research motivations, and proposed the study objectives and scope.

**Chapter 2** reviews significant literature on *CFSTs* with high strength concrete, high strength steel and preload effect, focusing on but not limited to experimental investigations. In addition, current design guidelines for *CFST* columns recommended in Eurocode 4 and AISC 360-10 are briefly introduced and compared with each other.

**Chapter 3** presents experimental investigations on the basic mechanical properties of *UHSC* with different mix proportion designs, including workability, density, compressive strength, splitting tensile strength, flexural strength, static modulus of elasticity and Poisson's ratio. Based on the experimental results, recommendations for the design of *UHSC* are provided.

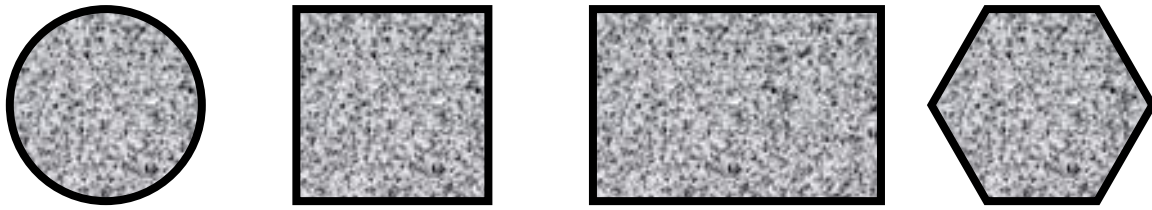
**Chapter 4** presents experimental investigations on the structural behaviour of 4 series of stub *CFST* columns employing *UHSC* and *HSS* under concentric loading. For Series 1 tests, 11 small scale specimens were tested for primary feasibility study on the application of *UHSC* in *CFST* columns with normal strength steel tubes. For Series 2 tests, 16 full scale specimens were tested for further verification, including both of single- and double-tube specimens with both of *UHSC* and normal strength concrete (*NSC*). For Series 3 tests, 8 specimens were tested to evaluate the coarse aggregate effect on the performance of *CFST* columns with *UHSC*. For Series 4 tests, 21 specimens were tested to evaluate the performance of *CFST* columns with *UHSC* and *HSS*. Since the *UHSC* used in this study is very brittle, the ductility requirement on the *CFST* columns is discussed. For evaluation, the test values of ultimate resistance are compared with the predictions by Eurocode 4, and design recommendations are proposed.

**Chapter 5** presents an experimental investigation on the structural behaviour of *CFST* beams employing *UHSC* and *HSS* under flexural moment. There are 8 composite specimens tested and the test results are compared with Eurocode 4 predictions. Based on the comparison, design recommendations are proposed.

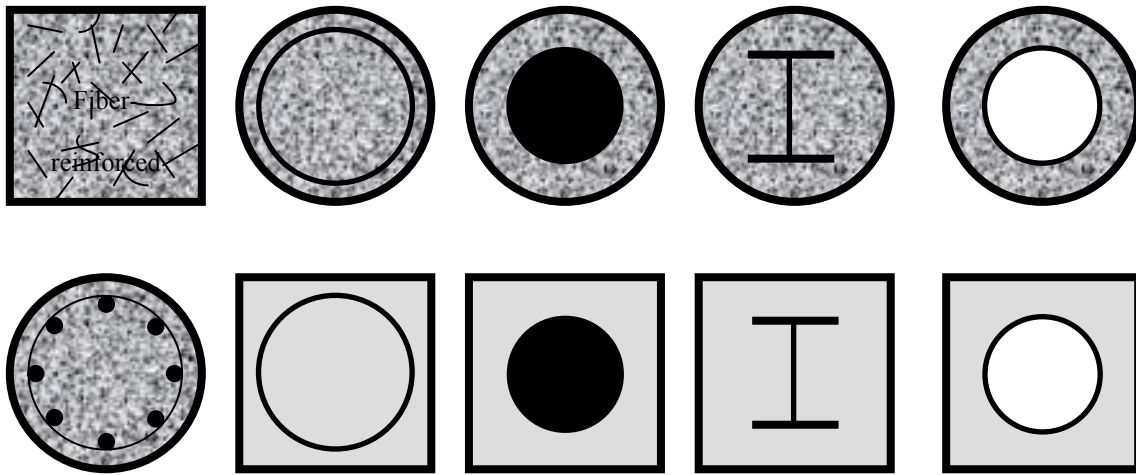
**Chapter 6** presents an experimental investigation on the structural behaviour of slender *CFST* beam-columns employing *UHSC* and *HSS* under concentric and eccentric compressive loading. There are 14 composite specimens tested. Based on the comparison of test results with Eurocode 4 predictions, design recommendations are proposed.

**Chapter 7** studies the preload effect on the overall buckling compressive resistance of *CFST* columns during constructions. A design method based on modified Eurocode 4 approach, incorporating the effect of preload, is proposed to evaluate the overall buckling resistance of *CFST* columns. Parametrical analyses were carried out, including relative slenderness ratio of the composite columns and the amount of preload applied on the steel tubes. The predictions obtained from the proposed method were compared against the test results from eight full-scale composite column specimens, and some other published data. Finite element analyses were also performed for systematic verification.

**Chapter 8** draws some significant conclusions and proposes future work on the topic of *CFSTs* with *UHSC*, *HSS* and preload effect.



(a) Plain *CFSTs*



(b) Reinforced *CFSTs*

Figure 1.1: Typical cross-sections of *CFSTs*

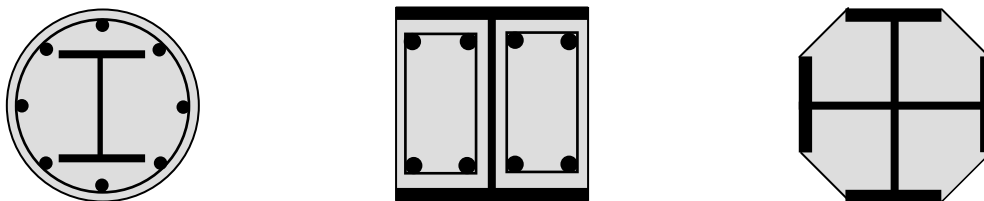


Figure 1.2: Typical fully and partially concrete encased steel sections



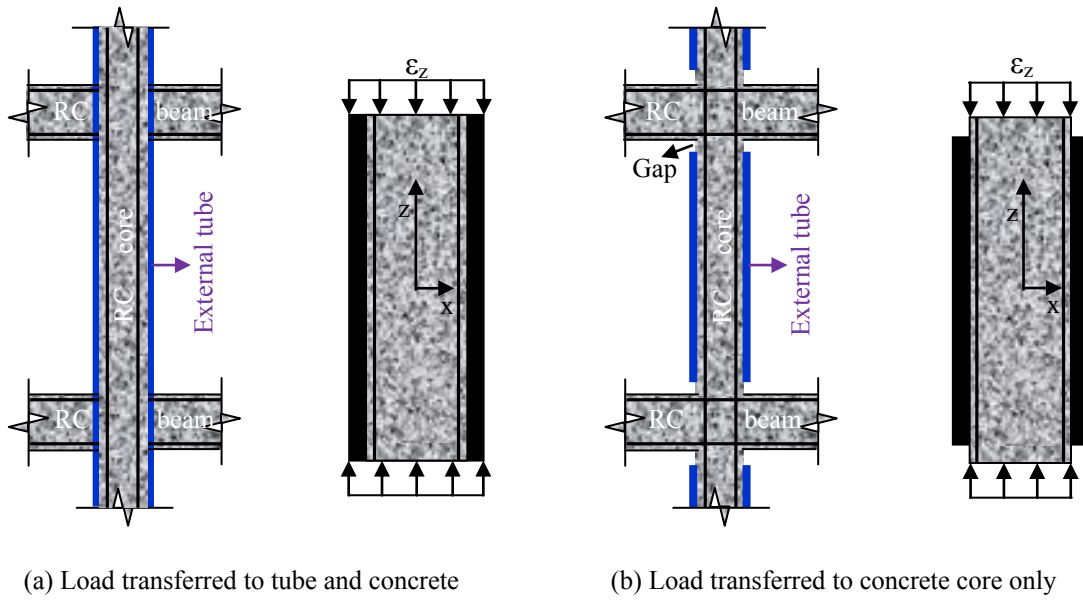


Figure 1.3: Loading cases of axially compressed *CFST* columns

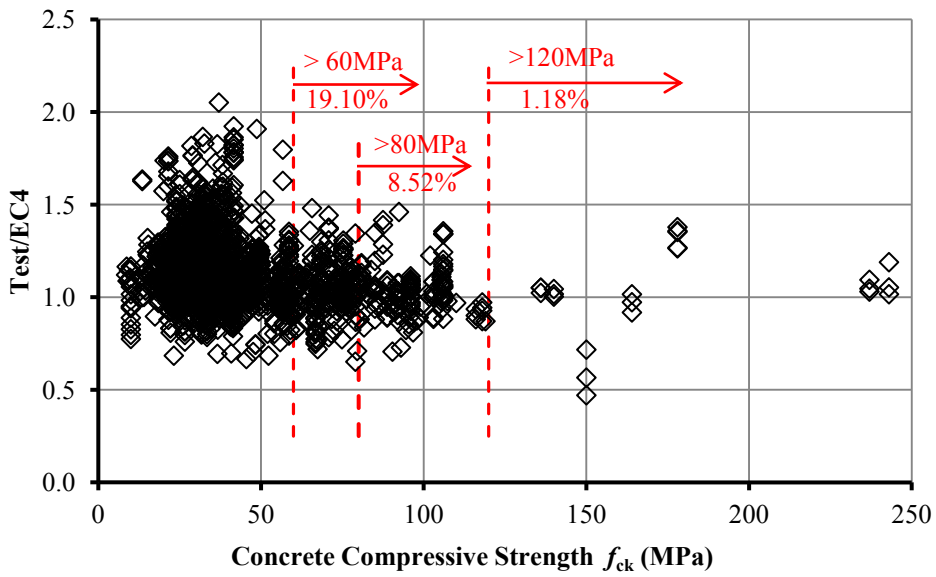


Figure 1.4: Tests on *CFSTs* with different concrete strengths

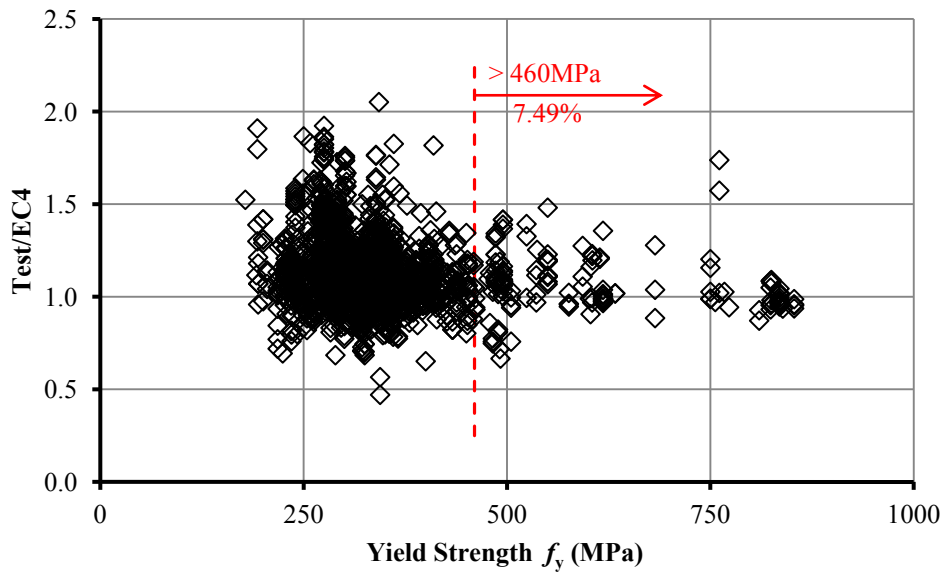


Figure 1.5: Tests on *CFSTs* with different steel strengths

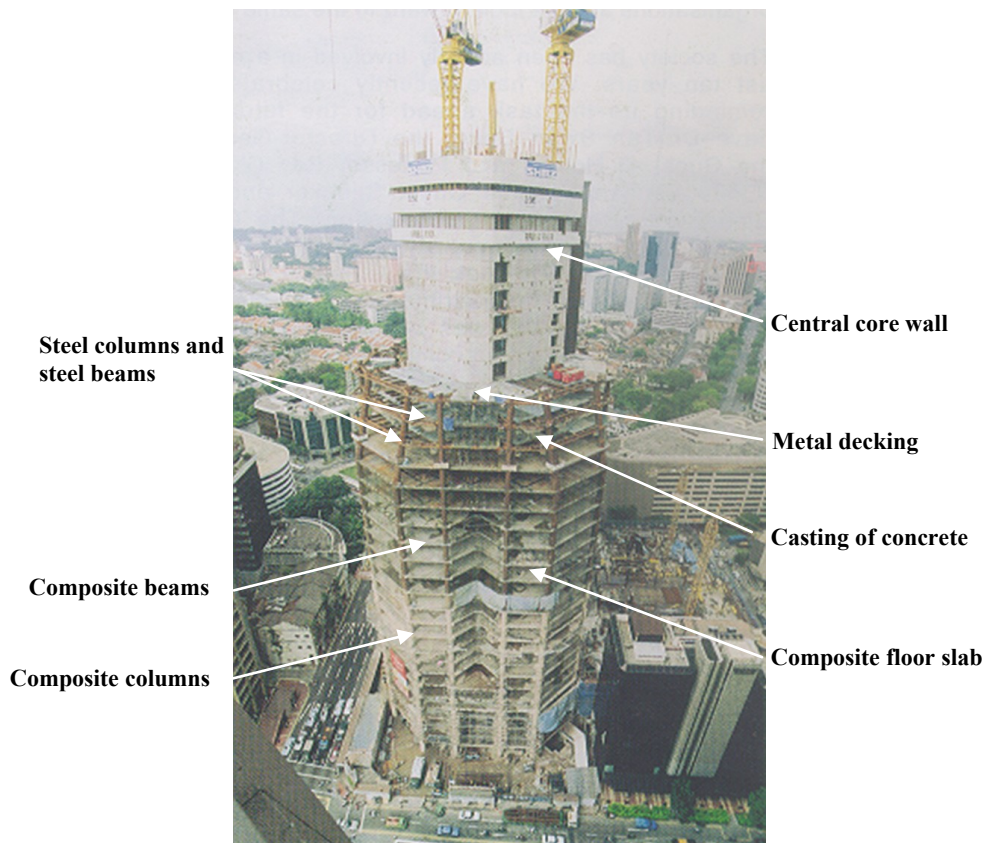


Figure 1.6: Composite construction of a 50-storey building (Liew, 2004)



Figure 1.7: Hollow circular steel columns before infilling with concrete (Liew, 2004)

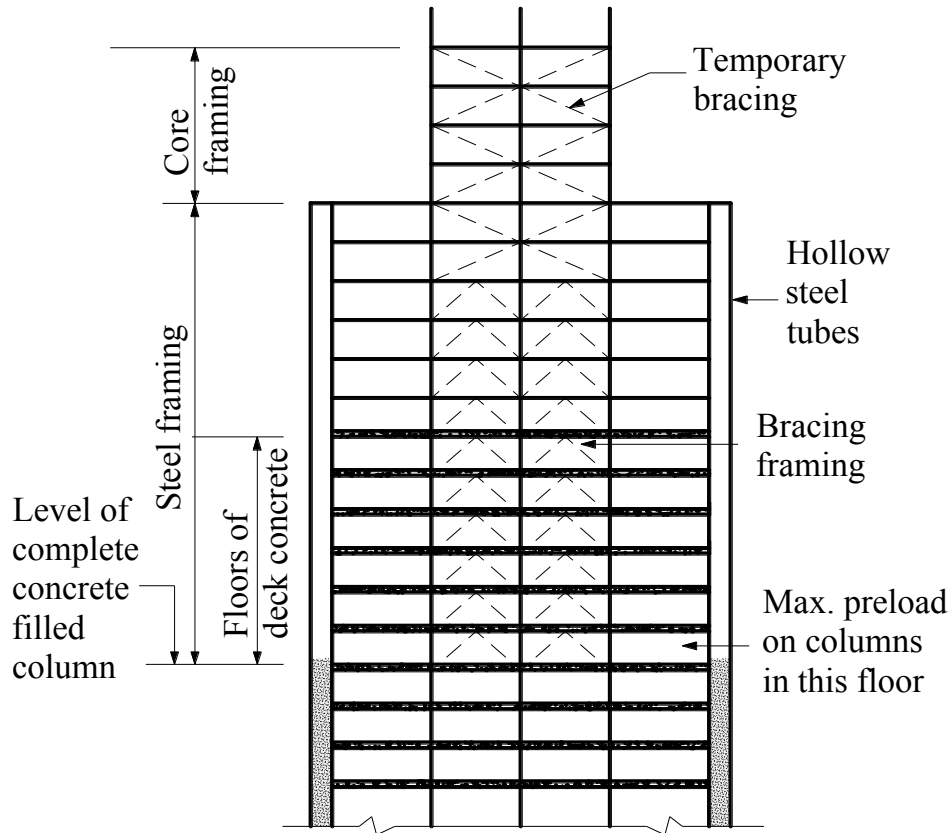


Figure 1.8: Fast-track construction sequence of a typical composite building

## Chapter 2 Literature Review

### 2.1 General

A general overview has been presented in Section 1.2.2 of **Chapter 1**, according to 1,948 test data samples collected from existing experimental investigations on *CFSTs* (including columns, beams and beam-columns) with non-slender hollow steel sections (at least class 3) subjected to static load. It indicates that most of the tests focus on *CFSTs* with normal strength materials and there are limited experiments in the range of high strength materials. In addition, there are also limited investigations on *CFST* columns with preload effect.

This chapter firstly reviews some significant literature on *CFSTs* with high strength concrete, high strength steel and preload effect, focusing on but not limited to experimental investigations. After that, current design guidelines for *CFST* columns recommended in Eurocode 4 (2004) and AISC 360-10 (2010) are briefly introduced and compared with each other.

### 2.2 *CFSTs* with High Strength Concrete

With the maturity of technology in developing high strength concrete, it is becoming more and more popular in construction, especially in composite columns where the

ductility of high strength concrete can be highly improved with the help of steel. In recent years, several experimental investigations have been reported on high strength concrete filled steel tube columns.

For the static axial behaviour, Liu et al (2003; 2005) presented some tests on concrete filled rectangular hollow steel sections involving high strength concrete in the range of cylinder strengths from 55MPa to 106MPa and steel yield strengths in the range from 300MPa to 550MPa. It was shown that Eurocode 4 could provide accurate predictions on average but with maximum underestimation up to 20% and overestimation up to 10%. Han et al (2005) tested 50 circular and square hollow structural steel stub columns with self-consolidating concrete of cube strengths between 50MPa and 90MPa and steel yield strengths in the range from 282MPa to 404MPa. The comparison showed that Eurocode 4 overestimated the ultimate strength by 0.6% for circular sections and 2.7% for square sections. Lue et al (2007) reported tests on 24 concrete filled square tubes with concrete cylinder strengths between 29MPa and 84MPa and steel yield strength 380MPa. It was revealed that Eurocode 4 provided conservative predictions. Yu et al (2008) carried out an investigation on 28 thin-walled hollow square and circular steel tubes employing self-consolidating concrete with cube strength 121.6MPa and steel yield strength 404MPa. The results showed that Eurocode 4 could provide conservative predictions on ultimate strength for circular sections but overestimated by 6% for square sections. These investigations have provided significant contributions to the research progress in the cross-sectional resistances of high strength concrete filled steel tube columns.

For the static flexural behaviour, Varma et al (2002a) investigated some 110MPa high strength concrete filled square steel tubes subjected to axial load and monotonically

increasing flexural loading. The steel yield strengths were in the range from 269MPa to 660MPa. The moment capacity could be accurately predicted by the American Concrete Institute code provisions. Gho and Liu (2004) studied the flexural behavior of 12 concrete filled rectangular steel hollow section specimens with high strength concrete of cylinder strengths between 56.3MPa and 90.9MPa and steel yield strengths in the range from 409MPa to 438MPa. It was shown that Eurocode 4 underestimated the flexural strengths by 11%. These researches are highly commendable for providing important information on the flexural performance of high strength concrete filled steel tube columns.

For the combined concentrically and eccentrically loaded behavior, Liu (2004; 2005; 2006) performed a series of tests on high strength concrete filled rectangular steel tube columns subjected to concentric and eccentric loading. The cylinder strengths of the high strength concrete were about 60MPa and 90MPa, and the steel yield strengths were about 495MPa and 550MPa. It was concluded that Eurocode 4 underestimated the concentrically loaded columns by 1% but overestimated the eccentrically loaded columns by less than 5%. These tests are noteworthy in that coupled different loading conditions were considered.

For the seismic behavior, Varma et al (2002b; 2004) conducted a series of tests on the seismic behavior of high strength concrete filled square beam columns subjected to constant axial load and cyclically varying flexural loading. Cylinder strength of the high strength concrete was up to 110MPa, and the steel yield strengths were about 269MPa, 471MPa and 660MPa. The results showed that the elastic flexural section stiffness under cyclic loading decreased rapidly due to tension cracking of concrete and local buckling of steel tubes. The total dissipated energy was dominated by the dissipated flexural energy in

the plastic hinge region. The investigations are important in that the performance in ductility was discussed as well as the ultimate resistances.

### **2.3 CFSTs with High Strength Steel**

High strength steel has attracted researchers' interest in its application for multi-storey and high-rise constructions. Several experimental investigations on concrete filled high strength steel tubes have been reported.

Mursi and Uy (2004) presented an investigation on the resistance of slender concrete filled high strength steel box columns, employing thin walled steel sections to consider elastic and inelastic local buckling. The yield strength of the high strength steel was about 761MPa and the cylinder compressive strength of concrete was about 20MPa. A numerical model was developed in order to study the behavior of slender concrete filled high strength steel columns incorporating material and geometric non-linearity. The numerical results were verified with experimental results. Finally, it proposed a design recommendation for strength evaluation of slender composite columns using high strength steel plates with thin-walled steel sections.

Uy (2001) carried out an experimental investigation on the ultimate resistance of short concrete filled high strength steel box columns. The yield strength of the high strength steel was about 750MPa and the cylinder compressive strength of concrete was about 30MPa. A numerical model was presented and calibrated with test results. The test results and numerical predictions were compared with predictions by Eurocode 4 approach. The comparison showed that Eurocode 4 approach overestimated the ultimate resistance.



Local buckling is the most significant problem and it may limit the usage of the strength of high strength steel, because only very thin wall thickness is needed for high strength steel to work with normal strength concrete. Liang et al (2007) carried out finite element analyses on the local and post-local buckling behavior of steel plates in concrete filled thin-walled steel tube beam-columns. Initial geometric imperfections and residual stresses presented in steel plates, material yielding and strain hardening were taken into account in the nonlinear analysis. Based on the results, a set of design formulae were proposed to predict the critical local buckling and ultimate strength of steel plates in concrete filled steel tube beam-columns.

Uy (2008) investigated the stability and ductility characteristics of concrete filled columns using high performance steels, including both high strength steel with yield strength 690MPa and stainless steel with 0.2% proof stress 340MPa which exhibit improved strength as well as corrosion resistance, hardness, etc. Local and overall buckling might be the most significant problem. Both experimental and theoretical studies were carried out to solve the problem, and the results were compared with current design procedures to provide some suggestions.

## **2.4 CFSTs with Preload Effect**

Some numerical analyses and experimental investigations have been conducted to investigate the preload effect on the behaviour of circular and square *CFST* stub and intermediate columns.

Xiong and Zha (2007) carried out finite element analyses of preload effect on the behavior of circular and square *CFST* columns. The numerical estimations were verified with some published experimental results. Parametric studies were conducted including initial preload ratio, slenderness, eccentricity ratio, material strengths, etc. Based on the numerical results, some formulae were proposed to predict the preload effect on the capacities of *CFST* columns.

Han and Yao (2003) tested 19 preloaded concrete filled circular and square steel tube specimens subjected to axial or eccentric compression. Based on the test results, some formulae were proposed by using regression analysis method, considering several parameters such as preload ratio, slenderness ratio, steel contribution ratio, and so on.

Zhang et al (1997) conducted an experimental investigation on 29 eccentrically compressed concrete filled steel tube specimens with or without preload. The results showed that the capacities could be reduced by 2%-8% if preload ratio did not exceed 0.65.

Huang et al (1996) conducted a numerical and experimental investigation on axially compressed concrete filled steel tube specimens with or without preload. A numerical model was proposed and compared with some test results. The results showed that significant preload effect on the capacities might be produced for long columns.

Uy and Das (1997) developed a linear folded plate finite element method to analyze another kind of preload problem in *CFST* columns during construction. The preload refers to a hydrostatic lateral pressure on internal surface of steel tube, and it is caused by wet

concrete during concrete pumping. The hydrostatic load may cause excessive lateral deflections and it is required to determine adequate slenderness limits in order to ensure these deflections are kept to an acceptable limit. Based on their work, the authors provide guidelines to solve the problem.

## 2.5 Current Design Guidelines for CFST Columns

### 2.5.1 Eurocode 4

Generally, CFST columns can be designed according to the resistance interaction curve for combined compression and bending shown in Figure 2.1 and the ultimate resistance  $(N_u, M_u)$  can be calculated by:

$$\left\{ \begin{array}{l} AC: \frac{N_u - N_{pm,Rk}}{N_{pl,Rk} - N_{pm,Rk}} + \frac{M_u / \alpha_M}{M_{pl,Rk}} = 1 \\ CD: \frac{N_u - 0.5N_{pm,Rk}}{N_{pm,Rk} - 0.5N_{pm,Rk}} + \frac{M_u / \alpha_M - M_{pl,Rk}}{M_{max,Rk} - M_{pl,Rk}} = 1 \\ BD: \frac{N_u}{0.5N_{pm,Rk}} + \frac{M_u / \alpha_M - M_{max,Rk}}{M_{pl,Rk} - M_{max,Rk}} = 1 \end{array} \right. \quad (2.1)$$

where  $\alpha_M$  is a coefficient taken as 0.9 for S235 and S355 steel inclusive and 0.8 for steel grades S420 and S460.

#### 2.5.1.1 Point A: pure axial compression

Point A in Figure 2.1 represents the plastic cross-sectional resistance under compression which can be calculated for sections without reinforcement by:

$$N_A = N_{pl,Rk} = A_a f_y + A_c f_{ck} \quad (2.2)$$

where  $A_a$  is the cross-sectional area of steel tube,  $A_c$  is the cross-sectional area of concrete core,  $f_y$  is the yield strength of steel tube, and  $f_{ck}$  is the compressive strength of concrete.

Confinement effect may be considered for concrete-filled circular tubes with relative slenderness not exceeding 0.5 and the ratio of eccentricity to diameter less than 0.1, and then the plastic cross-sectional resistance under compression can be calculated by:

$$N_A = N_{pl,Rk} = \eta_a A_a f_y + A_c f_{ck} \left( 1 + \eta_c \frac{t}{d} \frac{f_y}{f_{ck}} \right) \quad (2.3)$$

where  $t$  is the thickness and  $d$  is the diameter of steel tube.

For members under concentric compression, the values  $\eta_a = \eta_{a0}$  and  $\eta_c = \eta_{c0}$  are given by:

$$\begin{cases} \eta_{a0} = 0.25(3 + 2\lambda) & (\text{but } \leq 1.0) \\ \eta_{c0} = 4.9 - 18.5\lambda + 17\lambda^2 & (\text{but } \geq 0) \end{cases} \quad (2.4)$$

where  $\lambda$  is the relative slenderness defined as:

$$\lambda = \sqrt{N_{pl,Rk} / N_{cr}} = \sqrt{\frac{N_{pl,Rk}}{\pi^2 (EI)_{eff} / L_e^2}} = \sqrt{\frac{N_{pl,Rk}}{\pi^2 (E_a I_a + 0.6 E_{cm} I_c) / L_e^2}} \quad (2.5)$$

For members under combined compression and bending with the ratio of eccentricity to diameter less than 0.1, the values  $\eta_a$  and  $\eta_c$  should be determined by:

$$\begin{cases} \eta_a = \eta_{a0} + (1 - \eta_{a0})(10e / d) \\ \eta_c = \eta_{c0}(1 - 10e / d) \end{cases} \quad (2.6)$$

#### 2.5.1.2 Point B: pure flexure

Point B in Figure 2.1 represents the plastic cross-sectional resistance under pure bending which can be calculated for sections without reinforcement by:

$$M_B = M_{pl,Rk} = (W_{pa} - W_{pan})f_y + 0.5(W_{pc} - W_{pcn})f_{ck} \quad (2.7)$$

where  $W_{pa}$  and  $W_{pc}$  are the plastic section moduli for the steel section and concrete core section, and  $W_{pan}$  and  $W_{pcn}$  are the plastic section moduli of the corresponding components within the region of  $2h_n$  from the middle line of the composite section where  $h_n$  is the depth of the neutral axis from the middle line. The formulae for calculation of sectional properties are listed in **Appendix I**.

### 2.5.1.3 Point C

Point C in Figure 2.1 is an intermediate point where:

$$\begin{cases} N_C = N_{pm,Rk} = f_{ck}A_c \\ M_C = M_B \end{cases} \quad (2.8)$$

### 2.5.1.4 Point D: maximum moment resistance

Point D in Figure 2.1 represents the maximum plastic cross-sectional resistance moment in the presence of a compressive normal force can be calculated by:

$$\begin{cases} N_D = \frac{1}{2}N_C \\ M_D = M_{\max,Rk} = W_{pa}f_y + 0.5W_{pc}f_{ck} \end{cases} \quad (2.9)$$

### 2.5.1.5 Slenderness effect

The slenderness effect can be considered by taking into account member imperfections and amplifying the greatest first-order moment force within the member length. For

*CFST* columns without reinforcement, the imperfection is taken as  $L/300$ . The amplification factor,  $k$ , can be conservatively taken as:

$$k = \frac{1}{1 - N / N_{cr,eff}} \quad (2.10)$$

where  $N_{cr,eff} = 0.9\pi^2 (E_a I_a + 0.5E_c I_c) / L^2$  is the critical load considering the member's effective stiffness.

For concentrically and eccentrically compressed slender *CFST* beam-columns, the moment resistance  $M_u$  in Equation (2.1) can be expressed as:

$$M_u = kN_u e \quad (2.11)$$

where  $e = e_0 + e_i$ ,  $e_0$  is the eccentricity of loading at the member ends and  $e_i$  is the member imperfection.

By incorporating Equation (2.11), Equation (2.1) can be expressed for concentrically and eccentrically compressed slender *CFST* beam-columns as:

$$\left\{ \begin{array}{l} AC: \frac{N_u - N_{pm,Rk}}{N_{pl,Rk} - N_{pm,Rk}} + \frac{kN_u e / \alpha_M}{M_{pl,Rk}} = 1 \\ CD: \frac{N_u - 0.5N_{pm,Rk}}{N_{pm,Rk} - 0.5N_{pm,Rk}} + \frac{kN_u e / \alpha_M - M_{pl,Rk}}{M_{max,Rk} - M_{pl,Rk}} = 1 \\ BD: \frac{N_u}{0.5N_{pm,Rk}} + \frac{kN_u e / \alpha_M - M_{max,Rk}}{M_{pl,Rk} - M_{max,Rk}} = 1 \end{array} \right. \quad (2.12)$$

Alternatively, a simplified method can be used for slender *CFST* beam-columns under concentric compression only, and the overall buckling resistance may be evaluated by:

$$N_u = \chi N_{pl,Rk} \quad (2.13)$$

where  $\chi$  is the slenderness reduction factor expressed as:

$$\chi = \frac{1}{\Phi + \sqrt{\Phi^2 - \lambda^2}} \quad \text{but } \chi \leq 1 \quad (2.14)$$

where  $\Phi = 0.5[1 + \alpha(\lambda - 0.2) + \lambda^2]$ , and  $\alpha = 0.21$  is the imperfection factor for *CFST* columns without reinforcement. For relative slenderness  $\lambda \leq 0.2$ , the slenderness reduction may be ignored and only cross sectional resistance checks apply.

#### 2.5.1.6 Limitations

There are several significant limitations to adopt Eurocode 4 for the design of composite *CFST* columns as follows:

- (a) It is limited to structural steel grades S235 to S460 and normal weight concrete of strength classes C20/25 to C50/60;
- (b) The steel contribution ratio,  $\delta = A_a f_{yd} / N_{pl,Rd}$ , should be in the range from 0.2 to 0.9;  $N_{pl,Rd}$  is the design value of plastic cross-sectional resistance under compression, which is calculated by Equation (2.2) with design value, instead of characteristic value, of material strength, i.e.  $f_{yd} = f_y / \gamma_a$  and  $f_{cd} = f_{ck} / \gamma_c$  where  $\gamma_a = 1.0$  and  $\gamma_c = 1.5$ ;
- (c) The effect of local buckling of the cross-sections may be neglected, provided that the maximum values of Table 2.1 are not exceeded;
- (d) By using simplified method, the relative slenderness should not exceed 2.0, the ratio of the depth to the width of the composite cross-section should be within the

limits 0.2 and 5.0, and the longitudinal reinforcement used in calculation should not exceed 6% of the concrete area.

## 2.5.2 AISC 360-10

Only the design method by using resistance interaction curves for compact sections will be introduced in this section, since most hollow steel sections in practice are compact according to the classification shown in Table 2.2 as recommended in AISC 360-10.

The general resistance interaction curves are plotted in Figure 2.2 as referred to *AISC Steel Construction Manual Design Examples V14.0* (2011).

### 2.5.2.1 Point A: pure axial compression

Point A in Figure 2.2 represents the plastic cross-sectional resistance under compression which can be calculated for sections without reinforcement by:

$$P_A = P_{n0} = f_y A_a + C_2 f_{ck} A_c \quad (2.15)$$

where  $C_2 = 0.85$  for rectangular sections and  $0.95$  for round sections.

### 2.5.2.2 Point B: pure flexure

Point B in Figure 2.2 represents the plastic cross-sectional resistance under pure bending which can be calculated for sections without reinforcement by:

$$M_B = (W_{pa} - W_{pan}) f_y + 0.5 (W_{pc} - W_{pcn}) (C_2 f_{ck}) \quad (2.16)$$



### 2.5.2.3 Point C

Point C in Figure 2.2 is an intermediate point where:

$$\begin{cases} P_C = C_2 f_{ck} A_c \\ M_C = M_B \end{cases} \quad (2.17)$$

### 2.5.2.4 Point D: maximum moment resistance

Point D in Figure 2.2 represents the maximum plastic cross-sectional resistance moment in the presence of a compressive normal force calculated by:

$$\begin{cases} P_D = \frac{1}{2} P_C \\ M_D = W_{pd} f_y + 0.5 W_{pc} (C_2 f_{ck}) \end{cases} \quad (2.18)$$

### 2.5.2.5 Point E: optional

Point E in Figure 2.2 is an optional point that helps better define the interaction curve.  $h_E = h_n + h/4$ .

### 2.5.2.6 Slenderness effect

A slenderness reduction factor,  $\chi'$ , is defined as:

$$\begin{cases} \frac{P_{n0}}{P_e} \leq 2.25: \chi' = \frac{P_n}{P_{n0}} = 0.658 \frac{P_{n0}}{P_e} \\ \frac{P_{n0}}{P_e} > 2.25: \chi' = \frac{P_n}{P_{n0}} = 0.877 \frac{P_e}{P_{n0}} \end{cases} \quad (2.19)$$

where  $P_e$  is the elastic critical buckling load determined by

$$\begin{cases} P_e = \frac{\pi^2 (EI)_{eff}}{L_e^2} = \frac{\pi^2 (E_a I_a + C_3 E_{cm} I_c)}{L_e^2} \\ C_3 = 0.6 + 2 \frac{A_a}{A_c + A_a} \leq 0.9 \end{cases} \quad (2.20)$$

The slenderness reduction is considered by multiplying the compressive cross-sectional resistance by the reduction factor but without reduction in moment resistance as shown in Figure 2.2.

#### 2.5.2.7 Limitations

There are several significant limitations to adopt AISC 360-10 for the design of composite *CFST* columns as follows:

- (a) It is limited to structural steel yielding strength up to 525MPa, normal weight concrete of cylinder strength from 21MPa to 70MPa, and light weight concrete of cylinder strength from 21MPa to 42MPa;
- (b) The cross-sectional area of the steel section shall comprise at least 1% of the total composite cross section;
- (c) Composite sections should be classified for local buckling according Table 2.2.

### 2.5.3 Comparison between the two codes

The design guidelines for *CFST* columns recommended in the two codes are similar but with several differences as follows:

- (a) A reduction in concrete strength is considered in AISC 360-10 as 0.85 for rectangular sections and 0.95 for circular sections, while no reduction in concrete strength is considered in Eurocode 4;
- (b) The confinement effect on concrete strength can be considered in Eurocode 4 for circular sections with relative slenderness not exceeding 0.5 and eccentricity ratio less than 0.1 while it is not considered in AISC 360-10;
- (c) A reduction factor  $\alpha_M$  in moment resistance is considered in Eurocode 4 according to different steel grades while it is not considered in AISC 360-10;
- (d) The contribution of concrete section to the effective composite stiffness  $(EI)_{\text{eff}}$  is taken as  $[0.6 + 2A_a/(A_a+A_c)]E_{cm}I_c$  in AISC 360-10 while it is only taken as  $0.6E_{cm}I_c$  in Eurocode 4;
- (e) The slenderness effect is considered in Eurocode 4 by taking into account member imperfections and amplifying the greatest first-order moment force within the member length while it is considered in AISC 360-10 by multiplying the cross-sectional compressive resistance by a reduction factor but with no reduction in moment resistance;

- (f) The values of the wall slenderness limits of hollow steel tube sections stipulated in AISC 360-10 is larger than those stipulated in Eurocode 4 for compact sections, especially for rectangular sections (refer to Table 2.1 and Table 2.2).

## 2.6 Summary

A detailed literature review has been presented in this chapter, focusing on the topics of *CFSTs* with high strength concrete, high strength steel and preload effect. It is found that more work should be done to verify the applicability of high strength materials in *CFSTs* and to assess the preload effect on the behaviour of *CFSTs*.

In addition, current design guidelines for *CFSTs* recommended in Eurocode 4 (2004) and AISC 360-10 (2010) have been introduced in this chapter. They are only applicable for normal strength concrete and steel, and the preload effect is not covered. Therefore, sufficient work should be done to extend current design guidelines or propose new provisions for *CFSTs* with high strength concrete, high strength steel or preload effect.

Essentially, the rationales of design guidelines in the two codes are the same. There are just several minor differences, such as different values taken for some design factors. Therefore, only Eurocode 4 (2004) will be assessed for *CFST* columns in following chapters.

Table 2.1: Maximum values ( $d/t$ ) and ( $h/t$ ) with  $f_y$  in MPa as recommended in EC4

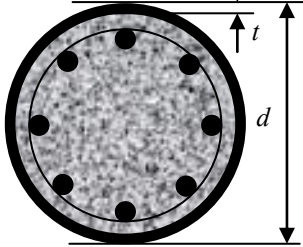
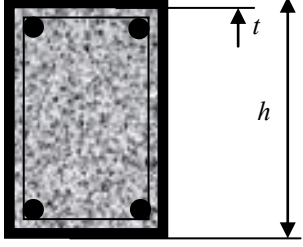
Cross-section		Max values
Circular hollow steel sections		$\max(d/t) = 90 \frac{235}{f_y}$
Rectangular hollow steel sections		$\max(h/t) = 52 \sqrt{\frac{235}{f_y}}$

Table 2.2: Classification for local buckling as recommended in AISC 360-10

Description of element	Ratio	Compact/ Noncompact	Noncompact/ Slender	Maximum Permitted
(a) Subject to axial compression				
Walls of rectangular hollow steel sections and boxes of uniform thickness	$b/t$ $h/t$	$2.26 \sqrt{\frac{E_a}{f_y}}$	$3.00 \sqrt{\frac{E_a}{f_y}}$	$5.00 \sqrt{\frac{E_a}{f_y}}$
Round hollow steel sections	$d/t$	$0.15E_a/f_y$	$0.19E_a/f_y$	$0.31E_a/f_y$
(b) Subject to flexure				
Flanges of rectangular hollow steel sections and boxes of uniform thickness	$b/t$	$2.26 \sqrt{\frac{E_a}{f_y}}$	$3.00 \sqrt{\frac{E_a}{f_y}}$	$5.00 \sqrt{\frac{E_a}{f_y}}$
Webs of rectangular hollow steel sections and boxes of uniform thickness	$h/t$	$3.00 \sqrt{\frac{E_a}{f_y}}$	$5.70 \sqrt{\frac{E_a}{f_y}}$	$5.70 \sqrt{\frac{E_a}{f_y}}$
Round hollow steel sections	$d/t$	$0.09E_a/f_y$	$0.31E_a/f_y$	$0.31E_a/f_y$

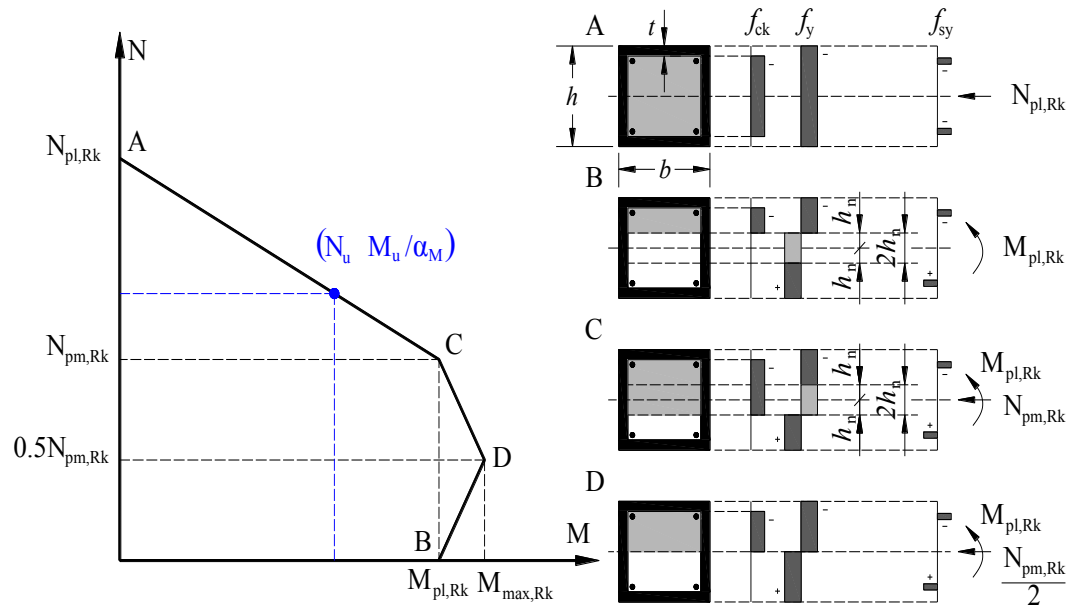


Figure 2.1: Resistance interaction curve as recommended in EC4

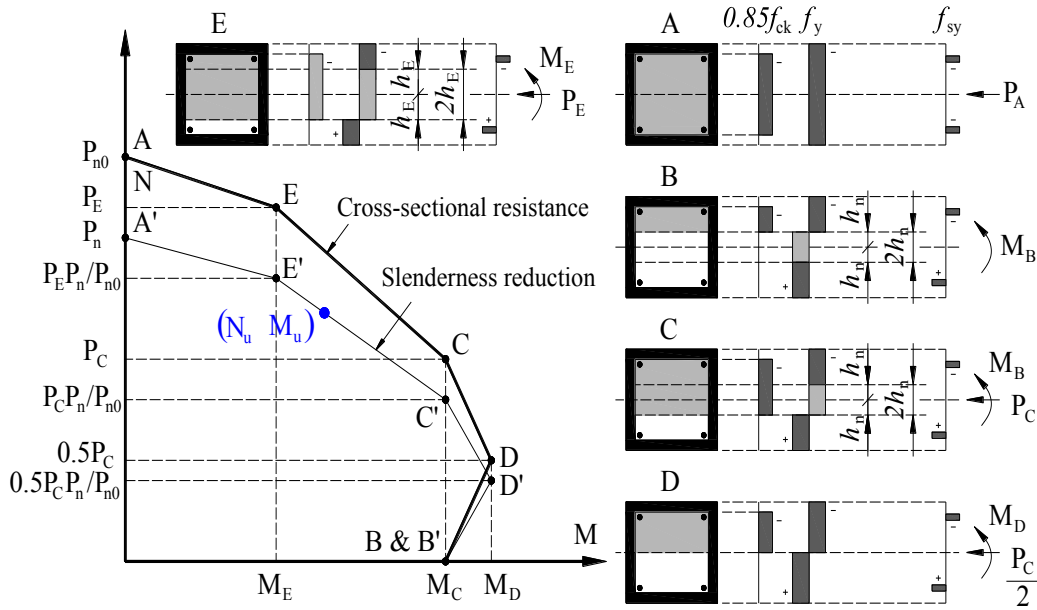


Figure 2.2: Resistance interaction curve as recommended in AISC 360-10

## Chapter 3 Basic Mechanical Properties of Ultra High Strength Concrete

### 3.1 General

As stated in **Chapter 1** and **Chapter 2**, it is necessary to do more investigations on the application of high strength concrete in *CFST* columns. Different mix proportion designs for ultra high strength concrete (*UHSC*) have been developed for this study. Prior to the investigations on composite columns, this chapter presents an experimental investigation on the basic mechanical material properties of *UHSC* with different mix proportions and maximum sizes of coarse aggregates, including workability, density, compressive strength, splitting tensile strength, flexural strength, static modulus of elasticity and Poisson's ratio, referred to relevant ASTM standards. Based on the experimental results, some recommendations for the design of *UHSC* will be provided.

### 3.2 Experimental Investigation

#### 3.2.1 Basic materials

The basic materials used in the study to produce *UHSC* are Ducorit® D4, ordinary granite coarse aggregates and water.

#### 3.2.1.1 Ducorit® D4

Ducorit® D4 is one of the commercial Ducorit® products provided by Densit A/S in Denmark. It is a type of ultra high performance cement-based material made from cementitious mineral powder, super plasticizer and fine mineral aggregates (bauxite). Sieve analysis was conducted to check the size grading details. The test results are shown in Table 3.1, and the average value curve for the four samples is shown in Figure 3.1. It can be observed that the maximum grain size is less than 4.75mm and 49% is less than 0.6mm on average. The sieved Sample 1 of Ducorit® D4 is shown in Figure 3.2.

#### 3.2.1.2 Coarse aggregates

Two different maximum sizes of crushed ordinary granites were used as the coarse aggregates. One is about 10mm and the other is about 20mm. Sieve analysis was conducted to determine the grading of the coarse aggregates. The test results are summarized in Table 3.2, and they are shown in Figure 3.3 for the coarse aggregates with maximum size of about 10mm and in Figure 3.4 for the coarse aggregates with maximum size of about 20mm, compared with the grading requirements for coarse aggregates size number 8 and 67 respectively as stated in ASTM C33-07. The physical properties for the coarse aggregates are listed in Table 3.3.

### 3.2.2 Mix proportions

The *UHSC* used in this study was produced by mixing different proportions of coarse aggregates and Ducorit® D4. Based on the void ratio of the coarse aggregates shown in Table 3.3, the maximum volume proportions for 10mm and 20mm coarse aggregates



could be up to 50.4% and 56.2% respectively. In this study, two different coarse aggregates volume proportions of about 20% and 40% were adopted. For comparison, the mix proportion design without coarse aggregates was also investigated. Based on the mix proportion of Ducorit® D4 which has been provided by the company, all the other mix proportions for UHSC are designed and shown in Table 3.4.

### 3.2.3 Specimens

To consider the curing age effect on the mechanical properties, the compressive strength, tensile strength, flexural strength and static modulus of elasticity were evaluated at different curing ages of 3, 7, 28 and 91 days. Therefore, a large amount of concrete specimens were needed, and then three batches of concrete were cast for each mix proportion design. All the specimens were prepared by placing fresh concrete into the dedicated moulds evenly. To ensure that the concrete specimens be well compacted, the specimens were vibrated before letting them to set. All the specimens were demoulded approximately 24 hours after casting. Then they were cured in an environment-controlled room till the targeted curing ages with the temperature maintained at  $23.0 \pm 2.0^{\circ}\text{C}$  and relative humidity greater than 90%, referred to ASTM C192/C192M-02. The number of specimens tested for each mix proportion design is shown in Table 3.5, where the specimens tested at 28days are from the three batches while the specimens tested at each of other curing ages are from the same batch.

### 3.2.4 Workability

Workability of the fresh concrete was tested using the slump flow test instead of the conventional slump test. The method uses the traditional slump cone and a base plate

which has a dimension of at least 900mm × 900mm. In this study, the slump cone was placed in an upright position instead of inverted position. Both set-ups are permitted as stated in ASTM C1611/C1611M-09b.

The slump flow spread is calculated by:

$$S_{flow} = \frac{d_{max} + d_{perp}}{2} \quad (3.1)$$

where  $d_{max}$  is the maximum spread and  $d_{perp}$  is the spread in the perpendicular direction.

The test values of slump flow spread for all the mix proportion designs are shown in Table 3.6 and Figure 3.5. It can be seen that the slump flow spread decreases as the proportion of coarse aggregates increases. This is expected as the coarse aggregates have angular and irregular shape and rough surface. The movement of adjacent particles has been restricted due to the higher inter-particle interface. Moreover, the angular shaped aggregates need more cement paste to be fully coated as they have high surface-to-volume ratio. Therefore, less cement paste will be available for lubrication effect. In addition, the slump flow spread increases as the nominal maximum size of coarse aggregates increases, because the paste needed to fully coat the coarse aggregates with bigger maximum size decreases. This can be justified by the decrease in void ratio of the coarse aggregates with bigger maximum size as shown in Table 3.3. Therefore, the smaller the proportion and the bigger the maximum size of coarse aggregates, the better is the workability.

### 3.2.5 Density

Density of all the concrete cylinder and cube specimens was tested right after they had been demoulded, by measuring the weight of concrete specimens in air and weight of concrete specimens immersed in water.

The density of the concrete specimens is calculated by:

$$\rho_c = \frac{w_{c,a}}{w_{c,a} - w_{c,w}} \rho_w \quad (3.2)$$

where  $w_{c,a}$  the weight in air,  $w_{c,w}$  is the weight in water, and  $\rho_w$  is the density of water. Referred to ASTM C39/C39M-05, it should be calculated to the nearest 10kg/m<sup>3</sup>.

The average test value of density for each mix proportion design is shown in Table 3.7 and Figure 3.6. It can be seen that the value of density decreases as the mix proportion of coarse aggregates increases, regardless of the nominal maximum size of coarse aggregates. Due to the lower density of coarse aggregates, the more the coarse aggregates, the lower is the concrete density.

### 3.2.6 Compressive properties

Compressive strength tests were conducted on both of cylinder and cube specimens at different curing ages.

### 3.2.6.1 Compressive cylinder strength

Both of 75mm ( $d$ )  $\times$  150mm ( $h$ ) and 100mm ( $d$ )  $\times$  200mm ( $h$ ) cylinder specimens were tested under compression, as listed in Table 3.5. Six cylinder specimens with dimension of 75mm ( $d$ )  $\times$  150mm ( $h$ ) were tested at the curing age of 28days only for each mix proportion design, and the results were compared with those obtained from 100mm ( $d$ )  $\times$  200mm ( $h$ ) cylinder specimens at the same curing age to check the size effect on compressive strength. Eighteen cylinder specimens with dimension of 100mm ( $d$ )  $\times$  200mm ( $h$ ) were tested at different curing ages for each mix proportion design, of which three specimens were tested at curing ages of 3, 7 and 91 days respectively and nine specimens were tested at curing age of 28 days with three specimens attached with strain gauges vertically at the mid-height to obtain the stress-strain relationship curves up to failure.

The compressive cylinder strength is calculated by:

$$f_{c,cyl} = \frac{4F}{\pi d^2} \quad (3.3)$$

where  $F$  is the maximum compressive load.

The average test values of compressive cylinder strength for each mix proportion design at different curing ages are listed in Table 3.8, and the strength of cylinder with dimension 100mm ( $d$ )  $\times$  200mm ( $h$ ) at different curing ages is also shown in Figure 3.7. It can be observed that the strength keeps increasing with the curing age and it is developed much faster at early ages. Compared with the value of the strength at 28 days, 70% ~ 80% strength can be achieved within the first 3 days and 80% ~ 90% strength can be achieved

within the first week. In addition, the strength at curing age of 13 weeks is only higher by no more than 13%.

### 3.2.6.2 Compressive cube strength

Fifteen cube specimens with dimension of 100mm ( $b$ )  $\times$  100mm ( $b$ )  $\times$  100mm ( $b$ ) were tested at different curing ages for each mix proportion design as shown in Table 3.5, of which three specimens were tested at curing ages of 3, 7 and 91 days respectively, and six specimens were tested at curing age of 28 days.

The compressive cube strength is calculated by:

$$f_{c,cube} = \frac{F}{b^2} \quad (3.4)$$

The average test values of compressive cube strength for each mix proportion design at different curing ages are shown in Table 3.9 and Figure 3.8. Similar to compressive cylinder strength, it can also be observed that the cube strength keeps increasing with the curing age and it is developed much faster at early ages. Compared with the value of the strength at 28 days, 70% ~ 80% strength can be achieved within the first 3 days and 80% ~ 90% strength can be achieved within the first week. In addition, the strength at curing age of 13 weeks is only higher by no more than 13%.

### 3.2.6.3 Modulus of elasticity and Poisson's ratio

As listed in Table 3.5 for modulus of elasticity tests, twenty-seven cylinder specimens with dimension of 100mm ( $d$ )  $\times$  200mm ( $h$ ) were tested at different curing ages for each

mix proportion design, of which six specimens were tested at curing ages of 3 and 7 days respectively, twelve specimens were tested at curing age of 28 days with three specimens attached with additional strain gauges at the mid-height to measure the lateral strain for the calculation of the Poisson's ratio, and three specimens were tested at curing age of 91 days. These tests were conducted by the same Denison compression machine used for ultimate compressive strength tests, loaded up to 40% of the ultimate compressive strength. The shortening displacement was measured by attaching an extensometer. Since these tests were non-destructive, the cylinder specimens were re-used to do ultimate compressive and splitting tensile strength tests.

The static modulus of elasticity and Poisson's ratio are calculated by:

$$E_{cm} = \frac{\sigma_2 - \sigma_1}{\varepsilon_2 - 0.000050} \quad (3.5)$$

$$\nu = \frac{\varepsilon_{t2} - \varepsilon_{t1}}{\varepsilon_2 - 0.000050} \quad (3.6)$$

where  $\sigma_2$  is the stress at 40% of ultimate strength,  $\sigma_1$  is the stress at compressive strain 0.000050,  $\varepsilon_2$  and  $\varepsilon_{t2}$  are the compressive strain and hoop tensile strain at 40% of ultimate strength, and  $\varepsilon_{t1}$  is the hoop tensile strain at compressive strain 0.000050.

The average test values of modulus of elasticity and Poisson's ratio for each mix proportion design at different curing ages are shown in Table 3.10 and Figure 3.9. It can be observed that the modulus of elasticity keeps increasing with the curing age and it is developed much faster at early ages. Compared with the value at 28 days, more than 86% strength can be achieved within the first 3 days and more than 93% strength can be achieved within the first week. In addition, the value at curing age of 13 weeks is only higher no more than 5%. The Poisson's ratio of UHSC at curing age of 28 days varies

from 0.21 to 0.23, which is slightly higher than that of conventional normal strength concrete in the range from 0.18 to 0.20.

#### 3.2.6.4 Compressive stress-strain relationship

For each mix design, there are three cylinder specimens tested at curing age of 28 days with stain gauges to obtain the compressive stress-strain curves as shown in Figure 3.10. It can be observed that there are no significant softening and degradation phases. Therefore, the *UHSC* investigated in this study is very brittle and it behaves in a quite linear compressive stress-strain relationship.

To assess the linearity of compressive stress-strain responses, the secant modulus  $E_{0.95}$  at 95% of the peak stress is compared with the elastic modulus  $E_{cm}$  as defined in Section 3.2.6.3 and the ratio of  $E_{cm}/E_{0.95}$  is used as an indicator for linearity as shown in Table 3.11. The ratio of *UHSC* ranges from 1.09 to 1.14, which is much smaller than that of normal strength concrete. For normal weight concrete, the ratio is approximately 3.5 for concrete with compressive strength of 7MPa and 1.25 for concrete with compressive strength of 70MPa (Popovics, 1998). The smaller the ratio, the better is the linearity behaviour. Therefore, *UHSC* exhibits a better performance than normal weight concrete in term of linearity behaviour.

#### 3.2.6.5 Cylinder strength versus cube strength

The compressive strength values of cylinder ( $d = 100\text{mm}$ ) and cube ( $b = 100\text{mm}$ ) specimens tested at the same curing age for the same mix are compared with each other as shown in Table 3.12 and Figure 3.11. The ratio of compressive cylinder strength to cube

strength ranges from 0.95 to 1.08, with a mean value of 1.02 and standard deviation of 0.04. Linear least-squared best fit line, which is forced through the origin, is plotted in Figure 3.11 to examine the relationship between the compressive cylinder strength and cube strength. It can be observed that the relationship can be approximately expressed as:

$$f_{cm,cyl,100} = 1.02 f_{cm,cube,100} \quad (3.7)$$

which is different from normal strength concrete. For concrete classes from C12/15 to C60/75, the compressive cylinder strength is about 80% of cube strength; for concrete classes from C60/75 to C90/105, the compressive cylinder strength is 15MPa lower than cube strength.

For normal strength concrete during the compressive testing, micro-cracks are initiated under high stress level (higher than 40% compressive strength) but they may be delayed or prevented from propagating by coarse aggregates. With the increase in the amount of micro-cracks, significant expanding in radial direction is developed but it is constrained at the two ends due to friction effect. For shorter specimens, the friction constraint effect is stronger, leading to a higher strength. Therefore, the cube strength is higher than cylinder strength for normal strength concrete. However, for the ultra-high strength concrete tested in this study, it was much more brittle. Once micro-cracks were initiated, the coarse aggregates on the propagating path were instantly crushed through and the specimens were failed. Therefore, the specimens performed almost in elastic behaviour up to failure, and there was no significant expanding in radial direction. The friction constraint effect could be ignored. Therefore, the cylinder strength was almost the same as the cube strength for the ultra-high strength concrete tested in this study.



### 3.2.6.6 Scale effect

To assess the scale effect on compressive cylinder strength, the compressive strength of cylinder with diameter 100mm is compared with that of cylinder with diameter 75mm at curing age of 28 days, as shown in Table 3.13 and Figure 3.12. The ratio of compressive strength of 75mm cylinder to that of 100mm cylinder ranges from 0.93 to 0.97, with a mean value of 0.942 and standard deviation of 0.014. Linear least-squared best fit line, which is forced through the origin, is plotted in Figure 3.12 to examine the relationship between the compressive strength of 75mm cylinder and that of 100mm cylinder. It can be observed that the relationship can be approximately expressed as:

$$f_{cm,cyl,75} = 0.94 f_{cm,cyl,100} \quad (3.8)$$

which is different from normal strength concrete. For normal strength concrete, the compressive strength of 75mm cylinder is about 5% higher than that of 100mm cylinder. For high strength concrete, Patnaik and Patnaikuni (2002) investigated the correlation of strength of 75mm diameter and 100mm diameter cylinders for concrete in the range from 110MPa to 160MPa, and the test results indicated that the strength difference between 75mm diameter cylinders and 100mm diameter cylinders could be ignored for concrete in the range from 110MPa to 160MPa and the strength of 75mm diameter cylinders might be smaller than that of 100mm diameter cylinders for concrete with strength higher than 150MPa, which is similar to the test results of this study. For the ultra-high strength concrete tested in this study, the friction constraint effect at the two ends during compressive testing could be ignored. However, for smaller specimens, the effect of imperfections such as loading eccentricity should be stronger, leading to a lower strength. Therefore, the strength of 75mm diameter cylinders was lower than that of 100mm diameter cylinders for the ultra-high strength concrete tested in this study.

### 3.2.6.7 Effect of maximum coarse aggregate size

To assess the effect of maximum coarse aggregate size on compressive strength, the values of compressive strength for cube and cylinder specimens with different maximum sizes of coarse aggregates are compared with each other as shown in Table 3.14 and Figure 3.13. The ratio ranges from 0.979 to 1.040, with a mean value of 1.003 and standard deviation of 0.014. Linear least-squared best fit line, which is forced through the origin, is plotted in Figure 3.13 to examine the relationship between compressive strength of specimens with 10mm coarse aggregates and that of specimens with 20mm coarse aggregates. It can be observed that the compressive strength is independent on the maximum coarse aggregate size.

To assess the effect of maximum coarse aggregate size on modulus of elasticity, the values of modulus of elasticity for cylinder specimens with different maximum sizes of coarse aggregates are compared with each other as shown in Table 3.15 and Figure 3.14. The ratio ranges from 0.983 to 1.032, with a mean value of 1.014 and standard deviation of 0.018. Linear least-squared best fit line, which is forced through the origin, is plotted in Figure 3.14 to examine the relationship between modulus of elasticity of specimens with 10mm coarse aggregates and that of specimens with 20mm coarse aggregates. It can be observed that the smaller maximum size of coarse aggregates may lead to slighter lower value of modulus of elasticity. However, the differences are insignificant and they can be ignored.

In addition, it can be observed from Table 3.10 that larger maximum size of coarse aggregates may lead to smaller Poisson's ratio. The Poisson's ratio is 0.23 for specimens

with 10mm coarse aggregates and 0.21 for specimens with 20mm coarse aggregates. However, The Poisson's ratio is also 0.23 for specimens without coarse aggregates.

#### 3.2.6.8 Effect of coarse aggregate proportion

To assess the effect of coarse aggregate proportion on compressive strength as shown in Table 3.8 and Table 3.9, the values of compressive strength at curing age of 28 days for cube and cylinder specimens with different proportions of coarse aggregates are compared with each other as shown in Figure 3.15. To use 19% or 38% proportions of coarse aggregates, it leads to a reduction of about 3.8% and 9.6% respectively for compressive cube strength, 4.5% and 17.9% respectively for compressive 100mm-cylinder strength, and 7.8% and 20.1% respectively for compressive 75mm-cylinder strength. The compressive strength decreases as the proportion of coarse aggregates increases. In addition, the smaller the specimen size, the more is the reduction.

To assess the effect of coarse aggregate proportion on modulus of elasticity as shown in Table 3.10, the values of modulus of elasticity at curing age of 28 days for cylinder specimens with different proportions of coarse aggregates are compared with each other as shown in Figure 3.16. To use 19% or 38% proportions of coarse aggregates, it leads to a reduction of about 8.0% and 11.2% respectively in modulus of elasticity. The modulus of elasticity decreases as the mix proportion of coarse aggregates increases.

Furthermore, it can be observed from Table 3.10 that the Poisson's ratio is independent on the mix proportion of coarse aggregates.

### 3.2.7 Tensile properties

Referred to ASTM C496/C496M-04, splitting tensile strength tests were conducted on fifteen cylinder specimens with dimension of 100mm ( $d$ )  $\times$  200mm ( $h$ ) for each mix proportion design as shown in Table 3.5, of which three specimens were tested at curing ages of 3, 7 and 91 days respectively, and six specimens were tested at curing age of 28 days.

The splitting tensile strength is calculated by:

$$f_{ct,sp} = \frac{2F}{\pi dh} \quad (3.9)$$

where  $F$  is the maximum splitting force.

#### 3.2.7.1 Ultimate strength

The test results of splitting tensile strength tests are shown in Table 3.16 and Figure 3.17. It can be observed that the splitting tensile strength keeps increasing with the curing age and it is developed much faster at early ages. Compared with the value at 28 days, 78% ~ 87% strength can be achieved within the first 3 days and 85% ~ 93% strength can be achieved within the first week. In addition, the value at curing age of 13 weeks is only higher by no more than 11%.

#### 3.2.7.2 Effect of maximum coarse aggregate size

To assess the effect of maximum coarse aggregate size on splitting tensile strength, the values of splitting tensile strength for specimens with different maximum sizes of coarse

aggregates are compared with each other as shown in Table 3.17 and Figure 3.18. The ratio ranges from 0.974 to 1.021, with a mean value of 0.997 and standard deviation of 0.017. Linear least-squared best fit line, which is forced through the origin, is plotted in Figure 3.18 to examine the relationship between splitting tensile strength of specimens with 10mm coarse aggregates and that of specimens with 20mm coarse aggregates. It can be observed that the splitting tensile strength is independent on the maximum coarse aggregate size.

### 3.2.7.3 Effect of coarse aggregate proportion

To assess the effect of coarse aggregate proportion on splitting tensile strength as shown in Table 3.16, the values of splitting tensile strength of specimens at curing age of 28 days with different proportions of coarse aggregates are compared with each other as shown in Figure 3.19. To use 19% or 38% proportions of coarse aggregates, it leads to a reduction of about 20.94% and 24.40% respectively in splitting tensile strength. The splitting tensile strength decreases as the mix proportion of coarse aggregates increases.

### 3.2.8 Flexural properties

Referred to ASTM C78-02, flexural tensile strength tests were conducted under third-point loading on fifteen prism specimens with dimension of 100mm ( $b$ )  $\times$  100mm ( $h$ )  $\times$  400mm ( $l$ ) for each mix proportion design as shown in Table 3.5, of which three specimens were tested at curing ages of 3, 7 and 91 days respectively, and six specimens were tested at curing age of 28 days.

The flexural tensile strength (modulus of rupture) is calculated by:

$$f_{ct,r} = \frac{Fl_e}{bh^2} \quad (3.10)$$

where  $F$  is the maximum transverse force, and  $l_e = 300\text{mm}$  is the effective span.

### 3.2.8.1 Ultimate strength

The test results of flexural tensile strength tests are shown in Table 3.18 and Figure 3.20. It can be observed that the flexural tensile strength keeps increasing with the curing age and it is developed much faster at early ages. Compared with the value at 28 days, 83% ~ 84% strength can be achieved within the first 3 days and 88% ~ 93% strength can be achieved within the first week. In addition, the value at curing age of 13 weeks is only higher by no more than 16%.

### 3.2.8.2 Flexural tensile stress-deflection curves

For each mix design, there are three cylinder specimens tested at curing age of 28 days to obtain the flexural tensile stress versus deflection curves as shown in Figure 3.21. It can be observed that there are no significant softening and degradation phases, similar to the compressive stress-strain curves shown in Figure 3.10. Therefore, the *UHSC* investigated in this study is very brittle and it behaves in a quite linear flexural tensile stress-deflection relationship. By adding ordinary coarse aggregates, no significant improvement on the ductility of *UHSC* was observed. Once the ultimate strength was reached, a crack penetrated across the cross-section. In this study, the crack observed in each prism specimen was passing through the middle third of the span length and the aggregates were crushed along the cracking path.

#### 3.2.8.3 Effect of maximum coarse aggregate size

To assess the effect of maximum coarse aggregate size on flexural tensile strength, the values of flexural tensile strength for specimens with different maximum sizes of coarse aggregates are compared with each other as shown in Table 3.19 and Figure 3.22. The ratio ranges from 0.964 to 1.025, with a mean value of 0.985 and standard deviation of 0.019. Linear least-squared best fit line, which is forced through the origin, is plotted in Figure 3.22 to examine the relationship between flexural tensile strength of specimens with 10mm coarse aggregates and that of specimens with 20mm coarse aggregates. It can be observed that there is no significant influence of maximum coarse aggregate size on the flexural tensile strength.

#### 3.2.8.4 Effect of coarse aggregate proportion

To assess the effect of coarse aggregate proportion on flexural tensile strength as shown in Table 3.18, the values of flexural tensile strength of specimens at curing age of 28 days with different proportions of coarse aggregates are compared with each other as shown in Figure 3.23. To use 19% or 38% proportions of coarse aggregates, it leads to a reduction of about 9.80% and 17.34% respectively in flexural tensile strength. The flexural tensile strength decreases as the mix proportion of coarse aggregates increases.

### 3.3 Design Recommendations

A detailed experimental investigation on the basic mechanical properties has been presented in previous section, which is briefly summarized in Table 3.20 for several significant properties by focusing on the values at curing age of 28 days. However, in

practice for primary design, only few properties may be tested, and then the values of other properties would be estimated by using some empirical formulae. Based on the experimental investigation presented in previous section, some design recommendations will be proposed in this section.

### 3.3.1 Recommendations on compressive strength

Recommended in Eurocode 2 (2004) for normal weigh concrete from C12/15 to C90/105, the compressive strength of concrete at various ages  $f_{cm}(t)$  may be estimated by:

$$f_{cm}(t) = e^{\alpha \left(1 - \sqrt{\frac{28}{t}}\right)} f_{cm} \quad (3.11)$$

where  $\alpha$  is a coefficient which depends on the type of cement.

For the *UHSC* used in this study, based on regression analysis of the test values shown in Table 3.8 and Table 3.9, the value of  $\alpha$  is equal to 0.146 with an  $R^2$  value of 0.9463. Therefore, the compressive strength of *UHSC* at various ages  $f_{cm}(t)$  may be estimated by:

$$f_{cm}(t) = e^{0.146 \left(1 - \sqrt{\frac{28}{t}}\right)} f_{cm} \quad (3.12)$$

### 3.3.2 Recommendations on modulus of elasticity

Recommended in Eurocode 2 (2004) for normal weigh concrete from C12/15 to C90/105, the modulus of elasticity at various ages  $E_{cm}(t)$  may be estimated by:

$$E_{cm}(t) = (f_{cm}(t) / f_{cm})^{0.3} E_{cm} \quad (3.13)$$



For the UHSC used in this study, based on regression analysis of the test values shown in Table 3.8 and Table 3.10, the elastic modulus of UHSC at various ages  $E_{cm}(t)$  may be estimated by (with an  $R^2$  value of 0.9546):

$$E_{cm}(t) = (f_{cm}(t) / f_{cm})^{0.5} E_{cm} \quad (3.14)$$

In addition, as recommended in Eurocode 2 (2004), the modulus of elasticity at 28 days may be estimated by:

$$E_{cm} = 22000 \left( \frac{f_{cm}}{10} \right)^{0.3} \quad \text{in MPa} \quad (3.15)$$

Another formula recommended in ACI-318 (2008) for normal weight concrete is expressed as:

$$E_{cm} = 4730 \sqrt{f_{cm}} \quad \text{in MPa} \quad (3.16)$$

For the UHSC used in this study, based on regression analysis of the test values shown in Table 3.8 and Table 3.10, a better expression with an  $R^2$  value of 0.8395 is obtained as:

$$E_{cm} = 4590 \sqrt{f_{cm}} \quad \text{in MPa} \quad (3.17)$$

### 3.3.3 Recommendations on tensile strength

Recommended in Eurocode 2 (2004) for normal weigh concrete from C12/15 to C90/105, the tensile strength at various ages  $f_{ct}(t)$  can be determined by splitting tensile strength  $f_{ct,sp}(t)$  as:

$$f_{ct}(t) = 0.9 f_{ct,sp}(t) = 0.9 \left( e^{\alpha \left( 1 - \sqrt{\frac{28}{t}} \right)} \right)^{\beta} f_{ct,sp} \quad (3.18)$$

where  $\beta = 1$  for  $t < 28$  and  $\beta = 2/3$  for  $t \geq 28$ .

For the *UHSC* used in this study, it is found that the curves could be better fit the test values shown in Table 3.16 when  $\beta$  is taken as a constant of  $2/3$  throughout the time and  $\alpha$  is taken as the same value as that in Equation (3.12). The regression analysis displays an  $R^2$  value of 0.8876. Therefore, the splitting tensile strength of *UHSC* at various ages  $f_{ct,sp}(t)$  may be estimated by:

$$f_{ct,sp}(t) = \left( e^{0.146 \left( 1 - \sqrt{\frac{28}{t}} \right)} \right)^{2/3} f_{ct,sp} = e^{0.097 \left( 1 - \sqrt{\frac{28}{t}} \right)} f_{ct,sp} \quad (3.19)$$

In addition, as recommended in Eurocode 2 (2004), the tensile strength at 28 days may be estimated by:

$$\begin{cases} f_{ct} = 0.9 f_{ct,sp} = 0.30 f_{ck}^{2/3} & \leq C50 / 60 \\ f_{ct} = 0.9 f_{ct,sp} = 2.12 \ln(1.8 + f_{ck} / 10) & > C50 / 60 \end{cases} \quad (3.20)$$

Another formula recommended in ACI-318 (2008) for normal weight concrete is expressed as:

$$f_{ct,sp} = 0.56 \sqrt{f_{cm}} \quad \text{in MPa} \quad (3.21)$$

For the *UHSC* used in this study, a better estimation is:

$$f_{ct,sp} = 0.296 f_{cm}^{2/3} \quad (3.22)$$

based on regression analysis of the test results shown in Table 3.8 and Table 3.16 with an  $R^2$  value of 0.7517.

### 3.3.4 Recommendations on flexural tensile strength

Recommended in ACI-318 (2008) for normal weight concrete, the flexural tensile strength at 28 days can be estimated by:

$$f_{ct,r} = 0.6\sqrt{f_{cm}} \quad \text{in MPa} \quad (3.23)$$

For the *UHSC* used in this study, by regression analysis on the test results shown in Table 3.18, it is found that the power of  $f_{cm}$  has to take the value of 0.80 and scalar factor is 0.261 with an  $R^2$  value of 0.8668, i.e.:

$$f_{ct,r} = 0.261f_{cm}^{0.8} \quad (3.24)$$

## 3.4 Summary

A detailed experimental investigation on the basic mechanical properties of *UHSC* has been presented in this chapter. It is found that the *UHSC* could achieve ultra high strength but it was very brittle under uniaxial compression. The 28-days compressive cylinder strength ranges from 145MPa to 177MPa, the modulus of elasticity ranges from 54GPa to 62GPa, the Poisson's ratio ranges from 0.21 to 0.23, the density ranges from 2610kg/m<sup>3</sup> to 2690kg/m<sup>3</sup>, and the flow spread of fresh concrete ranges from 41cm to 74cm. The splitting tensile strength is about 1/20 of compressive cylinder strength, and the flexural tensile strength is about 1/10 of compressive cylinder strength.

The strength keeps increasing with the curing age and it is developed much faster at early ages. For compressive strength, compared with the strength value at 28 days, 70% ~ 80% strength can be achieved within the first 3 days and 80% ~ 90% strength can be achieved within the first week. In addition, the strength at curing age of 13 weeks is higher by no more than 13%.

Different from normal strength concrete, the comparison between 100mm-cylinder strength and 100mm-cube strength of *UHSC* has indicated that the cylinder strength is about 2% higher than cube strength, and the comparison between 75mm-cylinder strength and 100mm-cylinder strength has shown that 75mm-cylinder strength is about 6% lower than 100mm-cylinder strength.

By adding ordinary coarse aggregates, no significant improvement on the brittleness was observed. However, the compressive strength decreases as the proportion of coarse aggregates increases. To use 19% or 38% proportions of coarse aggregates, it leads to a reduction of about 3.8% and 9.6% respectively in cube strength, and 4.5% and 17.9% respectively in 100mm-cylinder strength. Therefore, lower strength *UHSC* can be obtained and the cost can be significantly reduced.

The bigger the maximum size of coarse aggregates, the better is the workability; but there is no significant effect of maximum coarse aggregate size on the ultimate strength, modulus of elasticity, density and Poisson's ratio. The greater the mix proportion of coarse aggregates, the worse is the workability, and the lower is the ultimate strength, modulus of elasticity and density; but there is no significant effect on the Poisson's ratio.

Based on the test results, design recommendations are suggested. The proposed formulae can be used to provide predictions for primary design.

Table 3.1: Size grading of Ducorit® D4

Sieve size (mm)		4.75	2.36	1.18	0.6	0.3	0.15	0.075
Percentage passing	Sample 1	100%	81.10%	64.79%	49.37%	39.12%	29.24%	10.25%
	Sample 2	100%	80.86%	64.25%	48.92%	38.51%	25.61%	9.97%
	Sample 3	100%	79.81%	63.59%	48.13%	37.87%	22.41%	6.36%
	Sample 4	100%	81.87%	65.20%	49.52%	39.14%	26.25%	11.40%
	Average	100%	80.91%	64.46%	48.98%	38.66%	25.88%	9.49%

Table 3.2: Size grading of coarse aggregates

Sieve size (mm)		25	19	12.5	9.5	4.75	2.36	1.18
Percentage passing	10mm CA	-	-	100%	96.84%	19.77%	2.61%	1.49%
	20mm CA	100%	94.25%	56.61%	34.41%	3.05%	0.11%	-

Table 3.3: Physical properties of coarse aggregates

Maximum size	10mm	20mm
Shape	Angular and highly irregular	
Texture	Crystalline	
Bulk specific density	2.6	
Absorption capacity	0.8%	
Effective absorption	0.5%	
Loose bulk density, $\rho_b$	1310kg/m <sup>3</sup>	1461kg/m <sup>3</sup>
Percentage of void, $v$	49.6%	43.8%

Table 3.4: Mix proportions per cube meter of UHSC

No.	Mix proportions (kg/m <sup>3</sup> )			Air dry CA	
	Water	D4	Air dry CA	Max. size (mm)	Proportion in volume
D00	190	2503	0	-	-
D <sub>10</sub> 20	154	1998	499	10	19%
D <sub>10</sub> 40	119	1498	998	10	38%
D <sub>20</sub> 20	154	1998	499	20	19%
D <sub>20</sub> 40	119	1498	998	20	38%

Table 3.5: Number of specimens tested for each mix proportion design

Mechanical Properties	Specimens		Curing age (day)			
	Type	Dimension (mm)	3	7	28	91
Compression	cylinder	100 ( <i>d</i> ) × 200 ( <i>h</i> )	3	3	9	3
		75 ( <i>d</i> ) × 150 ( <i>h</i> )	-	-	6	-
	cube	100 ( <i>b</i> ) × 100 ( <i>b</i> ) × 100 ( <i>b</i> )	3	3	6	3
Splitting tension	cylinder	100 ( <i>d</i> ) × 200 ( <i>h</i> )	3	3	6	3
Flexural tension	prism	100 ( <i>b</i> ) × 100 ( <i>h</i> ) × 400 ( <i>l</i> )	3	3	6	3
Modulus of elasticity	cylinder	100 ( <i>d</i> ) × 200 ( <i>h</i> )	6	6	12	3
Poisson's ratio	cylinder	100 ( <i>d</i> ) × 200 ( <i>h</i> )	-	-	3	-

Table 3.6: Test values of slump flow spread

No.	D00	D <sub>10</sub> 20	D <sub>10</sub> 40	D <sub>20</sub> 20	D <sub>20</sub> 40
S <sub>flow</sub> (mm)	735	635	415	685	515

Table 3.7: Test values of density

No.	D00	D <sub>10</sub> 20	D <sub>10</sub> 40	D <sub>20</sub> 20	D <sub>20</sub> 40
ρ <sub>c</sub> (kg/m <sup>3</sup> )	2690	2650	2610	2650	2610

Table 3.8: Compressive cylinder strength

Mix	Size $d$ (mm)	Curing age (day)	No. of specimen	Compressive cylinder strength		
				$f_{cm,cyl}$ (MPa)	StdDev (MPa)	COV
D00	100	3	3	123.8	10.4	8.41%
	100	7	3	141.4	1.5	1.09%
	100	28	9	177.3	10.6	5.99%
	100	91	3	185.5	8.0	4.30%
	75	28	6	171.4	2.8	1.66%
D <sub>10</sub> 20	100	3	3	119.6	4.3	3.61%
	100	7	3	136.7	7.3	5.35%
	100	28	9	168.8	3.4	2.01%
	100	91	3	172.0	5.0	2.91%
	75	28	6	157.7	3.2	2.03%
D <sub>10</sub> 40	100	3	3	110.8	2.3	2.08%
	100	7	3	126.5	4.7	3.75%
	100	28	9	146.3	6.8	4.65%
	100	91	3	157.4	5.6	3.57%
	75	28	6	137.8	4.7	3.44%
D <sub>20</sub> 20	100	3	3	121.2	1.1	0.88%
	100	7	3	136.8	3.2	2.36%
	100	28	9	170.0	3.6	2.15%
	100	91	3	171.7	6.0	3.50%
	75	28	6	158.3	3.9	2.44%
D <sub>20</sub> 40	100	3	3	112.0	4.0	3.60%
	100	7	3	129.1	2.3	1.77%
	100	28	9	145.0	9.9	6.85%
	100	91	3	163.8	9.4	5.73%
	75	28	6	136.0	5.9	4.37%



Table 3.9: Compressive cube strength

Mix	Size $b$ (mm)	Curing age (day)	No. of specimen	Compressive cube strength		
				$f_{cm,cube}$ (MPa)	StdDev (MPa)	COV
D00	100	3	3	130.6	2.8	2.16%
	100	7	3	143.8	5.8	4.04%
	100	28	6	164.0	10.8	6.55%
	100	91	3	185.0	3.4	1.82%
D <sub>10</sub> 20	100	3	3	122.7	6.5	5.33%
	100	7	3	134.3	6.1	4.56%
	100	28	6	158.1	6.5	4.08%
	100	91	3	169.5	5.1	2.98%
D <sub>10</sub> 40	100	3	3	104.4	4.3	4.10%
	100	7	3	120.6	6.2	5.10%
	100	28	6	148.4	4.4	3.00%
	100	91	3	158.5	3.1	1.98%
D <sub>20</sub> 20	100	3	3	120.2	4.1	3.43%
	100	7	3	133.2	5.9	4.39%
	100	28	6	157.4	5.2	3.32%
	100	91	3	170.4	1.6	0.95%
D <sub>20</sub> 40	100	3	3	106.4	1.8	1.69%
	100	7	3	120.5	3.1	2.53%
	100	28	6	148.1	8.0	5.39%
	100	91	3	158.5	6.3	3.97%

Table 3.10: Modulus of elasticity and Poisson's ratio

Mix	Curing age (day)	Modulus of elasticity				Poisson's ratio			
		No.	$E_{cm}$ (GPa)	StdDev (GPa)	COV	No.	$\nu$	StdDev	COV
D00	3	6	53.7	1.02	1.90%				
	7	6	59.0	1.19	2.01%				
	28	12	61.7	1.71	2.77%	3	0.23	0.01	2.55%
	91	3	62.6	0.80	1.28%				
D <sub>10</sub> 20	3	6	51.6	0.93	1.81%				
	7	6	55.3	2.21	4.00%				
	28	12	57.7	2.78	4.82%	3	0.23	0.01	2.55%
	91	3	59.0	0.91	1.54%				
D <sub>10</sub> 40	3	6	46.8	1.97	4.21%				
	7	6	51.8	2.22	4.29%				
	28	12	54.0	1.13	2.09%	3	0.23	0.02	6.74%
	91	3	55.4	1.11	2.00%				
D <sub>20</sub> 20	3	6	50.8	1.15	2.27%				
	7	6	55.9	2.32	4.16%				
	28	12	58.1	2.31	3.98%	3	0.21	0.03	12.60%
	91	3	60.8	1.44	2.36%				
D <sub>20</sub> 40	3	6	48.0	1.92	4.00%				
	7	6	51.5	2.34	4.55%				
	28	12	55.6	2.52	4.53%	3	0.21	0.01	4.76%
	91	3	57.1	0.95	1.66%				

Table 3.11: Secant and elastic modulus

Mix	$E_{0.95}$ (GPa)	$E_{cm}$ (GPa)	$E_{cm}/E_{0.95}$	
D00	52.0	60.574	1.17	1.14
	56.0	63.42	1.13	
	55.1	62.297	1.13	
D <sub>10</sub> 20	52.7	58.959	1.12	1.11
	54.5	59.339	1.09	
	55.0	61.222	1.11	
D <sub>10</sub> 40	51.1	55.4	1.08	1.09
	50.2	54.306	1.08	
	50.5	55.531	1.10	
D <sub>20</sub> 20	50.6	58.399	1.15	1.13
	54.9	61.204	1.11	
	53.8	59.589	1.11	
D <sub>20</sub> 40	52.4	56.847	1.09	1.09
	53.1	56.931	1.07	
	52.7	58.833	1.12	
Mean				1.11
Standard deviation				0.02

Table 3.12: Compressive cylinder versus cube strength

Mix	$f_{cm,cyl,100}/f_{cm,cube,100}$			
	3 days	7 days	28 days	91 days
D00	0.95	0.98	1.08	1.00
D <sub>10</sub> 20	0.97	1.02	1.07	1.01
D <sub>10</sub> 40	1.06	1.05	0.99	0.99
D <sub>20</sub> 20	1.01	1.03	1.08	1.01
D <sub>20</sub> 40	1.05	1.07	0.98	1.03

Table 3.13: Scale effect on compressive cylinder strength

Mix	$f_{cm,cyl,100}$	$f_{cm,cyl,75}$	$f_{cm,cyl,75}/f_{cm,cyl,100}$
D00	177.3	171.4	96.6%
D <sub>10</sub> 20	168.8	157.7	93.5%
D <sub>10</sub> 40	146.3	137.8	94.2%
D <sub>20</sub> 20	170.0	158.3	93.1%
D <sub>20</sub> 40	145.0	136.0	93.8%
Mean			94.2%
Standard deviation			0.014

Table 3.14: Effect of maximum coarse aggregate size on compressive strength

Specimen Type	CA proportion	Curing ages (days)	Strength (MPa)		
			10mm CA	20mm CA	Ratio
100mm-cube	19%	3	122.7	120.2	0.979
		7	134.3	133.2	0.992
		28	158.1	157.4	0.996
		91	169.5	170.4	1.005
	38%	3	104.4	106.4	1.019
		7	120.6	120.5	0.999
		28	148.4	148.1	0.998
		91	158.5	158.5	1.000
100mm-cylinder	19%	3	119.6	121.2	1.013
		7	136.7	136.8	1.001
		28	168.8	170.0	1.007
		91	172.0	171.7	0.998
	38%	3	110.8	112.0	1.011
		7	126.5	129.1	1.020
		28	146.3	145.0	0.992
		91	157.4	163.8	1.040
75mm-cylinder	19%	28	157.7	158.3	1.003
	38%	28	137.8	136.0	0.987
Mean					1.003
Standard deviation					0.014

Table 3.15: Effect of maximum coarse aggregate size on modulus of elasticity

Specimen Type	CA proportion	Curing ages (days)	Modulus of elasticity (GPa)		
			10mm CA	20mm CA	Ratio
100mm-cylinder	19%	3	51.6	50.8	0.983
		7	55.3	55.9	1.010
		28	57.7	58.1	1.008
		91	59.0	60.8	1.030
	38%	3	46.8	48.0	1.025
		7	51.8	51.5	0.995
		28	54.0	55.6	1.029
		91	55.4	57.1	1.032
Mean					1.014
Standard deviation					0.018

Table 3.16: Splitting tensile strength

Mix	Curing age (days)	No. of specimen	Splitting tensile strength		
			$f_{ct,sp}$ (MPa)	StdDev (MPa)	COV
D00	3	3	8.21	0.31	3.77%
	7	3	9.00	0.75	8.35%
	28	6	10.51	0.56	5.31%
	91	3	10.82	0.76	7.02%
D <sub>10</sub> 20	3	3	6.95	0.80	11.57%
	7	3	7.80	0.73	9.39%
	28	6	8.42	0.36	4.31%
	91	3	8.99	0.31	3.40%
D <sub>10</sub> 40	3	3	6.49	0.26	3.96%
	7	3	7.06	0.64	9.05%
	28	6	7.93	0.61	7.67%
	91	3	8.67	0.26	3.01%
D <sub>20</sub> 20	3	3	7.09	0.61	8.57%
	7	3	7.61	0.06	0.83%
	28	6	8.20	0.46	5.55%
	91	3	9.09	0.55	6.04%
D <sub>20</sub> 40	3	3	6.41	0.60	9.38%
	7	3	7.02	0.03	0.40%
	28	6	7.96	0.72	9.04%
	91	3	8.74	0.38	4.39%

Table 3.17: Effect of maximum coarse aggregate size on splitting tensile strength

Specimen Type	CA proportion	Curing ages (days)	Splitting tensile strength (MPa)		
			10mm CA	20mm CA	Ratio
100mm-cylinder	19%	3	6.95	7.09	1.021
		7	7.80	7.61	0.976
		28	8.42	8.20	0.974
		91	8.99	9.09	1.012
	38%	3	6.49	6.41	0.988
		7	7.06	7.02	0.995
		28	7.93	7.96	1.003
		91	8.67	8.74	1.007
Mean					0.997
Standard deviation					0.017



Table 3.18: Flexural tensile strength

Mix	Curing age (day)	No. of specimen	Flexural tensile strength		
			$f_{ct,r}$ (MPa)	StdDev (MPa)	COV
D00	3	3	13.91	0.11	0.76%
	7	3	15.06	0.09	0.60%
	28	6	16.65	0.43	2.61%
	91	3	19.18	0.59	3.07%
D <sub>10</sub> 20	3	3	12.68	0.65	5.11%
	7	3	13.46	0.81	6.01%
	28	6	15.17	0.88	5.81%
	91	3	17.07	0.32	1.90%
D <sub>10</sub> 40	3	3	11.57	0.62	5.34%
	7	3	12.26	0.57	4.68%
	28	6	13.91	0.73	5.22%
	91	3	16.10	0.47	2.89%
D <sub>20</sub> 20	3	3	12.42	0.33	2.69%
	7	3	13.47	0.82	6.06%
	28	6	14.86	0.67	4.48%
	91	3	16.59	0.26	1.58%
D <sub>20</sub> 40	3	3	11.35	0.79	6.94%
	7	3	12.57	0.85	6.77%
	28	6	13.61	0.56	4.11%
	91	3	15.52	0.37	2.39%

Table 3.19: Effect of maximum coarse aggregate size on flexural tensile strength

CA proportion	Curing ages (days)	Flexural tensile strength (MPa)		
		10mm CA	20mm CA	Ratio
19%	3	12.68	12.42	0.979
	7	13.46	13.47	1.001
	28	15.17	14.86	0.980
	91	17.07	16.59	0.972
38%	3	11.57	11.35	0.981
	7	12.26	12.57	1.025
	28	13.91	13.61	0.978
	91	16.10	15.52	0.964
Mean				0.985
Standard deviation				0.0193

Table 3.20: Summary of basic mechanical properties

Mix No.	D00	D <sub>10</sub> 20	D <sub>10</sub> 40	D <sub>20</sub> 20	D <sub>20</sub> 40
Maximum aggregate size (mm)	-	10	10	20	20
Aggregate volume proportion	0%	19%	38%	19%	38%
Flow spread, $S_{\text{flow}}$ (mm)	735	635	415	685	515
Density, $\rho$ (kg/m <sup>3</sup> )	2690	2650	2610	2650	2610
Compressive cylinder strength, $f_{\text{cm,cyl}}$ (MPa)	177	169	146	170	145
Compressive cube strength, $f_{\text{cm,cube}}$ (MPa)	164	158	148	157	148
Splitting tensile strength, $f_{\text{ct,sp}}$ (MPa)	10.5	8.4	7.9	8.2	8.0
Flexural tensile strength, $f_{\text{ct,r}}$ (MPa)	16.6	15.2	13.9	14.9	13.6
Elastic modulus, $E_{\text{cm}}$ (GPa)	61.7	55.3	54.0	58.1	55.6
Poisson's ratio, $\nu$	0.23	0.23	0.23	0.21	0.21

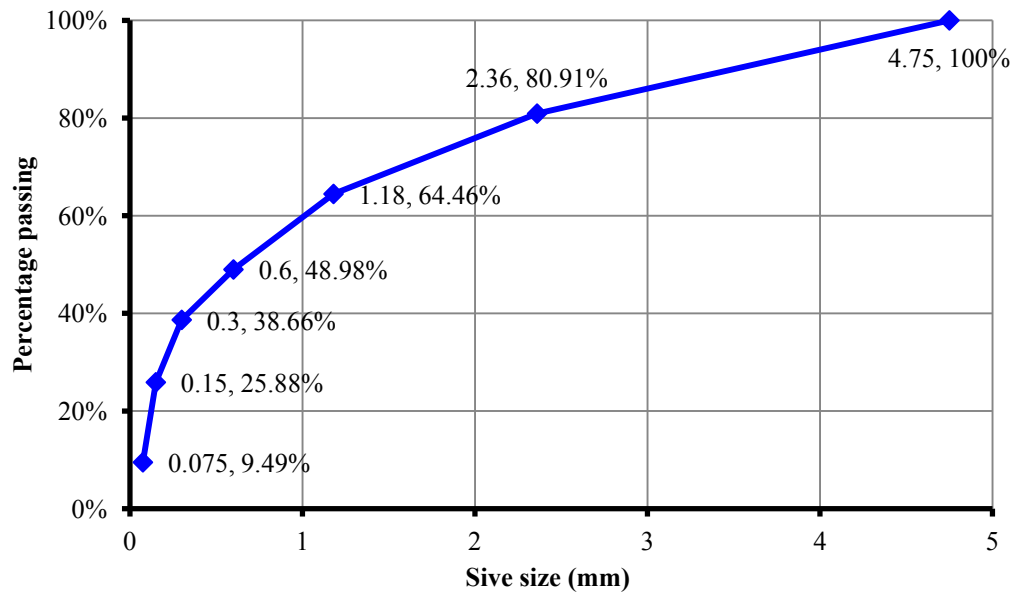


Figure 3.1: Size grading curve for Ducorit® D4



Figure 3.2: Sieved Ducorit® D4

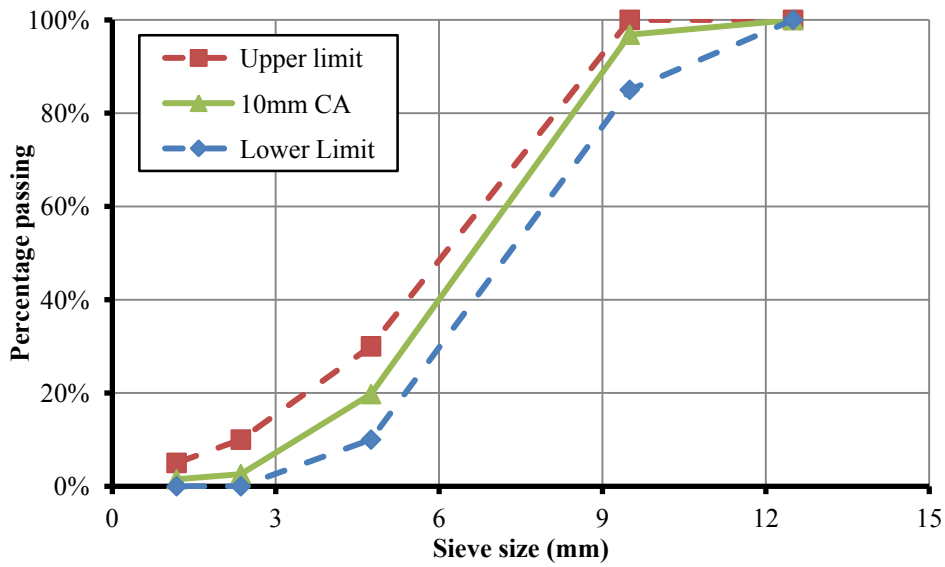


Figure 3.3: Size grading curves for 10mm coarse aggregates

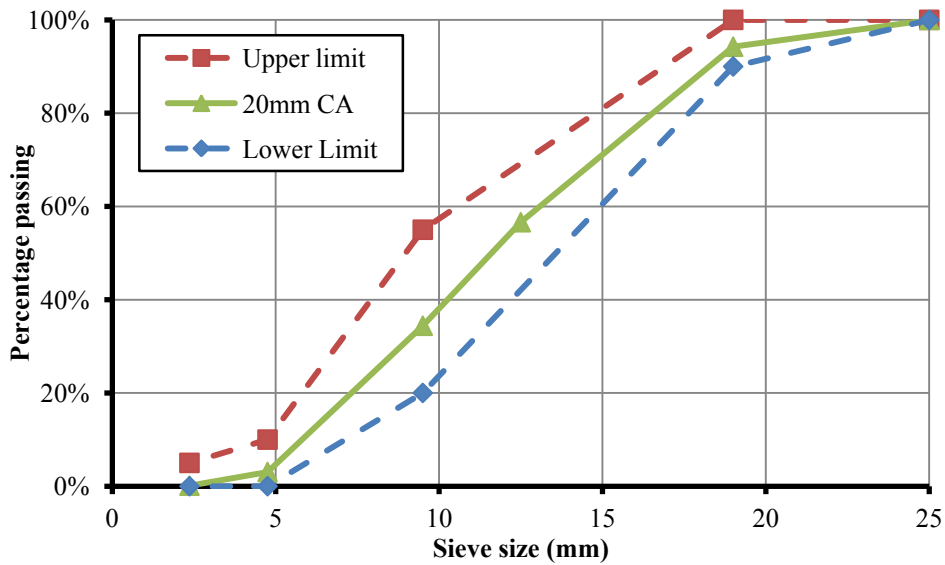


Figure 3.4: Size grading curves for 20mm coarse aggregates

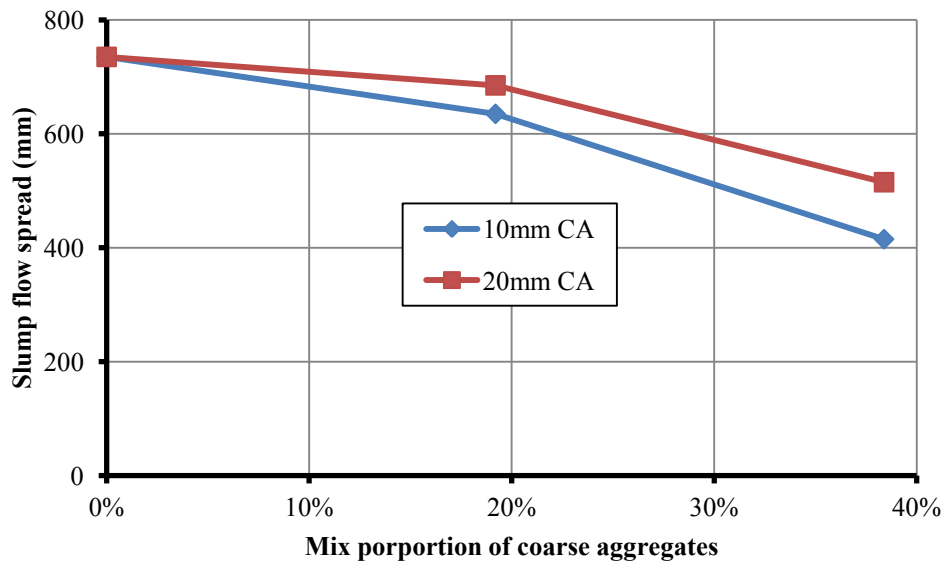


Figure 3.5: Slump flow spread curves

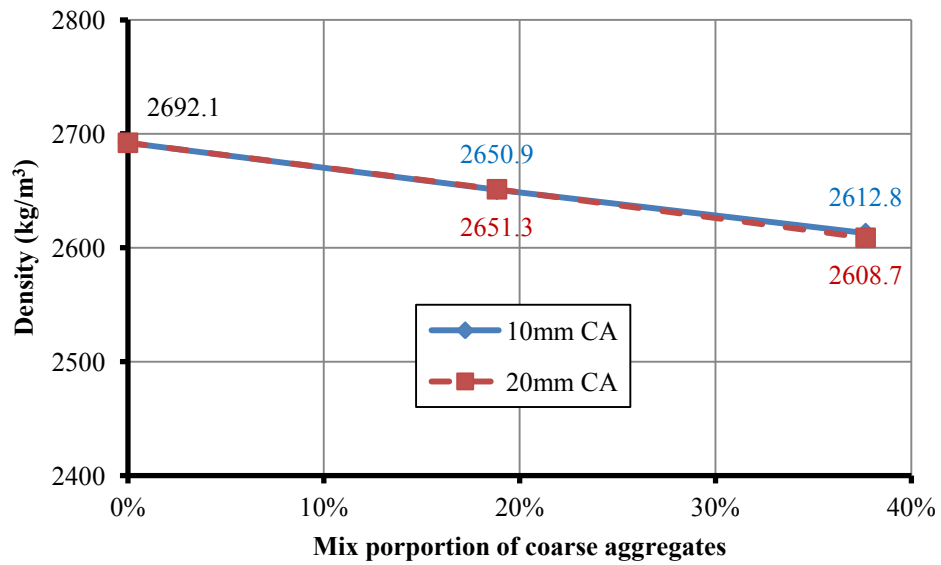


Figure 3.6: Test values of density

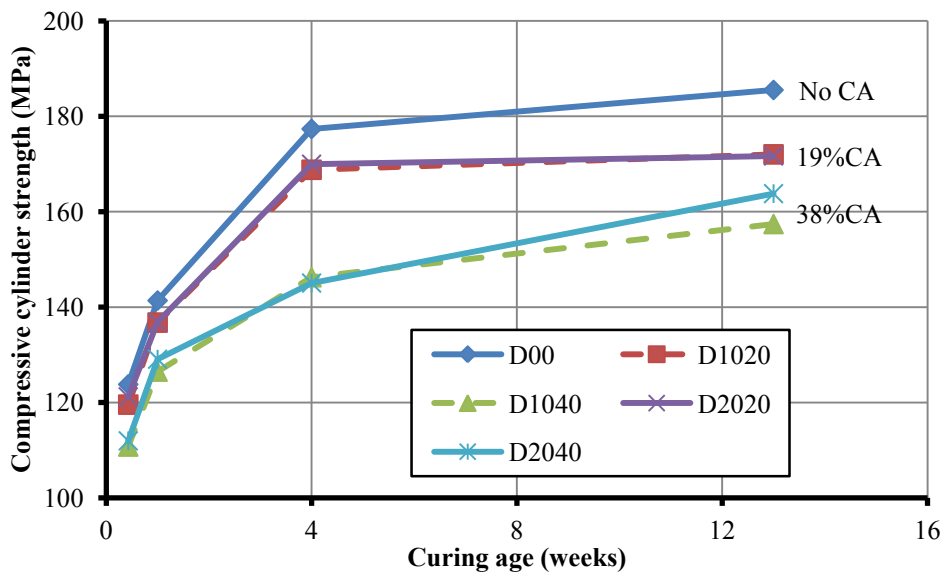


Figure 3.7: Compressive cylinder strength at different curing ages

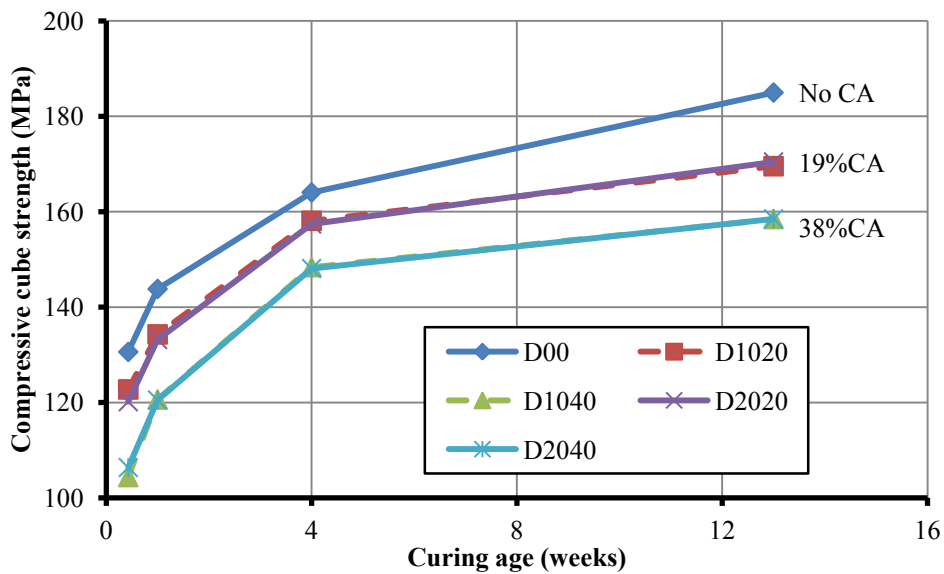


Figure 3.8: Compressive cube strength at different curing ages

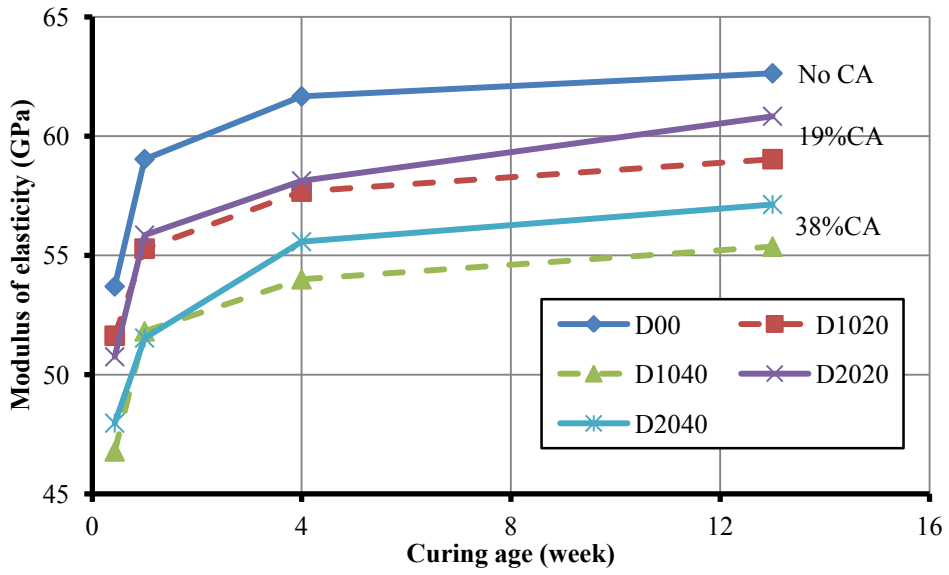


Figure 3.9: Modulus of elasticity at different curing ages

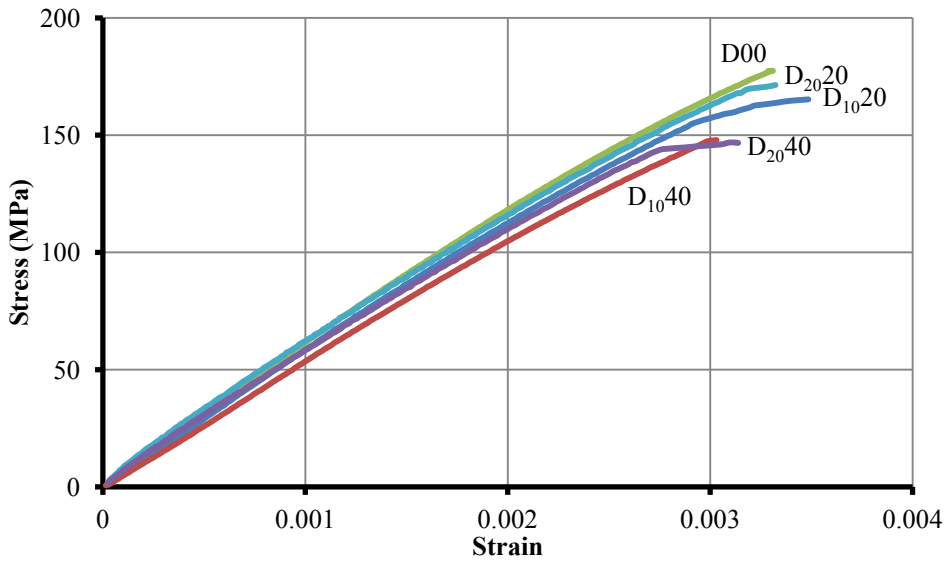


Figure 3.10: Compressive stress - strain curves

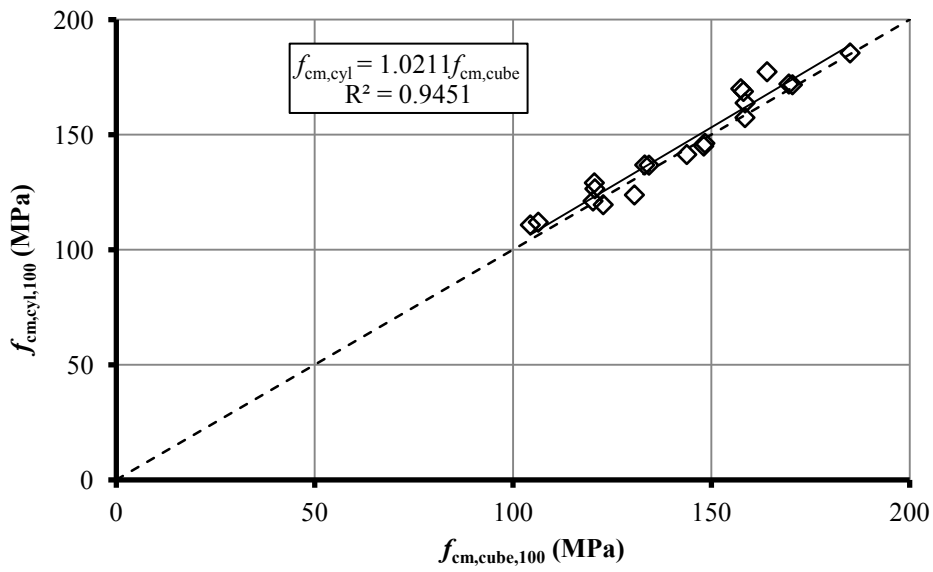


Figure 3.11: Compressive cylinder strength versus cube strength

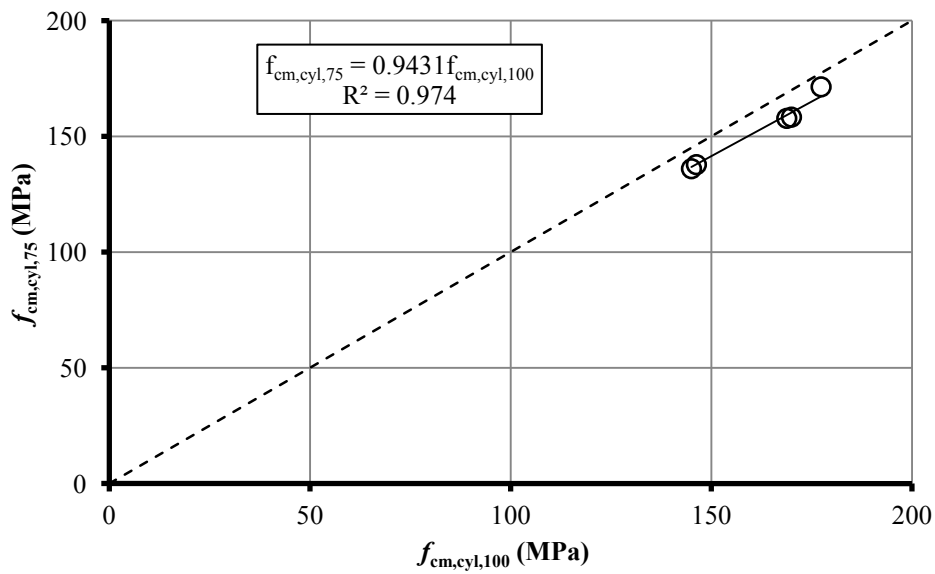


Figure 3.12: Scale effect on compressive cylinder strength



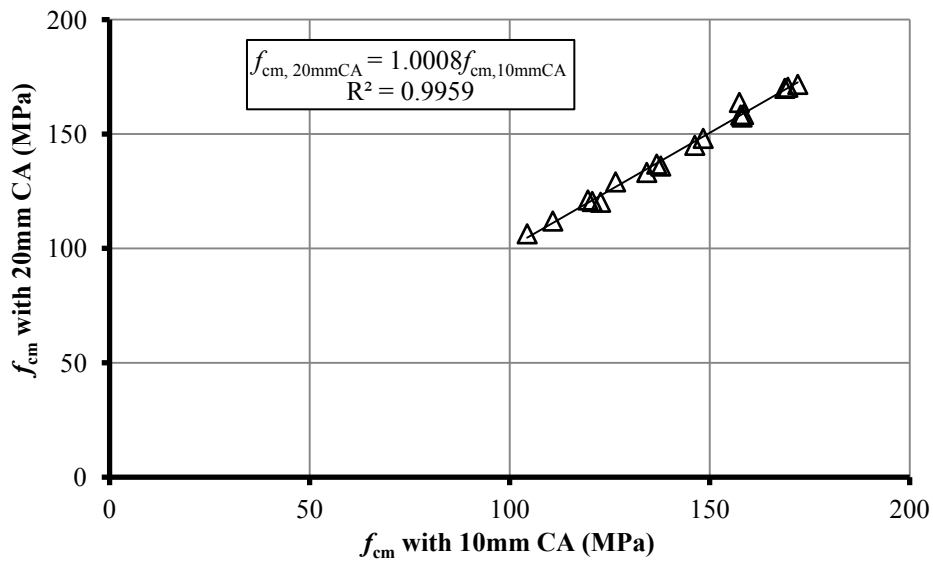


Figure 3.13: Effect of maximum coarse aggregate size on compressive strength

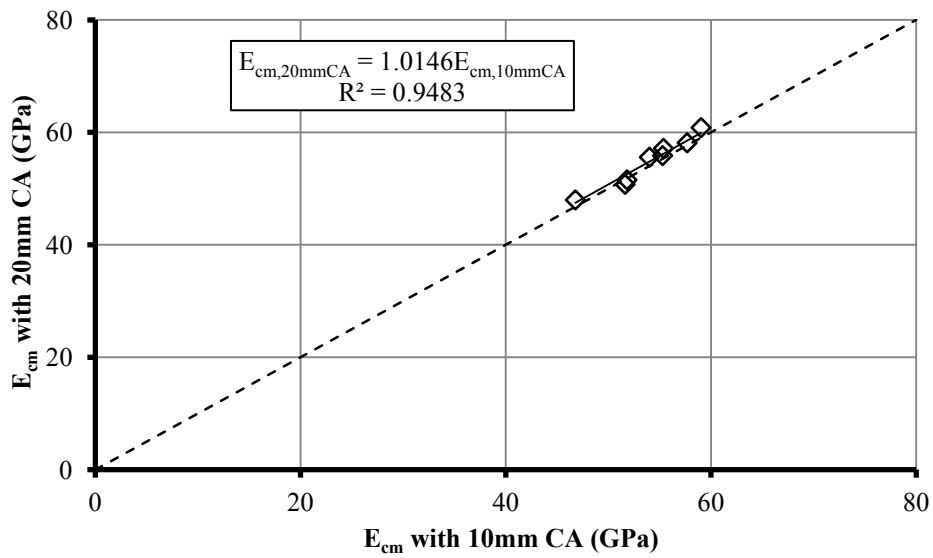


Figure 3.14: Effect of maximum coarse aggregate size on modulus of elasticity

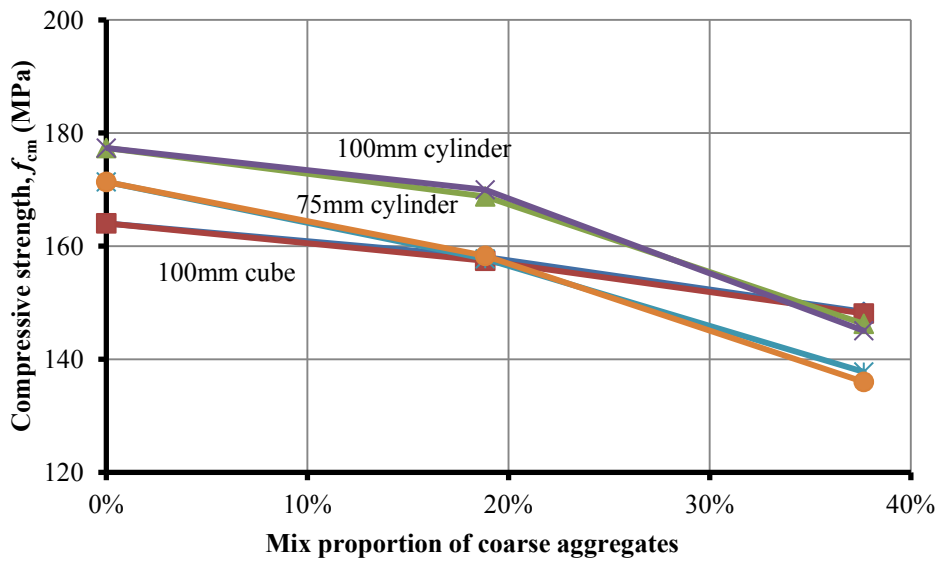


Figure 3.15: Effect of coarse aggregate proportion on compressive strength

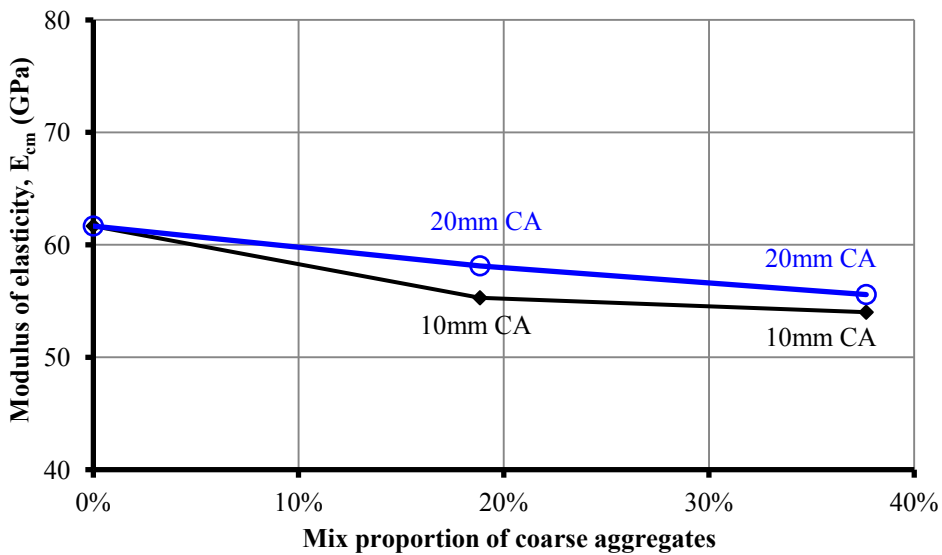


Figure 3.16: Effect of coarse aggregate proportion on modulus of elasticity

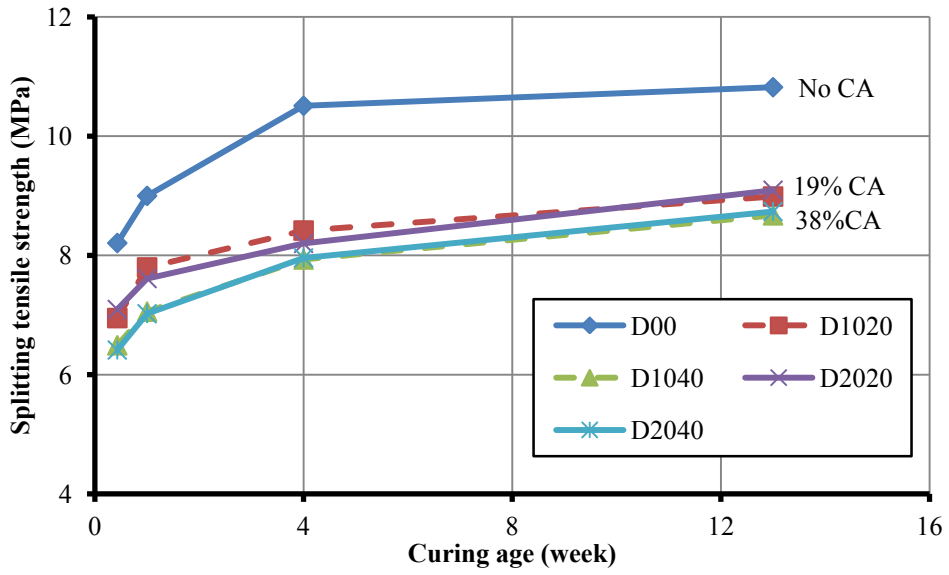


Figure 3.17: Splitting tensile strength at different curing ages

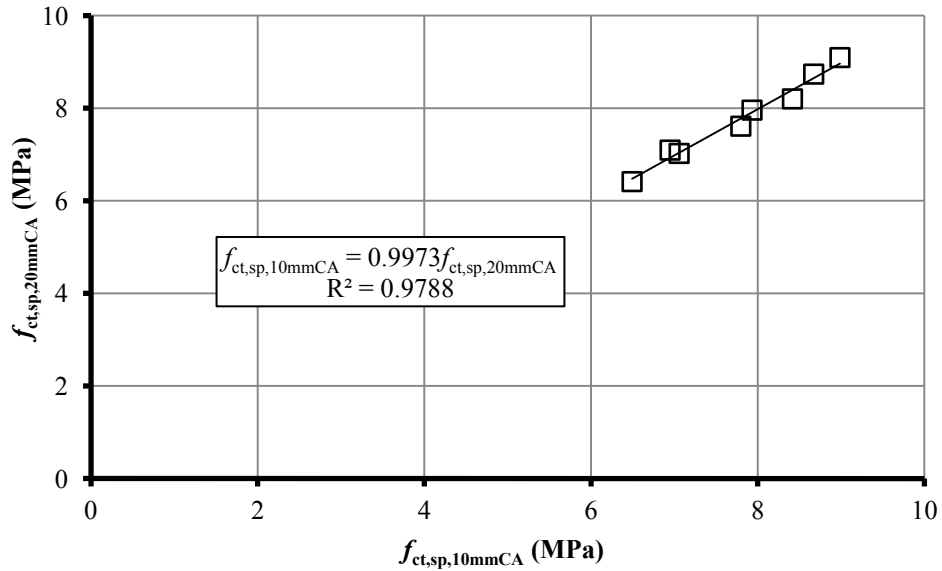


Figure 3.18: Effect of maximum coarse aggregate size on splitting tensile strength

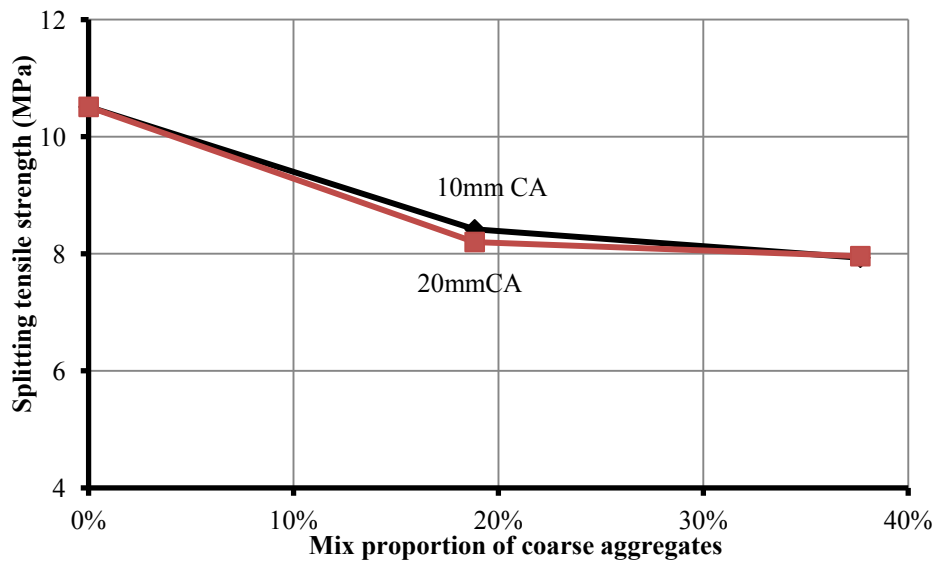


Figure 3.19: Effect of coarse aggregate proportion on splitting tensile strength

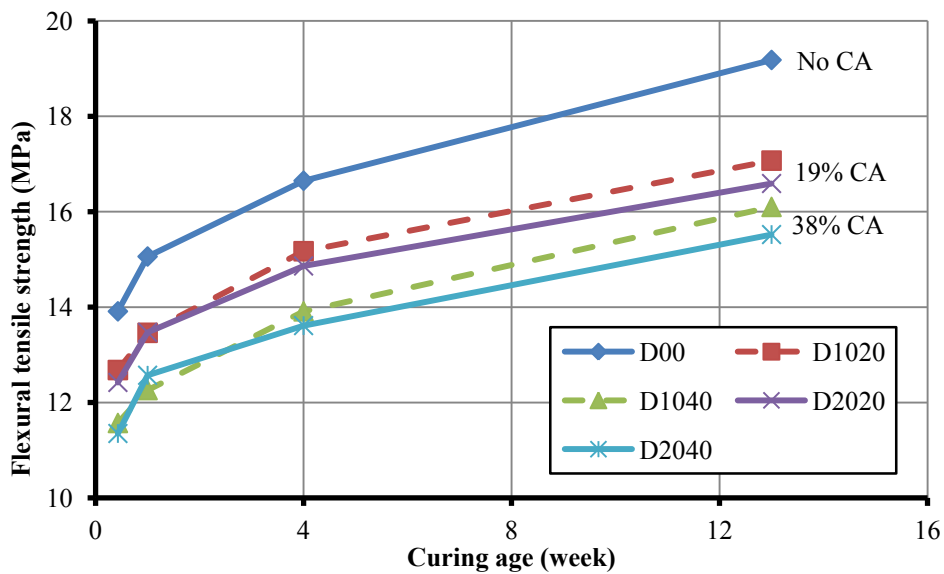


Figure 3.20: Flexural tensile strength at different curing ages

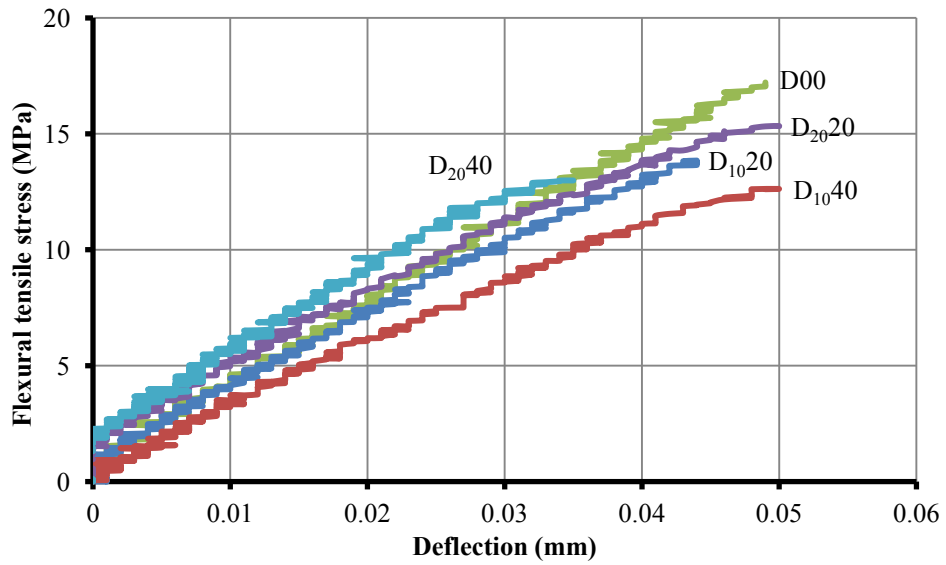


Figure 3.21: Flexural tensile stress - deflection curves

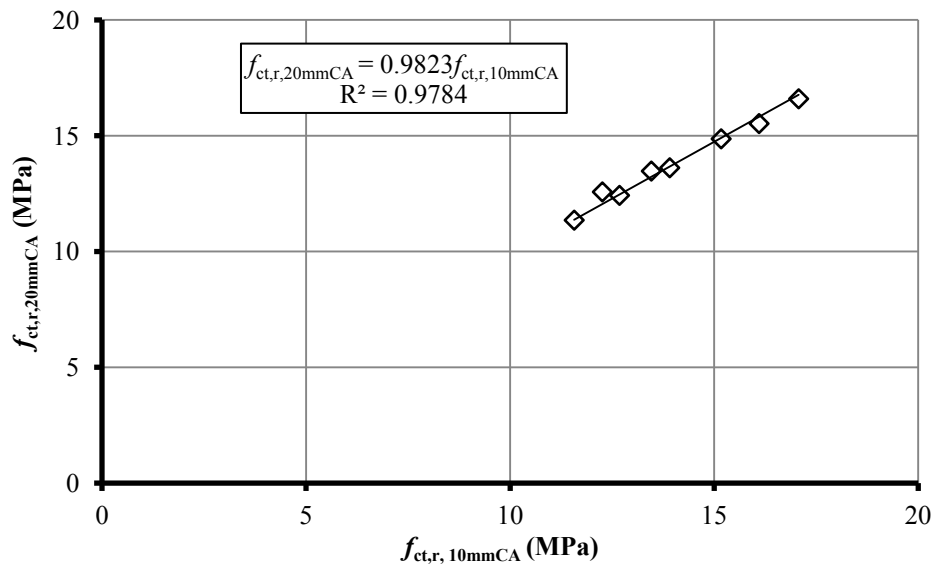


Figure 3.22: Effect of maximum coarse aggregate size on flexural tensile strength

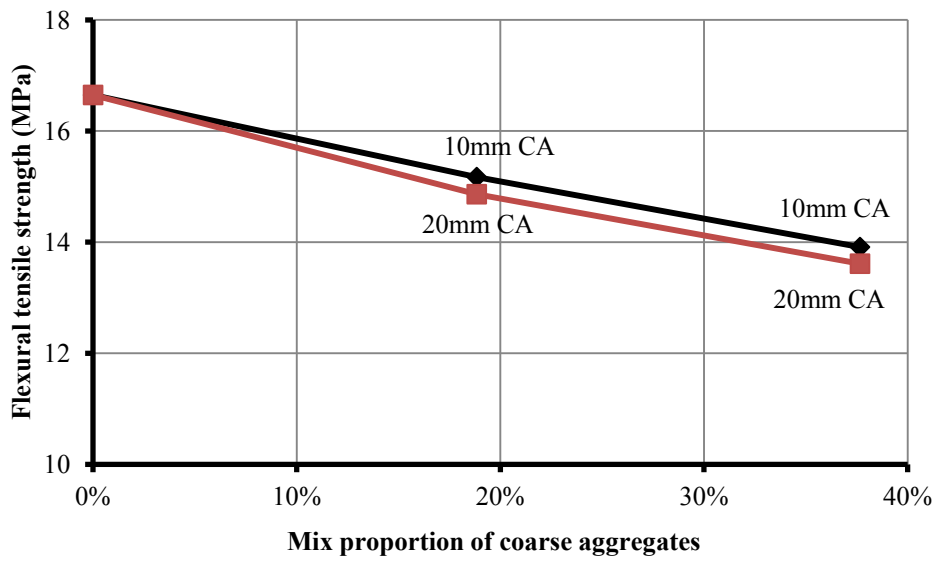


Figure 3.23: Effect of coarse aggregate proportion on flexural tensile strength

## Chapter 4 Stub CFST Columns with High Strength Materials under Concentric Compression

### 4.1 General

Experimental investigations on the basic mechanical properties of *UHSC* with different mix proportion designs have been presented in **Chapter 3**. The *UHSC* is developed to be used in *CFST* columns in this study.

This chapter presents experimental investigations on four series of stub *CFST* columns employing *UHSC* and *HSS* under concentric compression. For Series 1 tests, 11 small scale specimens were tested for primary feasibility study on the application of *UHSC* in *CFST* columns with normal strength steel tubes. For Series 2 tests, 16 full scale specimens were tested for further verification, including both of single- and double-tube specimens with both of *UHSC* and normal strength concrete (*NSC*). For Series 3 tests, 8 specimens were tested to evaluate the coarse aggregate effect on the performance of *CFST* columns with *UHSC*. For Series 4 tests, 21 specimens were tested to evaluate the performance of *CFST* columns with *UHSC* and *HSS* sections. Since the *UHSC* used in this study is very brittle, the ductility requirement on the *CFST* columns is discussed. For evaluation, the test values of ultimate resistance are compared with the predictions by Eurocode 4, and then some design recommendations will be proposed.

## 4.2 Ductility Requirements

Structures and members are usually required to have sufficient ductility that they can still stand for serviceability even under significant ductile deformations which may be caused by accidental actions. An axial shortening limit for axially compressed composite columns is proposed and defined as following:

$$\varphi_{\text{lim}} = \frac{\Delta L_{\text{lim}}}{L} = 0.5 \sqrt{\frac{f_y}{E_a}} \quad (4.1)$$

where  $\varphi_{\text{lim}}$  is the limit of axial shortening ratio,  $\Delta L_{\text{lim}}$  is the limit of axial shortening, and  $L$  is the original length of a composite column. For  $f_y = 235\text{MPa}$  and  $E_a = 210\text{GP}$ ,  $\varphi_{\text{lim}} = 1.7\%$ , and for  $f_y = 800\text{MPa}$ ,  $\varphi_{\text{lim}} = 3.1\%$ .

Deformations beyond the limit are significant, and the remaining resistance beyond this limit is regarded as the residual resistance. To meet ductility requirements, the residual resistance should not be less than the actions under serviceability limit state. For gravity load combination, the service load is up to 70% of the ultimate resistance according to the partial factors for actions and materials used in Eurocode 4 (2004). Therefore, to ensure a safe design, the residual resistance should be at least equal to 70% of the designed ultimate resistance, which means the residual resistance ratio should not be lower than 0.7 expressed as:

$$\frac{N_r}{N_u} \geq 0.7 \quad (4.2)$$

where  $N_r$  is the residual resistance and  $N_u$  is the ultimate resistance.



### 4.3 Series 1 Tests: Small Scale *CFST* Columns with *UHSC*

For feasibility study on the application of *UHSC* in *CFST* columns, there were 11 small scale specimens, including 3 circular hollow steel tube columns and 8 circular *CFST* columns, tested under two different loading cases. One case was that the loading was imposed on the concrete core only, and the other was that the loading was imposed simultaneously on both of the concrete core and steel tube.

#### 4.3.1 Material properties

The materials used in this series of tests included *UHSC* mixed with and without high strength steel fiber and Grade S355 hot finished circular hollow steel sections. For each batch of concrete, at least three cylinders of size 100mm ( $d$ )  $\times$  200mm ( $h$ ) were cast and cured at ambient temperature as the same for curing composite specimens. They were tested at the same time when the corresponding composite specimens were tested to obtain the basic mechanical properties, referred to relevant ASTM standards as introduced in **Chapter 3**. For each type of steel sections, at least three coupon samples were tested, referred to ASTM E8M-04.

##### 4.3.1.1 *UHSC*

Two different mix proportion designs were used for this series of specimens. One was the first mix design shown in Table 3.4 of **Chapter 3**, and the other was mixed with 1% high tensile strength steel fiber in volume based on the former design. The steel fiber, shown in Figure 4.1, was used in order to improve the performance of *UHSC*. Its basic properties are shown Table 4.1. For each mix design, one batch concrete was cast. During casting,

the fresh concrete was gradually poured into *CFST* specimens from the top with vibrating to get compact. The basic properties for each batch are summarized in Table 4.2.

#### 4.3.1.2 Steel sections

Grade S355 hot finished circular hollow sections with nominal dimensions of 114.3mm × 3.6mm and 114.3mm × 6.3mm were used for the steel tubes in this series of tests. The basic mechanical properties are shown in Table 4.3, where the sections are classified according to Eurocode 3 (2005). The setup for the coupon sample tests is shown Figure 4.2 and the stress-strain curves are shown in Figure 4.3 for CHS114.3mm × 3.6mm and Figure 4.4 for CHS114.3mm × 6.3mm.

#### 4.3.2 Specimens

There were 11 specimens with column diameter 114.3mm and height 250mm, including 3 circular hollow steel tube columns, 6 *UHSC* filled steel tube columns and 2 steel fiber reinforced *UHSC* filled steel tube columns. The specimen configuration details are given in Table 4.4, where  $\lambda$  is relative slenderness and  $\delta$  is the steel contribution ratio according to Eurocode 4 as introduced in **Chapter 2**. The overall buckling of these specimens under compression can be ignored since all the values of relative slenderness are less than 0.2. All the values of steel contribution ratio are in the range from 0.2 to 0.9 as limited in Eurocode 4.

### 4.3.3 Test setup and loading procedure

Two specimens, S1-2-1(a) and S1-2-1(b), were axially loaded only on the concrete cores and the other specimens were loaded simultaneously on both of the steel tubes and concrete cores as shown in Figure 4.5. For the specimens loaded simultaneously, a pair of hoop ring stiffeners, which was made of high tensile strength steel, was provided to clamp the ends of the specimens, in order to avoid premature local failure at both ends due to stress concentration.

The strain values at the middle height of specimens and the axial shortening displacements were measured and recorded along with the axial loading values. The strain values were monitored by four post yielding cross-strain gauges which were placed at  $90^{\circ}$  apart and fixed to the external surface of the steel tube. Each strain gauge consists of two components, one aligned in the longitudinal direction and the other in the circumferential direction. The axial shortening displacements were measured by four linear varying displacement transducers (*LVDTs*) which were also placed at  $90^{\circ}$  apart. The axial loading was imposed gradually by a displacement/load control actuator with a maximum capacity of 10,000kN.

The loading was imposed gradually by controlling the axial displacement loading rate. Generally, a quasi-static loading procedure was introduced in four steps: (1) preload the specimen at a low displacement rate of 0.2mm/min up to 10% of its resistance estimated by Equation (2.2) introduced in **Chapter 2**; (2) unload at a higher rate of 0.5mm/min; (3) reload at the same low rate as in the first step up to 60% ~ 70% of its resistance, then decrease the rate down to 0.1mm/min and continue loading beyond the peak load with

significant visible deformations; and (4) finally in the post-peak range, increase the rate up to 0.5mm/min and continue loading until severe failure occurred.

#### 4.3.4 Test results and observations

##### 4.3.4.1 Load-shortening relationship

The load-axial shortening curves for all specimens are shown from Figure 4.6 to Figure 4.10. From these curves, the testing values of the ultimate resistance,  $N_{test,u}$ , and the residual resistance,  $N_{test,r}$ , are obtained and summarized in Table 4.5. For the specimens loaded simultaneously on both concrete core and steel tube, the values of residual resistance were taken as the maximum load values beyond the limit of axial shortening defined by Equation (4.1); for the two specimens loaded only on *UHSC* core, they were taken as the maximum values beyond 22mm axial shortening which was much larger than the calculated value from Equation (4.1). Generally, the residual resistance was the second peak load from the load-axial shortening curves.

The curves for the three hollow steel tube specimens are shown in Figure 4.6. It can be observed that S1-1-1(a), which was of Class 2 section, could almost reach the expected plastic resistance but it was degraded immediately after that; while S1-1-2(a) and S1-1-2(b), which were of Class 1 sections, could achieve the expected plastic resistances and developed significant hardening effect after yielding.

The curves for the two specimens loaded on concrete core only are shown in Figure 4.7 where the interaction between steel tube and concrete core can be observed. At the initial loading stage, the steel tube was resisting the load together with the *UHSC* core relying

on the interfacial bond between the two materials. The bond was subsequently broken due to the relative slip produced; subsequently, the load was mainly resisted by the *UHSC* core and the load-displacement curve became softer. After that, when the axial shortening displacement of the *UHSC* core was increasing at a rate faster than the steel tube, significant confinement effect and friction forces were developed due to the faster expanding of concrete core. Thus some load was transferred from the core to the steel tube, and the load-displacement curve became stiffer. Finally, the steel tube and concrete core were compressed together again.

A larger relative slip displacement between the steel tube and concrete core occurred in S1-2-1(a) than S1-2-1(b) and thus higher confinement stress would be produced at the peak load. Therefore, the longitudinal compressive strength of *UHSC* core in S1-2-1(a) should be increased more than S1-2-1(b). This explains the reason why the ultimate strength of S1-2-1(a) was higher than S1-2-1(b) as shown in Figure 4.7, although they were identical specimens. At the peak load, the *UHSC* core was crushed and its strength was degraded rapidly, leading to steep softening of the loading curve. After that, the confinement stress was increased quickly due to the dilation effect of the *UHSC* core. The residual resistance of S1-2-1(a) was almost kept constant for a continuous period of axial deformation up to 40mm. For S1-2-1(b), there was some strength recovery at about 10mm displacement. Since the maximum confinement stress that the steel tube could provide was the same for the two specimens, the values of residual resistance for both the specimens were almost identical, i.e., 2317kN for S1-2-1(a) and 2293kN for S1-2-1(b).

The ductility and strength of the *UHSC* cores were enhanced significantly due to much higher tri-axial compression in specimens S1-2-1(a) and S1-2-1(b), compared with the

other composite specimens which were loaded simultaneously on both of the steel tubes and concrete cores leading to lower confinement stresses produced on the *UHSC* cores as shown from Figure 4.8 to Figure 4.10. These figures show that the *UHSC* cores were cracked suddenly at smaller axial displacements, and the loading dropped down steeply after the peak load. In addition, S1-3-2(a)&(b), in which the concrete cores were reinforced with 1% steel fiber, and S1-3-3(a)&(b), which had higher values of steel contribution ratio, had higher values of ultimate resistance and residual resistance ratio than specimens S1-3-1(a) &(b) which did not have such strong enhancement.

From Table 4.5, it can be observed that, for the first three hollow steel tube specimens, the residual resistance ratio,  $N_{test,r}/N_{test,u}$ , was 0.86 for S1-1-1(a) with Class 2 sections, showing sufficient ductile post-peak behaviour since it was greater than 0.7 as defined in Equation (4.2); and it was up to 1.0 for S1-1-2(a) and S1-1-2(b) with Class 1 sections, showing much better ductile post-peak behaviour. For the two composite specimens loaded on *UHSC* core only, the residual resistance ratio was about 0.85 on average, showing good ductility. For the other composite specimens loaded simultaneously on both *UHSC* core and steel tube, the residual resistance ratio was the lowest for S1-3-1(a) and S1-3-1(b) at about 0.71 on average, higher for S1-3-2(a) and S1-3-2(b) at about 0.79 which were reinforced with steel fiber, and the highest for S1-3-3(a) and S1-3-3(b) at about 0.92 which had higher steel contribution ratio.

Therefore, the ductility and ultimate resistance of *CFST* columns can be enhanced if steel fiber is added, the steel contribution ratio is increased, or stronger tri-axial confinement is provided to the concrete core. On the contrary, the ultimate resistance of *CFST* columns

may be reduced if some axial preload is imposed only on the steel tubes, which will be presented in details in **Chapter 7**.

#### 4.3.4.2 Failure of UHSC core

For the *CFST* specimens loaded simultaneously on both of concrete cores and steel tubes, very loud cracking/crushing noise emanating from the specimens was heard around the peak load during testing. Then it was followed by a deep steep drop in loading which could be observed from the corresponding loading curves as shown from Figure 4.8 to Figure 4.10. Soon after the drop, visual inspection was carried out on the specimens and no visible deformation was observed. Therefore, the noise would be thought to be originated from the inner cracking/crushing of the *UHSC* core.

All the specimens after testing in this series of tests are shown in Figure 4.11. The external steel tubes of some failed specimens were removed to reveal the inner *UHSC* core as shown in Figure 4.12. For S1-2-1(a) which was loaded only on the *UHSC* core only, its *UHSC* core remained intact, showing good ductility; for S1-3-1(a) and S1-3-2(b) which were loaded simultaneously on both of steel tubes and *UHSC* cores, the *UHSC* cores cracked apart, showing brittleness.

## 4.4 Series 2 Tests: Full Scale *CFST* Columns with both *UHSC* and *NSC*

For further verification, there were 16 full scale specimens, including 2 circular hollow single-tube columns, 6 circular single-tube *CFST* columns and 8 circular double-tube *CFST* columns, tested under axial compression loaded simultaneously on both of concrete core and steel tubes. The single- and double-tube *CFST* columns are schematically shown

in Figure 4.13. For the double-tube specimens, four plate stiffeners were welded onto each end of each specimen to connect the external and internal tubes. One significant advantage of double-tube *CFST* columns over single-tube *CFST* columns is that the encased internal tube together with concrete core can still resist the service load if the external tube is failed under fire. In this case, the concrete filled in-between the double tubes can act as a fire protection cover.

#### **4.4.1 Material properties**

The materials used in this series of tests included *NSC*, *UHSC* mixed with and without high strength steel fiber, and Grade S355 hot finished circular hollow steel sections.

##### 4.4.1.1 *NSC*

The *NSC* used in this study was made from ordinary Portland cement, sand, coarse aggregates with maximum size 10mm, and a proper volume of water. The mix proportion design is shown Table 4.6. For this study, only one batch was cast.

##### 4.4.1.2 *UHSC*

Similar to Series 1 tests, there were also two different mix proportion designs used for this series of specimens. Only one difference was that one design was mixed with 0.5% instead of 1.0% high tensile strength steel fiber. Two batches of concrete were cast for the plain *UHSC*, and one batch was cast for the steel fiber reinforced *UHSC*.



Compression tests carried out on concrete cylinders showed that *UHSC* had much higher strength than normal strength concrete but it was much more brittle. The failure modes for different types of concrete are shown in Figure 4.14. Plain *UHSC* cylinders were crushed into pieces once the maximum loads were reached while *NSC* and steel fiber reinforced *UHSC* cylinders exhibited some post-peak ductility. The reason is that the presence of steel fiber and coarse aggregates could delay or even prevent the initiating and propagating of the cracking. Very loud cracking noise was heard during the testing of plain *UHSC* and steel fiber reinforced *UHSC* cylinders. Due to the reinforcement of steel fiber, the ultimate compressive strength was enhanced, and the performance on brittleness was improved.

The basic material properties for all batches of concrete are summarized in Table 4.7, tested at the same time when the corresponding composite specimens were tested. It should be noted that the concrete strength  $f_{ck}$  should be based on concrete cylinder samples of size 150mm ( $d$ )  $\times$  300mm ( $h$ ) according to Eurocode 2 (2004). Since only concrete cylinder samples of size 100mm ( $d$ )  $\times$  200mm ( $h$ ) were tested in this series of tests, size effect was considered for *NSC* and the test values were divided by 1.05 (Cook, 1989) to estimate the concrete strength  $f_{ck}$  as defined in Eurocode 2 (2004). For *UHSC*, the size effect can be ignored as investigated in **Chapter 3**.

#### 4.4.1.3 Steel sections

Four different types of Grade S355 hot finished circular hollow sections, 114.3mm  $\times$  3.6mm, 114.3mm  $\times$  6.3mm, 219.1mm  $\times$  5mm and 219.1mm  $\times$  10mm were used for the specimens in this series of tests. The first two were the same as those used in Series 1

tests and their basic properties have been shown in Table 4.3. For the other two additional steel sections, the basic mechanical properties are summarized in Table 4.8. The stress-strain curves from coupon tests for the first two sections have been shown in Figure 4.3 and Figure 4.4, and the stress-strain curves for the other two additional sections are shown in Figure 4.15 for CHS219.1mm  $\times$  5mm and Figure 4.16 for CHS219.1mm  $\times$  10mm.

#### 4.4.2 Specimens

There were 16 specimens with column diameter 219.1mm and height 600mm, including 8 single-tube columns and 8 double-tube columns. These specimens were classified into four groups based on different types of steel sections. The specimen configuration details are shown in Table 4.9 for single-tube specimens and Table 4.10 for double-tube specimens. The first group, Group S2-1, had four single-tube specimens with steel section CHS219.1mm  $\times$  5mm, including one hollow tube column, one *NSC* filled tube column, one *UHSC* filled tube column, and one steel fiber reinforced *UHSC* filled tube column. Compared with Group S2-1, only one difference for the second group, Group S2-2, was that steel section CHS219.1mm  $\times$  10mm was used instead of CHS219.1mm  $\times$  5mm. The third group, Group S2-3, had four double-tube specimens with steel section CHS219.1mm  $\times$  5mm for the external tube and CHS114.3mm  $\times$  3.6mm for the internal tube, including one *NSC* filled tube column, one *UHSC* filled tube column, one column with *NSC* filled in-between the double tubes and *UHSC* filled in the internal tube, and one column with *NSC* filled in-between the double tubes and steel fiber reinforced *UHSC* filled in the internal tube. Compared with Group S2-3, the difference for the fourth group, Group S2-4, was that steel sections CHS219.1mm  $\times$  10mm and CHS114.3mm  $\times$  6.3mm were used instead of CHS219.1mm  $\times$  5mm and CHS114.3mm  $\times$  3.6mm respectively.

### 4.4.3 Test setup and loading procedure

All the specimens in this series of tests were loaded simultaneously on both of steel tubes and concrete cores as shown in Figure 4.17. Similar to Series 1 tests, a pair of hoop ring stiffeners but with bigger sizes was used to clamp the ends of the specimens. The arrangement of strain gauges and *LVDTs* used for this series of tests was the same as that used for Series 1 tests.

The loading procedure was also similar to that used in Series 1 tests. Only one difference was that higher loading rate values were used in this series of tests. A rate of 0.3mm/min was used instead of 0.2mm/min in the first step, 1.0mm/min was used instead of 0.5mm/min in the second step, 0.3mm/min and 0.2mm/min were used respectively instead of 0.2mm/min and 0.1mm/min in the third step, and 0.8mm/min was used instead of 0.5mm/min in the fourth step.

### 4.4.4 Test results and observations

#### 4.4.4.1 Load-shortening relationship

The load-axial shortening curves are shown in four figures from Figure 4.18 to Figure 4.21, with each group specimens in one figure. From these curves, the testing values of the ultimate resistance,  $N_{test,u}$ , and the residual resistance,  $N_{test,r}$ , are obtained and summarized in Table 4.11. The residual resistance was taken as the maximum load beyond the axial shortening limit defined by Equation (4.1). Generally, it was the second peak load from the load-axial shortening curves.

The first two groups included all the single-tube specimens as shown in Figure 4.18 and Figure 4.19. Section CHS219mm×5mm was used for the specimens in Group S2-1 and CHS219mm×10mm was used for the specimens in Group S2-2. Similar to hollow specimen S1-1-1(a) in Series 1 tests, hollow specimen S2-1-1 of CHS219mm×5mm was of a Class 3 section and it could not develop the full plastic resistance after yielding as shown in Figure 4.18, while hollow specimen S2-2-1 of CHS219mm×10mm was of a Class 1 section and developed the full plastic resistance and hardening effect as shown in Figure 4.19. Similar effect can also be observed from the *NSC* filled tube specimens S2-1-2 and S2-2-2; however, compared with hollow specimens S2-1-1 and S2-2-1 respectively, *CFST* specimens S2-1-2 developed higher plastic resistance and S2-2-2 achieved its ultimate strength at a larger displacement due to the confinement effect provided by the steel tube and the constraint afforded by the concrete core.

The other four single-tube specimens in the first two groups achieved higher ultimate resistance due to the usage of *UHSC*. However, the post-peak load behavior was more brittle than *NSC* filled tube specimens. The *UHSC* core cracked suddenly and the loading dropped steeply. The concrete cores of specimens S2-1-4 and S2-2-4 were reinforced with 0.5% steel fiber and thus they had higher values of ultimate resistance and residual resistance ratio than S2-1-3 and S2-2-3 respectively. Specimens S2-2-3 and S2-2-4 had higher values of steel contribution ratio than specimens S2-1-3 and S2-1-4 respectively, and thus they had higher values of ultimate resistance and residual resistance ratio. Therefore, these tests confirm that steel fiber and higher steel contribution ratio can help to enhance the resistance and ductility of *CFST* columns as observed in Series 1 tests.

The other two groups included all the double-tube specimens as shown in Figure 4.20 and Figure 4.21. Section CHS219mm×5mm for the external tube and section CHS114.3mm × 3.6mm for the internal tube were used for the specimens in Group S2-3, and Section CHS219mm×10mm for the external tube and section CHS114.3mm × 6.3mm for the internal tube were used for the specimens in Group S2-4. Similar to *NSC* filled tube specimen S2-1-2 in Group S2-1, the *NSC* filled specimen S2-3-1 also developed significant plastic resistance as shown in Figure 4.20, although both of its external and internal steel tubes are of large diameter-to-thickness ratios. The other *NSC* filled specimen S2-4-1 developed better plastic resistance and hardening effect as shown in Figure 4.21, because its external and internal steel tubes are of smaller diameter-to-thickness ratios.

From Figure 4.20 and Figure 4.21, it can be observed that the *UHSC* filled specimens S2-3-2 and S2-4-2 developed much higher ultimate resistance than the *NSC* filled specimens S2-3-1 and S2-4-1; however, the loading dropped steeply after the peak load due the brittleness of *UHSC* core. The other four specimens were infilled with *NSC* in between the external and internal tubes and with *UHSC* in the centre cores. They demonstrated significant ductility after the peak load. The drop in loading after the peak load was not too steep and it was recovered soon. The second peak load was even higher than the first peak load, as shown for specimens S2-4-3 and S2-4-4 in Figure 4.21. Compared with S2-3-3 and S2-4-3 respectively, the internal *UHSC* cores of S2-3-4 and S2-4-4 were reinforced with 0.5% steel fiber and these two specimens had higher values of ultimate resistance.

Similar to the *UHSC* filled steel tube specimens tested in Series 1, very loud cracking/crushing noise emanating from the specimens tested in this series was also heard around the peak load during the testing of the specimens with *UHSC*. The loading dropped steeply right after the peak load but no visible deformation could be observed. All the specimens after testing in this series of tests are shown Figure 4.22, compared with all the specimens tested in Series 1.

### **4.5 Series 3 Tests: Coarse Aggregate Effect on *CFST* Columns with *UHSC***

To extend the investigation reported in above sections to exploring the use of ordinary granite aggregates with an aim to reduce the cost of *UHSC* for composite construction, this section presents an additional experimental investigation done on 8 full scale specimens, including 4 single-tube *UHSC*-filled columns and 4 double-tube *UHSC*-filled columns, tested under axial compression loaded simultaneously on both of concrete core and steel tubes.

#### **4.5.1 Material properties**

The materials used in this series of tests included *UHSC* reinforced with different proportions and sizes of ordinary coarse aggregates, and hot finished circular hollow steel sections.

#### 4.5.1.1 UHSC

Four different mix proportion designs, the same as the first three and the last one respectively shown in Table 3.4 of **Chapter 3**, were used for this series of specimens. The first one was plain *UHSC* without coarse aggregates, the second one was reinforced with 19% coarse aggregates of maximum size 10mm, the third one was reinforced with 38% coarse aggregates of maximum size 10mm, and the fourth one was reinforced with 38% coarse aggregates of maximum size 20mm. For each mix design, one batch concrete was cast. The basic properties for each batch tested during testing corresponding composite specimens are summarized in Table 4.12. Compression tests carried out on concrete cylinders showed that they were very brittle. The *UHSC* cylinders without coarse aggregates were crushed into pieces and very loud crushing noise was heard when the maximum loads were reached. However, the presence of ordinary coarse aggregates seemed to have some marginal improvement on the brittleness of *UHSC*. The noise generated from failure was not as loud as plain *UHSC*. The failed cylinder specimens are shown in Figure 4.23.

#### 4.5.1.2 Steel sections

Two different types of hot finished circular hollow sections, 114.3mm × 6.3mm and 219.1mm × 6.3mm, were used for the specimens in this series of tests. The first one was the same as that used in Series 1 and Series 2 and its basic properties has been shown in Table 4.3. For the other additional steel section, the basic mechanical properties are shown in Table 4.13. The stress-strain curves from coupon tests for the first section have been shown in Figure 4.4, and the stress-strain curves for the other one are shown in Figure 4.24.

## 4.5.2 Specimens

There were 8 specimens with column diameter 219.1mm and height 600mm, including 4 single-tube columns and 4 double-tube columns. CHS219.1×6.3 was used as the external steel tube for all the specimens and CHS114.3×6.3 was used as the internal tube for the 4 double-tube specimens. The specimen configuration details are shown in Table 4.14 for the single-tube specimens and Table 4.15 for double-tube specimens.

## 4.5.3 Test setup and loading procedure

All the specimens in this series of tests were loaded simultaneously on both of steel tubes and concrete cores as shown in Figure 4.25. The test setup and instrumentations were almost the same as those used for Series 2 tests shown in Figure 4.17. Only one difference was that four plate stiffeners, instead of hoop ring stiffeners, were welded onto each end of every specimen in order to avoid premature local failure at both ends due to imperfections and stress concentration.

The loading procedure was the same as that used for Series 2 tests.

## 4.5.4 Test results and observations

### 4.5.4.1 Load-shortening relationship

The load-axial shortening curves for all the specimens shown in Figure 4.26 for the single-tube specimens and Figure 4.27 for the double-tube specimens. From these curves,



the testing values of the ultimate resistance,  $N_{test,u}$ , and the residual resistance,  $N_{test,r}$ , are obtained and summarized in Table 4.16. Generally, the residual resistance was the second peak load from the load-axial shortening curves.

As observed for the specimens tested in Series 1 and Series 2, very loud cracking/crushing noise was heard around the first peak load during the testing of the four single-tube specimens, due to the brittleness of the *UHSC* core. A steep drop in the load-displacement curves was observed right after the peak load as shown in Figure 4.26. Soon after the load drop, visual inspection was carried out on the specimens and no visible deformation was observed. Therefore, the noise was thought to be originated from the crushing of the *UHSC* core. However, no such loud noise was heard for the double-tube specimens, and the drop from the maximum load shown in Figure 4.27 was not as steep as those for the single tube specimens.

The four single-tube specimens had the same steel section but infilled with *UHSC* reinforced with different proportions and maximum sizes of ordinary coarse aggregates, as well as the four double-tube specimens. The curves for the four single-tube specimens shown in Figure 4.26 almost overlap each other with slight differences in the ultimate resistance and in the range of large axial shortenings which should be mainly due to the slight differences in the values of *UHSC* strength, as well as the curves for the four double-tube specimens shown in Figure 4.27. Therefore, the presence of ordinary coarse aggregates had no significant influence on the reduction in the ultimate resistance and on the post-peak behaviour of the composite columns. However, the cost could be highly reduced by employing ordinary coarse aggregates. In addition, the use of 10mm or 20mm

aggregates does not seem to have any size effect on the ultimate resistance and post-peak ductility performance of the composite specimens.

It has been shown in Figure 4.14 that the presence of coarse aggregates could delay or even prevent the propagation of cracking in *NSC* and then performance of *NSC* on brittleness is much better than plain *UHSC*. However, the coarse aggregates used in this study had no significant influence on the ductility of *UHSC* filled steel tube columns. The main reason should be that the ordinary granite coarse aggregate used in this study was not strong enough to prevent the initiating and propagating of cracks in *UHSC*. The cracks were propagated through the aggregates as shown in Figure 4.28. Along the propagating path of cracking, the aggregates were also crushed. Therefore, high strength coarse aggregates should be used to improve the ductility of *UHSC* filled steel tube columns more efficiently.

The values of residual strength for all the specimens are summarized in Table 4.16. It is observed that the double-tube specimens had higher values of residual strength ratio,  $N_{test,r}/N_{test,u}$ . It indicates that the higher the steel contribution ratio, the higher is the residual strength ratio, and the better is the ductility. The same result can also be observed from Figure 4.29 for the comparison of single-tube specimens with double-tube specimens. According to the criteria as defined in Equation (4.2), almost all the double-tube specimens, of which the steel contribution ratio was higher than 0.3, had sufficient ductility performance; while almost all the single-tube specimens did not have sufficient ductility due to lower steel contribution ratio less than 0.3.

All the specimens before casting of concrete and after testing in this series of tests are shown in Figure 4.30.

#### **4.6 Series 4 Tests: CFST Columns with UHSC and HSS**

Further to the three series of experimental investigations on the structural behaviour of axially compressed circular UHSC filled mild steel tube columns presented previously, this section will present another series of experimental investigation on the structural behaviour of axially compressed square UHSC filled HSS tube columns.

##### **4.6.1 Material properties**

The materials used in this series of tests included UHSC reinforced with different proportions and sizes of ordinary coarse aggregates, Grade S690 high tensile strength steel plates, and Grade S355 hot finished square hollow steel section.

###### **4.6.1.1 UHSC**

Five different mix proportion designs, the same as those shown in Table 3.4 of **Chapter 3**, were used for this series of specimens. The first one was plain UHSC without coarse aggregates, the second one was reinforced with 19% coarse aggregates of maximum size 10mm, the third one was reinforced with 38% coarse aggregates of maximum size 10mm, and the fourth one was reinforced with 19% coarse aggregates of maximum size 20mm, and the fifth one was reinforced with 38% coarse aggregates of maximum size 20mm. For each mix design, one batch concrete was cast. The basic properties for each batch tested during testing corresponding composite specimens are summarized in Table 4.17.

#### 4.6.1.2 Steel sections

Three different types of *HSS* square hollow sections, 80mm × 8mm, 150mm × 8mm and 150mm × 12mm, were used for the specimens in this series of tests. These sections were welded box sections fabricated from high tensile strength steel plates. Two different thickness values of high tensile strength steel plates were used, 8mm and 12mm. In addition, a 6mm thick mild steel backing strip was adopted. For comparison, one hot finished square hollow section, 150mm×12.5mm, was also used. The mechanical properties for all the sections are summarized in Table 4.18. The stress-strain curves from coupon tests are shown from Figure 4.31 to Figure 4.34. It can be found the yield strength of the *HSS* is up to 779MPa but it is not as ductile as normal strength steel, with less elongation and weaker hardening effect.

#### 4.6.2 Specimens

There were 21 square specimens with column breadth 150mm and height 450mm, including 17 single-tube specimens and 4 double-tube specimens as schematically shown in Figure 4.35 and Figure 4.36. Based on different dimension details of the cross-sections as shown in Figure 4.37 and Figure 4.38, all the specimens were classified into four groups as S4-1, S4-2, S4-3 and S4-4. Groups S4-1 and S4-2 included single-tube specimens with welded box sections made of high strength steel plates, Group S4-3 included single-tube specimens with mild steel hot finished hollow sections, and Group S4-4 included double-tube specimens with welded box sections made of high strength steel plates. The composite specimen configuration details are summarized in Table 4.19.

### 4.6.3 Test setup and loading procedure

All the specimens in this series of tests were loaded simultaneously on both of steel tubes and concrete cores as shown in Figure 4.39. To avoid premature local failure at both ends due to initial imperfection, two endplates were welded to each single-tube specimen and shear connectors were utilized for double-tube specimens. The arrangement of strain gauges and *LVDTs* used for this series of tests was the same as that used for previous three series of tests.

A quasi-static loading procedure was introduced in four steps: (1) preload the specimen at a rate of 5kN/s up to 10% of its resistance estimated by Equation (2.2) introduced in **Chapter 2**; (2) unload at a rate of 1.0mm/min; (3) reload at the same rate as that in Step 1 to 60% ~ 70% of its resistance, and then change the rate to 0.2mm/min until the peak load is achieved; (4) finally in the post-peak range, increase the rate up to 0.5mm/min until complete failure occurs.

### 4.6.4 Test results and observations

#### 4.6.4.1 Load-shortening relationship

The axial load-shortening curves for all the specimens are shown in groups as Group S4-1 in Figure 4.40, Group S4-2 in Figure 4.41, Group S4-3 in Figure 4.42, and Group S4-4 in Figure 4.43. From these curves, the testing values of the ultimate resistance,  $N_{test,u}$ , and the residual resistance,  $N_{test,r}$ , are obtained and summarized in Table 4.20.

Hollow steel tube specimens S4-1-6 and S4-2-6 had much lower values of resistance than the composite specimens as shown in Figure 4.40 and Figure 4.41. The wall thickness of

S4-1-6 was 8mm, much thinner than S4-2-6 which was 12mm thick. Therefore, the resistance of S4-1-6 was dropping soon after yielding, while the resistance of S4-2-6 keeps increasing after yielding.

For the composite specimens in each group, they had the same steel sections but infilled with *UHSC* reinforced with different proportions and maximum sizes of ordinary coarse aggregates. The same as observed in Series 3 tests, it can also be observed from Figure 4.40 to Figure 4.43 that the curves for the composite specimens in each group almost overlap each other with slight differences in the ultimate resistance and in the range of large axial shortenings which should be mainly due to the slight differences in the values of *UHSC* strength. These tests confirm that the presence of ordinary coarse aggregates should have no significant influence on the reduction in the ultimate resistance and on the post-peak behaviour of the composite columns. However, the cost can be highly reduced by employing ordinary coarse aggregates.

In addition, it can be observed that the loading was increasing straightly up to the peak load and then it was dropping down. For the specimens with high tensile strength steel sections, the values of steel contribution ratio for the specimens in Groups S4-1 were much lower than those specimens in Groups S4-2 and S4-4. Therefore, the loading was dropping faster for the specimens in Group S4-1. Different from the curves for all the specimens with high tensile strength steel sections, the curves for the specimens with mild steel hot finished hollow sections shown in Figure 4.42 developed a significant plateau beyond the peak load, because there was significant hardening effect for the mild steel sections as shown in Figure 4.34 while there was almost no hardening effect for the high tensile strength steel as shown in Figure 4.31 and Figure 4.32.

Furthermore, all the curves for this series of tests had no significant second peak load as observed from those curves in previous three series of tests. The main reason should be that the confinement effect in square *CFST* columns is much weaker than circular *CFST* columns.

All the specimens before casting of concrete and after testing in this series of tests are shown in Figure 4.44.

## 4.7 Evaluation of Test Results

### 4.7.1 Mechanics of composite action between concrete core and steel tube

#### 4.7.1.1 Effect of Poisson's ratio

Poisson's ratio, defined as the absolute value of the ratio of transverse strain to longitudinal strain under uniaxial loading, plays a significant role in analyzing the load sharing mechanism between the concrete core and the steel tube.

For mild structural steel, the Poisson's ratio value almost keeps at about 0.3 before yielding, and then it increases rapidly approximating to 0.5 after yielding. For *NSC*, it is at about 0.2 under low compressive stress level, and increases rapidly after reaching 80% ~ 90% of the ultimate strength due to the initiating of micro-cracks, and finally approaches a value of about 0.5 at the ultimate strength. The value exceeds 0.5 after the ultimate strength due to dilation effect. The Poisson's ratio for *UHSC* is about 0.23, slightly higher than that of *NSC*, under low compressive stress level.

The longitudinal stress-strain curve for the hollow steel tube S2-2-1 is plotted in Figure 4.45, together with the Poisson's ratio measured as the ratio of circumferential strain to longitudinal strain. The estimated Poisson's ratio values were decreasing instead of increasing right after yielding, mainly due to the influence of the hoop ring stiffeners and imperfections. The variations of Poisson's ratios for *NSC* and *UHSC* are shown in Figure 4.46 and Figure 4.47 respectively, obtained from the compressive test results on cylinders. Different from *NSC*, the stress-strain curve for *UHSG* is almost linearly elastic up to the ultimate strength. Once the ultimate strength is reached, the concrete cylinder will crack and fracture into pieces. Corresponding idealized numerical approximations with softening phases are also shown in Figure 4.45, Figure 4.46 and Figure 4.47 as references. It should be noted that the true stress and strain values are converted from the test nominal values and shown in the three figures.

Figure 4.48 shows a simplified model for a concrete filled tube subjected to longitudinal compressive strain  $\varepsilon_z$ . Assuming that there is no interaction at the interface which means that the concrete core and steel tube are free to expand, the tensile strains at a point "P" at the interface in circumferential and radial directions should be:

$$\begin{cases} \varepsilon_{\theta,c}^P = \varepsilon_{r,c}^P = \nu_c \varepsilon_z & \text{(based on the properties of concrete core)} \\ \varepsilon_{\theta,a}^P = \varepsilon_{r,a}^P = \nu_a \varepsilon_z & \text{(based on the properties of steel tube)} \end{cases} \quad (4.3)$$

The displacement at the point "P" in the radial direction should be:

$$\begin{cases} u_{r,c}^P = \left(\frac{d}{2} - t\right) \varepsilon_{r,c}^P = \nu_c \left(\frac{d}{2} - t\right) \varepsilon_z \\ u_{r,a}^P = \left(\frac{d}{2} - t\right) \varepsilon_{r,a}^P = \nu_a \left(\frac{d}{2} - t\right) \varepsilon_z \end{cases} \Rightarrow \frac{u_{r,c}^P}{u_{r,a}^P} = \frac{\nu_c}{\nu_a} \quad (4.4)$$



Considering the deformation compatibility  $u_{r,c}^P \leq u_{r,a}^P$ , it obtains:

$$\begin{cases} v_c < v_a : \text{separation or tensile debonding stress produced} \\ v_c = v_a : \text{keeping in touch but no interaction} \\ v_c > v_a : \text{concrete core confined by steel tube} \end{cases} \quad (4.5)$$

Therefore, the assumption is correct only when the Poisson's ratio value of concrete is equal to that of steel, or free separation occurs when it is smaller; otherwise, tensile debonding or compressive stresses should be produced at the interface. Thus, confinement effect can be produced only if the Poisson's ratio value of concrete is greater than that of steel, unless effective transverse restraints are imposed on steel tubes.

For commonly used mild steel in the range of S275 to S460, it should have been yielded when concrete achieves its ultimate strength. Therefore, effective confinement stresses can only start at right before the concrete core reaches its ultimate strength. Before that, tensile stresses or separation may occur at the interface. Ignoring the debonding tensile stresses, Figure 4.49 shows the general variations of longitudinal stresses and  $\varepsilon_{\theta}^P/\varepsilon_z^P$  at the point "P" in the simple model as shown in Figure 4.48, compared with the variations of uniaxial stresses and Poisson's ratios of mild steel and NSC shown in Figure 4.45 and Figure 4.46. Initially, the Poisson's ratio value of concrete is less than that of steel. The concrete core and steel tube are transversely expanding freely and hence the ratios of circumferential strain to longitudinal strain are respectively equal to their Poisson's ratios. After that, the Poisson's ratio value of concrete is increasing and exceeds that of steel. The concrete core will be confined by steel tube. Values of  $\varepsilon_{\theta,c}^P/\varepsilon_z^P$  will be less than the Poisson's ratio values of concrete and values of  $\varepsilon_{\theta,a}^P/\varepsilon_z^P$  will be greater than the Poisson's ratio values of steel. To keep deformation compatibility,  $\varepsilon_{\theta,c}^P/\varepsilon_z^P = \varepsilon_{\theta,a}^P/\varepsilon_z^P$ . The

confinement effect improves the ductility and compressive strength of *NSC*, but reduces the compressive strength of steel tube since tensile stress is produced in the circumferential direction in the tube section. This is the reason why an enhancement factor is considered for concrete strength while a reduction factor is considered for steel strength in Equation (2.3) introduced in **Chapter 2**, when the confinement effect is considered. However, for *UHSC* filled steel tube columns tested in this study, the ultimate resistance was achieved at a very small deformation before significant confinement effect had been developed due to the brittleness of *UHSC*. Therefore, the confinement effect should not be considered for *CFST* columns with *UHSC*.

The simple model presented herein considers the worst case scenario. In practice, there may be some initial confinement stresses before loading due to self-expanding of concrete, circumferential restraint boundary conditions and so on. Some of the initial confinement stresses could be released at the initial stage of loading when the Poisson's ratio of concrete is less than that of steel; however, if not all are released, tensile debonding stresses will not occur. Efficient confinement stress will start earlier. After all, initial confinement stresses can improve the performance of composite columns. However, there also may be some significant initial imperfections, such as loading eccentricity, geometrical imperfections and concrete shrinkage, which will affect the performance.

#### 4.7.1.2 Effect of local buckling

Class 3 steel hollow circular sections cannot develop plastic resistance. Once yielding occurs, they are susceptible to plastic local buckling. Figure 4.50 shows history curves of the measured vertical strains at the middle height of columns and loading variations for

hollow steel tubes S2-1-1 of Class 3 section and S2-2-1 of Class 1 section. If there is no local buckling, the vertical strains should keep increasing as long as the axial shortening displacements are increasing. However, the vertical strain of S2-1-1 decreased once yielding occurred, which means that plastic local buckling was produced. On the contrary, S2-2-1 developed full plastic resistance.

For concrete filled tubes of Class 3 sections, separation or tensile stresses may still exist at the interface even after yielding, which means that the concrete core cannot provide efficient restraints for steel tube to prevent local buckling and even more the tensile debonding stresses may draw the steel tube to get buckled more easily. As a result, the expected final confinement effect should be discounted, not as strong as predicted by Equation (2.3) introduced in **Chapter 2**. Figure 4.51 shows history curves of the measured vertical strains at the middle height and loading variations for *NSC* filled tubes S2-1-2 of Class 3 section and S2-2-2 of Class 1 section. Better than the hollow steel tube S2-1-1, the vertical strain of the steel tube in S2-1-2 was increasing after yielding, but it locally buckled at a vertical displacement of less than 20mm, much earlier than the steel tube in S2-2-2 which buckled at about 40mm vertical displacement. Therefore, the confinement effect should be better limited to *CFST* columns with Class 1 and Class 2 steel sections; otherwise, the confinement effect should be ignored.

#### **4.7.2 Performance of *CFST* columns on ductility**

From all the test values of ultimate and residual resistance presented previously, it has been shown that all the hollow steel tube columns with non-slender sections, *NSC* filled steel tube columns, and *UHSC* filled steel tube columns loaded only on concrete core

possessed sufficient performance on ductility. However, some *UHSC* filled steel tube columns loaded simultaneously on both concrete core and steel tube showed weak ductile behaviour, especially for those with low steel contribution ratio.

The higher the residual resistance ratio, the better is the ductility. The test values of residual resistance ratio for all the single-tube *CFST* columns with *UHSC* are shown in Figure 4.52. For each type of columns, the higher the steel contribution ratio, the better is the ductility. In addition, circular columns possessed better ductility than square *CFST* columns even if they had lower steel contribution ratio, because the confinement effect was much stronger in circular columns than square columns. The square columns with mild steel sections showed better ductility than those with *HSS* sections even if they had lower steel contribution ratio, because there was much stronger hardening effect for mild steel than *HSS*. Furthermore, the presence of steel fiber could improve the ductility performance. Therefore, to meet the ductility requirements as defined in Equation (4.2), the steel contribution ratio should be greater than 0.3, or 1.0% steel fiber should be added into *UHSC*. If *HSS* is used, the lower limit of steel contribution ratio should be further increased.

#### 4.7.3 Test results of ultimate resistance compared with Eurocode 4 predictions

The test values of ultimate resistance for all the 56 specimens in the four series of tests are compared with Eurocode 4 (2004) predictions by simply extending the limitations on materials to the *UHSC* and *HSS* used in this study. The relevant design formulae have been introduced in **Chapter 2**.

For all the 7 hollow steel tube specimens, the comparisons are shown in Table 4.21. The first five are circular hollow steel tube columns with mild steel sections and the other two are square hollow steel tube columns with *HSS* sections. It can be observed that the ratio of test result to prediction ranges from 0.931 to 1.219, with a mean value of 1.074 and a standard deviation value of 0.123. Specimens with Class 1 sections have larger safety margins. Only for the specimen S2-1-1 with a Class 3 section, the prediction is overestimated by more than 5%, up to 7%.

For all the 4 *NSC* filled circular steel tube specimens, the comparisons are shown in Table 4.22. The first two are single-tube specimens and the other two are double-tube specimens. Both of the predictions with and without confinement effect,  $N_{pI,RK}$  and  $N_{pI,RK2}$ , are provided. It can be observed that the ratio of test result to prediction ranges from 1.022 to 1.282 with a mean value of 1.155 and a standard deviation value of 0.143, if the confinement effect is not considered; and it ranges from 0.866 to 1.090 with a mean value of 0.970 and a standard deviation value of 0.102, if the confinement effect is considered. Without confinement effect, all the predictions are underestimated, especially for the specimens S2-2-2 and S2-4-1 with Class 1 steel sections which are underestimated by 28%. However, if the confinement effect is considered, the prediction is overestimated by up to 13% for the single-tube specimen S2-1-2 with a Class 3 steel section, and by 9% for the double-tube specimen S2-3-1 with the same Class 3 steel section for the external tube. Therefore, the confinement effect should be ignored for *NSC* filled steel tube columns with Class 3 steel sections, as stated in Section 4.7.1.2 .

For all 16 the *UHSC* filled circular single-tube specimens, the comparisons are shown in Table 4.23. It can be observed that the ratio of test result to prediction ranges from 1.027

to 1.233 with a mean value of 1.104 and a standard deviation value of 0.055, if the confinement effect is not considered; and it ranges from 0.949 to 1.064 with a mean value of 1.004 and a standard deviation value of 0.035, if the confinement effect is considered. Without confinement effect, all the predictions are underestimated with an average safety margin of more than 10%. However, if the confinement effect is considered, a half of specimens are overestimated but by less than 5%. As stated previously, for *CFST* columns with *UHSC* tested in this study, the ultimate resistance was achieved at a very small deformation before significant confinement effect had been developed due to the brittleness of *UHSC*. Therefore, the Eurocode 4 limitation on concrete strength could be safely extended to *UHSC* for circular single-tube *CFST* columns. However, the confinement effect should be ignored.

For all the 10 *UHSC* filled circular double-tube specimens, the comparisons are shown in Table 4.24. It can be observed that the ratio of test result to prediction ranges from 0.939 to 1.181 with a mean value of 1.090 and a standard deviation value of 0.076, if the confinement effect is not considered; and it ranges from 0.884 to 1.072 with a mean value of 1.004 and a standard deviation value of 0.060, if the confinement effect is considered. Without confinement effect, only one specimen is overestimated by 6% and all other specimens are underestimated by up to 18%. However, if the confinement effect is considered, 4 out of 10 specimens are overestimated by up to 12%. Therefore, the Eurocode 4 limitation on concrete strength could also be safely extended to *UHSC* for circular double-tube *CFST* columns, but the confinement effect should be ignored.

For all the 5 *UHSC* filled square single-tube specimens with mild steel sections, the comparisons are shown in Table 4.25. It can be observed that the ratio of test result to

prediction ranges from 1.089 to 1.189 with a mean value of 1.139 and a standard deviation value of 0.039. All the predictions are underestimated with an average safety margin of 14%. Therefore, the Eurocode 4 limitation on concrete strength could be safely extended to *UHSC* for square single-tube *CFST* columns with mild steel sections.

For all the 10 *UHSC* filled square single-tube specimens with *HSS* sections, the comparisons are shown in Table 4.26. It can be observed that the ratio of test result to prediction ranges from 1.017 to 1.186 with a mean value of 1.099 and a standard deviation value of 0.055. All the predictions are underestimated with an average safety margin of 10%. Therefore, the Eurocode 4 limitations on materials could be safely extended to *UHSC* and *HSS* for square single-tube *CFST* columns.

For all the 4 *UHSC* filled square double-tube specimens with *HSS* sections, the comparison of test results with predictions is shown in Table 4.27. It can be observed that the ratio of test result to prediction ranges from 0.885 to 0.968 with a mean value of 0.908 and a standard deviation value of 0.040. All the predictions are overestimated by 9% on average, different from the predictions for other types of *CFST* columns presented previously. Therefore, to provide conservative predictions, Equation (2.2) introduced in **Chapter 2** should be modified for *UHSC* filled square *HSS* double-tube columns as,

$$N_{pl,Rk,m} = 0.85(A_a f_y + A_c f_{ck}) \quad (4.6)$$

All the test results for *CFST* specimens compared with Eurocode 4 predictions are shown in Figure 4.53 without confinement effect and Figure 4.54 with confinement effect.

## 4.8 Summary

Four series of tests on the structural behaviour of stub *CFST* columns employing *UHSC* and *HSS* have been presented in this chapter. The test results of 56 specimens have shown that ultra high compressive resistance, which is required for structural members in high-rise structures, can be achieved by employing *UHSC*. In addition, the compressive resistance can be higher if both of *UHSC* and *HSS* are used. Therefore, they are feasible to be adopted for high-rise constructions.

The ductility performance of *CFST* columns with *UHSC* should be considered, due to the brittleness of *UHSC*. The ductility can be improved if the compression load is imposed only on the *UHSC* core, steel fiber is added into *UHSC*, or higher steel contribution ratio is used. Based on the criteria recommended in this study, at least 1.0% steel fiber should be used, or lower limit on steel contribution ratio as defined in Eurocode 4 should be increased from 0.2 up to 0.3.

The usage of ordinary granite coarse aggregates has no significant influence on the resistance and ductility of *CFST* columns with *UHSC*. However, it leads to significant cost saving in the high-strength concrete filling.

For *CFST* columns with *UHSC*, the ultimate resistance can be achieved at a very small deformation before significant confinement effect have been developed due to the brittleness of *UHSC*. For *CFST* columns with *NSC* and Class 3 steel sections, local buckling may occur right after the yielding of steel tubes and no significant confinement effect can be developed at the ultimate resistance. Therefore, the confinement effect



should be ignored for *CFST* columns with *UHSC* or Class 3 steel sections, which has been confirmed by the comparisons of test results with Eurocode 4 predictions.

The comparisons of test results with Eurocode 4 predictions have indicated that the limitations on concrete cylinder strength and steel strength can be safely extended for *UHSC* up to 200MPa and *HSS* up to 780MPa for stub *CFST* columns. A reduction factor should be considered for *UHSC* filled square *HSS* double-tube columns; otherwise, Eurocode 4 can provide conservative predictions, if the confinement effect is not considered for those specimens with *UHSC* or Class 3 steel sections.

Table 4.1: Basic properties of high tensile strength steel fiber

Code	d (mm)	L (mm)	Aspect Ratio	Specific gravity	$f_y$ (MPa)	$E_a$ (GPa)	Coating
SF 13/80	0.16	13	80	7.85	2300	200	Brass

Table 4.2: Basic material properties of concrete used in Series 1

Batch No.	Type	$f_{ck}$ (MPa)	$E_{cm}$ (GPa)	$\nu_c$
S1B1	UHSC	173.5	63	0.24
S1B2	UHSC + 1%SF	184.2	63	0.24

Table 4.3: Basic properties of steel sections used in Series 1

Sections	d (mm)	t (mm)	$f_y$ (MPa)	$f_u$ (MPa)	$E_a$ (GPa)	$\frac{d}{t} \frac{f_y}{235}$	Section classification
CHS114.3×3.6	114.3	3.6	403	505	213	54 (< 70)	2
CHS114.3×6.3	114.3	6.3	428	519	209	33 (< 50)	1

Table 4.4: Specimen configuration details for Series 1

No.	L (mm)	Steel section	$f_y$ (MPa)	$f_{ck}$ (MPa)	$\lambda$	$\delta$
S1-1-1(a)	250	CHS114.3×3.6	403	-	0.088	-
S1-1-2(a)	250	CHS114.3×6.3	428	-	0.094	-
S1-1-2(b)	250	CHS114.3×6.3	428	-	0.094	-
S1-2-1(a)*	210	CHS114.3×6.3	428	173.5	0.110	0.493
S1-2-1(b)*	210	CHS114.3×6.3	428	173.5	0.110	0.493
S1-3-1(a)	250	CHS114.3×3.6	403	173.5	0.142	0.326
S1-3-1(b)	250	CHS114.3×3.6	403	173.5	0.142	0.326
S1-3-2(a)	250	CHS114.3×3.6	403	184.2**	0.145	0.313
S1-3-2(b)	250	CHS114.3×3.6	403	184.2**	0.145	0.313
S1-3-3(a)	250	CHS114.3×6.3	428	173.5	0.131	0.493
S1-3-3(b)	250	CHS114.3×6.3	428	173.5	0.131	0.493

\* Loaded only on the concrete core which was 210mm in height; the steel tubes were 250mm in height

\*\*The UHSC was reinforced by 1% steel fiber in volume

Table 4.5: Test values of ultimate and residual resistance for Series 1

No.	$N_{test,u}$ (kN)	$N_{test,r}$ (kN)	$N_{test,r}/N_{test,u}$	$\delta$
S1-1-1(a)	486	416	0.856	-
S1-1-2(a)	1039	1039	1.000	-
S1-1-2(b)	990	990	1.000	-
S1-2-1(a)	2866	2317	0.809	0.493
S1-2-1(b)	2595	2293	0.883	0.493
S1-3-1(a)	2422	1695	0.700	0.326
S1-3-1(b)	2340	1689	0.722	0.326
S1-3-2(a)	2497	1903	0.762	0.313
S1-3-2(b)	2314	1884	0.814	0.313
S1-3-3(a)	2610	2309	0.884	0.493
S1-3-3(b)	2633	2518	0.957	0.493

Table 4.6: Mix proportion design for NSC used in Series 2

Water/Cement	Water (kg/m <sup>3</sup> )	Cement (kg/m <sup>3</sup> )	Sand (kg/m <sup>3</sup> )	Coarse Aggregate (kg/m <sup>3</sup> )
0.5	225	450	625	1005

Table 4.7: Basic material properties of concrete used in Series 2

Batch No.	Type	$f_{ck}$ MPa	$E_{cm}$ GPa	$\nu_c$	$\rho_c$ kg/m <sup>3</sup>
S2B1	NSC	51.6	28	0.20	2317
S2B2	UHSC	185.1	66	0.23	2717
S2B3	UHSC	175.0	66	0.23	2704
S2B4	UHSC+0.5%SF	193.3	67	0.25	2703

Table 4.8: Basic properties of two additional steel sections used in Series 2

Sections	d (mm)	t (mm)	$f_y$ (MPa)	$f_u$ (MPa)	$E_a$ (GPa)	$\frac{d}{t} \frac{f_y}{235}$	Section classification
CHS219.1×5	219.1	5	380	511	205	71 (< 90)	3
CHS219.1×10	219.1	10	381	509	212	36 (< 50)	1

Table 4.9: Single-tube specimen configuration details for Series 2

No.	L (mm)	Steel section	$f_y$ (MPa)	$f_{ck}$ (MPa)	$\lambda$	$\delta$
S2-1-1	600	CHS219.1×5	380	-	0.109	-
S2-1-2	600	CHS219.1×5	380	51.6	0.142	0.520
S2-1-3	600	CHS219.1×5	380	185.1	0.191	0.232
S2-1-4	600	CHS219.1×5	380	193.3*	0.193	0.224
S2-2-1	600	CHS219.1×10	381	-	0.109	-
S2-2-2	600	CHS219.1×10	381	51.6	0.130	0.700
S2-2-3	600	CHS219.1×10	381	185.1	0.168	0.394
S2-2-4	600	CHS219.1×10	381	193.3*	0.170	0.384

\*The UHSC was reinforced by 0.5% steel fiber in volume

Table 4.10: Double-tube specimen configuration details for Series 2

No.	L (mm)	Steel sections	$f_y$ (MPa)		$f_{ck}$ (MPa)		$\lambda$	$\delta$
			External	Internal	In-between	Internal		
S2-3-1	600	CHS21.9×5/114.3×3.6	380	403	51.6	51.6	0.147	0.610
S2-3-2	600	CHS21.9×5/114.3×3.6	380	403	175.0	175.0	0.186	0.316
S2-3-3	600	CHS21.9×5/114.3×3.6	380	403	51.6	175.0	0.167	0.487
S2-3-4	600	CHS21.9×5/114.3×3.6	380	403	51.6	193.3*	0.169	0.473
S2-4-1	600	CHS21.9×10/114.3×6.3	381	428	51.6	51.6	0.137	0.774
S2-4-2	600	CHS21.9×10/114.3×6.3	381	428	175.0	175.0	0.166	0.503
S2-4-3	600	CHS21.9×10/114.3×6.3	381	428	51.6	185.1	0.151	0.665
S2-4-4	600	CHS21.9×10/114.3×6.3	381	428	51.6	193.3*	0.151	0.659

\*The UHSC was reinforced by 0.5% steel fiber in volume

Table 4.11: Test values of ultimate and residual resistance for Series 2

No.	$N_{\text{test,u}}$ (kN)	$N_{\text{test,r}}$ (kN)	$N_{\text{test,r}}/ N_{\text{test,u}}$	$\delta$
S2-1-1	1190	776	0.652	-
S2-1-2	3118	3055	0.980	0.520
S2-1-3	7837	3803	0.485	0.232
S2-1-4	8664	5691	0.657	0.224
S2-2-1	3050	3050	1.000	-
S2-2-2	5241	5241	1.000	0.700
S2-2-3	9085	7353	0.809	0.394
S2-2-4	9187	7479	0.814	0.384
S2-3-1	3626	3609	0.995	0.610
S2-3-2	8529	5175	0.607	0.316
S2-3-3	4968	4830	0.972	0.487
S2-3-4	5239	4171	0.796	0.473
S2-4-1	6300	6300	1.000	0.774
S2-4-2	9817	6960	0.709	0.503
S2-4-3	7022	7022	1.000	0.665
S2-4-4	7160	7160	1.000	0.659

Table 4.12: Basic material properties of concrete used in Series 3

Batch No.	Type	$f_{ck}$ (MPa)	$E_{cm}$ (GPa)
S3B1	UHSC without CA	163.0	62
S3B2	UHSC+19%CA (10mm)	175.4	58
S3B3	UHSC+38%CA (10mm)	148.8	54
S3B4	UHSC+38%CA (20mm)	174.5	56

Table 4.13: Basic properties of one additional steel section used in Series 3

Sections	d (mm)	t (mm)	$f_y$ (MPa)	$f_u$ (MPa)	$E_a$ (GPa)	$\frac{d}{t} \frac{f_y}{235}$	Section classification
CHS219.1×6.3	219.1	6.3	300	467	202	44 (< 50)	1

Table 4.14: Single-tube specimen configuration details for Series 3

No.	L (mm)	Steel section	$f_y$ (MPa)	$f_{ck}$ (MPa)	$\lambda$	$\delta$
S3-1-1	600	CHS219.1×6.3	300	163.0	0.174	0.258
S3-1-2	600	CHS219.1×6.3	300	175.4	0.181	0.244
S3-1-3	600	CHS219.1×6.3	300	148.8	0.172	0.276
S3-1-4	600	CHS219.1×6.3	300	174.5	0.182	0.245

Table 4.15: Double-tube specimen configuration details for Series 3

No.	L (mm)	Steel sections	$f_y$ (MPa)		$f_{ck}$ (MPa)	$\lambda$	$\delta$
			External	Internal			
S3-2-1	600	CHS219.1×6.3/114.3×6.3	300	428	163.0	0.175	0.390
S3-2-2	600	CHS219.1×6.3/114.3×6.3	300	428	175.4	0.182	0.373
S3-2-3	600	CHS219.1×6.3/114.3×6.3	300	428	148.8	0.174	0.412
S3-2-4	600	CHS219.1×6.3/114.3×6.3	300	428	174.5	0.183	0.374

Table 4.16: Test values of ultimate and residual resistance for Series 3

No.	$N_{test,u}$ (kN)	$N_{test,r}$ (kN)	$N_{test,r}/N_{test,u}$	$\delta$
S3-1-1	6915	4975	0.720	0.258
S3-1-2	7407	4741	0.640	0.244
S3-1-3	6838	3971	0.581	0.276
S3-1-4	7569	5071	0.670	0.245
S3-2-1	7640	6129	0.802	0.390
S3-2-2	7209	5667	0.786	0.373
S3-2-3	6882	5328	0.774	0.412
S3-2-4	8375	5481	0.654	0.374

Table 4.17: Basic material properties of concrete used in Series 4

Batch No.	Type	$f_{ck}$ (MPa)	$E_{cm}$ (GPa)	$\rho_c$ kg/m <sup>3</sup>
S4B1	UHSC without CA	152.3	62	2651
S4B2	UHSC+19%CA (10mm)	157.2	58	2658
S4B3	UHSC+38%CA (10mm)	147.0	54	2646
S4B4	UHSC+19%CA (20mm)	164.1	58	2665
S4B5	UHSC+38%CA (20mm)	148.0	56	2653

Table 4.18: Basic material properties of steel sections used in Series 4

Sections	b (mm)	t (mm)	$f_y$ (MPa)	$f_u$ (MPa)	$E_a$ (GPa)	Section classification
SHS80×8	80	8	779	846	200	1
SHS150×8	150	8	779	846	200	1
SHS150×12	150	12	756	825	199	1
SHS150×12.5	150	12.5	446	565	201	1

For the 6mm-thick mild steel backing strip,  $f_y = 325\text{MPa}$ ,  $f_u = 467\text{MPa}$ , and  $E_a = 201\text{GPa}$



Table 4.19: Specimen configuration details for Series 4

Group	No.	L (mm)	Steel sections	$f_y$ (MPa)	$f_{ck}$ (MPa)	$\lambda$	$\delta$
S4-1	S4-1-1	450	SHS150×8	779	152.3	0.173	0.688
	S4-1-2	450	SHS150×8	779	157.2	0.175	0.682
	S4-1-3	450	SHS150×8	779	147.0	0.174	0.696
	S4-1-4	450	SHS150×8	779	164.1	0.177	0.672
	S4-1-5	450	SHS150×8	779	148.0	0.174	0.695
	S4-1-6	450	SHS150×8	779	-	0.150	-
S4-2	S4-2-1	450	SHS150×12	756	152.3	0.171	0.777
	S4-2-2	450	SHS150×12	756	157.2	0.173	0.771
	S4-2-3	450	SHS150×12	756	147.0	0.172	0.783
	S4-2-4	450	SHS150×12	756	164.1	0.174	0.764
	S4-2-5	450	SHS150×12	756	148.0	0.172	0.782
	S4-2-6	450	SHS150×12	756	-	0.154	-
S4-3	S4-3-1	450	SHS150×12.5	446	152.3	0.149	0.655
	S4-3-2	450	SHS150×12.5	446	157.2	0.151	0.648
	S4-3-3	450	SHS150×12.5	446	147.0	0.150	0.663
	S4-3-4	450	SHS150×12.5	446	164.1	0.153	0.638
	S4-3-5	450	SHS150×12.5	446	148.0	0.150	0.662
S4-4	S4-4-1	450	SHS150×8/80×8	779	152.3	0.185	0.802
	S4-4-2	450	SHS150×8/80×8	779	157.2	0.187	0.797
	S4-4-3	450	SHS150×8/80×8	779	147	0.186	0.807
	S4-4-4	450	SHS150×8/80×8	779	164.1	0.188	0.790

Table 4.20: Test values of ultimate and residual resistance for Series 4

Group	No.	$N_{test,u}$ (kN)	$N_{test,r}$ (kN)	$N_{test,r}/N_{test,u}$	$\delta$
S4-1	S4-1-1	6536	4825	0.738	0.688
	S4-1-2	6715	4789	0.713	0.682
	S4-1-3	6616	4795	0.725	0.696
	S4-1-4	7276	4753	0.653	0.672
	S4-1-5	6974	4572	0.656	0.695
	S4-1-6	3695	2238	0.605	-
S4-2	S4-2-1	8585	7563	0.881	0.777
	S4-2-2	8452	7496	0.887	0.771
	S4-2-3	8687	7515	0.865	0.783
	S4-2-4	8730	7500	0.859	0.764
	S4-2-5	8912	7325	0.822	0.782
	S4-2-6	6456	6456	1.000	-
S4-3	S4-3-1	5953	5163	0.867	0.655
	S4-3-2	5911	5423	0.917	0.648
	S4-3-3	6039	5130	0.849	0.663
	S4-3-4	6409	5316	0.829	0.638
	S4-3-5	6285	5226	0.831	0.662
S4-4	S4-4-1	7058	6346	0.899	0.802
	S4-4-2	7143	6193	0.867	0.797
	S4-4-3	7032	5909	0.840	0.807
	S4-4-4	7880	6258	0.794	0.790

Table 4.21: Test results and predictions for hollow steel tube columns

No.	Steel section	$f_y$ (MPa)	Section classification	$N_{test,u}$ (kN)	$N_{pl,Rk}$ (kN)	$N_{test,u}/N_{pl,Rk}$
S1-1-1(a)	CHS114.3×3.6	403	2	486	505	0.963
S1-1-2(a)	CHS114.3×6.3	428	1	1039	915	1.136
S1-1-2(b)	CHS114.3×6.3	428	1	990	915	1.082
S2-1-1	CHS219.1×5	380	3	1190	1278	0.931
S2-2-1	CHS219.1×10	381	1	3050	2503	1.219
S4-1-6	SHS150×8	779	1	3695	3828	0.965
S4-2-6	SHS150×8	756	1	6456	5296	1.219
Mean						1.074
Standard deviation						0.123

Table 4.22: Test results and predictions for NSC filled circular steel tube columns

No.	$N_{test,u}$ (kN)	$N_{pl,Rk}$ (kN)	$N_{pl,Rk2}$ (kN)	$N_{test,u}/N_{pl,Rk}$	$N_{test,u}/N_{pl,Rk2}$
S2-1-2	3118	3050	3601	1.022	0.866
S2-2-2	5241	4109	5155	1.275	1.017
S2-3-1	3626	3490	3999	1.039	0.907
S2-4-1	6300	4914	5781	1.282	1.090
Mean				1.155	0.970
Standard deviation				0.143	0.102

Table 4.23: Test results and predictions for UHSC filled circular single-tube

No.	$N_{test,u}$ (kN)	$N_{pl,Rk}$ (kN)	$N_{pl,Rk2}$ (kN)	$N_{test,u} / N_{pl,Rk}$	$N_{test,u} / N_{pl,Rk2}$
S1-2-1(a)	2866	2324	2733	1.233	1.049
S1-2-1(b)	2595	2324	2733	1.117	0.949
S1-3-1(a)	2422	2068	2277	1.172	1.064
S1-3-1(b)	2340	2068	2277	1.132	1.028
S1-3-2(a)	2497	2164	2369	1.154	1.054
S1-3-2(b)	2314	2164	2369	1.069	0.977
S1-3-3(a)	2610	2324	2685	1.123	0.972
S1-3-3(b)	2633	2324	2685	1.133	0.980
S2-1-3	7837	7634	8030	1.027	0.976
S2-1-4	8664	7916	8303	1.094	1.043
S2-2-3	9085	8266	9080	1.099	1.001
S2-2-4	9187	8521	9323	1.078	0.985
S3-1-1	6915	6723	7152	1.029	0.967
S3-1-2	7407	7138	7545	1.038	0.982
S3-1-3	6838	6247	6682	1.095	1.023
S3-1-4	7569	7108	7512	1.065	1.008
Mean				1.104	1.004
Standard deviation				0.055	0.035

Table 4.24: Test results and predictions for UHSC filled circular double-tubes

No.	$N_{test,u}$ (kN)	$N_{pl,Rk}$ (kN)	$N_{pl,Rk2}$ (kN)	$N_{test,u}/N_{pl,Rk}$	$N_{test,u}/N_{pl,Rk2}$
S2-3-2	8529	7573	7955	1.126	1.072
S2-3-3	4968	4602	5045	1.080	0.985
S2-3-4	5239	4766	5200	1.099	1.008
S2-4-2	9817	8492	9194	1.156	1.068
S2-4-3	7022	5998	6787	1.171	1.035
S2-4-4	7160	6065	6849	1.181	1.045
S3-2-1	7640	7289	7791	1.048	0.981
S3-2-2	7209	7678	8154	0.939	0.884
S3-2-3	6882	6844	7350	1.006	0.936
S3-2-4	8375	7650	8123	1.095	1.031
Mean				1.090	1.004
Standard deviation				0.076	0.060

Table 4.25: Test results and predictions for UHSC filled square single-tube

No.	$N_{test,u}$ (kN)	$N_{pl,Rk}$ (kN)	$N_{test,u}/N_{pl,Rk}$
S4-3-1	5953	5351	1.113
S4-3-2	5911	5427	1.089
S4-3-3	6039	5269	1.146
S4-3-4	6409	5534	1.158
S4-3-5	6285	5284	1.189
Mean			1.139
Standard deviation			0.039

Table 4.26: Test results and predictions for UHSC filled square HSS single-tube

No.	$N_{test,u}$ (kN)	$N_{pl,Rk}$ (kN)	$N_{test,u}/N_{pl,Rk}$
S4-1-1	6536	6428	1.017
S4-1-2	6715	6511	1.031
S4-1-3	6616	6337	1.044
S4-1-4	7276	6629	1.097
S4-1-5	6974	6354	1.097
S4-2-1	8585	7579	1.133
S4-2-2	8452	7652	1.105
S4-2-3	8687	7500	1.158
S4-2-4	8730	7756	1.126
S4-2-5	8912	7515	1.186
Mean			1.099
Standard deviation			0.055

Table 4.27: Test results and predictions for UHSC filled square HSS double-tubes

No.	$N_{test,u}$ (kN)	$N_{pl,Rk}$ (kN)	$N_{test,u}/N_{pl,Rk}$
S4-4-1	7058	7975	0.885
S4-4-2	7143	8045	0.888
S4-4-3	7032	7900	0.890
S4-4-4	7880	8143	0.968
Mean			0.908
Standard deviation			0.040



Figure 4.1: High tensile strength steel fiber - SF 13/80

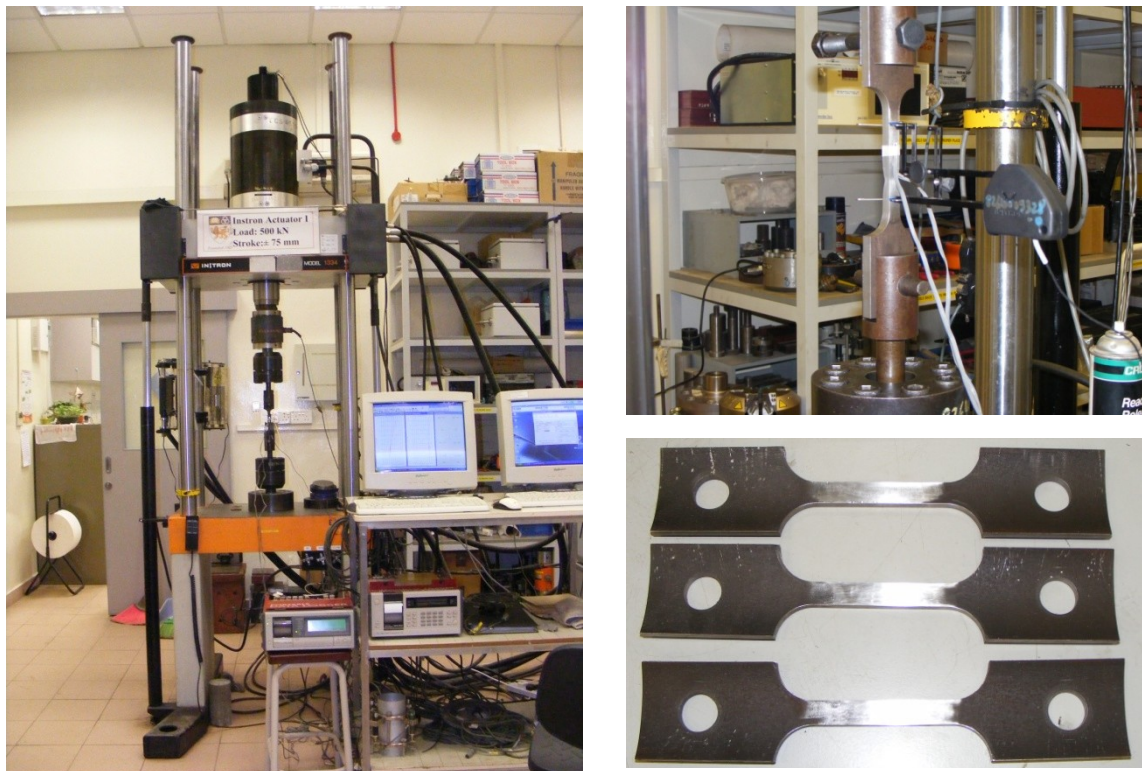


Figure 4.2: Coupon test samples and setup

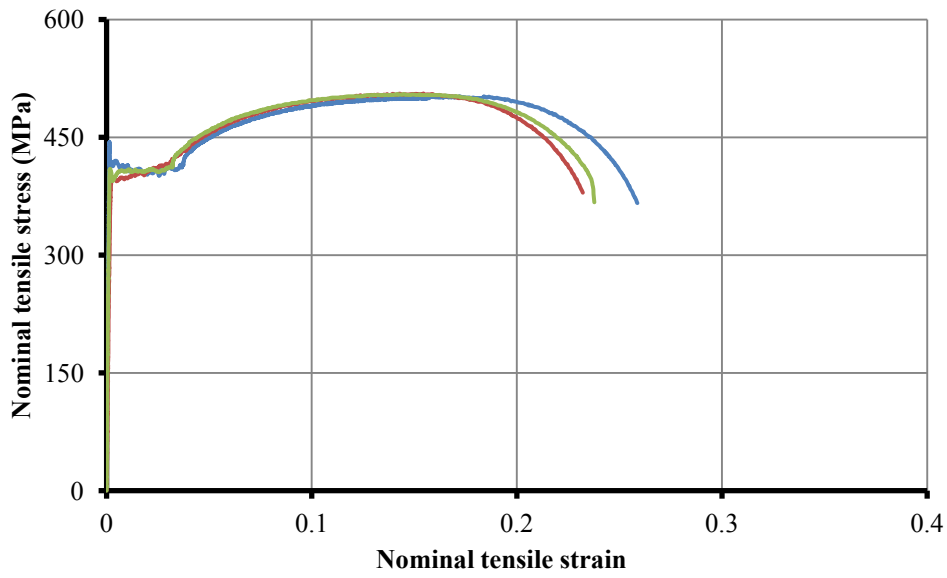


Figure 4.3: Coupon test stress-strain curves for CHS114.3mm×3.6mm

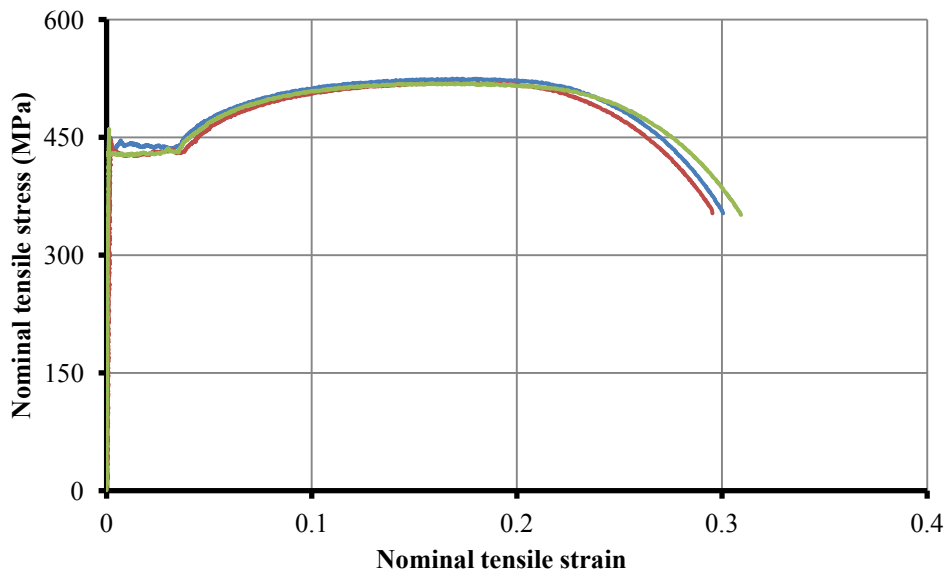
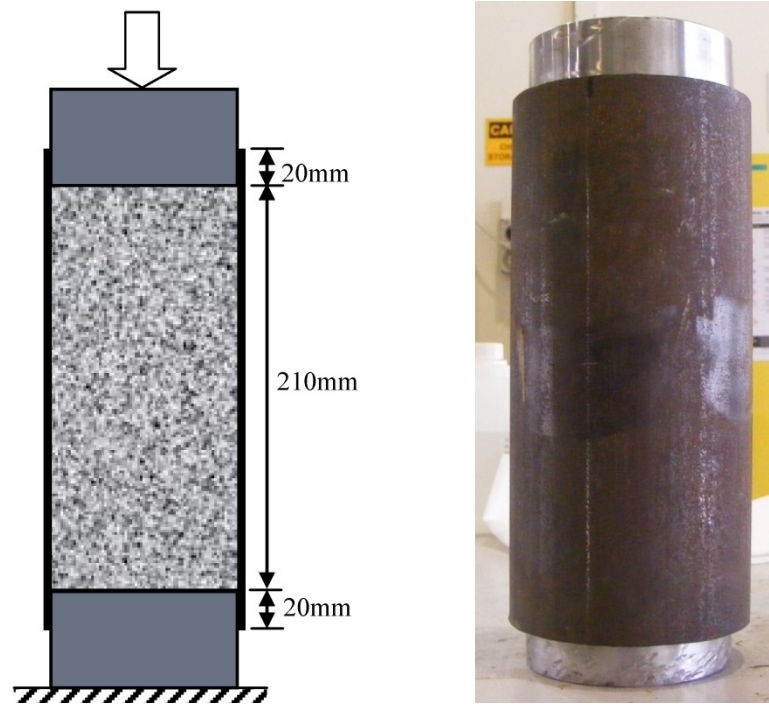
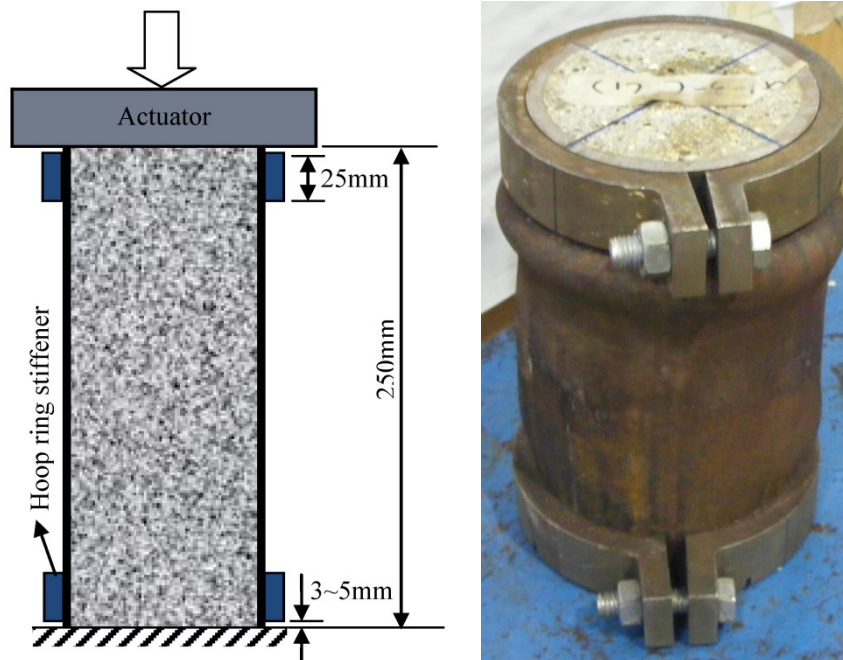


Figure 4.4: Coupon test stress-strain curves for CHS114.3mm×6.3mm





(a) Only loaded on the concrete core



(b) Loaded on both of the concrete core and steel tube

Figure 4.5: Different loading cases for specimens in Series 1

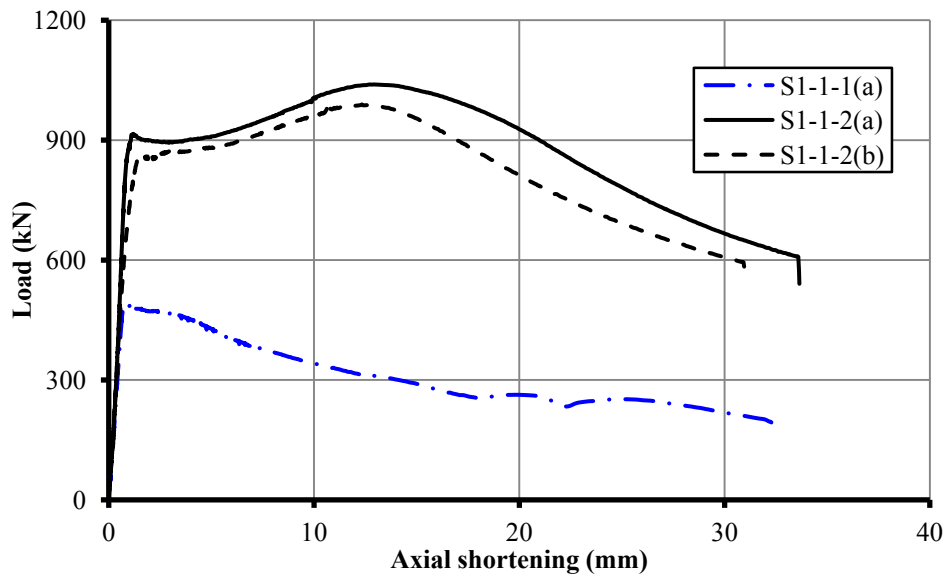


Figure 4.6: Load-shortening curves for S1-1-1(a), S1-1-2(a) and S1-1-2(b)

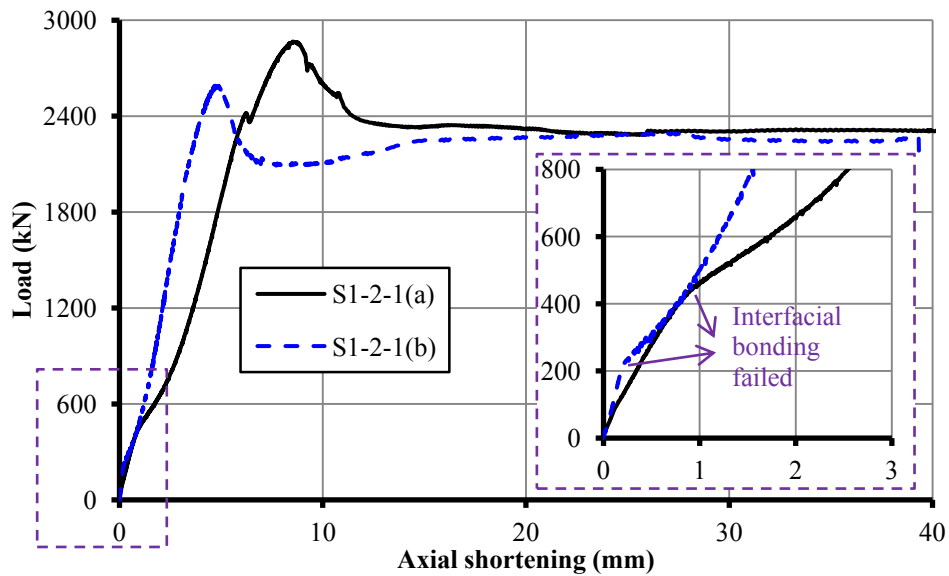


Figure 4.7: Load-shortening curves for S1-2-1(a) and S1-2-1(b)

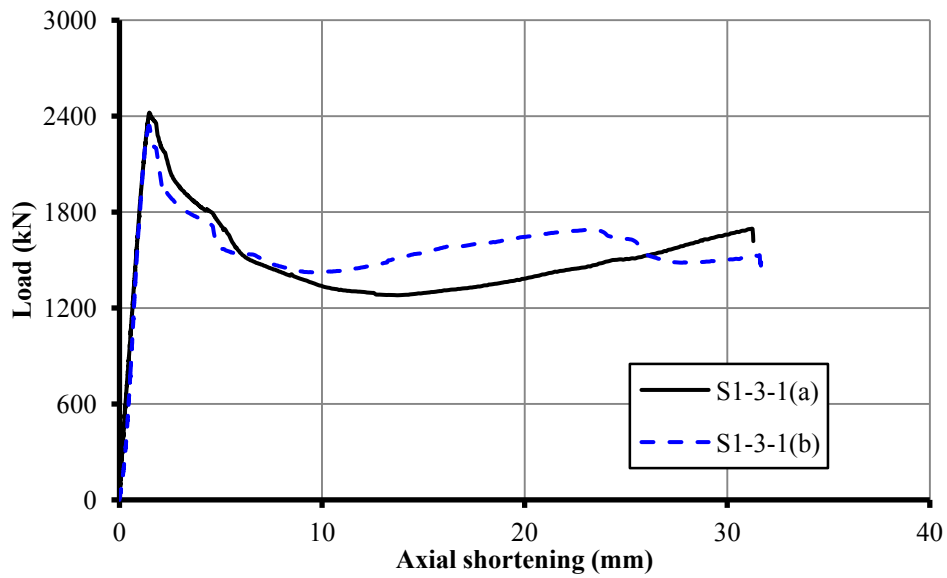


Figure 4.8: Load-shortening curves for S1-3-1(a) and S1-3-1(b)

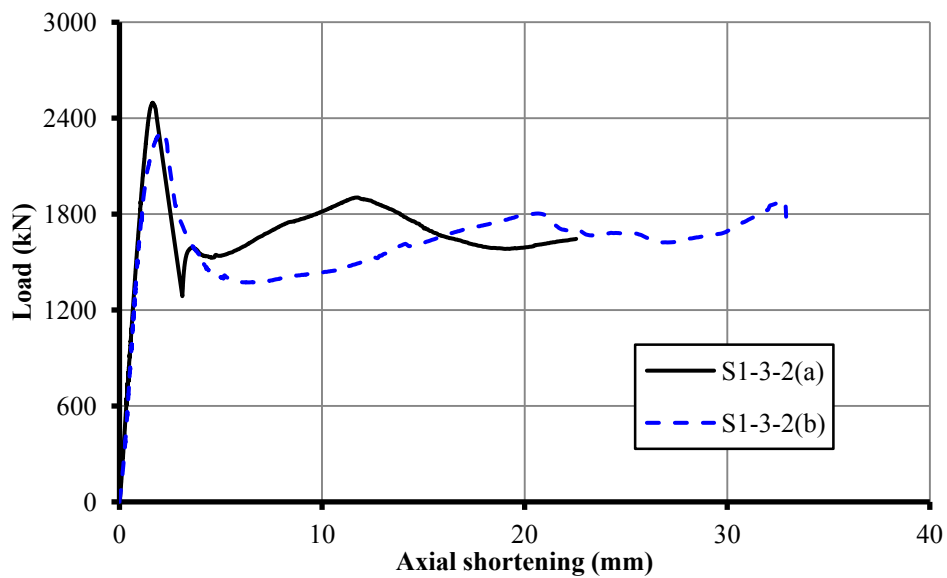


Figure 4.9: Load-shortening curves for S1-3-2(a) and S1-3-2(b)

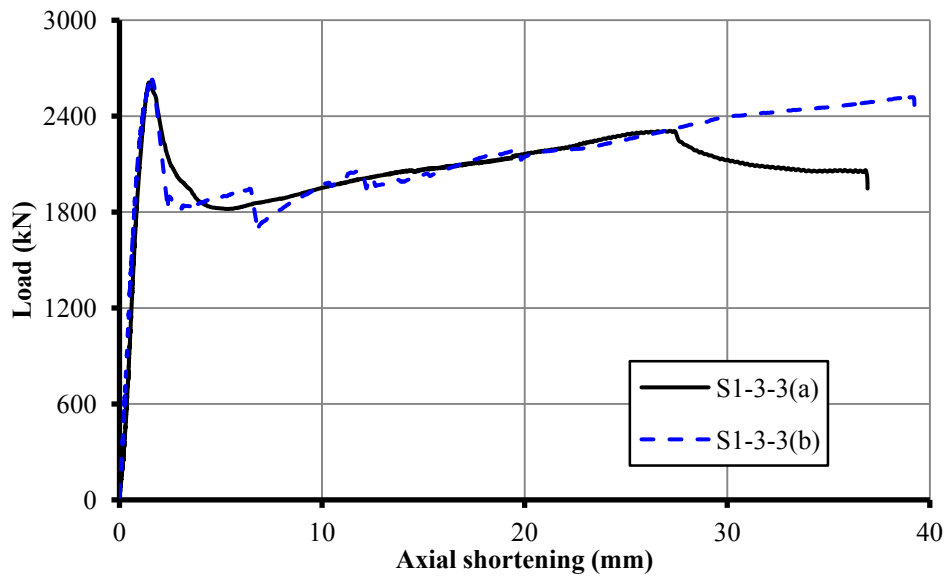


Figure 4.10: Load-shortening curves for S1-3-3(a) and S1-3-3(b)



Figure 4.11: All the tested specimens in Series 1



(a) S1-2-1(a) loaded only on *UHSC* core



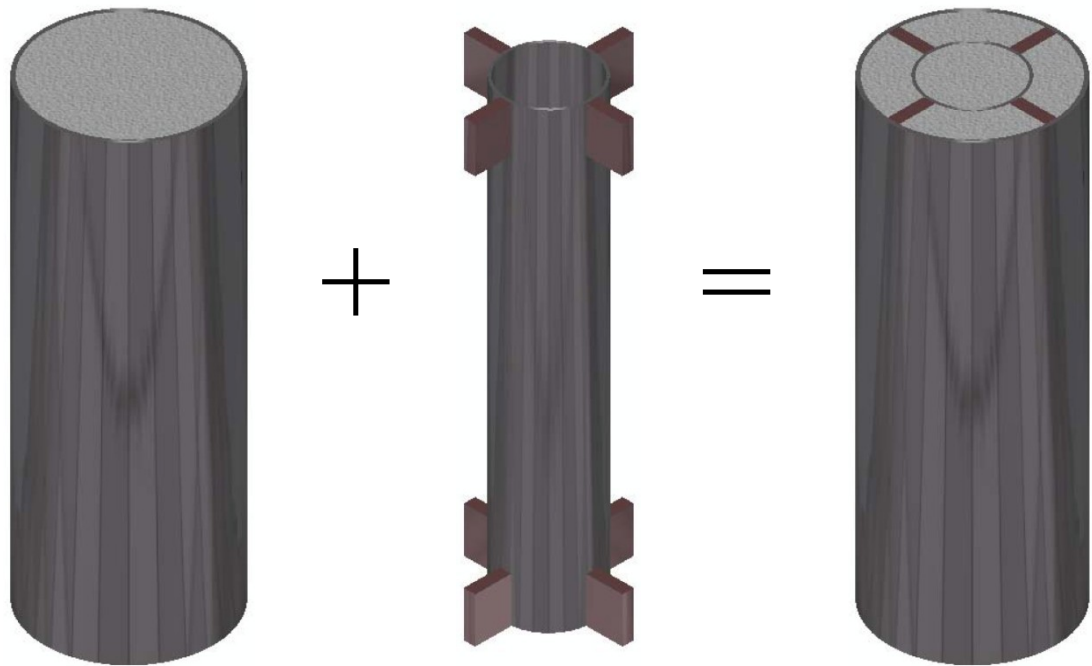
(b) S1-3-1(a) without *SF*



(c) S1-3-2(b) with 1% *SF*

Figure 4.12: Failure modes of *UHSC* cores in *CFST* columns





(a) Single-tube specimen

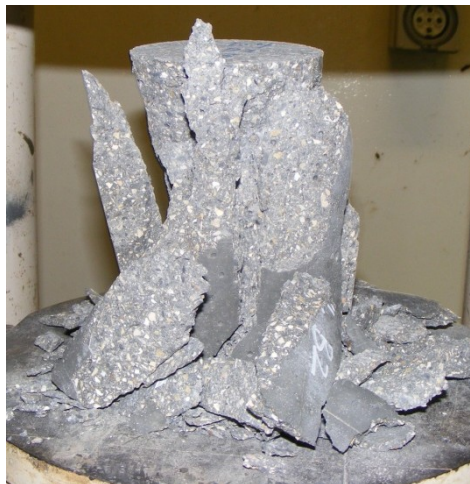
(b) Internal tube with shear connectors

(c) Double-tube specimen

Figure 4.13: Circular single- and double-tube *CFST* columns



(a) Normal strength concrete



(b) Plain *UHSC*



(c) *SF* reinforced *UHSC*

Figure 4.14: Failure modes for different types of concrete

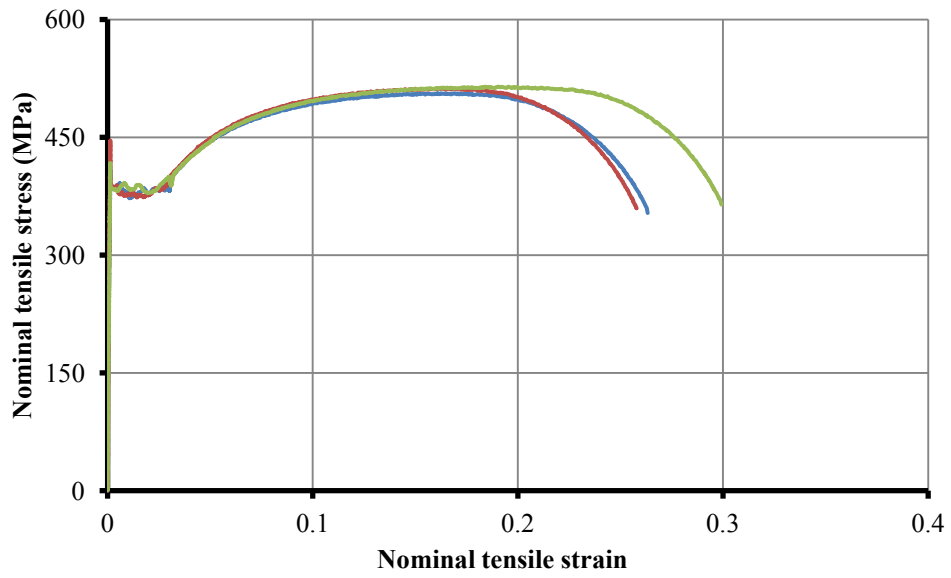


Figure 4.15: Coupon test stress-strain curves for CHS219.1mm×5mm

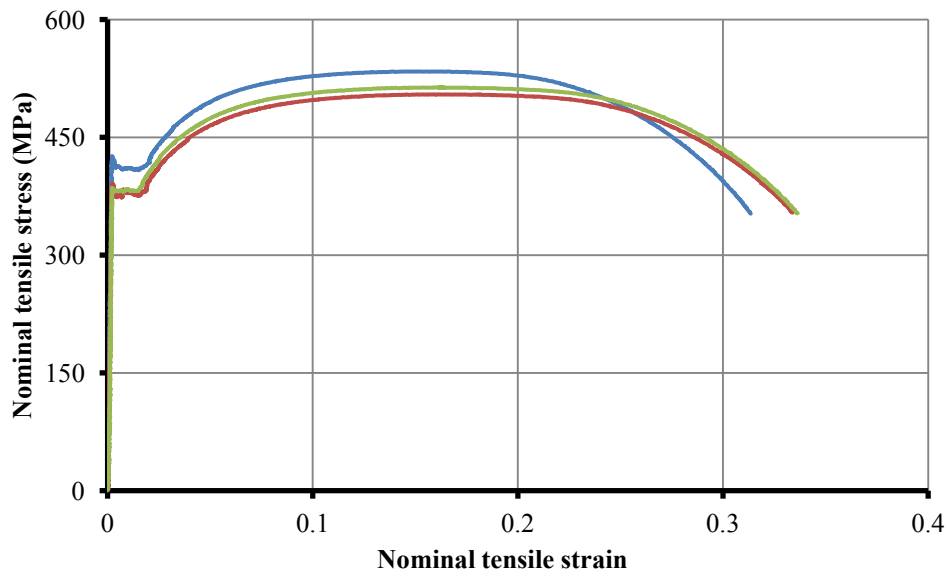


Figure 4.16: Coupon test stress-strain curves for CHS219.1mm×10mm

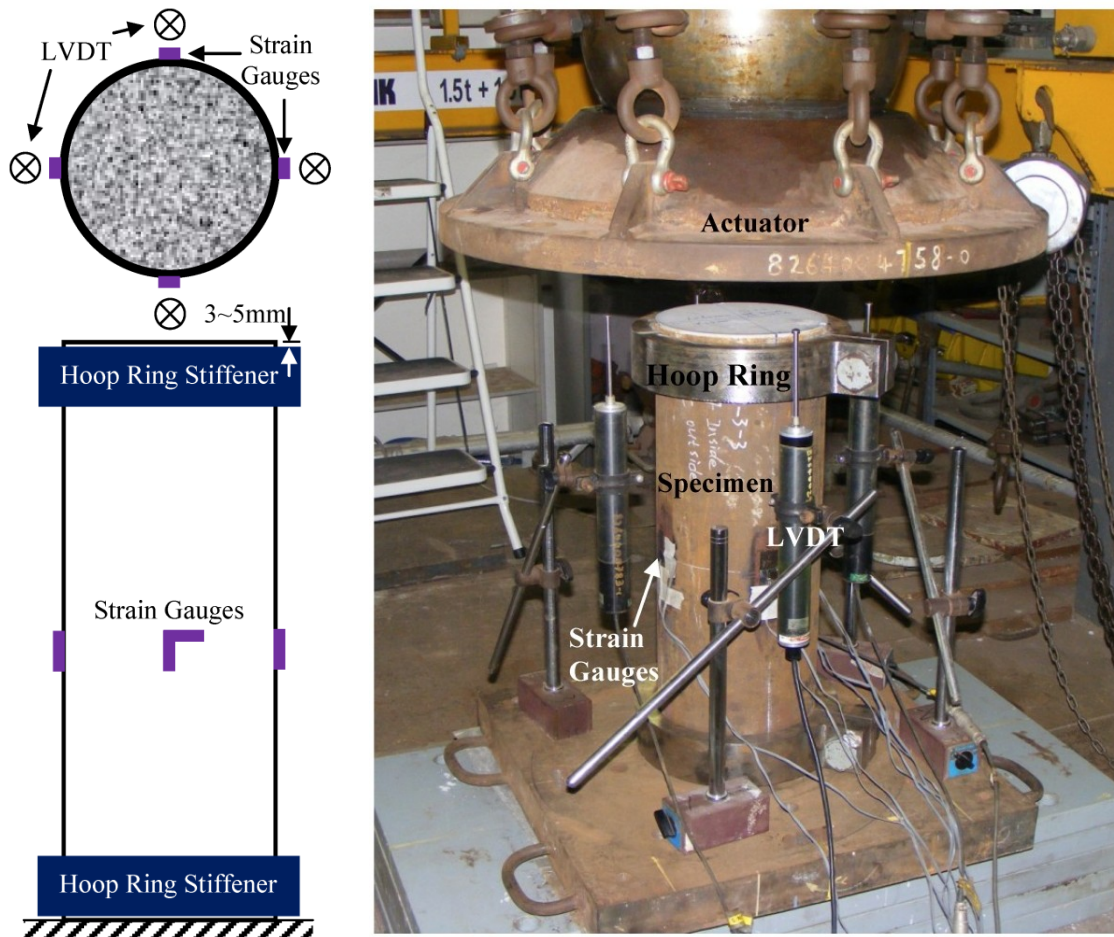


Figure 4.17: Test setup for specimens in Series 2



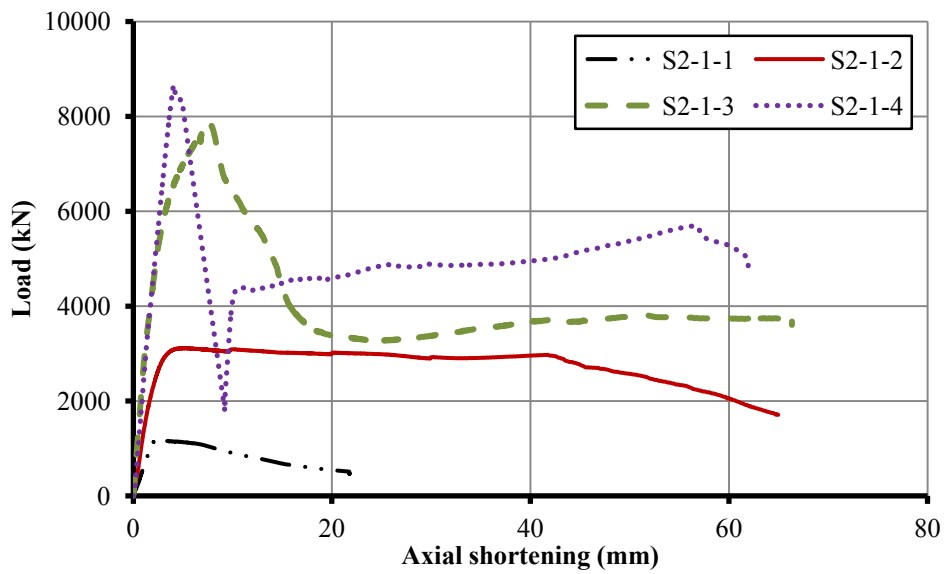


Figure 4.18: Load-shortening curves for Group S2-1 specimens in Series 2

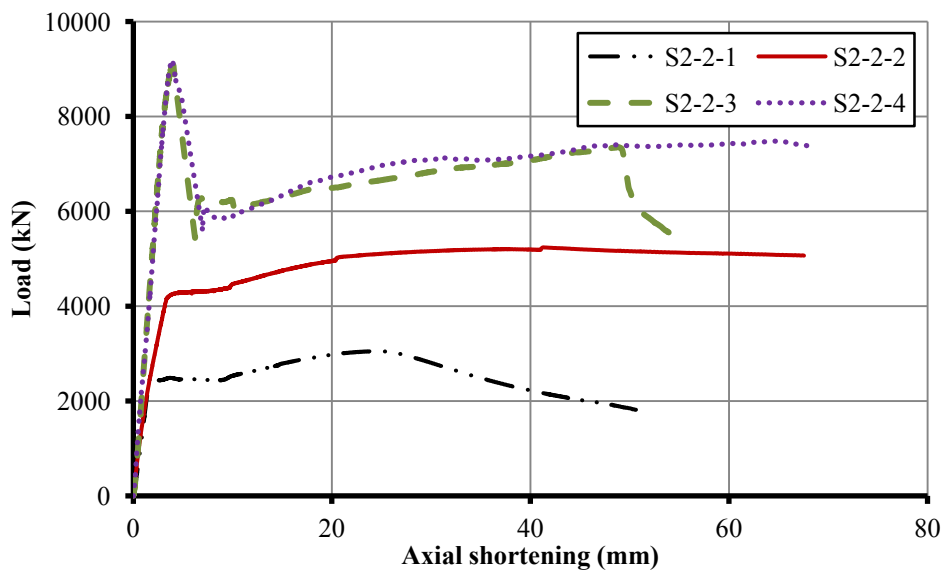


Figure 4.19: Load-shortening curves for Group S2-2 specimens in Series 2

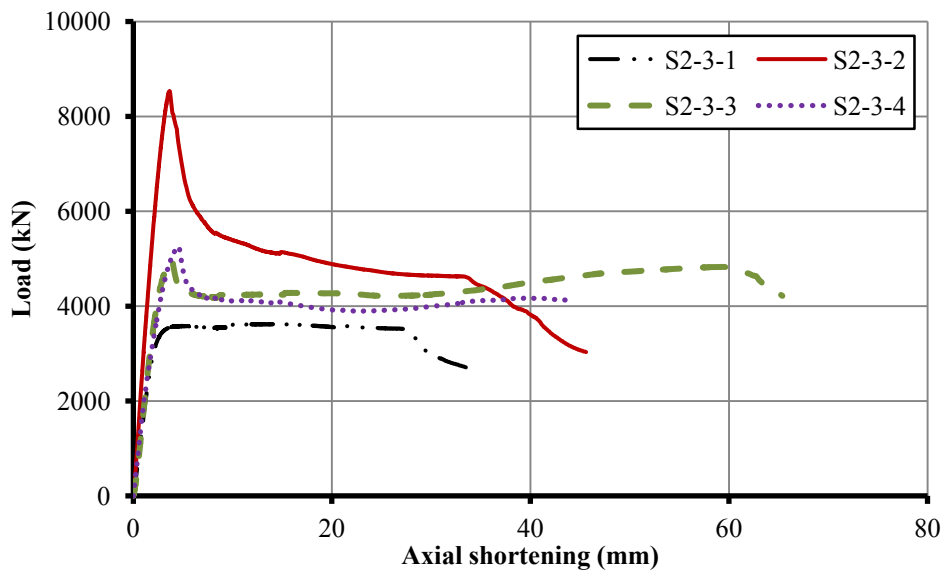


Figure 4.20: Load-shortening curves for Group S2-3 specimens in Series 2

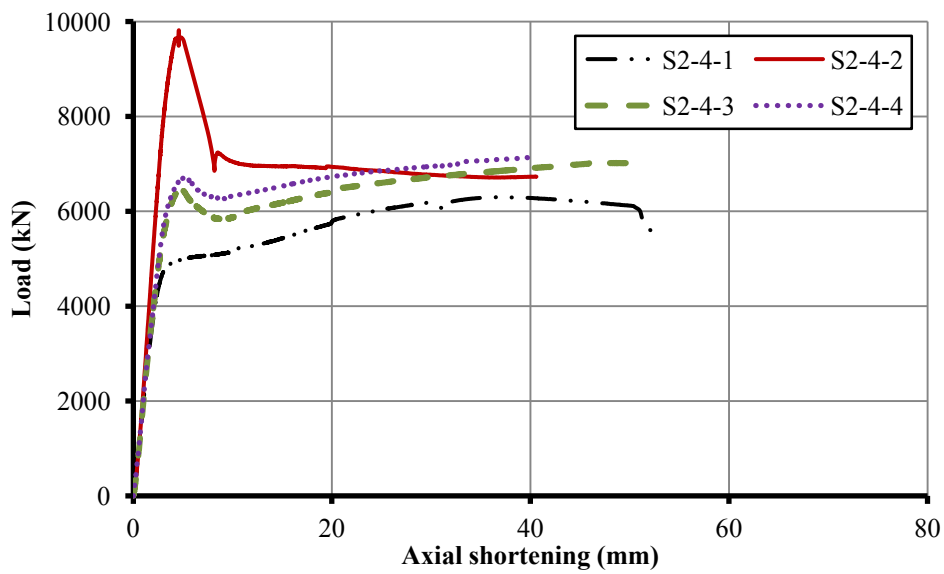


Figure 4.21: Load-shortening curves for Group S2-4 specimens in Series 2



Figure 4.22: All the tested specimens in Series 2 compared with those in Series 1



(a) UHSC without CA

(b) UHSC with 19%CA

(c) UHSC with 38%CA

Figure 4.23: Failure modes of UHSC reinforced with coarse aggregates

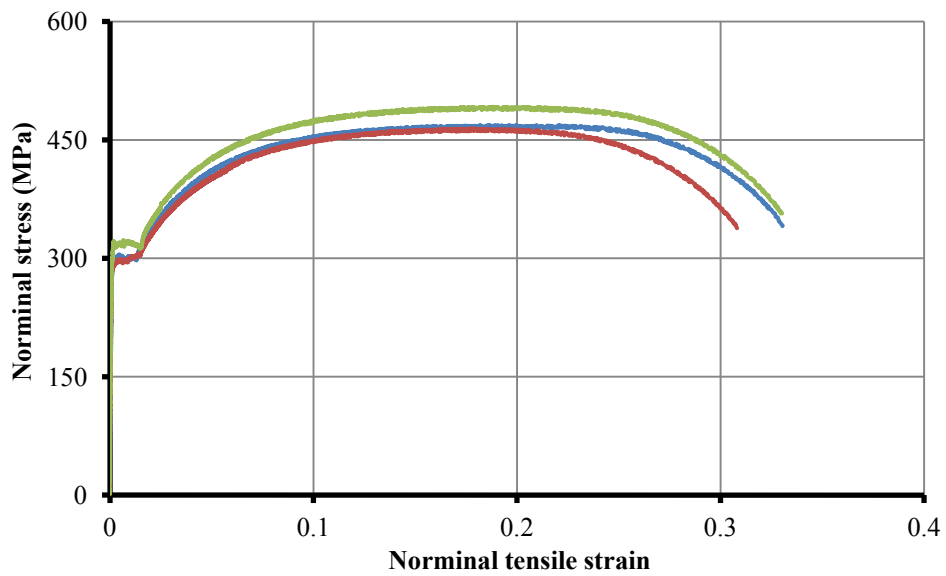


Figure 4.24: Coupon test stress-strain curves for CHS219.1mm×6.3mm



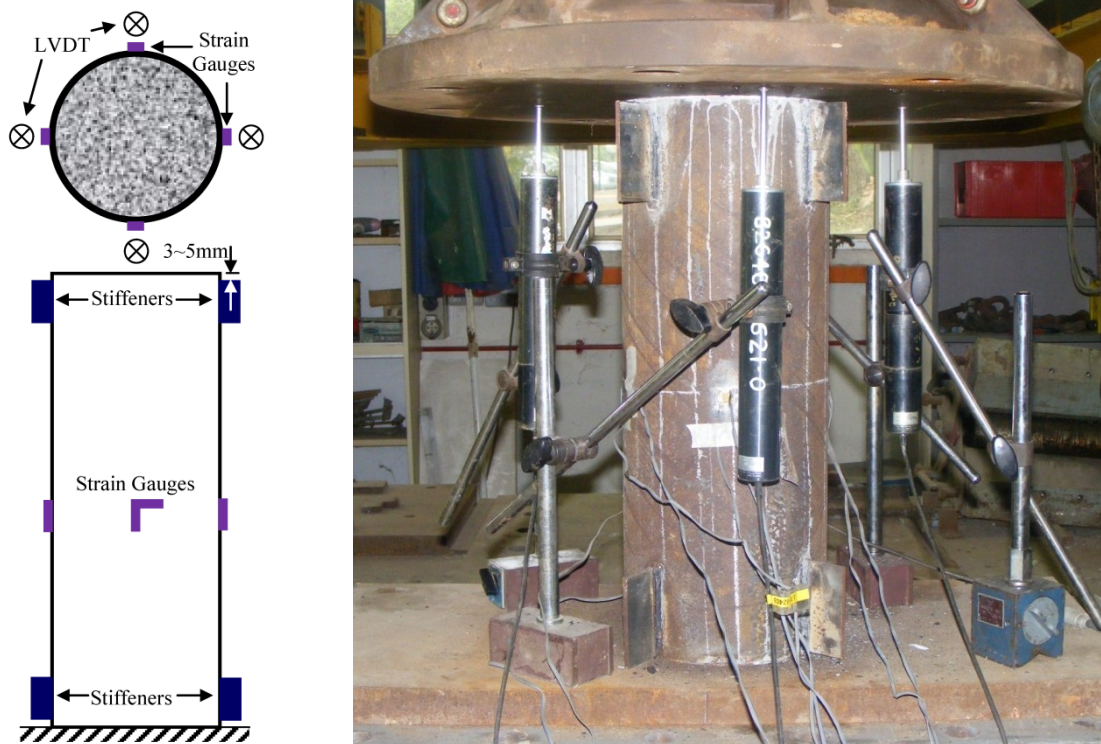


Figure 4.25: Test setup for specimens in Series 3

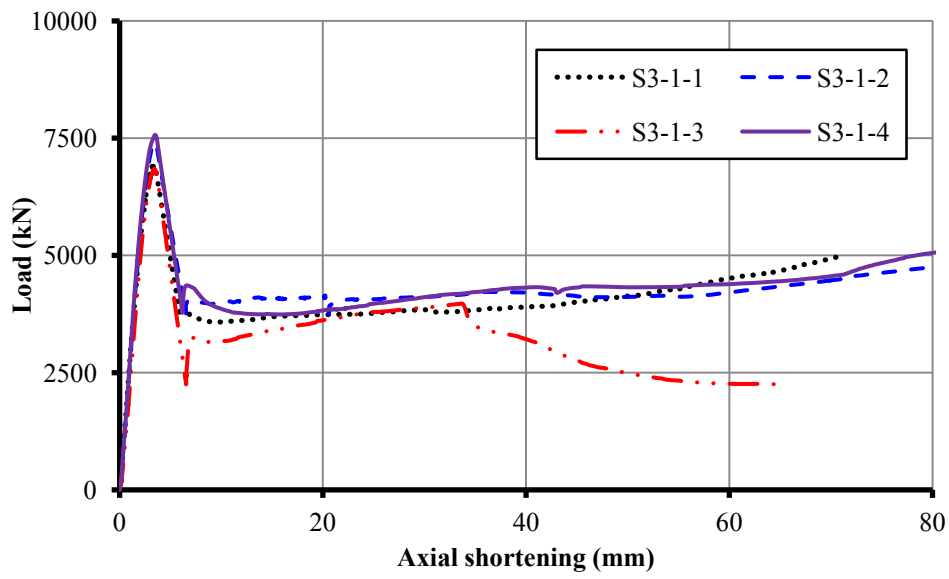


Figure 4.26: Load-shortening curves for single-tube specimens in Series 3

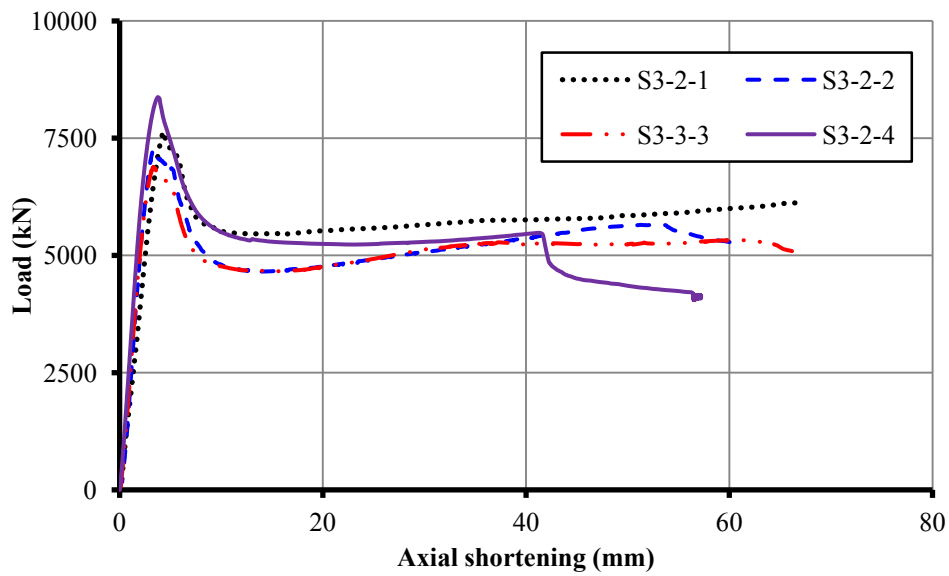


Figure 4.27: Load-shortening curves for double-tube specimens in Series 3

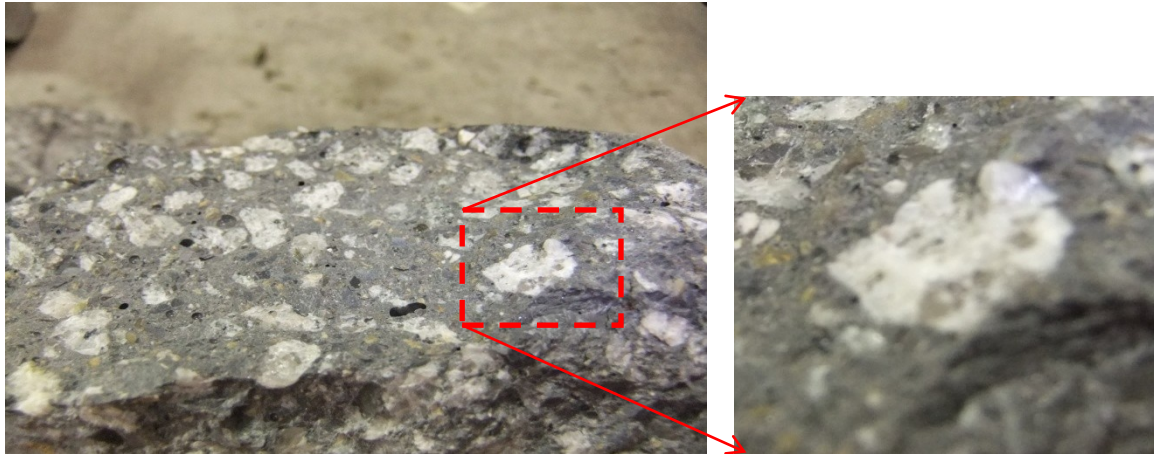
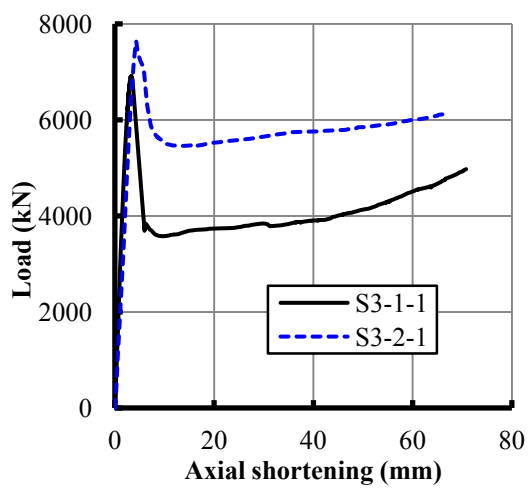
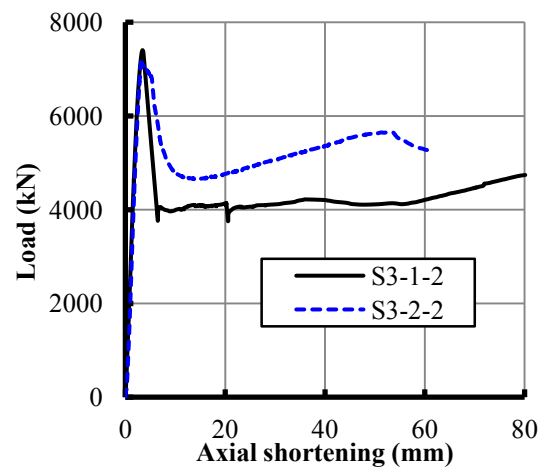


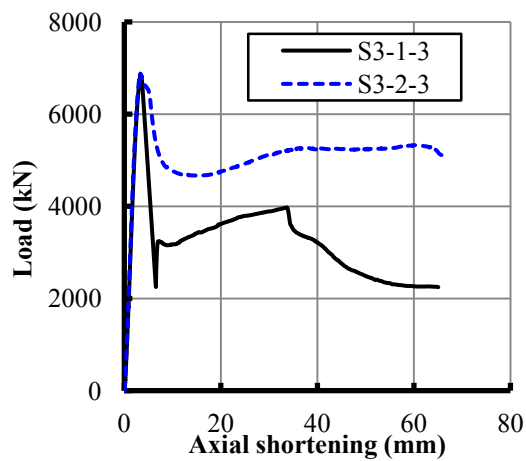
Figure 4.28: The failure of ordinary coarse aggregates in UHSC



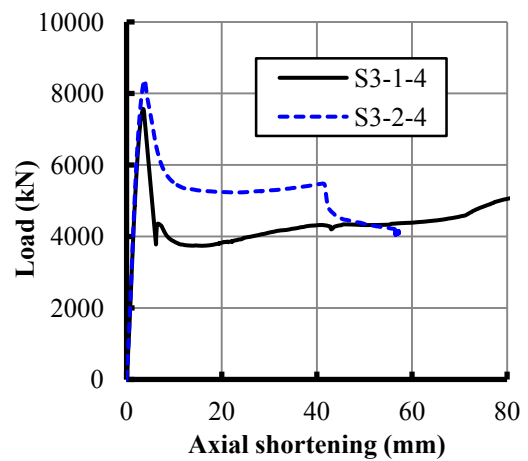
(a) S3-1-1 and S3-2-1



(b) S3-1-2 and S3-2-2



(a) S3-1-3 and S3-2-3



(a) S3-1-4 and S3-2-4

Figure 4.29: Comparison of single-tube specimens with double-tube specimens





(a) All the specimens before casting



(b) All the specimens after tested

Figure 4.30: All the specimens before casting and after tested in Series 3



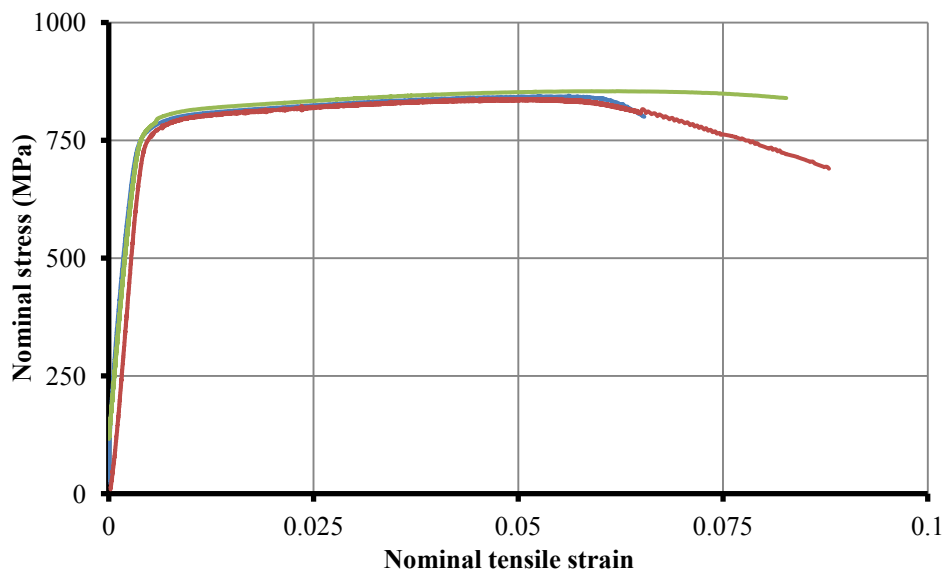


Figure 4.31: Coupon test stress-strain curves for 8mm-thick HSS plate

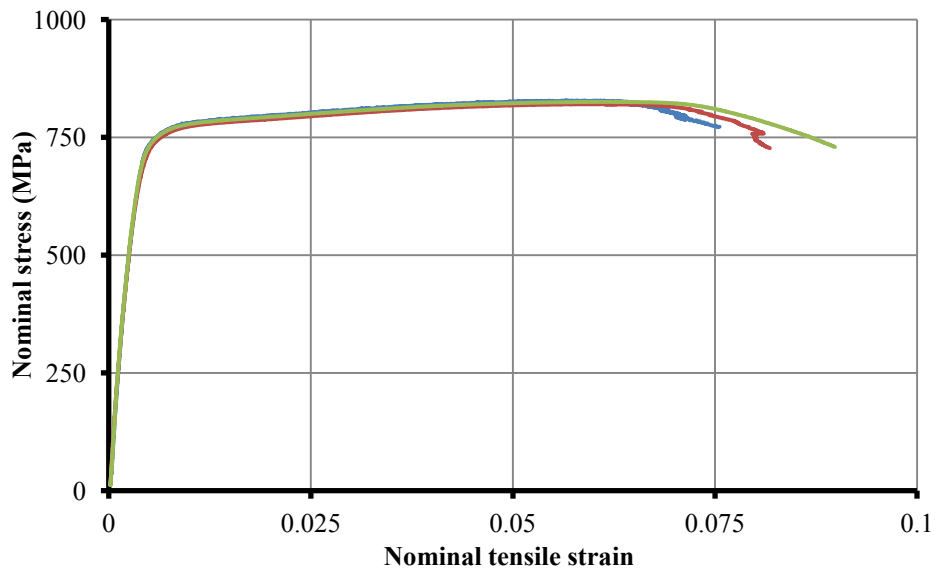


Figure 4.32: Coupon test stress-strain curves for 12mm-thick HSS plate

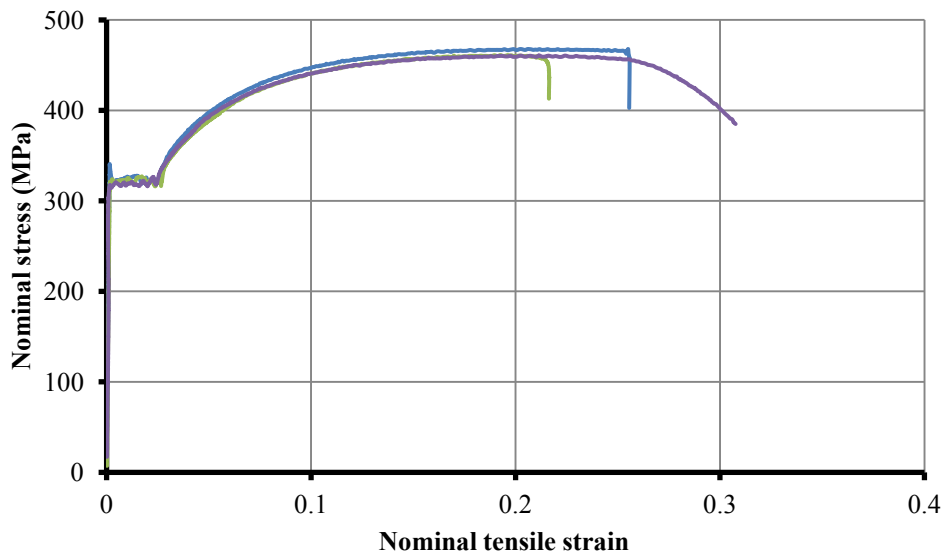


Figure 4.33: Coupon test stress-strain curves for 6mm-thick steel strip

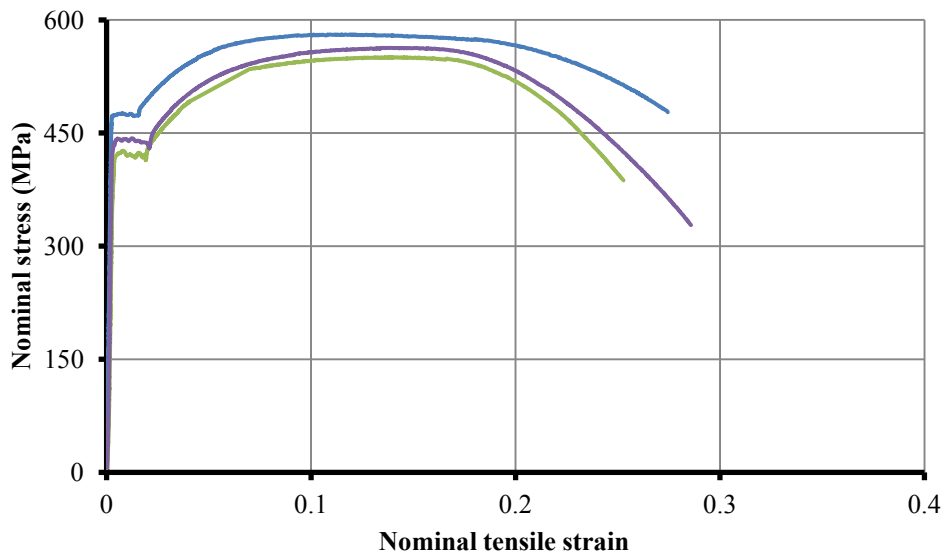


Figure 4.34: Coupon test stress-strain curves for SHS150mm×12.5mm

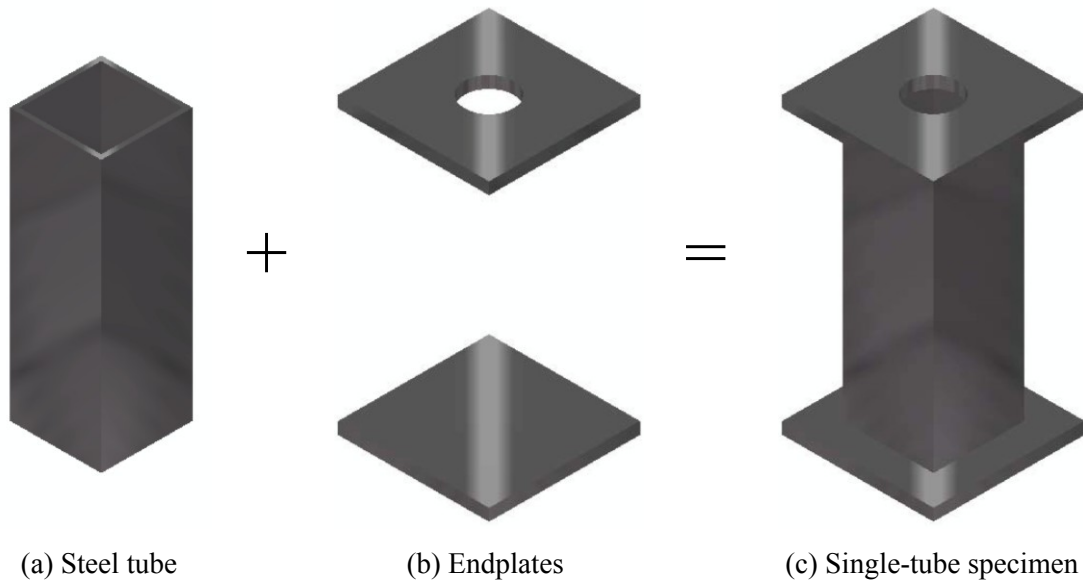


Figure 4.35: Square single-tube specimen without concrete casting

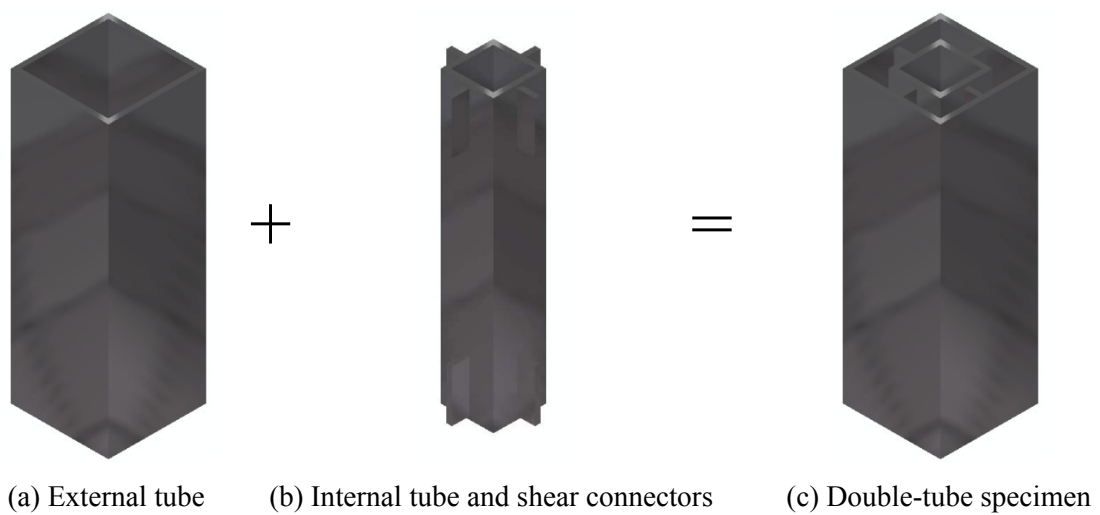


Figure 4.36: Square double-tube specimen without concrete casting

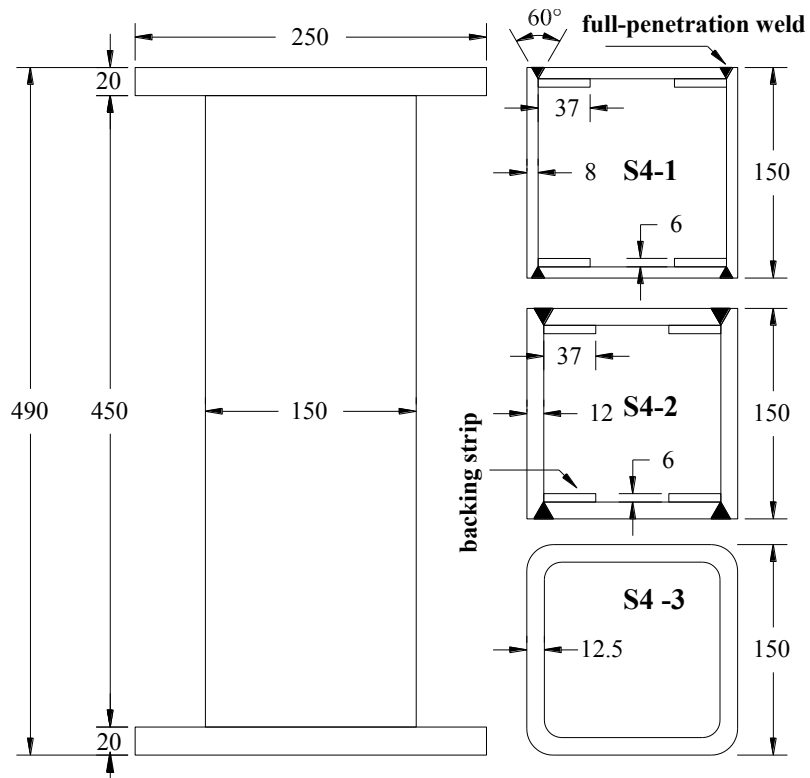


Figure 4.37: Dimension details for single-tube specimens

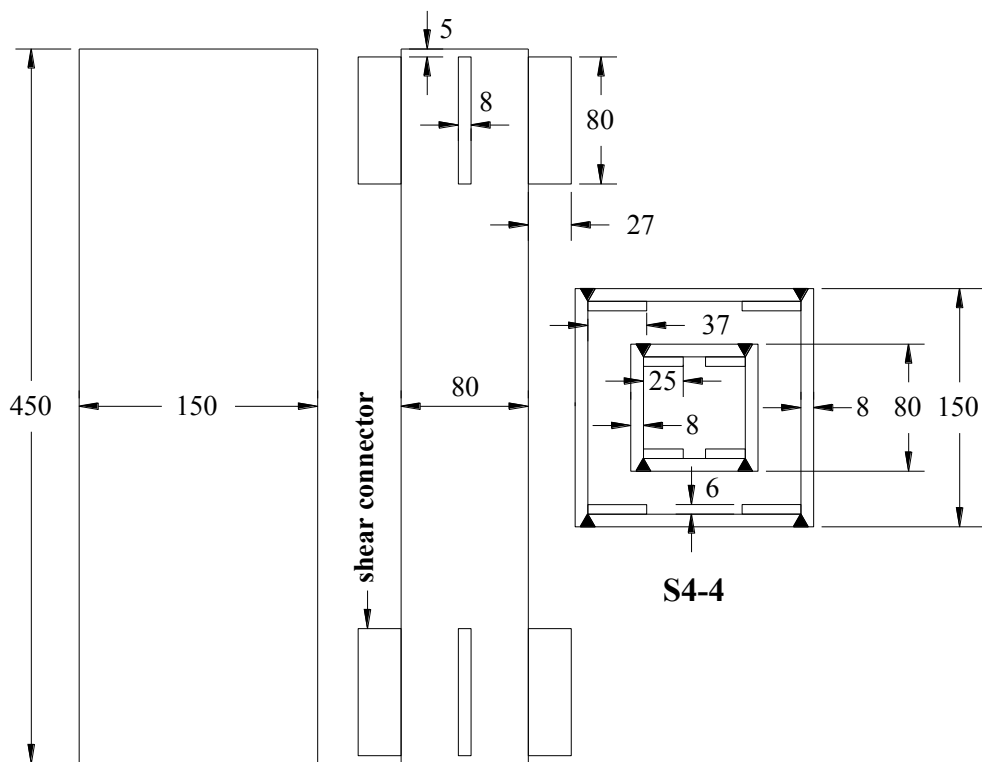


Figure 4.38: Dimension details for double-tube specimens

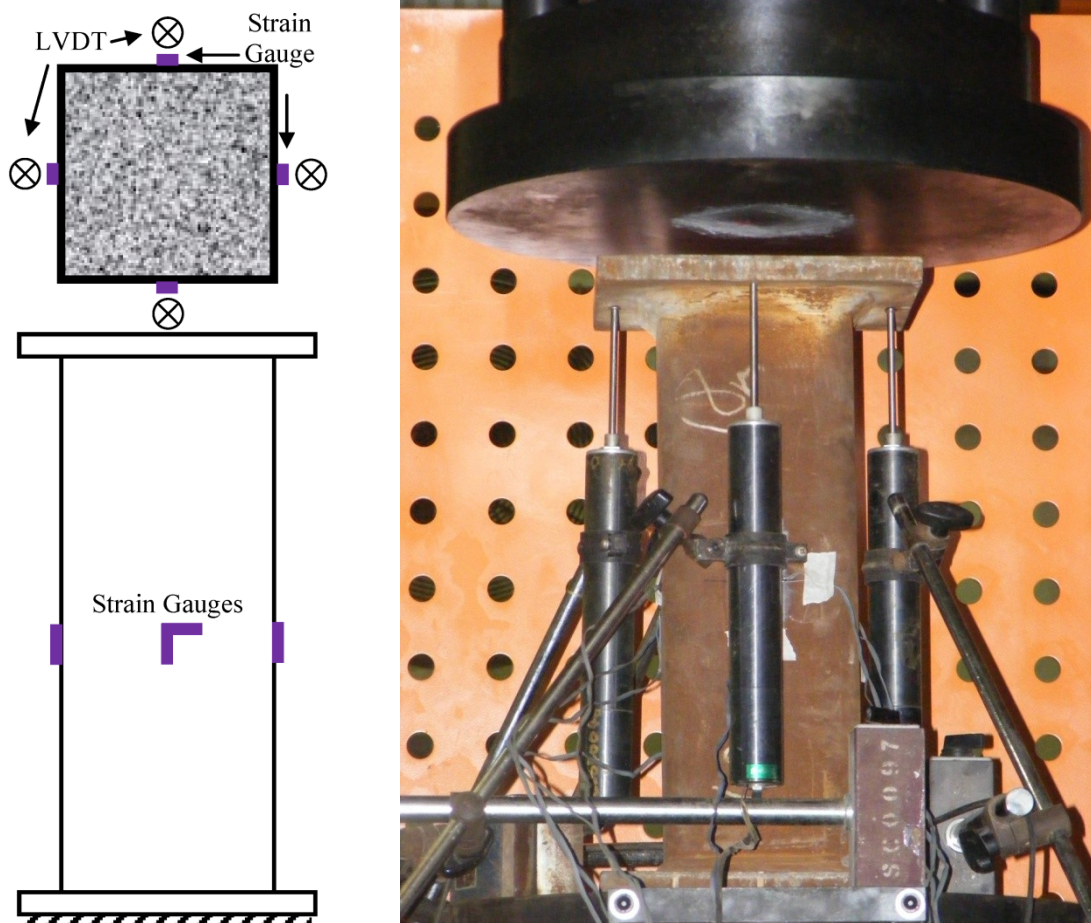


Figure 4.39: Test setup for specimens in Series 4

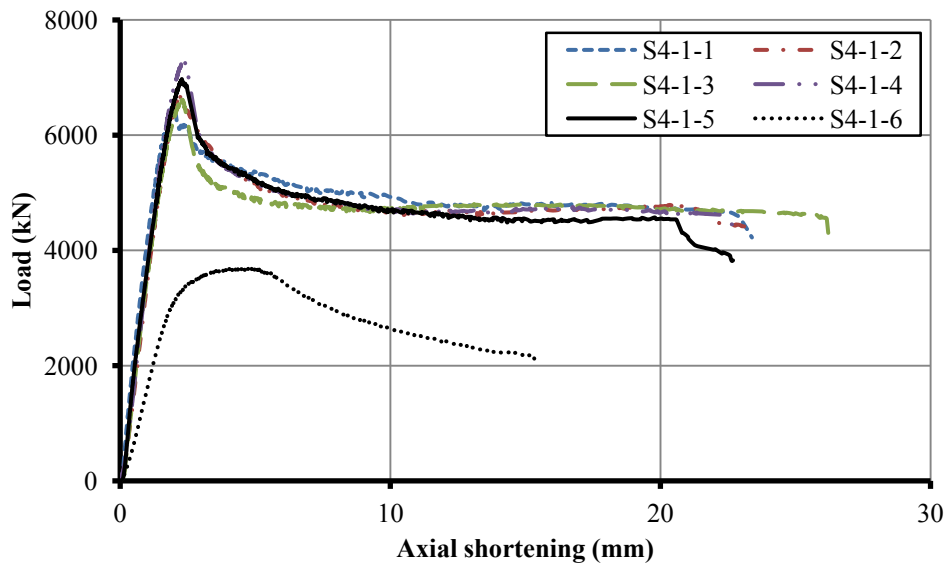


Figure 4.40: Load-shortening curves for Group S4-1 specimens in Series 4

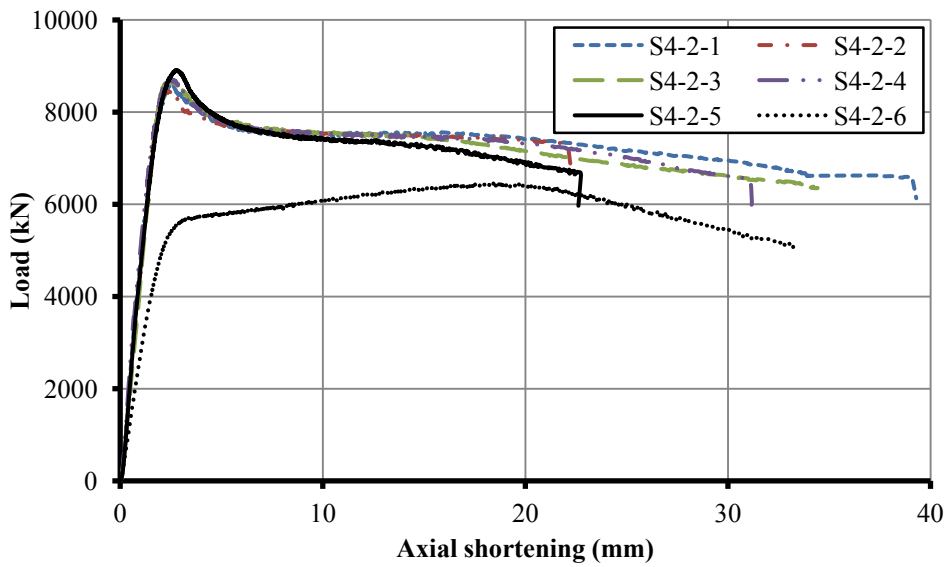


Figure 4.41: Load-shortening curves for Group S4-2 specimens in Series 4

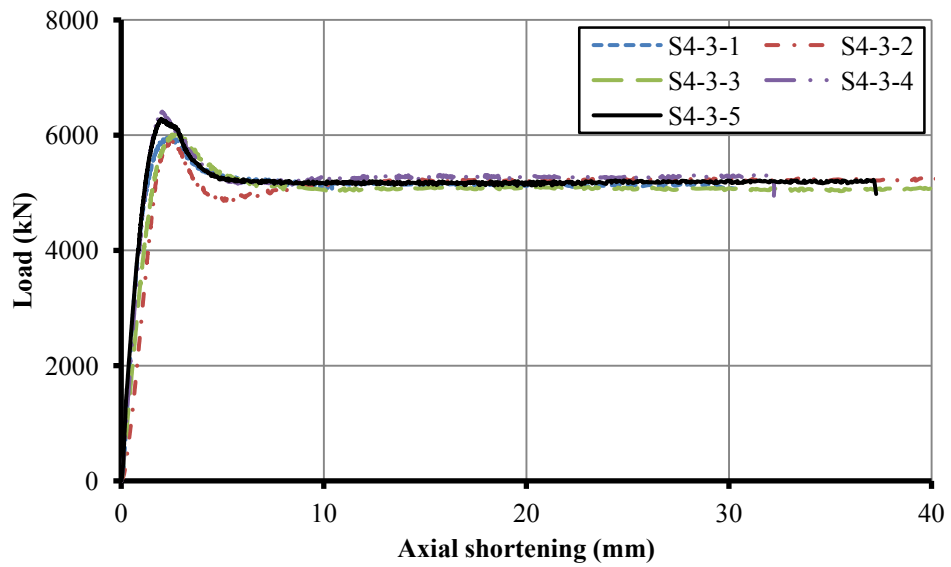


Figure 4.42: Load-shortening curves for Group S4-3 specimens in Series 4

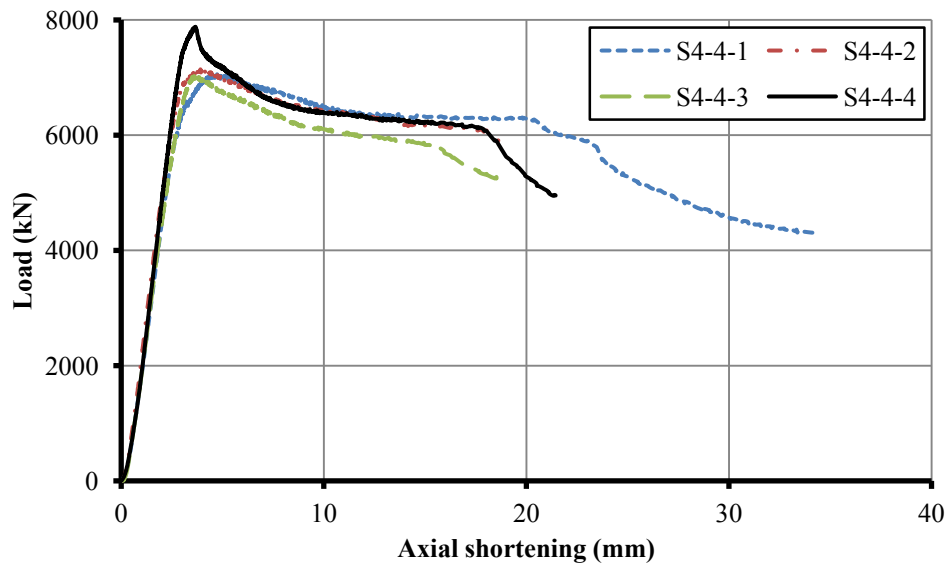


Figure 4.43: Load-shortening curves for Group S4-4 specimens in Series 4





(a) Four different cross-sectional sizes of steel tubes



(b) All the specimens after tested

Figure 4.44: All the specimens before casting and after tested in Series 4



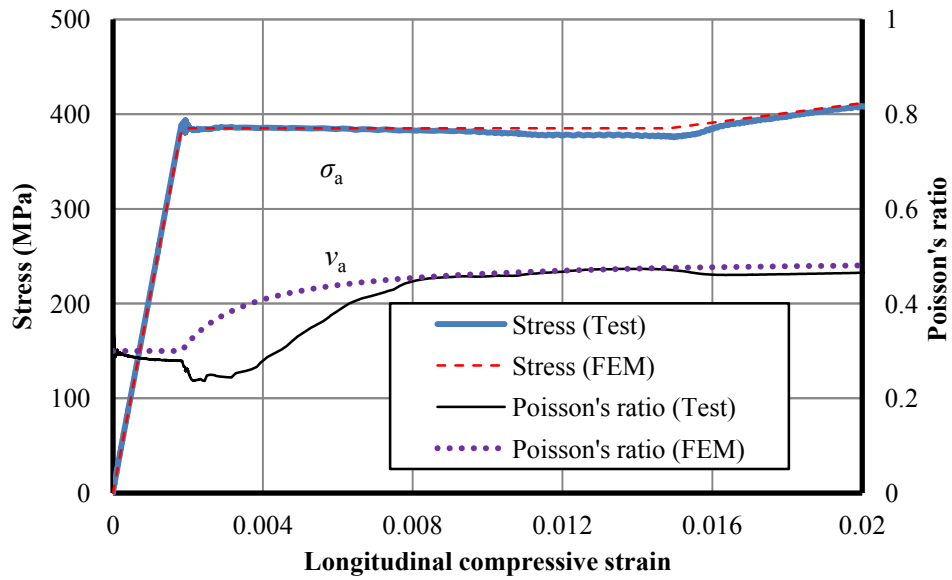


Figure 4.45: Variation of Poisson's ratio with longitudinal stresses for steel

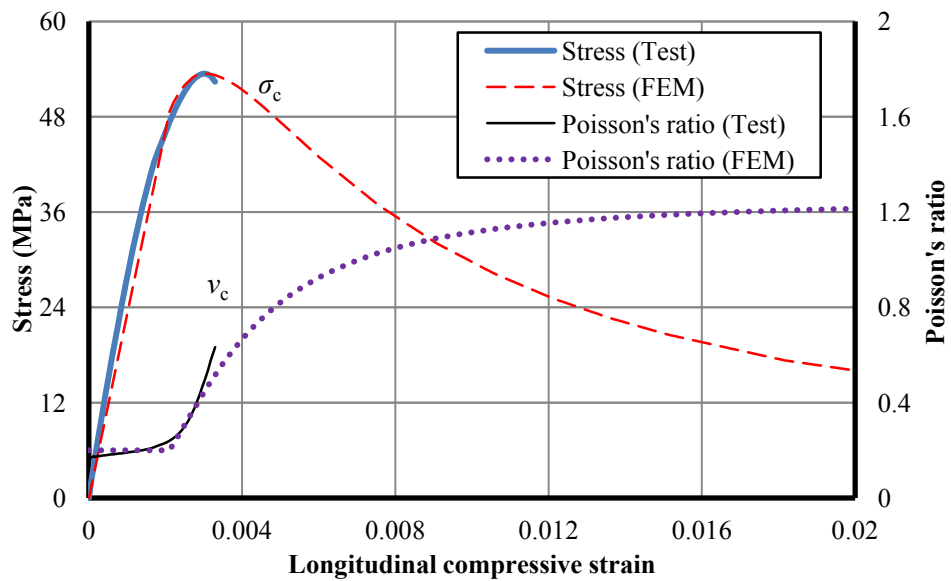


Figure 4.46: Variation of Poisson's ratio with longitudinal stresses for NSC

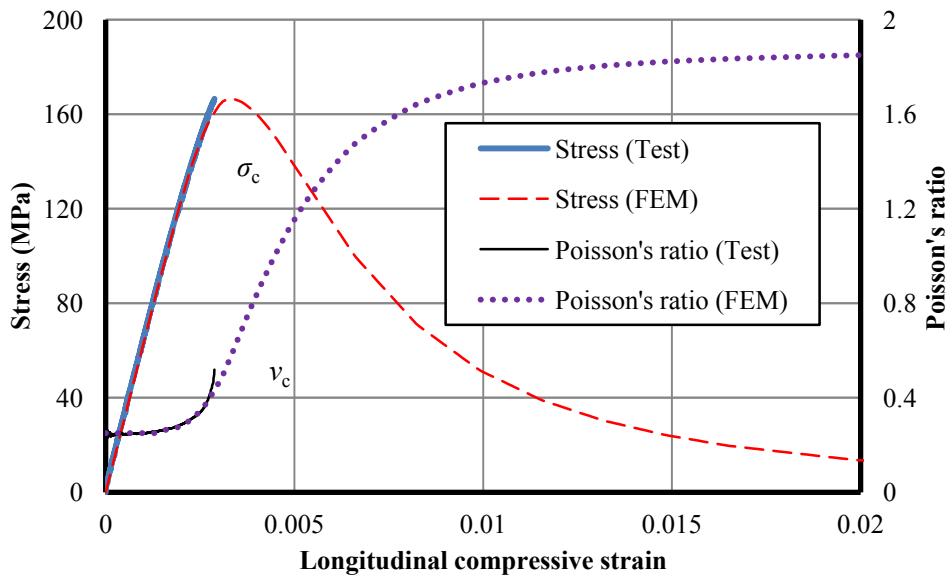


Figure 4.47: Variation of Poisson's ratio with longitudinal stresses for UHSC

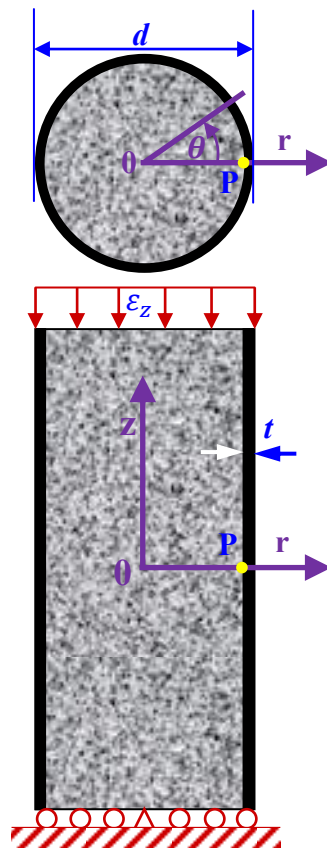


Figure 4.48: A simple model of CFST column under uniaxial compression

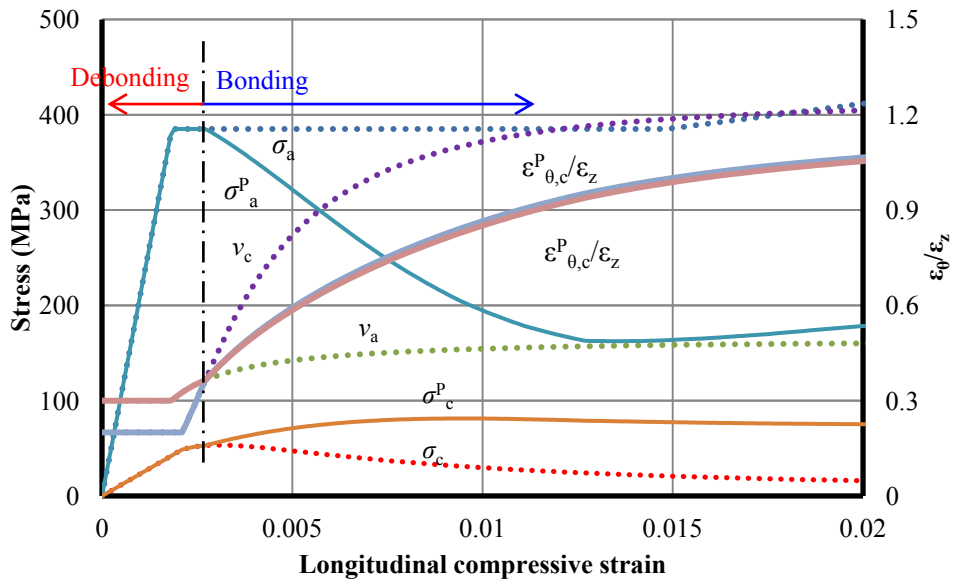


Figure 4.49: Variation of stresses and  $\varepsilon_{\theta}/\varepsilon_z$  in CFST columns

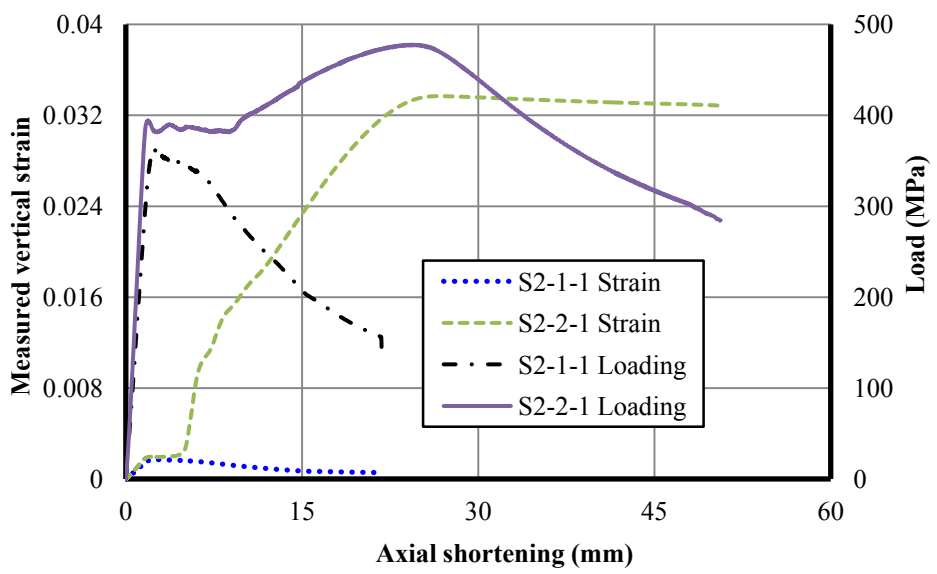


Figure 4.50: Measured strains and loading curves for S2-1-1 and S2-2-1

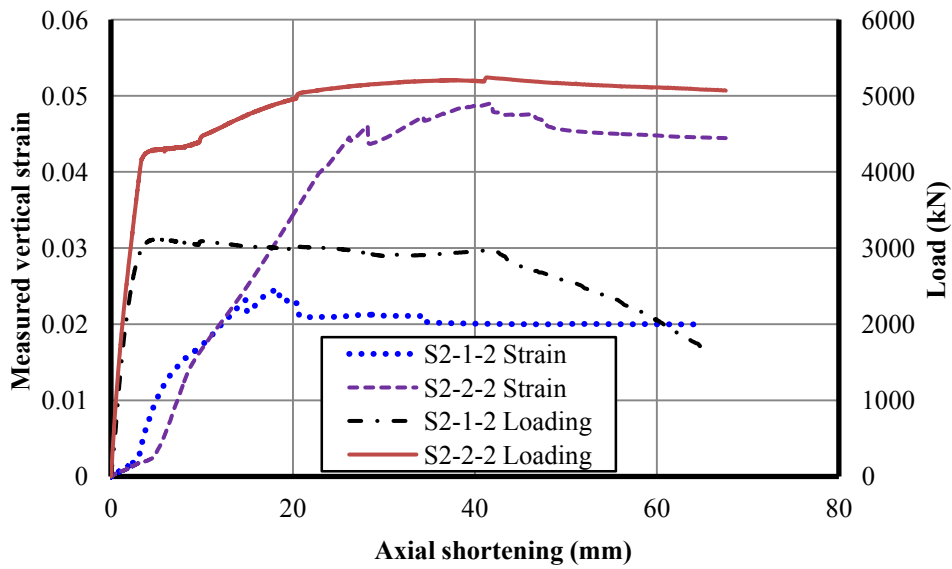


Figure 4.51: Measured strains and loading curves for S2-1-2 and S2-2-2

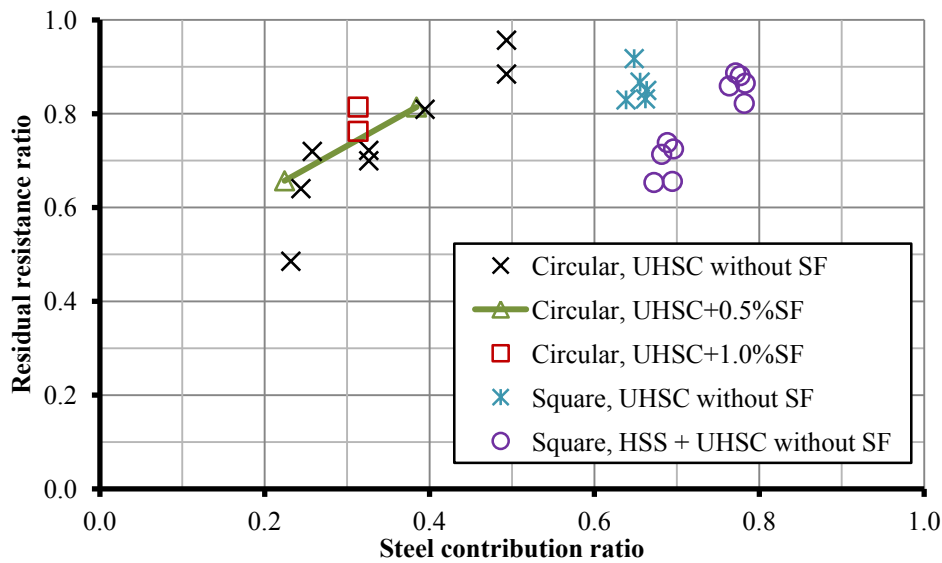


Figure 4.52: Residual resistance ratio for all single-tube CFST columns with UHSC

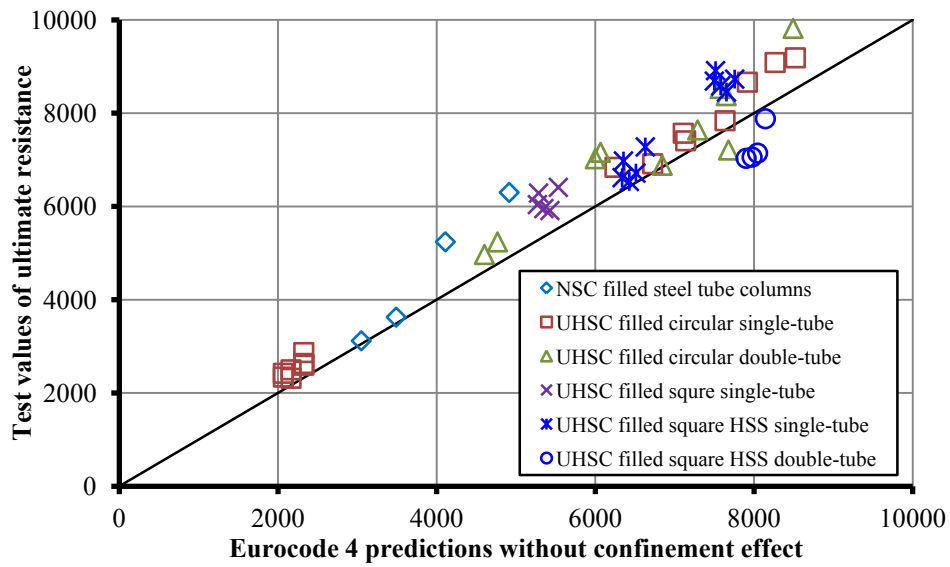


Figure 4.53: Test results compared with EC4 predictions without confinement effect

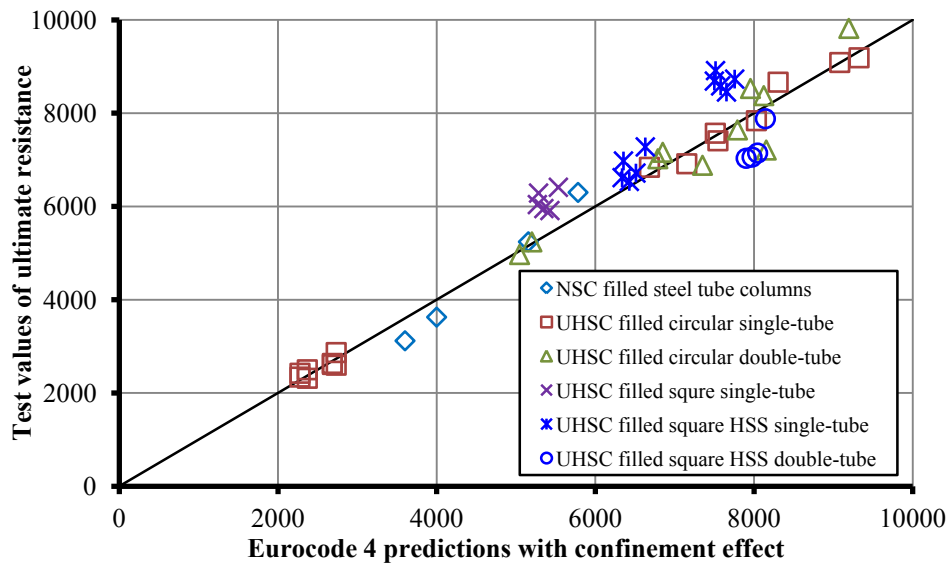


Figure 4.54: Test results compared with EC4 predictions with confinement effect

## Chapter 5 CFST Beams with High Strength Materials under Flexural Moment

### 5.1 General

The structural behaviour of stub *CFST* columns employing *UHSC* and *HSS* subjected to concentric compression has been presented in **Chapter 4** which is focusing on the cross-sectional resistance under compression. For the cross-sectional resistance under flexural moment, this chapter presents an experimental investigation on the structural behaviour of *CFST* beams employing *UHSC* and *HSS* subjected to pure bending. For evaluation, the test results are compared with the predictions by Eurocode 4 (2004) approach.

### 5.2 Experimental Investigation

#### 5.2.1 Materials

The materials used in this study included *UHSC*, circular and square mild steel hollow sections and square high tensile strength steel hollow sections. For each composite *CFST* specimen, at least three cylinders of size 100mm (*d*) × 200mm (*h*) were cast and cured at ambient temperature as the same for curing composite specimens. They were tested at the same time when the corresponding composite specimen was tested to obtain the basic mechanical properties, referred to relevant ASTM standards as introduced in **Chapter 3**.

For each type of steel sections, at least three coupon samples were tested, referred to ASTM E8M-04 as introduced in **Chapter 4**.

#### 5.2.1.1 UHSC

The first mix design without coarse aggregates shown in Table 3.4 of **Chapter 3** was used for all the specimens in this study. During casting, the fresh concrete was pumped into *CFST* specimens from the bottom as shown in Figure 5.1. The test values of material properties for each specimen will be given later, together with all specimen configuration details.

#### 5.2.1.2 Steel sections

Two types of hot finished mild steel circular hollow sections 114.3mm×6.3mm and 219.1mm×16mm, one hot finished mild steel square hollow section 200mm×12.5mm, and two types of high tensile strength steel square hollow sections 100mm×8mm and 200mm×12mm were used for all the specimens in this study. The stress-strain curves from coupon tests for the first three sections are respectively shown in Figure 5.2, Figure 5.3 and Figure 5.4. The last two high strength steel square hollow sections were welded box sections fabricated from the same batches of high tensile strength steel plates of 8mm and 12mm thick as stated in **Chapter 4**. In addition, the same 6mm-thick mild steel backing strip was adopted. The stress-strain curves from coupon tests have been shown in Figure 4.31 for the 8mm-thick *HSS* plate, Figure 4.32 for the 12mm-thick *HSS* plate, and Figure 4.33 for the 6mm-thick steel strip in **Chapter 4**. The mechanical properties for all the sections are summarized in Table 5.1.

### 5.2.2 Specimens

There were eight 3m-long *CFST* specimens, classified in accordance with their composite section configurations as shown in Figure 5.5, where “CS”, “CD”, “CDH”, “SS”, “SD” and “SDH” respectively represent concrete-filled “circular single-tube section”, “circular double-tube section”, “circular double-tube section with hollow internal tube”, “square single-tube section”, “square double-tube section” and “square double-tube section with hollow internal tube”.

The sectional configuration details for all specimens are shown in Table 5.2, where  $f_{y,e}$  and  $f_{y,i}$  are the yield strengths respectively for the external and internal tubes, and  $f_{ck}$  is the compressive strength obtained from the concrete cylinders tested at the same age of the corresponding *CFST* specimens. Grade S355 hot finished sections are used for first four specimens and S700 steel plates were used to fabricate the welded box sections for other four specimens. The details for the welded box sections are shown in Figure 5.6, where the material properties of the backing strip are shown in Table 5.1.

### 5.2.3 Test set-up and loading procedure

All the specimens were tested under bending about the major axis. The test set-up and instrumentations are shown in Figure 5.7 and Figure 5.8. There were 4 roller supports. The first one and the third one from the left could rotate only, and the second one and the last one could rotate and roll. The effective span which was taken as the distance between the end supports was 2400mm. The lateral deflection at one-third, middle and two-third of the effective span were measured by three *LVDTs* placed at the bottom. In addition, one *LVDT* was installed to monitor the horizontal movement at the center of the right



end-plate. For each specimen, eight post yield strain gauges were attached to the external surface of the steel tube at the mid-span to measure the strains in longitudinal direction. The transverse load was imposed by a displacement/load control actuator with a maximum capacity of 2000kN. The middle one-third effective span of 800mm-long was under pure bending.

The general loading procedure included four steps by controlling the actuator: (1) preload the specimen at a rate of 1.0mm/min up to 10% of its resistance estimated by Eurocode 4; (2) unload; (3) reload at the same rate of 1.0mm/min until the deflection at the middle span reached 150mm; (4) unload at the same rate. However, additional unload-reload loading procedures were conducted for the first three specimens shown in Table 5.2.

#### 5.2.4 Test results and observations

The moment at the middle one-third effective span as shown in Figure 5.7 and Figure 5.8 can be calculated by:

$$M = \frac{F}{2} \frac{L_e}{3} = \frac{1}{6} FL_e \quad (5.1)$$

where  $L_e = 2400\text{mm}$  for all the specimens tested in this study.

##### 5.2.4.1 Moment-deflection relationship

The deflection values at the middle span, one-third effective span and two-third span were measured by three *LVDTs* at the bottom as shown in Figure 5.7 and Figure 5.8. The moment-deflection curves for each specimen are shown from Figure 5.9 to Figure 5.16. It can be observed that all the specimens were very ductile under bending, without brittle or

sudden failure as observed from stub *CFST* column tests under compression presented in **Chapter 4**. Significant hardening effect was developed for the first four specimens with mild steel hot finished hollow sections, and a significant plateau was developed for the other four specimens with high strength steel welded box sections.

Additional unload-reload loading procedures were conducted for the first three specimens with mild steel hot finished circular hollow sections as shown in Figure 5.9, Figure 5.10 and Figure 5.11. The procedures were conducted when the deflection at middle span for the first time reached 50mm and 100mm for specimen N1-CS, 15mm, 30mm, 60mm and 120mm for specimen N2-CD, and 20mm, 40mm, 80mm and 120mm for specimen N3-CDH. It can be observed that there was some stiffness degradation during unload-reload loading procedures.

Without the additional unload-reload parts, the comparisons of moment-deflection curves are shown in Figure 5.17(a) for the first four specimens with mild steel hot finished hollow sections and Figure 5.17(b) for the other four specimens with high strength steel welded box sections. Due to the high strength of steel used for welded box sections, the maximum resistances for those specimens with welded box steel sections are much higher.

N1-CS was an ultra high strength concrete filled circular single-tube specimen, while one more internal tube was used for N2-CD. Therefore, the resistance of N2-CD was higher as shown in Figure 5.17(a). Different from N2-CD, the internal tube in N3-CDH was not cast with concrete. Thus, the resistance of N2-CD was slightly higher due to the small contribution of the concrete core in the internal tube. N4-SS was an ultra high strength concrete filled square single-tube specimen.

Different from N4-SS with hot finished hollow square steel section, welded box steel sections were used for the other four square specimens. Both N5-SS and N6-SS were ultra high strength concrete filled square single-tube specimens, and they were almost identical with slight difference in the concrete strength. Therefore, their curves almost overlap each other as shown in Figure 5.17(b). Different from N5-SS and N6-SS with single-tube sections, double-tube sections were used for N7-SD and N8-SDH. Therefore, their resistances were higher. Although the internal tube of N8-SDH was not cast with concrete, its resistance was slightly lower than N7-SD, due to the small contribution of concrete core in the internal tube.

#### 5.2.4.2 Moment-curvature relationship

As shown in Figure 5.7 and Figure 5.8, the curvature of the middle region should be the same along the length because this part was under pure bending. Therefore, the three contact points of the three *LVDTs* with the specimen bottom surface should be on a circle as shown in Figure 5.18.

The curvature of the bottom line of circular specimens or the bottom surface of square specimens can be expressed as:

$$\frac{1}{R} = \frac{2l_{AD}}{l_{AD}^2 + l_{BD}^2} \quad (5.2)$$

where  $R$  is the curvature radius.

The curvature radius of the middle plane is  $R_M = R - h/2$ . Therefore, the curvature of the middle plane can be expressed as:

$$\frac{1}{R_M} = \frac{1}{R - h/2} = \frac{2l_{AD}}{l_{AD}^2 + l_{BD}^2 - hl_{AD}} \quad (5.3)$$

where  $h$  is taken as the diameter for circular specimens and the depth for square specimens.

The curvature radius of the neutral plane is  $R_N = R - h/2 - h_n$ . Therefore, the curvature of the neutral plane can be expressed as:

$$\frac{1}{R_N} = \frac{1}{R - h/2 - h_n} = \frac{2l_{AD}}{l_{AD}^2 + l_{BD}^2 - (h + 2h_n)l_{AD}} \quad (5.4)$$

where  $h_n$  is the distance between the neutral plane and the middle plane. Initially, the value of  $h_n$  was equal to 0, since the moment was very small and thus there was no concrete crack in the tension zone. With the increase of moment, the concrete in the tension zone was cracked, and then the value of  $h_n$  was increased. However, compared with the value of  $R$ , the value of  $h_n$  is very small. Therefore, the curvature of the neutral plane can be approximately taken as the curvature of the middle plane, ignoring the influence of  $h_n$ .

Without the additional unload-reload parts and ignoring the influence of  $h_n$ , the comparisons of moment-curvature curves are shown in Figure 5.19(a) for the first four specimens with mild steel hot finished hollow sections and Figure 5.19(b) for the other four specimens with high strength steel welded box sections.

#### 5.2.4.3 Flexural stiffness degradation during unload-reload loading procedures

Additional unload-reload loading procedures were conducted for the first three specimens, and the flexural stiffness during unload-reload loading procedures was calculated based

on the moment-curvature curves as shown from Figure 5.20 to Figure 5.22. For specimen N1-CS, the initial elastic flexural stiffness was  $13166\text{kNm}^2$ , and the flexural stiffness was  $11221\text{kNm}^2$  during the first reloading procedure and  $10305\text{kNm}^2$  during the second reloading procedure. Compared with the value of initial flexural stiffness, it was reduced by 15% during the first reloading and by 22% during the second reloading. For specimen N2-CD, the initial elastic flexural stiffness was  $12869\text{kNm}^2$ , and the flexural stiffness was  $13517\text{kNm}^2$  during the first reloading,  $12225\text{kNm}^2$  during the second reloading,  $11748\text{kNm}^2$  during the third reloading and  $10572\text{kNm}^2$  during the fourth reloading. Compared with the value of initial flexural stiffness, it was increased by 5% during the first reloading but it was reduced by 5% during the second reloading, by 9% during the third reloading and by 18% during the fourth reloading. For specimen N3-CDH, the initial elastic flexural stiffness was  $13065\text{kNm}^2$ , and the flexural stiffness was  $12859\text{kNm}^2$  during the first reloading,  $11235\text{kNm}^2$  during the second reloading,  $11027\text{kNm}^2$  during the third reloading and  $9976\text{kNm}^2$  during the fourth reloading. Compared with the value of initial flexural stiffness, it was reduced by 2% during the first reloading, by 14% during the second reloading, by 16% during the third reloading and by 24% during the fourth reloading. All these results are summarized in Table 5.3, together with the measured values of flexural stiffness during unloading and the values of deflection at mid-span and loading level when the unload-reload loading procedures started. The reductions in flexural stiffness degradation during reloading under different loading levels are shown in Figure 5.23. It can be observed that significant stiffness degradation could be produced if unload-reload loading procedures started at loading level higher than 80%, but the degradation might be ignored if procedures started at loading level lower than 80%.

#### 5.2.4.4 Moment-longitudinal strain relationship

As shown in Figure 5.7 and Figure 5.8, the longitudinal strain values at eight locations of the middle span were measured. For the first three circular specimens, some strain gauges failed during unload-reload loading procedures. For other five square specimens, the values of strain gauges were well recorded. As shown in Figure 5.8(b), the first strain gauge measured the strain of the top surface, the second strain gauge measured the strain of the bottom surface, the third and fourth strain gauges measured the strain of the left and right surfaces at 3/4 height, the fifth and sixth strain gauges measured the strain of the left and right surfaces at middle height, and the seventh and eighth strain gauges measured the strain of the left and right surfaces at 1/4 height.

The moment-longitudinal strain curves are shown from Figure 5.24 to Figure 5.28, with compressive strain in positive value and tensile strain in negative value. It can be observed that all the measured values of longitudinal strain at different locations exceeded the yield strain at ultimate load, indicating that full plastic resistance of steel cross-section was attained.

#### 5.2.4.5 Variation of neutral axis location and curvature derived from strain distribution

It could be assumed that the cross-sections of the middle region remained plane during bending and there was no separation and relative slip at the interface between the concrete core and steel tube. Due to deformation compatibility, the strain should be linearly distributed along the cross-section as shown in Figure 5.29. The linear distribution can be derived from the measured values of the 8 strain gauges by linear regression, which can be expressed as:

$$h = R_N \varepsilon + h_n \quad (5.5)$$

where  $R_N$  is the curvature radius of the neutral plane and  $h_n$  is the distance from the location of neutral axis to the middle height, calculated by:

$$\begin{cases} R_N = \frac{\sum_{i=1}^8 (\varepsilon_i - \bar{\varepsilon})(h_i - \bar{h})}{\sum_{i=1}^8 (\varepsilon_i - \bar{\varepsilon})^2} \\ h_n = \bar{h} - R_N \bar{\varepsilon} \end{cases} \quad (5.6)$$

From above equation, the location variation of neutral axis can be obtained as shown in Figure 5.30 for the five square specimens with well recorded strain values. Initially, the neutral axis was at the middle height. With the increase in deflection and propagation of the concrete cracking in the tension zone, the values of  $h_n$  were increased. In the post-peak plastic range, the values of  $h_n$  were almost kept constant for the three single-tube specimens while they were slightly decreased for the two double-tube specimens.

From Equation (5.6), the curvature can be expressed by:

$$\frac{1}{R_N} = \frac{\sum_{i=1}^8 (\varepsilon_i - \bar{\varepsilon})^2}{\sum_{i=1}^8 (\varepsilon_i - \bar{\varepsilon})(h_i - \bar{h})} \quad (5.7)$$

Therefore, the curvature variation during bending can be calculated from above equation based on the variation of strain distribution and from Equation (5.4) based on the variation of deflection. The comparisons of the test values based on the two equations are shown from Figure 5.31 to Figure 5.35 for the five square specimens with well recorded

strain values. It can be observed that they were in agreement with each other very well, especially in the elastic range.

#### 5.2.4.6 Failure modes of the UHSC infilling

The failure modes of all the specimens at the maximum deflections are shown in Figure 5.36. To investigate the failure of concrete infilling, the steel tubes at the middle region were removed for specimens N2-CD and N5-SS after tested as shown in Figure 5.37. It can be observed that the concrete in tension zone was cracked and the concrete in compression zone was crushed.

### 5.3 Evaluation of Test Results

For evaluation, the test results are compared with Eurocode 4 predictions by simply extending the limitations on materials to the *UHSC* and *HSS* used in this study. The relevant design formulae have been introduced in **Chapter 2**.

#### 5.3.1 Test values of ultimate resistance compared with Eurocode 4 predictions

As shown in Figure 5.17, the loads kept increasing slightly even after significant deflections had been achieved. The ultimate loads were taken when the curvature reached  $0.2\text{m}^{-1}$  as shown in Figure 5.19. Compared with Eurocode 4 predictions, the test values of ultimate resistance and  $h_n$  are summarized in Table 5.4, where  $M_{pl,Rk}$  is the characteristic value of plastic bending resistance under pure bending and  $\alpha_M$  is a coefficient taken as 0.9 for S235 and S355 steel and 0.8 for S420 and S460 steel as stipulated in Eurocode 4.



Herein, the coefficient  $\alpha_M$  is also taken as 0.8 for the high tensile strength steel used in this study. The ultimate resistance  $M_u$  under pure bending can be expressed as:

$$M_u = \alpha_M M_{pl,Rk} \quad (5.8)$$

From Table 5.4, it can be observed that the average value of  $h_{n,test}/h_{n,EC4}$  is 0.921 and the standard deviation value is 0.098. Therefore, Eurocode 4 provides conservative values of  $h_n$ . Furthermore, all the values of  $M_{test}/M_{pl,Rk}$  are greater than 1.00. The average value of  $M_{test}/M_{pl,Rk}$  is 1.056 and the standard deviation value is 0.061 if the coefficient  $\alpha_M$  is not considered (or  $\alpha_M$  is taking as 1.0), while the average value of  $M_{test}/(\alpha M_{pl,Rk})$  is 1.262 and the standard deviation is 0.028 if the coefficient  $\alpha_M$  is considered. Therefore, very conservative values are provided by Eurocode 4 if the coefficient  $\alpha_M$  is considered. It indicates that all the specimens could achieve not only the design ultimate moment resistance but also the full plastic ultimate resistance. Therefore, based on the limited test data, Eurocode 4 can be safely extended to concrete filled steel tubes with *UHSC* and *HSS* under pure bending. The comparisons of test values of ultimate resistance with Eurocode 4 predictions are also shown in Figure 5.38.

### 5.3.2 Test values of flexural stiffness compared with Eurocode 4 predictions

Based on the moment-curvature curves shown in Figure 5.19, the values of flexural stiffness can be obtained. The curves were almost straight lines under low moments. For each specimen, the initial elastic flexural stiffness  $(EI)_{elastic}$  was taken as the slope of the straight line up to 40% of ultimate resistance by linear regression method, and the effective flexural stiffness  $(EI)_{secant}$  was taken as the secant flexural stiffness at 70% of ultimate resistance. It has been stated in **Chapter 4** that the service load can be up to 70%

of the ultimate resistance. Therefore, the secant flexural stiffness can be taken as a conservative estimation of the effective flexural stiffness for *CFST* beams at service limit state. The test values of initial elastic stiffness and secant stiffness are summarized in Table 5.5. As a reference, the values of effective flexural stiffness  $(EI)_{eff,II}$  of *CFST* beam-columns for use in second-order analysis as defined in Eurocode 4 are also shown in Table 5.5, which can be calculated by:

$$(EI)_{eff,II} = 0.9(E_a I_a + 0.5E_{cm} I_c) \quad (5.9)$$

From Table 5.5, it can be observed that the ratio of  $(EI)_{elastic}/(EI)_{eff,II}$  ranges from 0.888 to 1.148 with an average value of 1.017 and a standard deviation value of 0.090 and the ratio of  $(EI)_{secant}/(EI)_{eff,II}$  ranges from 0.718 to 0.881 with an average value of 0.822 and a standard deviation value of 0.052. Therefore, the effective flexural stiffness  $(EI)_{eff,II}$  as defined in Eurocode 4 for *CFST* beam-columns can also be taken as an estimation of the initial elastic flexural stiffness for *CFST* beams under pure bending, and  $0.8(EI)_{eff,II}$  is recommended to be used as a conservative estimation of effective flexural stiffness at service limit load for *CFST* beams.

## 5.4 Summary

An experimental investigation has been presented in this chapter on the structural behaviour of *CFST* beams employing *UHSC* and *HSS* subjected to pure bending. The test results of 8 specimens have shown that ultra high moment resistance, which is required for structural members in high-rise and long-span structures, can be achieved by employing *UHSC*. In addition, the moment resistance can be even higher if both of *UHSC* and *HSS* are used. Therefore, they are feasible to be adopted for high-rise constructions.

Although the *UHSC* used in this study was very brittle, the behaviour of *CFST* beams with *UHSC* and *HSS* were very ductile under bending, without brittle or sudden failure as observed from stub *CFST* column tests under compression presented in **Chapter 4**. There was no resistance degradation even if significant deflection had been achieved. The ultimate moment resistance was taken as the load value at a critical curvature value but not the maximum load value.

The comparisons of test results with Eurocode 4 predictions for ultimate moment resistance have indicated that the limitations on concrete cylinder strength and steel strength can be safely extended to *UHSC* up to 200MPa and *HSS* up to 780MPa for *CFST* beams. The full plastic moment resistance could be achieved, and very conservative predictions were provided if the reduction coefficient  $\alpha_M$  was considered as stipulated in Eurocode 4.

Significant flexural stiffness degradation during unload-reload loading procedures could be produced if the procedures started at loading level higher than 80% but the degradation might be ignored if the procedure started at loading level lower than 80%, indicating that the degradation can be ignored under service load. For *CFST* beams with *UHSC* and *HSS* under pure bending, the initial elastic flexural stiffness can be estimated by  $(EI)_{eff,II}$ , and the effective flexural stiffness at service limit state can be estimated by  $0.8(EI)_{eff,II}$ .

Table 5.1: Basic mechanical properties of steel sections

Sections	d or b (mm)	t (mm)	$f_y$ (MPa)	$f_u$ (MPa)	$E_a$ (MPa)	Classification
CHS114.3×6.3	114.3	6.3	421	524	185	1
CHS219.1×16	219.1	16	374	551	202	1
SHS200×12.5	200	12.5	465	559	206	1
SHS100×8	100	8	779	846	200	1
SHS200×12	200	12	756	825	199	1

For the 6mm-thick mild steel backing strip,  $f_y = 325\text{MPa}$ ,  $f_u = 467\text{MPa}$ , and  $E_a = 201\text{GPa}$

Table 5.2: Specimen configuration details

No.	Steel section(s)	$f_{y,e}$ (MPa)	$E_{a,e}$ (GPa)	$f_{y,i}$ (MPa)	$E_{a,i}$ (GPa)	$f_{ck}$ (MPa)	$E_{cm}$ (GPa)
N1-CS	CHS219.1×16	374	202	-	-	177	68
N2-CD	CHS219.1×16/114.3×6.3	374	202	421	185	173	68
N3-CDH	CHS219.1×16/114.3×6.3	374	202	421	185	177	68
N4-SS	SHS200×12.5	465	206	-	-	180	68
N5-SS	SHS200×12	756	199	-	-	180	68
N6-SS	SHS200×12	756	199	-	-	183	68
N7-SD	SHS200×12/100×8	756	199	779	200	178	68
N8-SDH	SHS200×12/100×8	756	199	779	200	177	68

Table 5.3: Flexural stiffness degradation during unload-reload procedure

No.		N1-CS		N2-CD		N3-CDH	
$(EI)_{\text{elastic}}$ (kNm <sup>2</sup> )		13166		12869		13065	
1 <sup>st</sup> un/re-load	Mid-Def (mm)	50		15		20	
	Loading level	89%		66%		77%	
	$(EI)_{\text{unload}}$ (kNm <sup>2</sup> )	11109	-16%	11749	-9%	11925	-9%
	$(EI)_{\text{reload}}$ (kNm <sup>2</sup> )	11221	-15%	13517	5%	12859	-2%
2 <sup>nd</sup> un/re-load	Mid-Def (mm)	100		30		40	
	Loading level	100%		82%		90%	
	$(EI)_{\text{unload}}$ (kNm <sup>2</sup> )	10184	-23%	11045	-14%	10630	-19%
	$(EI)_{\text{reload}}$ (kNm <sup>2</sup> )	10305	-22%	12225	-5%	11235	-14%
3 <sup>rd</sup> un/re-load	Mid-Def (mm)	-		60		80	
	Loading level	-		94%		98%	
	$(EI)_{\text{unload}}$ (kNm <sup>2</sup> )	-	-	10888	-15%	10371	-21%
	$(EI)_{\text{reload}}$ (kNm <sup>2</sup> )	-	-	11748	-9%	11027	-16%
4 <sup>th</sup> un/re-load	Mid-Def (mm)	-		120		120	
	Loading level	-		102%		102%	
	$(EI)_{\text{unload}}$ (kNm <sup>2</sup> )	-	-	9547	-26%	9221	-29%
	$(EI)_{\text{reload}}$ (kNm <sup>2</sup> )	-	-	10572	-18%	9976	-24%

Table 5.4: Test values of ultimate resistance and  $h_n$  compared with EC4 predictions

No	$h_{n,EC4}$ (mm)	$h_{n,test}$ (mm)	$M_{test}$ (kNm)	$M_{pl,Rk}$ (kNm)	$\alpha_M$	$h_{n,test}/h_{n,EC4}$	$M_{test}/M_{pl,Rk}$	$M_{test}/(\alpha_M M_{pl,Rk})$
N1-CS	42.6	-	340	292	0.9	-	1.164	1.293
N2-CD	33.9	-	370	329	0.9	-	1.124	1.249
N3-CDH	32.2	-	357	328	0.9	-	1.087	1.208
N4-SS	50.1	42.6	354	350	0.8	0.850	1.013	1.266
N5-SS	39.8	37.5	589	568	0.8	0.941	1.037	1.296
N6-SS	40.2	31.9	580	569	0.8	0.793	1.020	1.275
N7-SD	26.1	25.9	673	669	0.8	0.993	1.006	1.258
N8-SDH	23.8	24.5	668	667	0.8	1.030	1.001	1.251
Mean value						0.921	1.056	1.262
Standard deviation						0.098	0.061	0.028

Table 5.5: Test values of elastic and secant flexural stiffness compared with  $(EI)_{eff,II}$

No	$(EI)_{eff,II}$ kNm <sup>2</sup>	$(EI)_{elastic}$ kNm <sup>2</sup>	$(EI)_{secant}$ kNm <sup>2</sup>	$(EI)_{elastic}/(EI)_{eff,II}$	$(EI)_{secant}/(EI)_{eff,II}$
N1-CS	11470	13166	9898	1.148	0.863
N2-CD	11895	12869	9658	1.082	0.812
N3-CDH	11734	13065	10336	1.113	0.881
N4-SS	12256	11553	8800	0.943	0.718
N5-SS	12965	11510	10209	0.888	0.787
N6-SS	12965	12521	10480	0.966	0.808
N7-SD	13792	13903	11743	1.008	0.851
N8-SDH	13707	13563	11677	0.990	0.852
Mean value				1.017	0.822
Standard deviation				0.090	0.052



Figure 5.1: Casting of *UHSC* by pumping

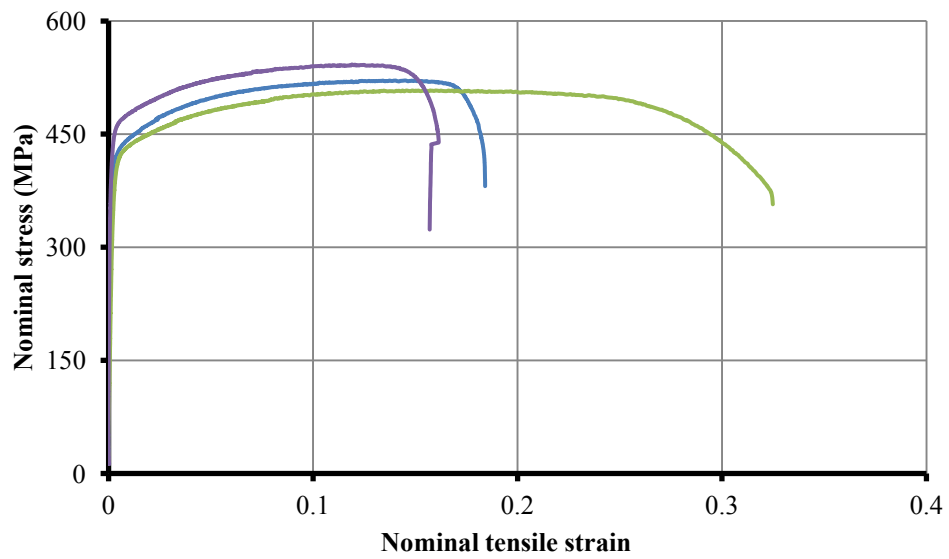


Figure 5.2: Coupon test stress-strain curves for CHS114.3mm×6.3mm

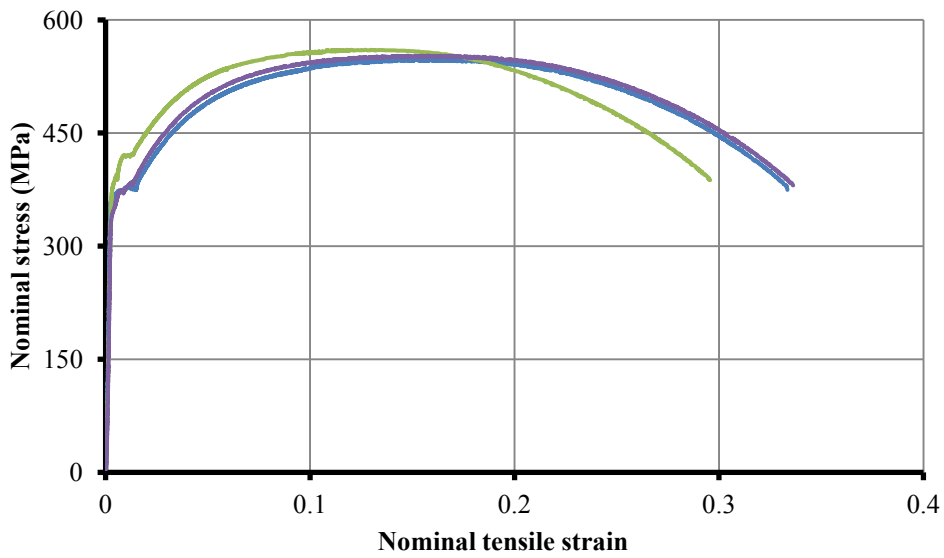


Figure 5.3: Coupon test stress-strain curves for CHS219.1mm×16mm

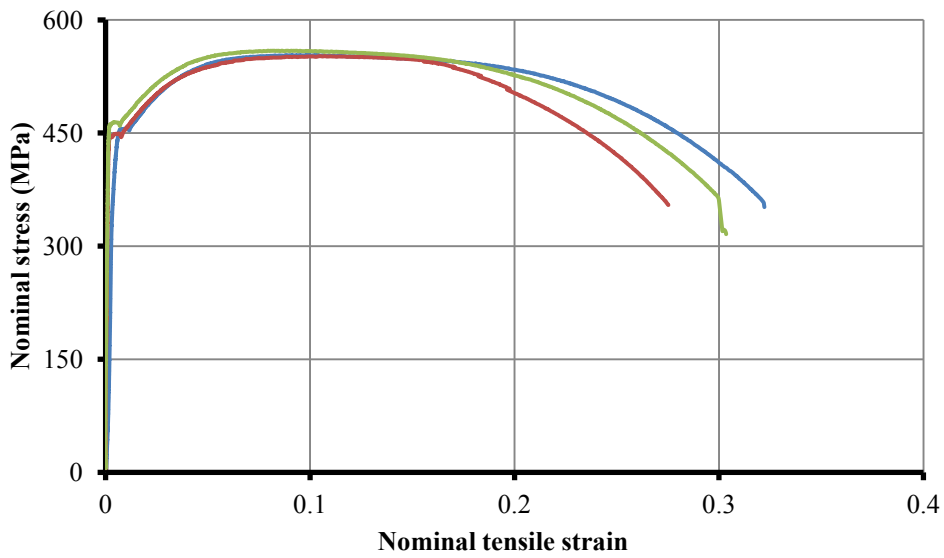


Figure 5.4: Coupon test stress-strain curves for SHS200mm×12.5m



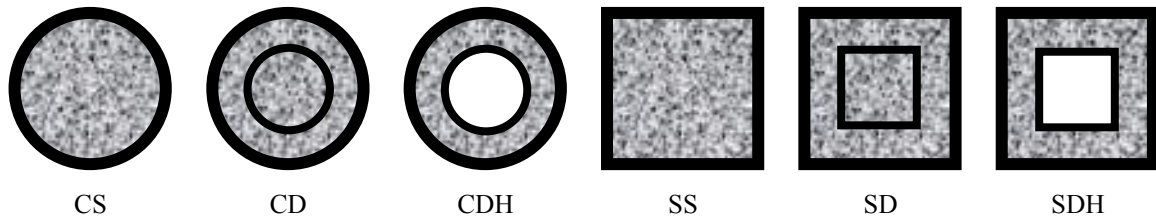


Figure 5.5: Different types of composite sections

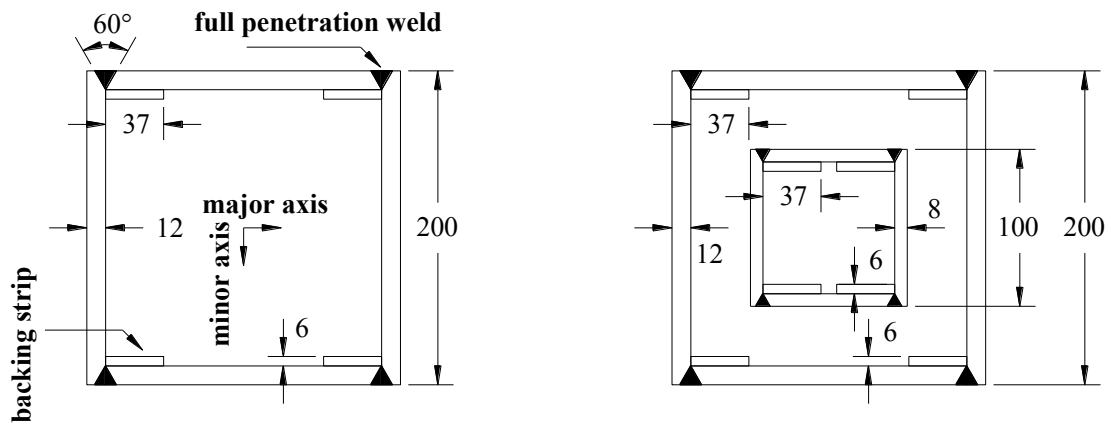
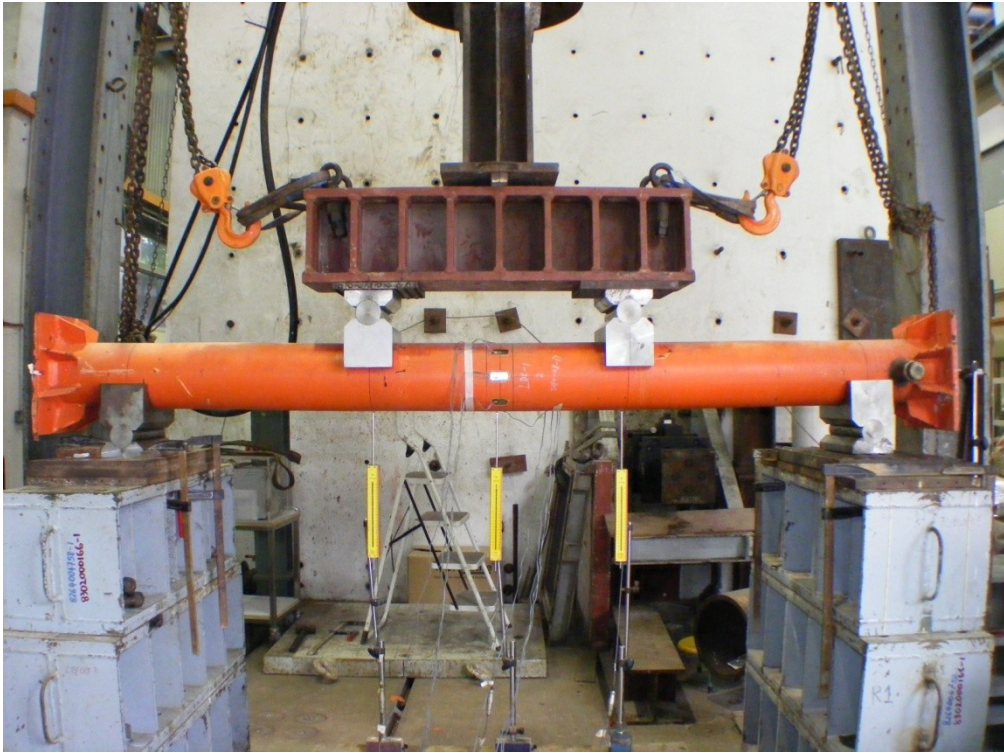
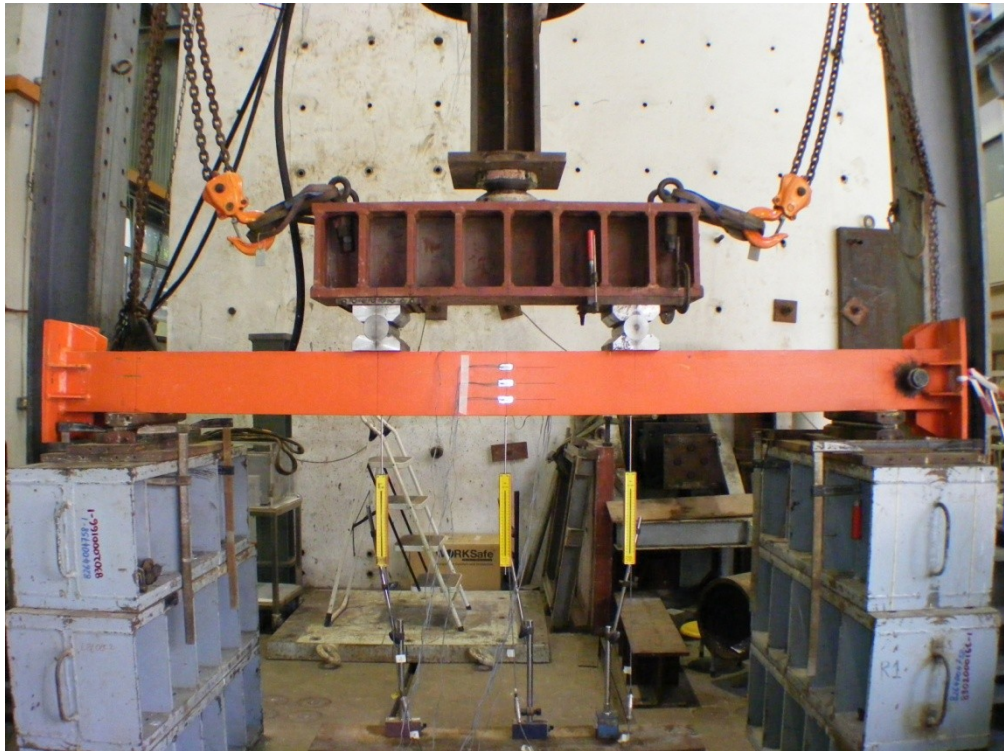


Figure 5.6: Dimension details of welded square box sections

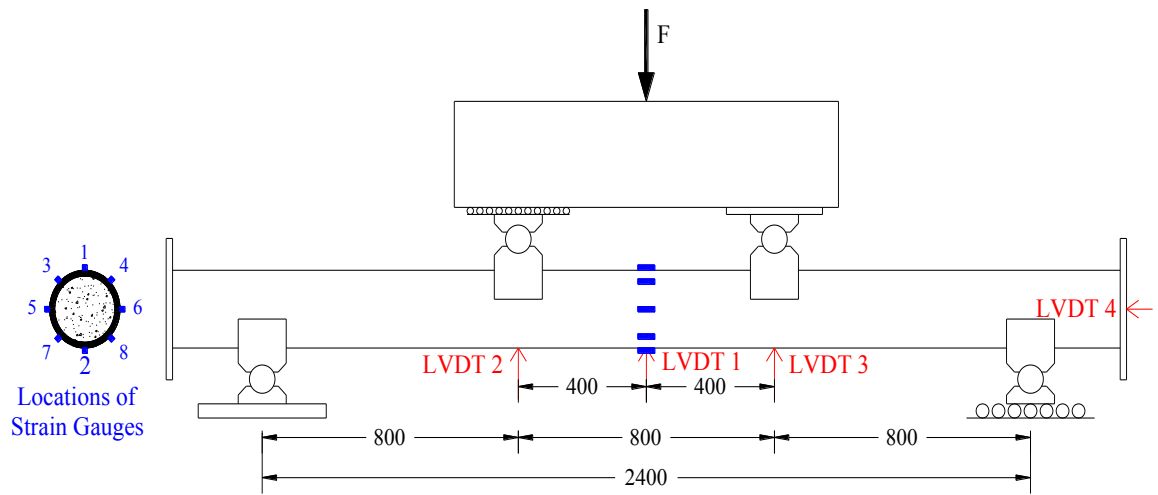


(a) Test set-up for circular specimens

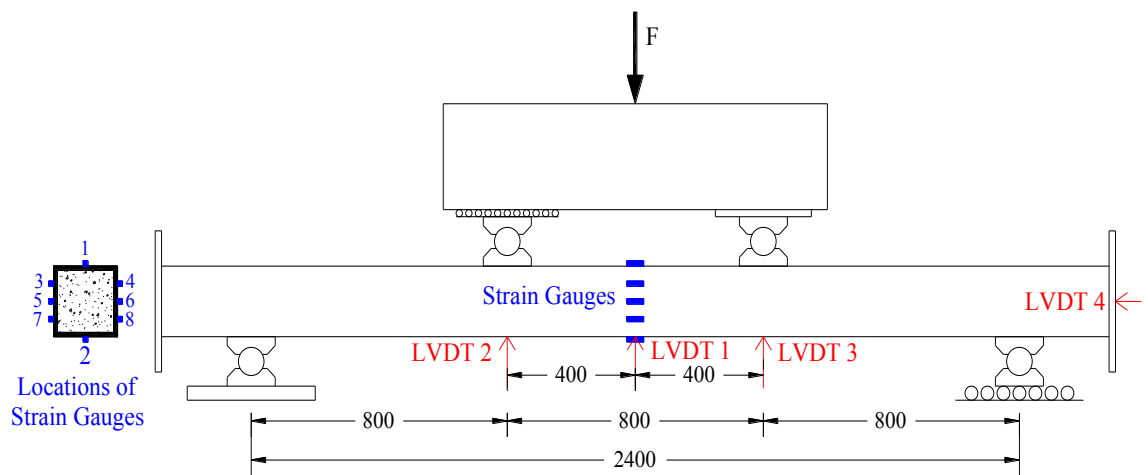


(b) Test set-up for square specimens

Figure 5.7: Test set-up



(a) Arrangement of *LVDTs* and strain gauges for circular specimens



(b) Arrangement of *LVDTs* and strain gauges for square specimens

Figure 5.8: Test instrumentations

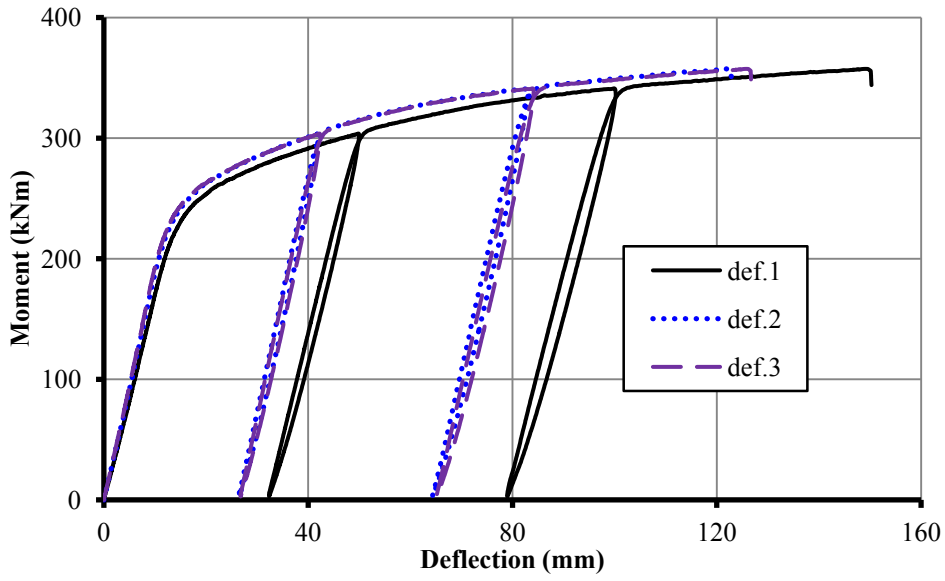


Figure 5.9: Moment-deflection curves for specimen N1-CS

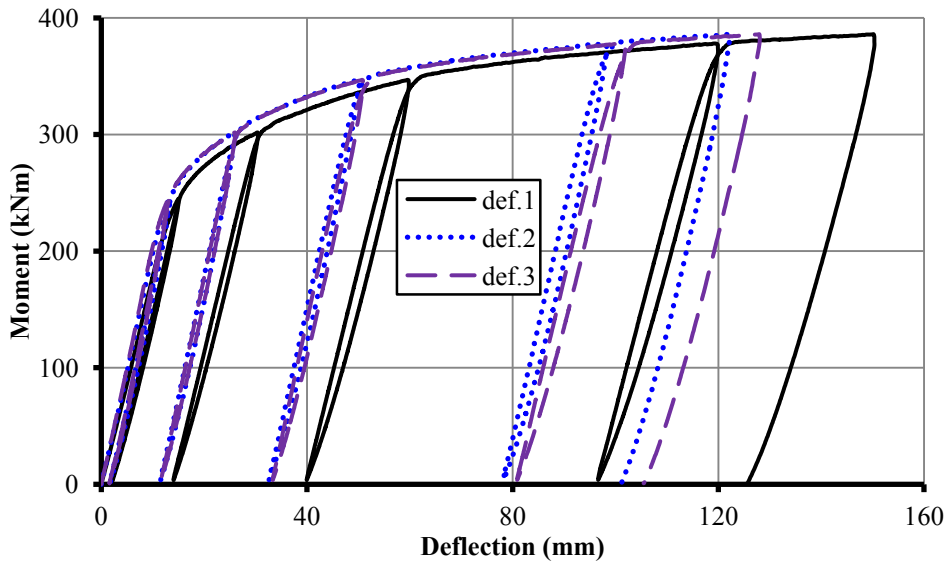


Figure 5.10: Moment-deflection curves for specimen N2-CD

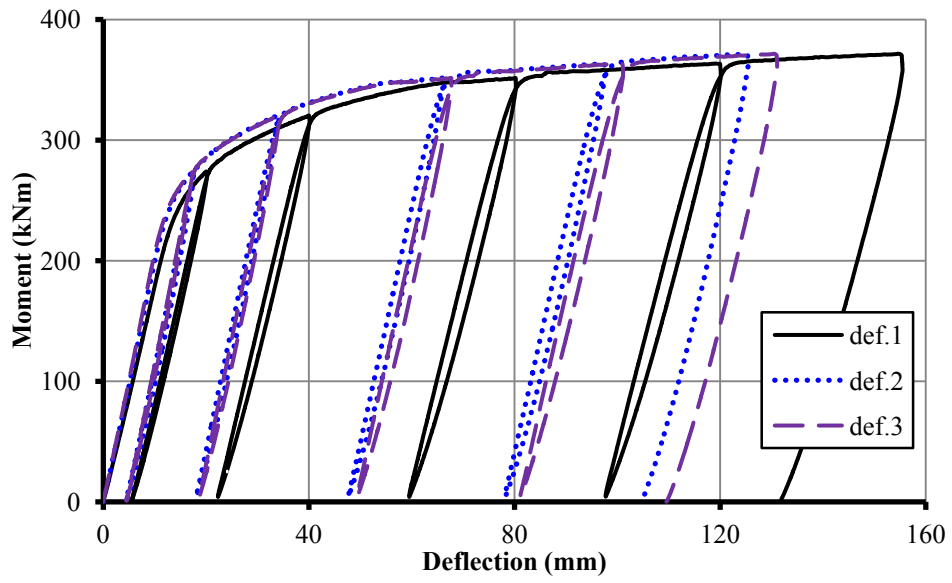


Figure 5.11: Moment-deflection curves for specimen N3-CDH

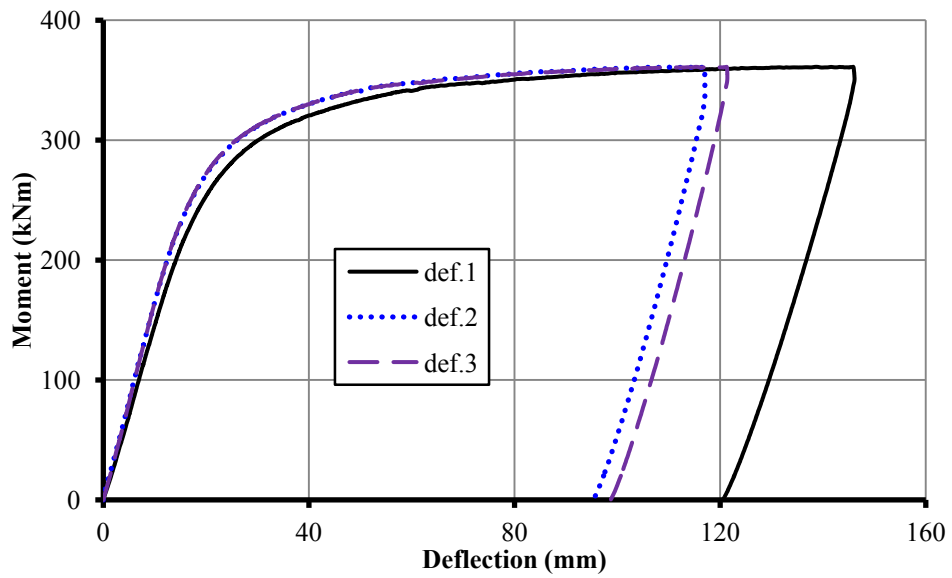


Figure 5.12: Moment-deflection curves for specimen N4-SS

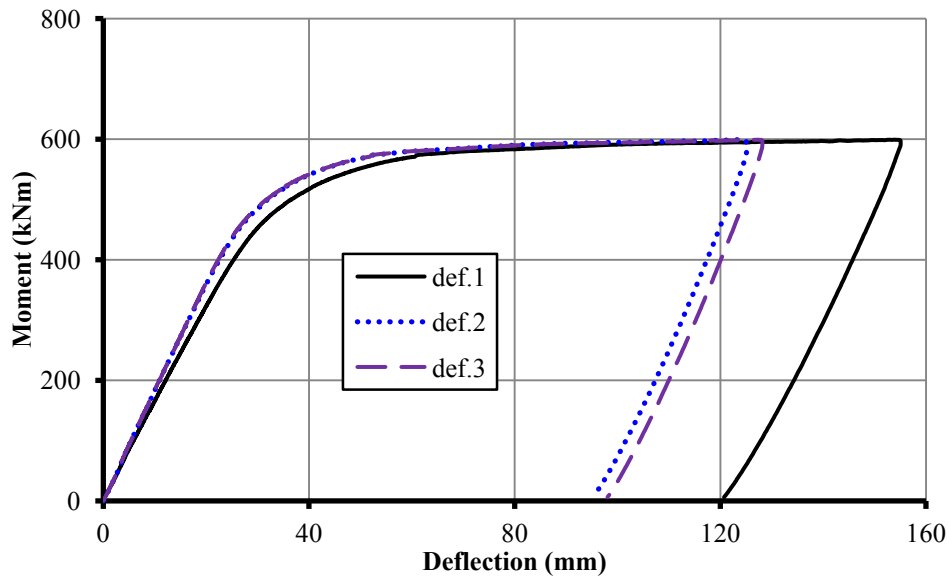


Figure 5.13: Moment-deflection curves for specimen N5-SS

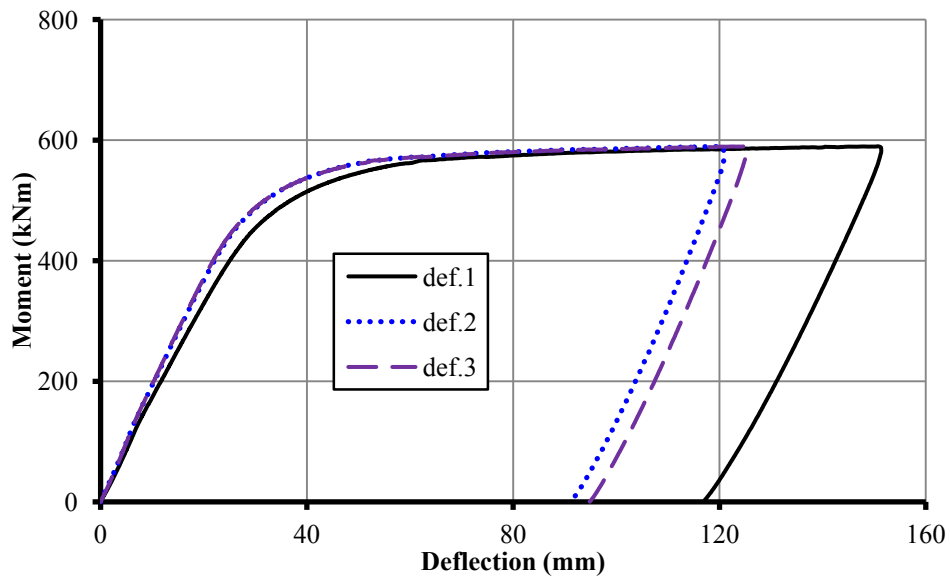


Figure 5.14: Moment-deflection curves for specimen N6-SS

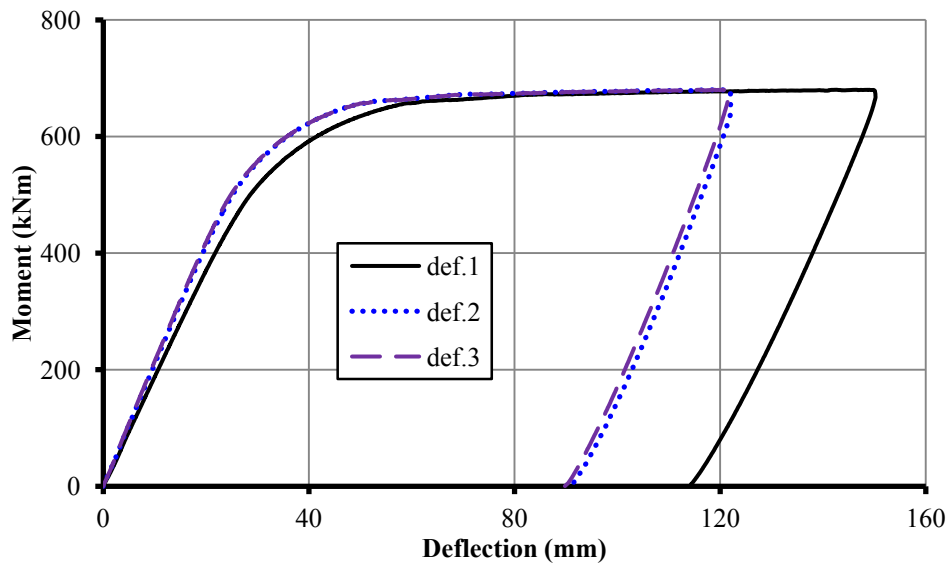


Figure 5.15: Moment-deflection curves for specimen N7-SD

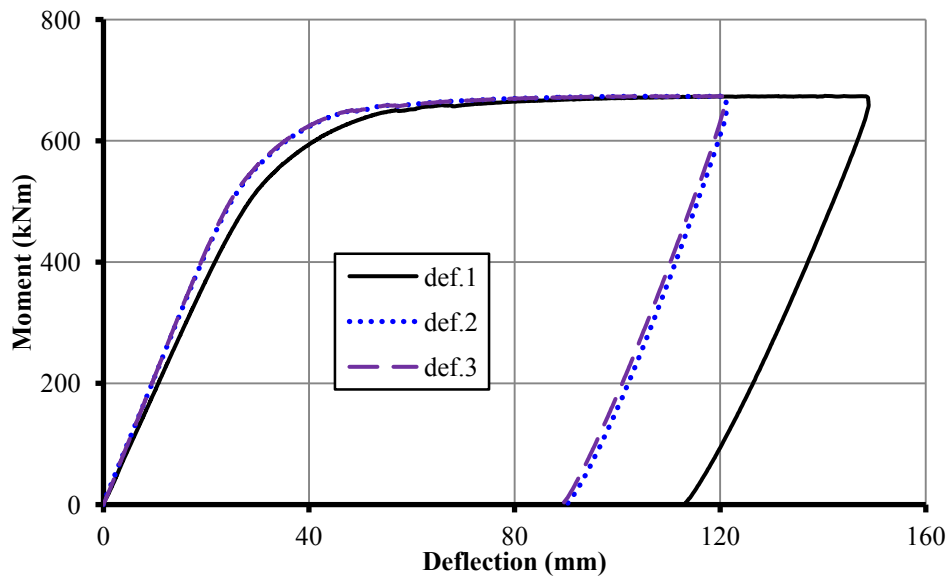
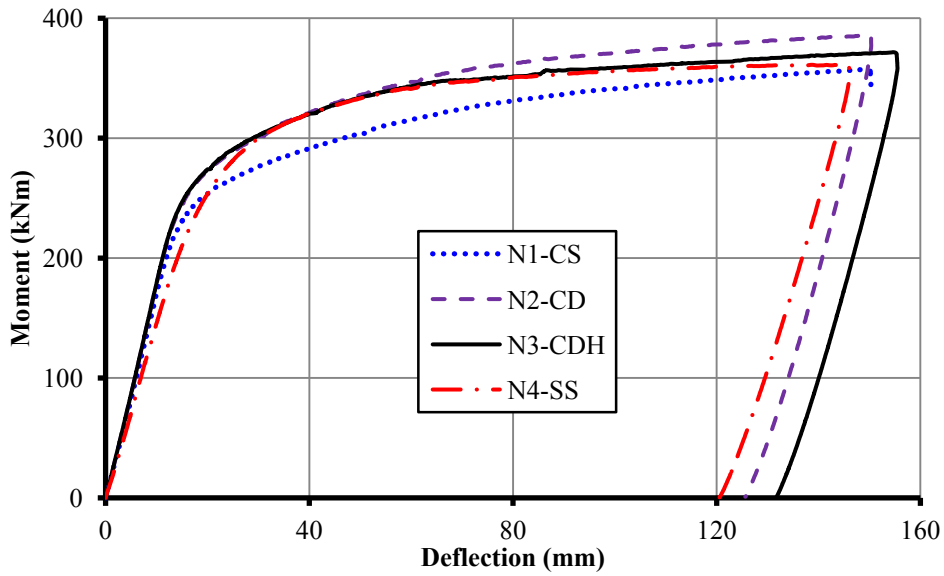
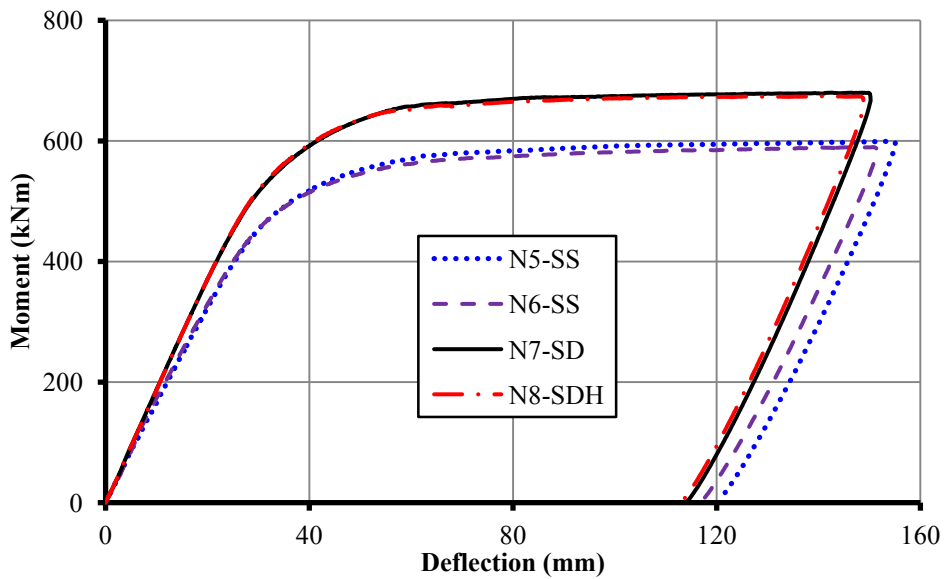


Figure 5.16: Moment-deflection curves for specimen N8-SDH



(a) Specimens with hot finished hollow steel sections



(b) Specimens with welded box steel sections

Figure 5.17: Comparison of moment-deflection curves



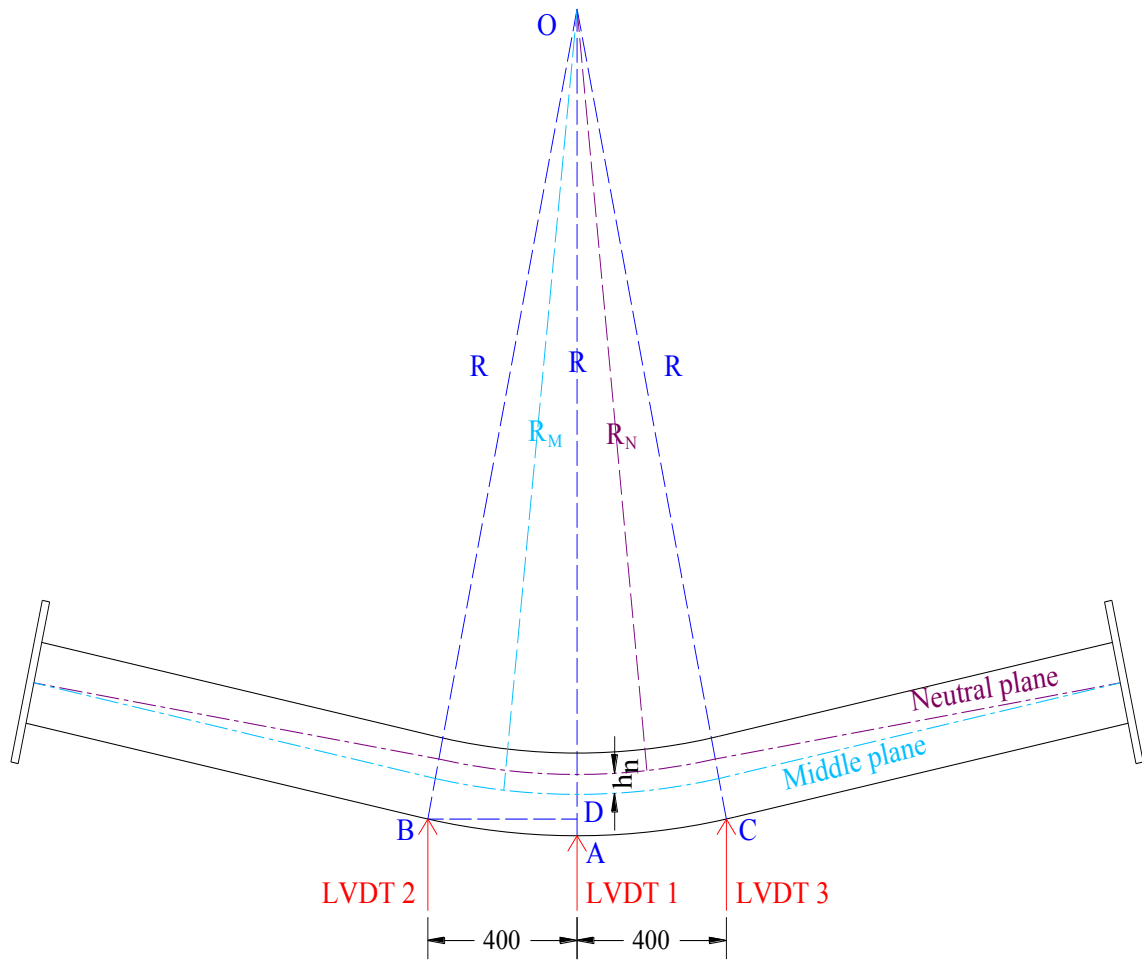
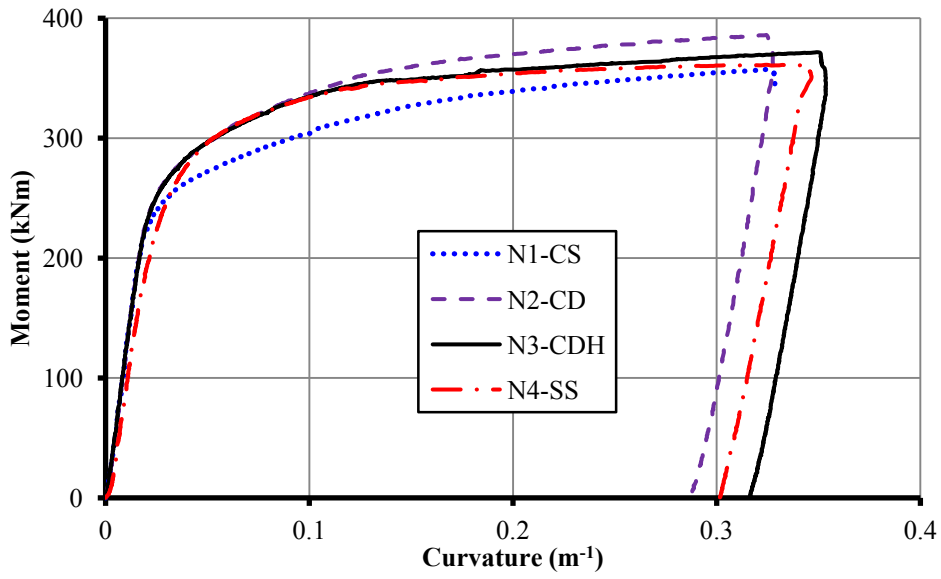
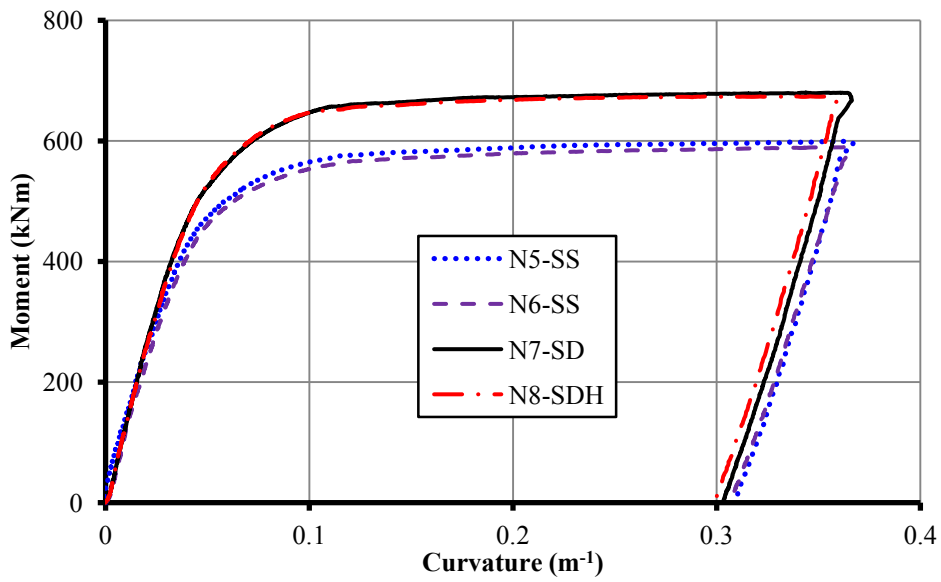


Figure 5.18: Curvature of the middle region under pure bending



(a) Specimens with hot finished hollow steel sections



(b) Specimens with welded box steel sections

Figure 5.19: Comparison of moment-curvature curves

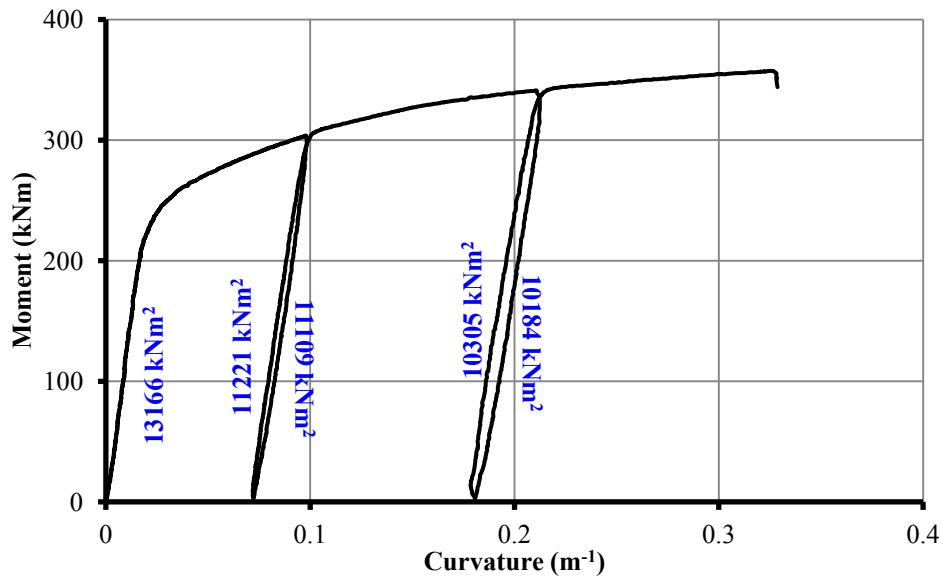


Figure 5.20: Flexural stiffness degradation during un/re-load procedure for N1-CS

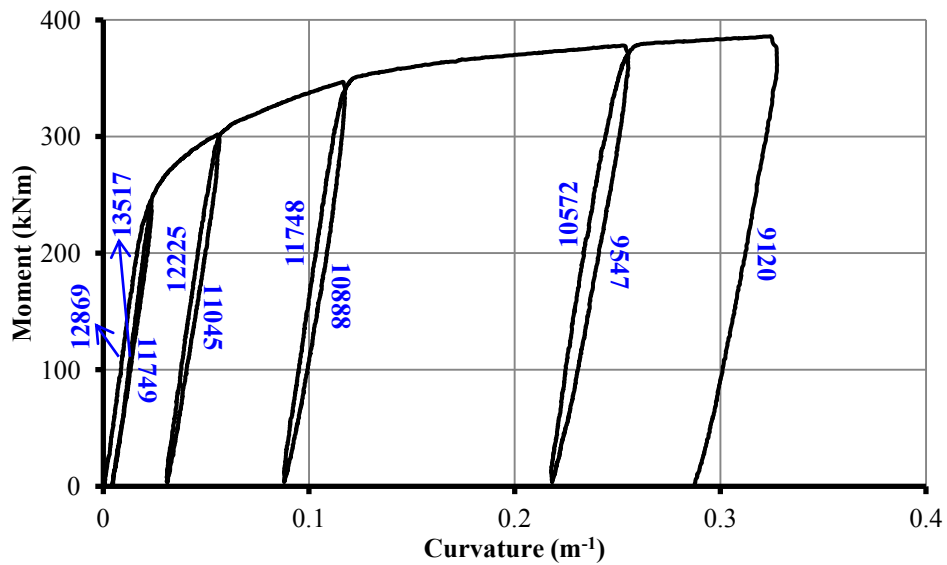


Figure 5.21: Flexural stiffness degradation during un/re-load procedure for N2-CD

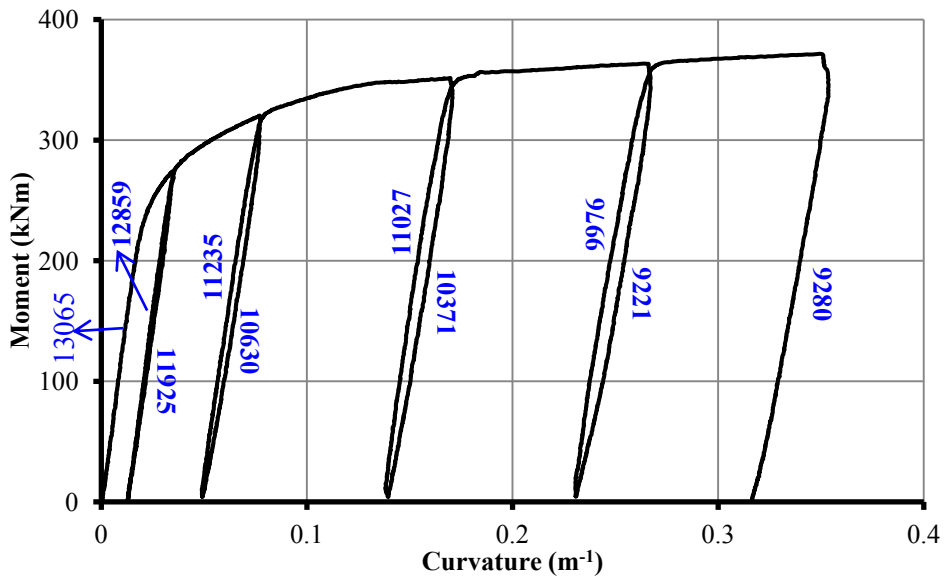


Figure 5.22: Flexural stiffness degradation during un/re-load procedure for N3-CDH

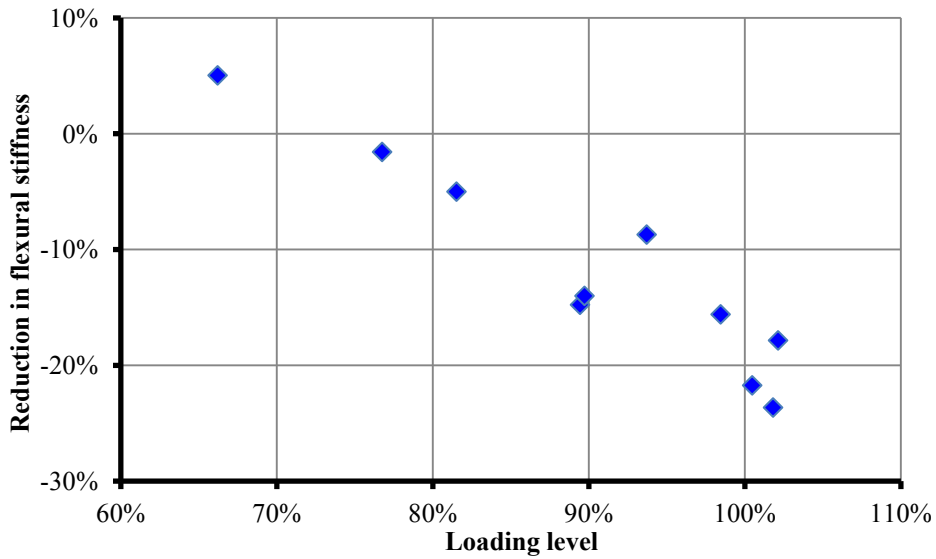


Figure 5.23: Flexural stiffness degradation at different loading levels

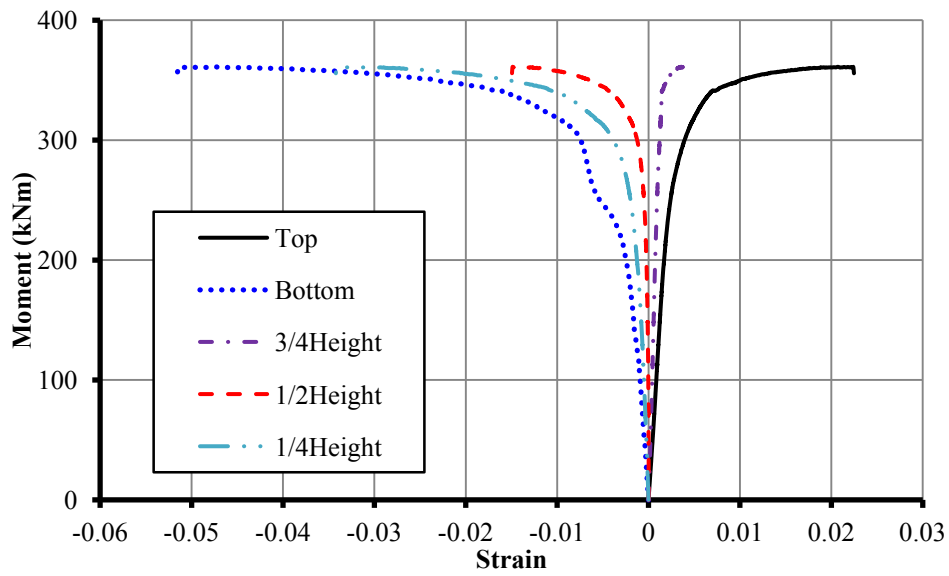


Figure 5.24: Moment-strain curves for specimen N4-SS

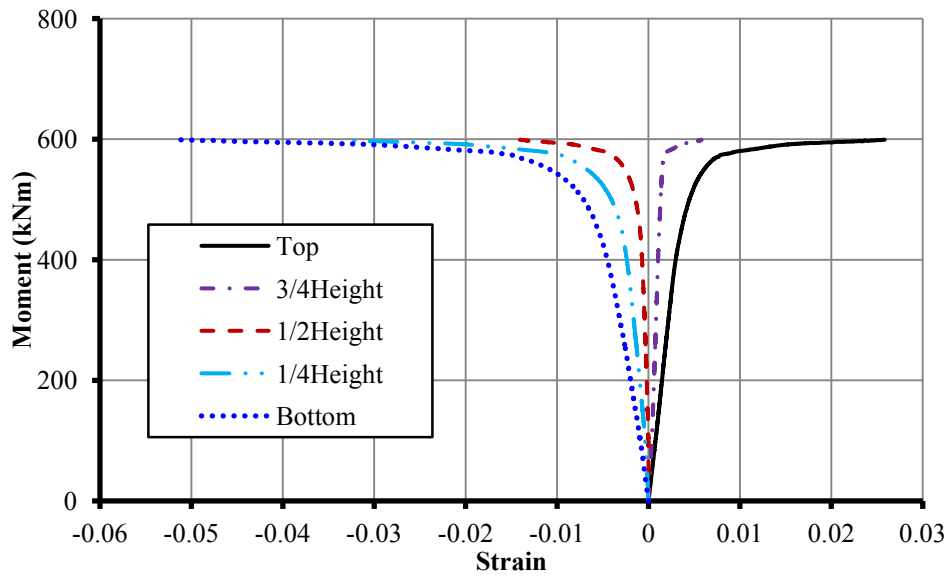


Figure 5.25: Moment-strain curves for specimen N5-SS

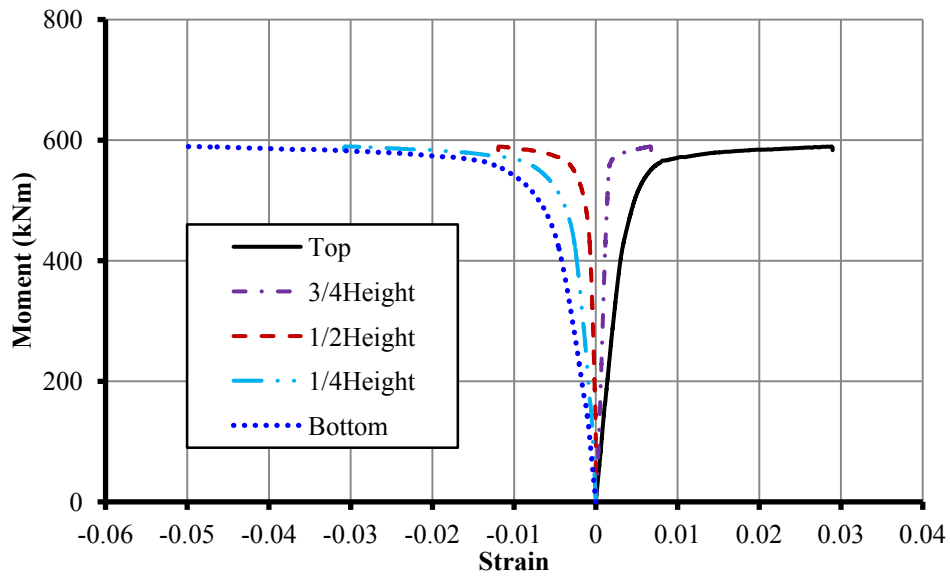


Figure 5.26: Moment-strain curves for specimen N6-SS

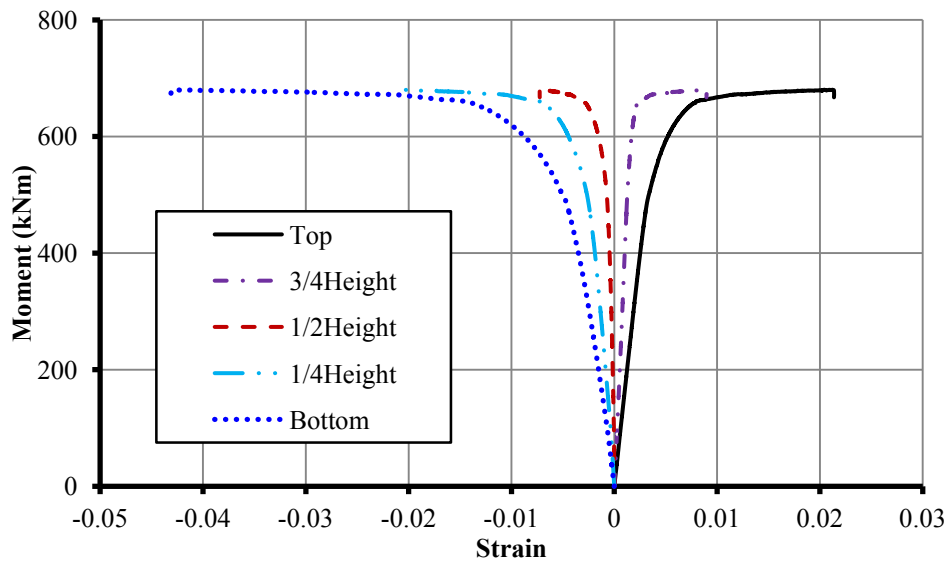


Figure 5.27: Moment-strain curves for specimen N7-SS

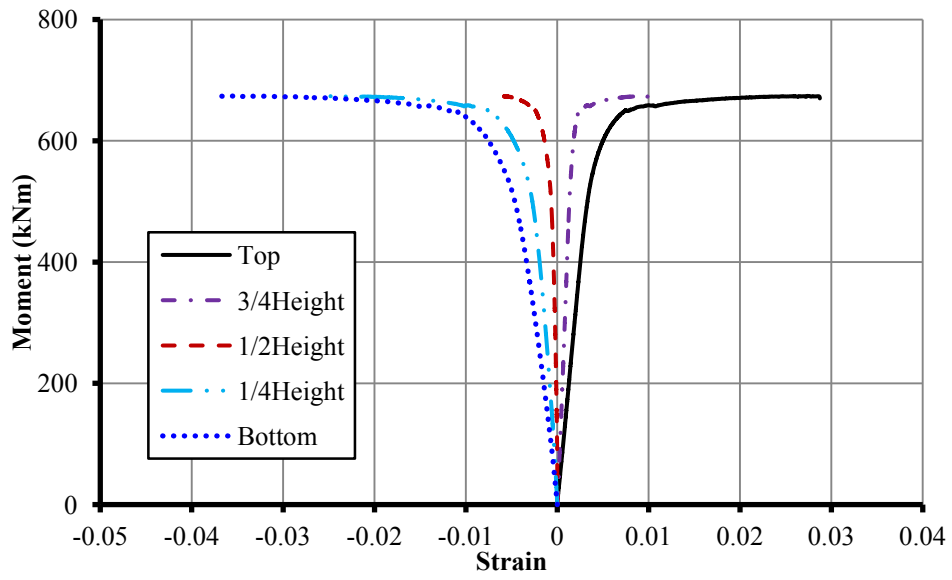
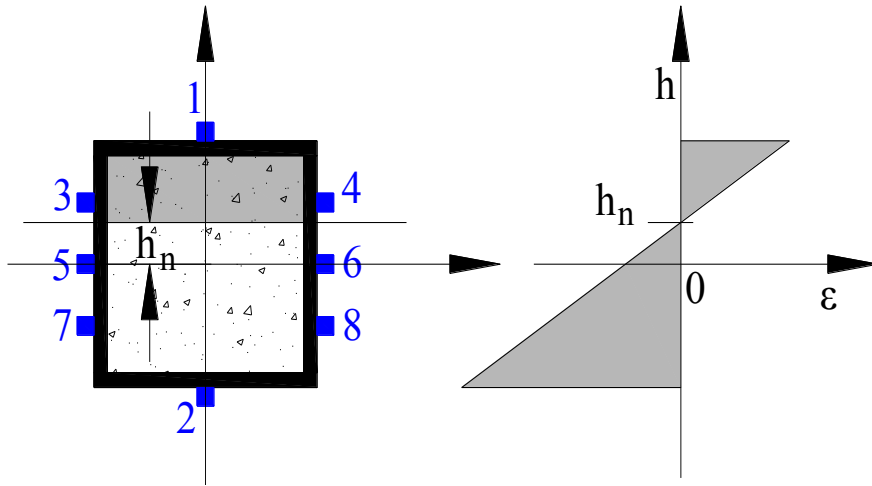
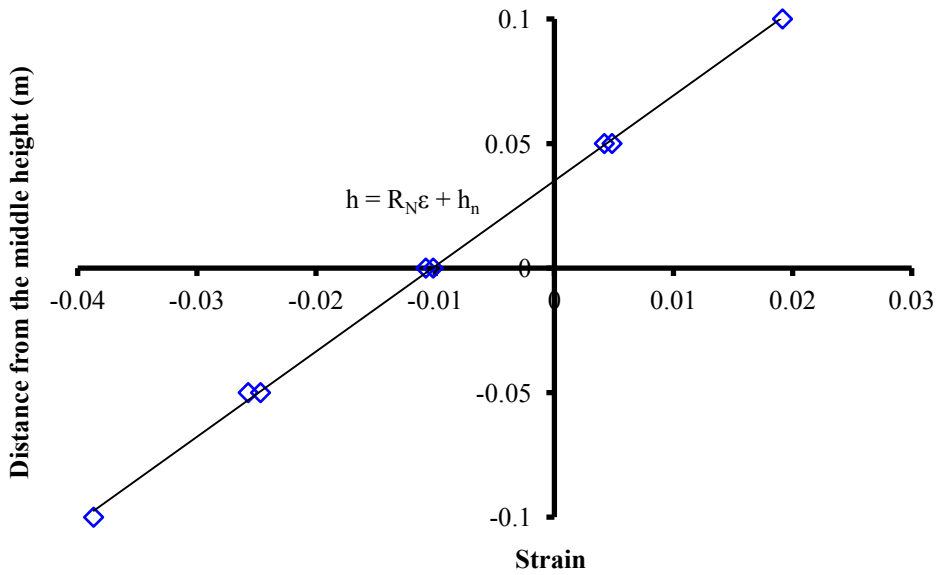


Figure 5.28: Moment-strain curves for specimen N8-SS



(a) Location of neutral axis and strain gauges      (b) Assumed linear strain distribution



(c) Linear strain distribution derived from test results

Figure 5.29: Strain distribution along cross-section height



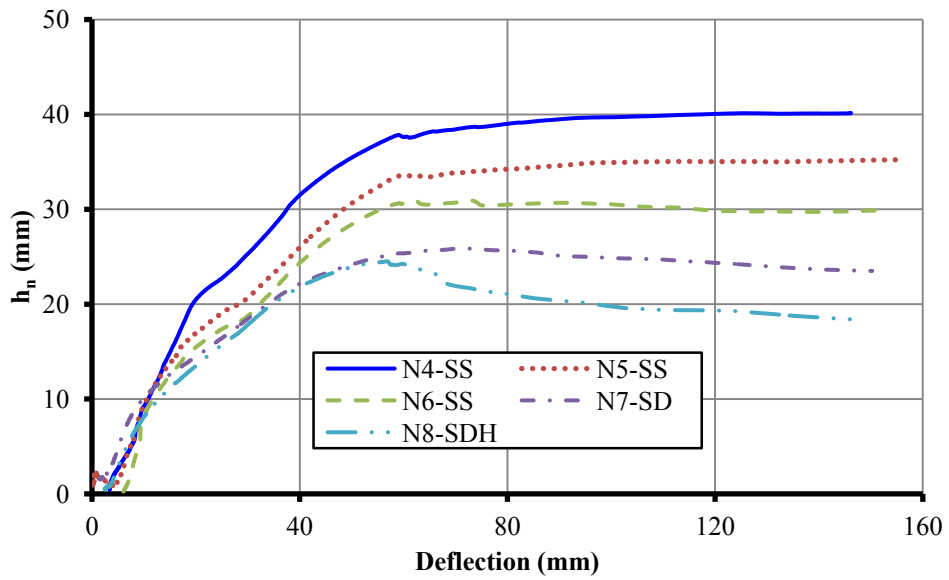


Figure 5.30: Variation of neutral axis location

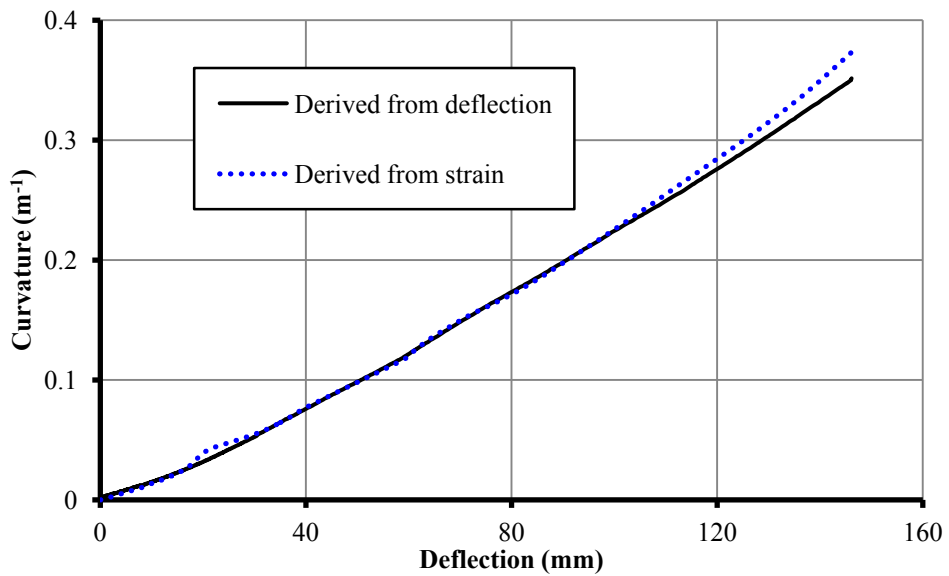


Figure 5.31: Variation of curvature derived from deflection and strain for N4-SS

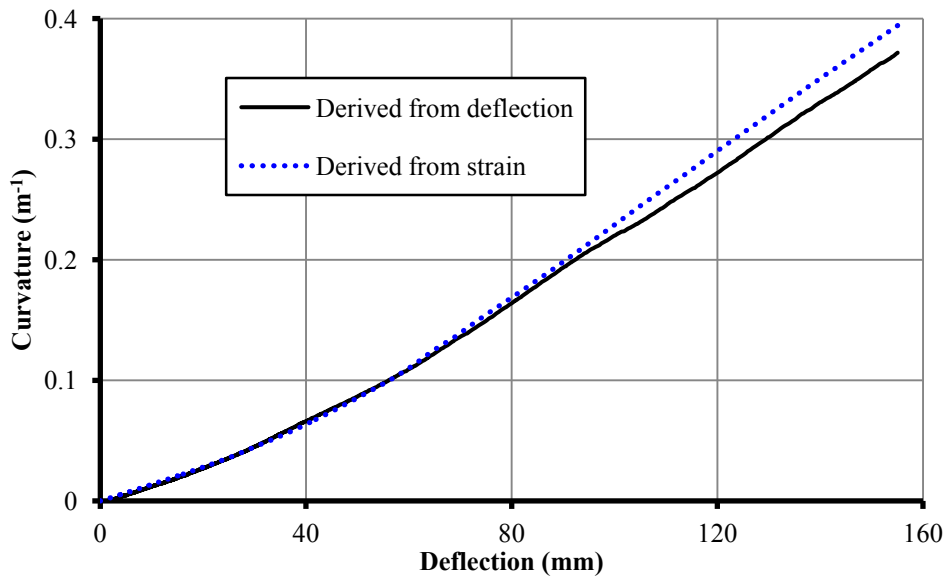


Figure 5.32: Variation of curvature derived from deflection and strain for N5-SS

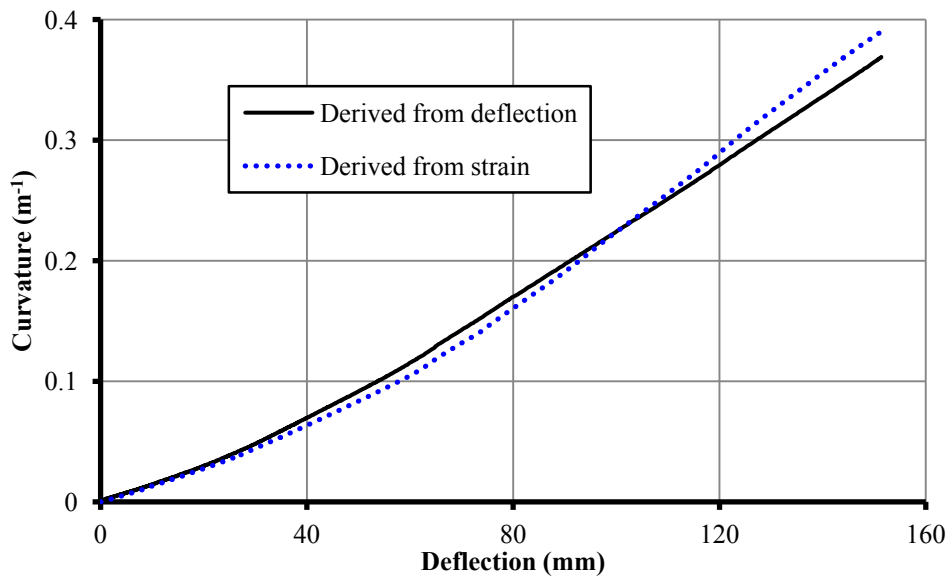


Figure 5.33: Variation of curvature derived from deflection and strain for N6-SS

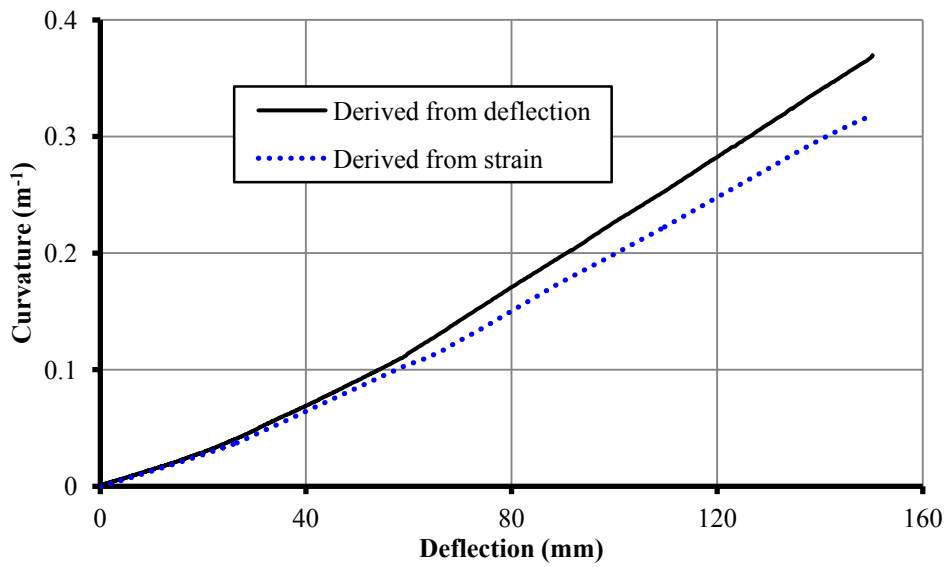


Figure 5.34: Variation of curvature derived from deflection and strain for N7-SD

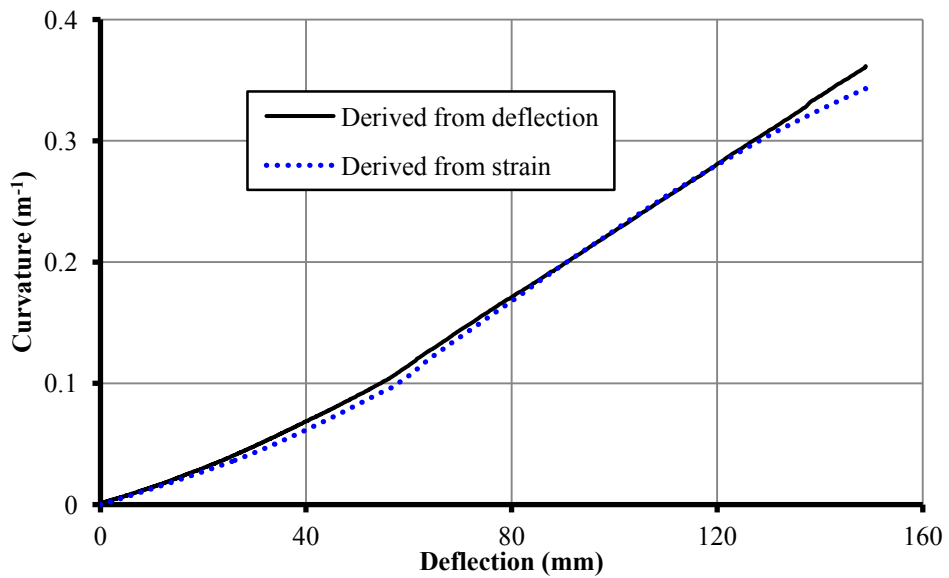
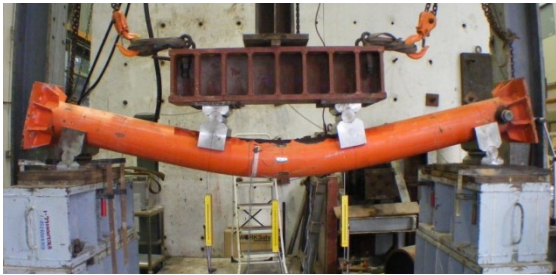
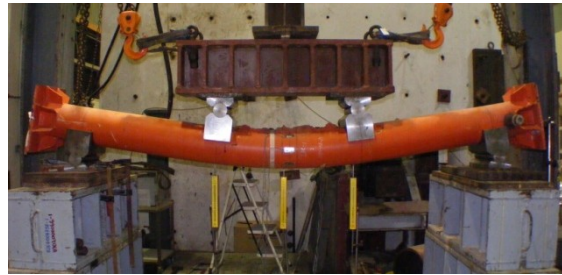


Figure 5.35: Variation of curvature derived from deflection and strain for N8-SDH



N1-CS



N2-CD



N3-CDH



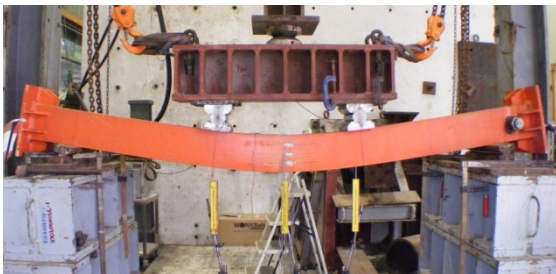
N4-SS



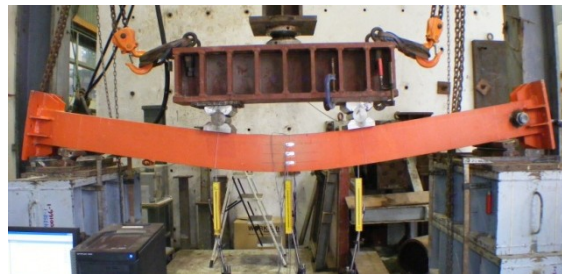
N5-SS



N6-SS



N7-SD



N8-SDH

Figure 5.36: Failure modes of test specimens at the maximum deflections



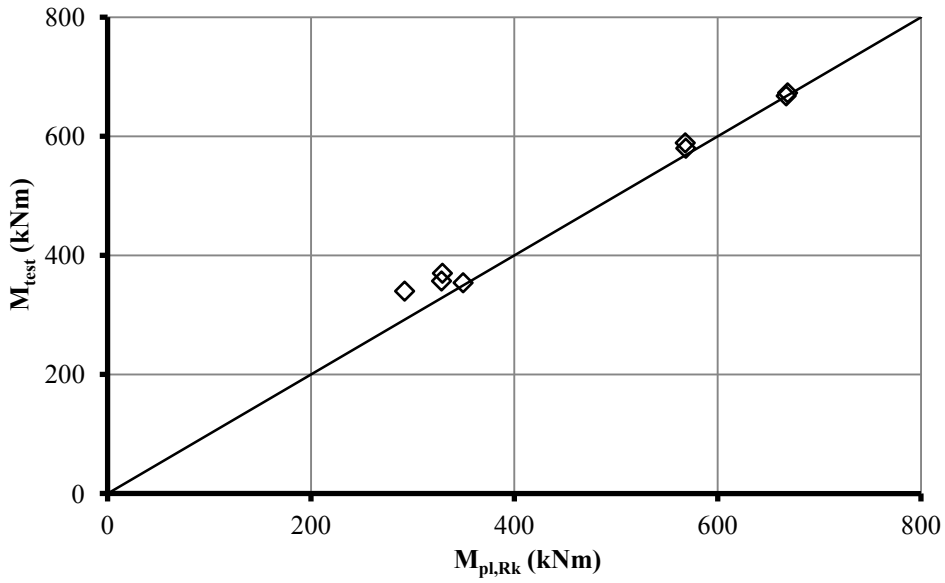


(a) Specimen N2-CD

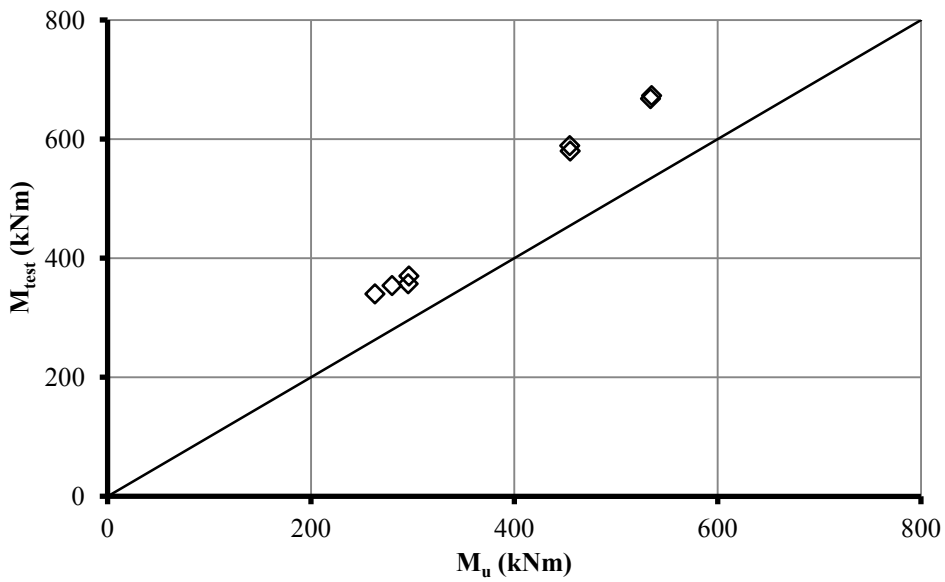


(b) Specimen N5-SS

Figure 5.37: Failure of *UHSC* infilling



(a) Comparison of  $M_{test}$  with  $M_{pl,Rk}$



(b) Comparison of  $M_{test}$  with  $M_u$

Figure 5.38: Comparison of test values of ultimate resistance with EC4 predictions

## Chapter 6 Slender CFST Beam-Columns with High Strength Materials under Concentric and Eccentric Compression

### 6.1 General

For the design of *CFST* members, essentially it only needs to check the cross-sectional resistance of the critical sections and the second order effect for slender members as introduced in **Chapter 2**. The second order effect of slender members can be considered by taking into account member imperfections and amplifying the greatest first-order moment force within the member length as stipulated in Eurocode 4, or it can be considered by taking into account member imperfections and multiplying the cross-sectional compressive resistance by a reduction factor as stipulated in Eurocode 4 and AISC 360-10.

The structural behaviour of stub *CFST* columns employing *UHSC* and *HSS* subjected to concentric compression has been presented in **Chapter 4** which aims to assess the cross-sectional resistance under compression, and the structural behaviour of *CFST* beams employing *UHSC* and *HSS* subjected to pure bending has been presented in **Chapter 5** which aims to assess the cross-sectional resistance under flexural moment. However, in practice, the *CFST* members are usually subjected to coupled compression and moment in most cases, and the second-order effect should be considered.

Based on previous investigations, this chapter presents an experimental investigation on the structural behaviour of *CFST* beam-columns employing *UHSC* and *HSS* subjected to concentric and eccentric compression, aiming to assess the cross-sectional resistance under coupled compression and moment. Fourteen slender specimens were tested to consider the second-order effect. For evaluation, the test results are compared with the predictions by Eurocode 4 (2004) approach.

## 6.2 Experimental Investigation

### 6.2.1 Materials

The materials used in this study included *UHSC*, circular and square mild steel hollow sections and square high tensile strength steel hollow sections. For each composite *CFST* specimen, at least three cylinders of size 100mm ( $d$ )  $\times$  200mm ( $h$ ) were cast and cured at ambient temperature as the same for curing composite specimens. They were tested at the same time when the corresponding composite specimen was tested to obtain the basic mechanical properties, referred to relevant ASTM standards as introduced in **Chapter 3**. For each type of steel sections, at least three coupon samples were tested, referred to ASTM E8M-04 as introduced in **Chapter 4**.

#### 6.2.1.1 UHSC

The first mix design without coarse aggregates shown in Table 3.4 of **Chapter 3** was used for all the specimens in this study. During casting, the fresh concrete was pumped into *CFST* specimens from the bottom which has been shown in Figure 5.1 of **Chapter 5**.



The test values of material properties for each specimen will be given later, together with all specimen configuration details.

#### 6.2.1.2 Steel sections

Four types of hot finished mild steel circular hollow sections 273mm × 10mm, 273mm × 16mm, 114.3mm × 6.3mm and 219.1mm × 16mm, one hot finished mild steel square hollow section 200mm × 12.5mm, and two types of high tensile strength steel square hollow sections 100mm×8mm and 200mm×12mm were used for all the specimens in this study. The stress-strain curves from coupon tests for the first two sections are respectively shown in Figure 6.1 and Figure 6.2. The other sections were the same as those presented in **Chapter 5**. The mechanical properties for all the sections are summarized in Table 6.1.

#### 6.2.2 Specimens

There were fourteen slender *CFST* specimens, classified in accordance with their composite section configurations which have been shown in Figure 5.5 of **Chapter 5**, where “CS”, “CD”, “CDH”, “SS”, “SD” and “SDH” respectively represent concrete-filled “circular single-tube section”, “circular double-tube section”, “circular double-tube section with hollow internal tube”, “square single-tube section”, “square double-tube section” and “square double-tube section with hollow internal tube”.

The configuration details for each specimen are shown in Table 6.2, where  $e_0$  was the initial eccentricity along only one axis,  $L$  was the effective length between the centres of the end roller supports and  $\lambda$  was the relative slenderness ratio as defined in Eurocode 4 introduced in **Chapter 2**. High tensile strength steel plates were used to fabricate the

welded box sections for specimens SS-2, SS-3, SD-1 and SDH-1 and hot finished mild steel hollow sections were used for other specimens. The details for the welded box sections have been shown in Figure 5.6 of **Chapter 5**.

### **6.2.3 Test set-up and loading procedure**

Four post yield strain gauges, placed at  $90^0$  apart, were attached to the external surface of steel tube at the mid-height of the specimen, as shown in Figure 6.3. Each strain gauge consists of two components, one aligned in the longitudinal direction and the other in the circumferential direction. The deflection at middle height was measured by two LVDTs at opposite positions. In addition, LVDTs were installed to measure the lateral deflection at one-fourth height and the vertical displacement at the column top. The vertical load was applied by a displacement/load control actuator with a maximum capacity of 10,000kN.

A quasi-static loading procedure was introduced by displacement control method in four steps: (1) preload the specimen at a rate of 0.5mm/min up to 10% of its resistance estimated by Eurocode 4 approach, (2) unload at a rate of 1.0mm/min, (3) reload at the rate of 0.5mm/min up to 70% ~ 80% of its estimated resistance, then change the rate down to 0.3mm/min until the load is lower than 80% the peak load, and (4) unload at a rate of 1.0mm/min.

## 6.2.4 Test results and observations

### 6.2.4.1 Load-deflection relationship

The load-deflection curves for each specimen are shown Figure 6.4 to Figure 6.17. From the curves beyond the peak loads, it can be found that resistance degradation was gradual without brittle or sudden failure as observed from stub *CFST* column tests under concentric compression presented in **Chapter 4**, especially for specimens subjected to eccentric loads.

The comparisons of load-deflection curves for specimens CS-1, CS-2 and CS-3 are shown in Figure 6.18. The main difference among these three specimens was that different values of eccentricity were applied. Axial load was imposed on CS-1 with no eccentricity, CS-2 with 20mm eccentricity, and CS-3 with 50mm eccentricity. It can be observed that the larger the eccentricity, the lower was the overall buckling resistance due to high end moments, and the more gradual was the loading curve.

Compared with specimens CS-1, CS-2 and CS-3 with diameter 219.1mm, a larger diameter steel section (CHS diameter 273mm) was used for specimens CS-4, CS-5 and CS-6 shown in Figure 6.19. Therefore, the overall buckling resistances were higher under the same loading conditions. Axial load was imposed on CS-4 with no eccentricity and on CS-5 and CS-6 with 50mm eccentricity. The steel tube in CS-6 was thicker than CS-5 but the difference in resistance was insignificant due to lower steel strength in CS-6. Another possible reason was that imperfection effect on CS-6 was stronger.

The load-deflection curves for circular double-tube specimens CD-1, CD-2 and CDH-1 are shown in Figure 6.20. Axial load was applied to CD-1 with no eccentricity and to CD-2 and CDH-1 with 20mm eccentricity. The overall buckling resistance of CDH-1 was lower than CD-2, because there was no concrete in the internal tube of CDH-1.

The load-deflection curves for square specimens are shown in Figure 6.21 for single-tube specimens and Figure 6.22 for double-tube specimens. Hot finished mild steel hollow section was used for SS-1, and welded box sections with high tensile strength steel were used for other specimens. An eccentricity of 20mm was applied to SS-1, SS-2 and SDH-1, and it was 50mm applied to SS-3 and SD-1. It can be observed that under the same loading conditions, the overall buckling resistance was higher for welded box columns made of higher strength steel plates.

#### 6.2.4.2 Failure modes of UHSC infilling

The failure modes of all the specimens at the maximum deflections are shown in Figure 6.23. To investigate the failure of concrete infilling, the steel tubes at the middle region were removed for specimens CS-2 and SDH-1 after tested as shown in Figure 6.24. It can be observed that the concrete in compression zone was crushed and the concrete in tensile zone was cracked.

### 6.3 Evaluation of Test Results

For evaluation, the test results are compared with Eurocode 4 predictions by simply extending the limitations on materials to the UHSC and HSS used in this study. The relevant design formulae have been introduced in **Chapter 2**.

### 6.3.1 Test values of ultimate resistance compared with Eurocode 4 predictions

The test values of ultimate resistance are compared with Eurocode 4 predictions as shown in Table 6.3 for concentrically compressed specimens and Table 6.4 for eccentrically compressed specimens. For concentrically loaded specimens, the EC4 predictions were calculated from Equation (2.13) of **Chapter 2** by the simplified method. The ratio of  $N_{\text{test}}/N_u$  ranges from 1.022 to 1.190 with an average value of 1.134 and a standard deviation value of 0.096. For eccentrically loaded specimens, the predictions were calculated from Equation (2.12) of **Chapter 2** by the general method with an imperfection deflection of  $e_i = L/300$ . According to Eurocode 4, the coefficient  $\alpha_M$  should be taken as 0.9 for S235 and S355 steel inclusive and 0.8 for steel grades S420 and S460. From Table 6.4, it can be observed that the ratio of  $N_{\text{test}}/N_u$  ranges from 1.078 to 1.349 with an average value of 1.178 and a standard deviation value of 0.099 if  $\alpha_M$  is taken as 0.8, while the ratio ranges from 1.024 to 1.289 with an average value of 1.117 and a standard deviation value of 0.093 if  $\alpha_M$  is taken as 0.9. Therefore, very conservative predictions are provided by Eurocode 4. The comparisons of test results with Eurocode 4 predictions are also shown in Figure 6.25.

It has been found in Chapter 5 that the full plastic moment resistance of *CFST* beams with *UHSC* and *HSS* under pure bending could be achieved, which means that the coefficient  $\alpha_M$  can be taken as 1.0 for *CFST* beams. By taking  $\alpha_M$  as 1.0 for eccentrically compressed specimens, the ratio of  $N_{\text{test}}/N_u$  ranges from 0.979 to 1.248 with an average value of 1.068 and a standard deviation value of 0.091 if  $\alpha_M$  is taken as 1.0. Only two specimens are

overestimated by less than 3%. Therefore, the full plastic moment resistance can also be used for *CFST* beam-columns.

## 6.4 Summary

An experimental investigation has been presented in this chapter on the structural behaviour of slender *CFST* beam-columns employing *UHSC* and *HSS* subjected to concentric and eccentric compression. The test results of 14 specimens indicate that ultra high overall buckling compressive resistance, which is required for structural members in high-rise and long-span structures, can be achieved by employing *UHSC*. In addition, the compressive resistance can be even higher if both of *UHSC* and *HSS* are used. Therefore, they are feasible to be adopted for high-rise constructions.

Although the *UHSC* used in this study was very brittle, the behaviour of slender *CFST* beam-columns with *UHSC* and *HSS* were rather ductile with smooth resistance degradation from the peak load, without brittle or sudden failure as observed from stub *CFST* column tests under compression presented in **Chapter 4**.

The comparisons of test results with Eurocode 4 predictions for have indicated that the limitations on concrete cylinder strength and steel strength can be safely extended to *UHSC* up to 200MPa and *HSS* up to 780MPa for slender *CFST* beam-columns. Very conservative predictions were provided if the reduction coefficient  $\alpha_M$  was considered at stipulated in Eurocode 4. In addition, the full plastic moment resistance could be used in the calculation by ignoring the reduction factor  $\alpha_M$  to obtain more accurate predictions.

Table 6.1: Basic mechanical properties of steel sections

Sections	d or b (mm)	t (mm)	$f_y$ (MPa)	$f_u$ (MPa)	$E_a$ (MPa)	Classification
CHS114.3×6.3	114.3	6.3	421	524	185	1
CHS219.1×16	219.1	16	374	551	202	1
CHS273×10	273	10	412	521	204	1
CHS273×10	273	16	401	522	203	1
SHS200×12.5	200	12.5	465	559	206	1
SHS100×8	100	8	779	846	200	1
SHS200×12	200	12	756	825	199	1

Table 6.2: Specimen configuration details

No.	Steel section(s)	$f_{ck}$ (MPa)	$E_{cm}$ (GPa)	$e_0$ (mm)	$L$ (mm)	$\lambda$
CS-1	CHS219.1×16	186	68	0	4195	1.100
CS-2	CHS219.1×16	181	68	20	3640	0.947
CS-3	CHS219.1×16	176	68	50	3640	0.940
CS-4	CHS273×10	180	68	0	4195	0.987
CS-5	CHS273×10	184	68	50	4450	1.055
CS-6	CHS273×16	180	68	50	4450	0.971
CD-1	CHS219.1×16/114.3×6.3	162	68	0	4195	1.076
CD-2	CHS219.1×16/114.3×6.3	174	68	20	3640	0.949
CDH-1	CHS219.1×16/114.3×6.3	182	68	20	3640	0.887
SS-1	SHS200×12.5	183	68	20	3640	0.968
SS-2	SHS200×12	176	68	20	3640	1.057
SS-3	SHS200×12	177	68	50	3640	1.058
SD-1	SHS200×12/100×8	161	68	50	3640	1.088
SDH-1	SHS200×12/100×8	176	68	20	3640	1.064

Table 6.3: Test results and EC4 predictions for concentrically loaded specimens

No	$N_{test}$ (kN)	$N_u$ (kN)	$N_{test}/N_u$
CS-1	6324	5321	1.188
CS-4	8592	8403	1.022
CD-1	6436	5409	1.190
Mean value			1.134
Standard deviation			0.096

Table 6.4: Test results and EC4 predictions for eccentrically loaded specimens

No	$N_{test}$ (kN)	$\alpha_M=0.8$		$\alpha_M=0.9$		$\alpha_M=1.0$	
		$N_u$ (kN)	$N_{test}/N_u$	$N_u$ (kN)	$N_{test}/N_u$	$N_u$ (kN)	$N_{test}/N_u$
CS-2	4389	4070	1.078	4288	1.024	4484	0.979
CS-3	3246	2861	1.135	3063	1.060	3249	0.999
CS-5	5083	3767	1.349	4096	1.241	4395	1.156
CS-6	5284	4698	1.125	4999	1.057	5274	1.002
CD-2	4674	4274	1.094	4485	1.042	4643	1.007
CDH-1	4175	3866	1.080	4030	1.036	4174	1.000
SS-1	5187	4612	1.125	4844	1.071	5051	1.027
SS-2	7136	5624	1.269	5828	1.225	6005	1.188
SS-3	4997	4247	1.177	4507	1.109	4742	1.054
SD-1	5439	4572	1.190	4807	1.131	5016	1.084
SDH-1	7627	5699	1.338	5919	1.289	6111	1.248
Mean value			1.178		1.117		1.068
Standard deviation			0.099		0.093		0.091



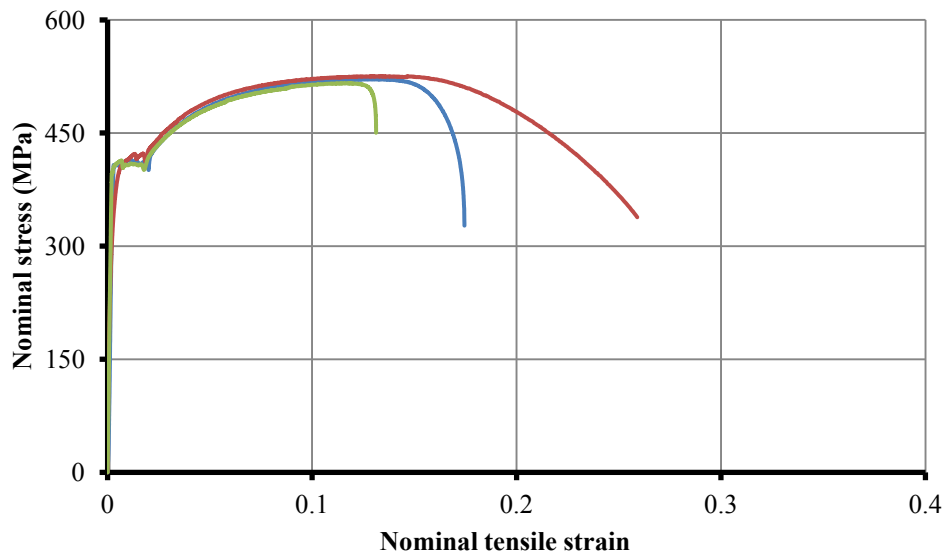


Figure 6.1: Coupon test stress-strain curves for CHS273mm×10mm

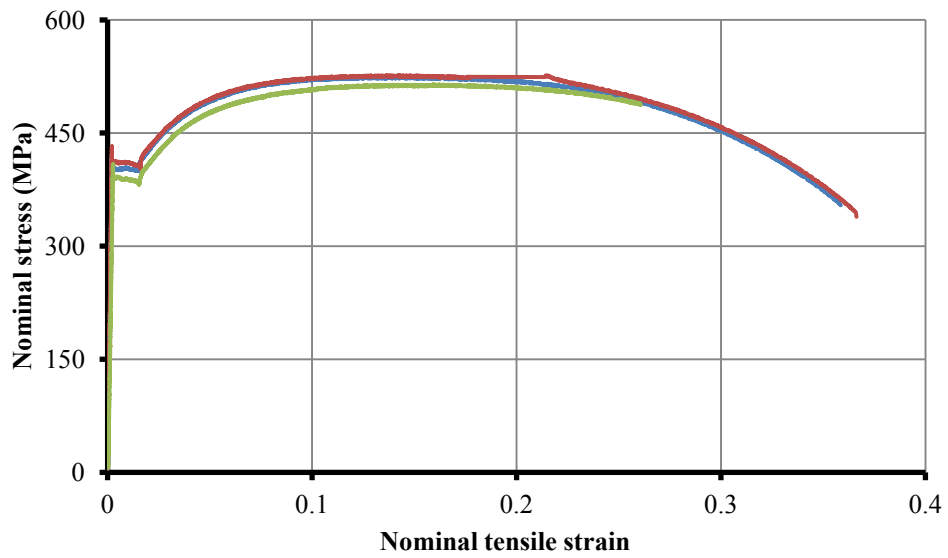


Figure 6.2: Coupon test stress-strain curves for CHS273mm×16mm

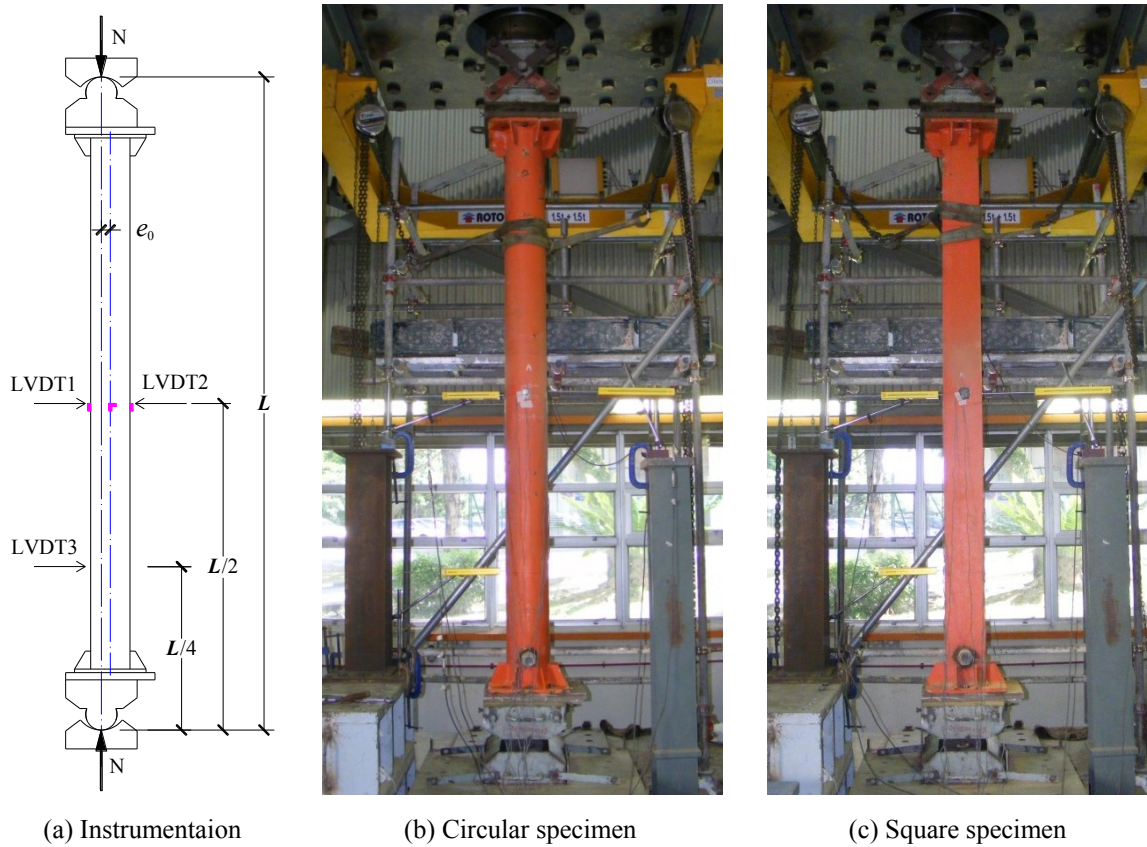


Figure 6.3: Test set-up and instrumentation

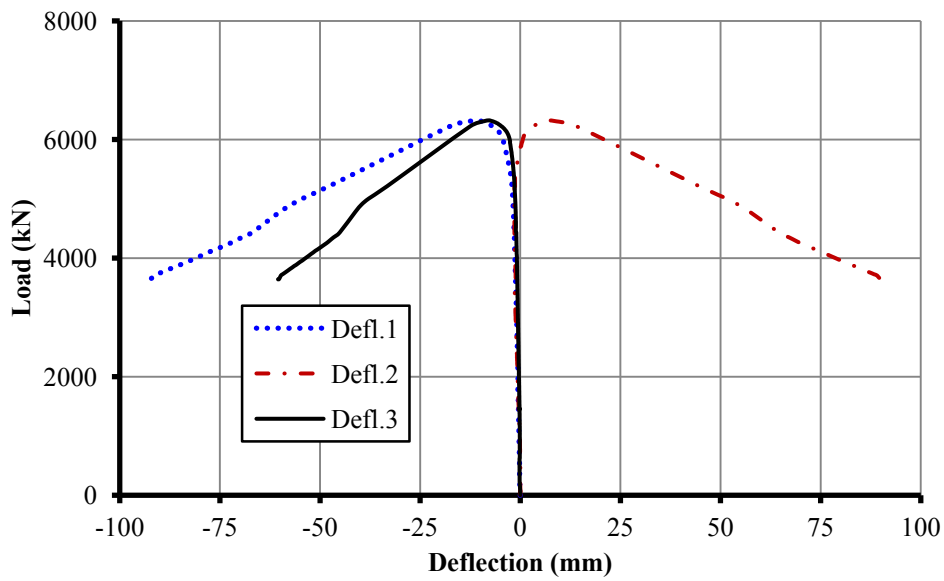


Figure 6.4: Load-deflection curves for specimen CS-1

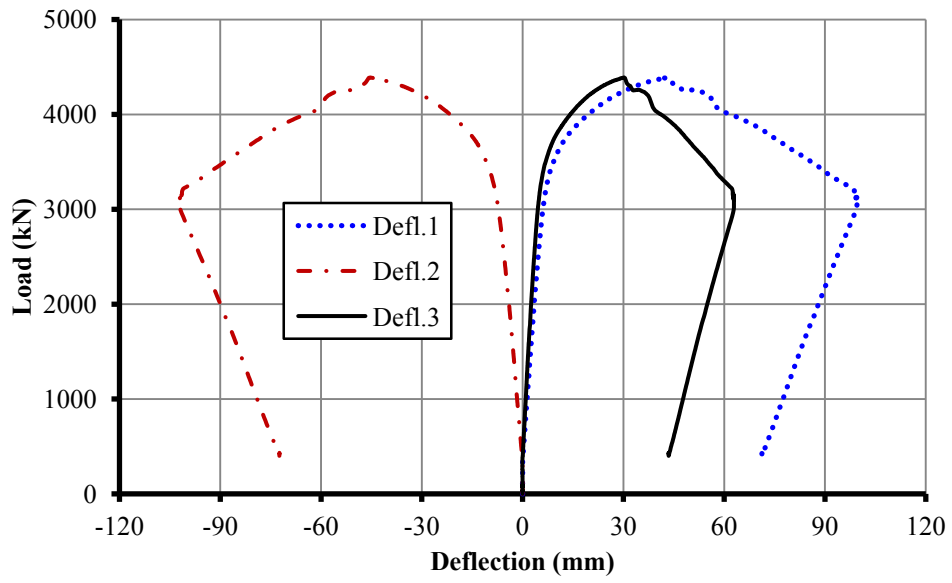


Figure 6.5: Load-deflection curves for specimen CS-2

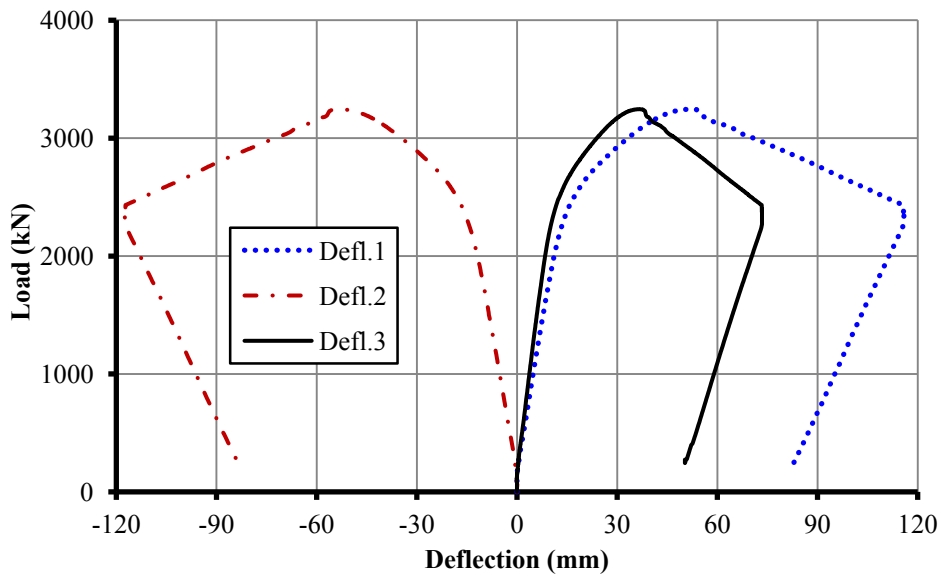


Figure 6.6: Load-deflection curves for specimen CS-3

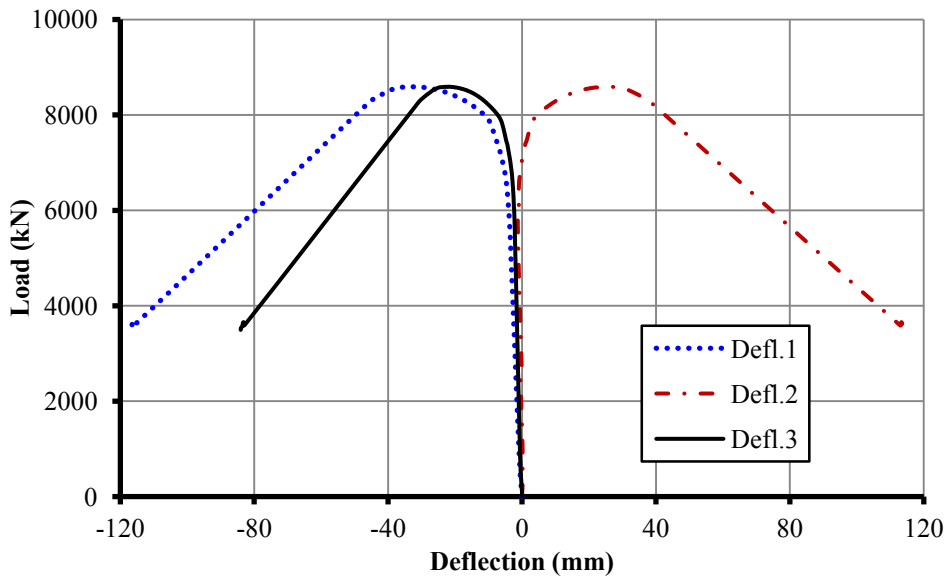


Figure 6.7: Load-deflection curves for specimen CS-4

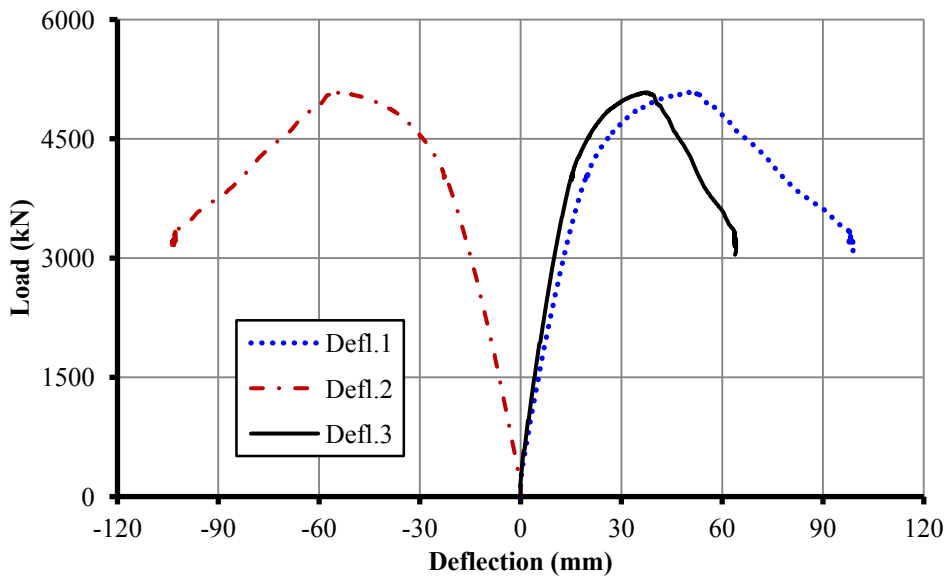


Figure 6.8: Load-deflection curves for specimen CS-5

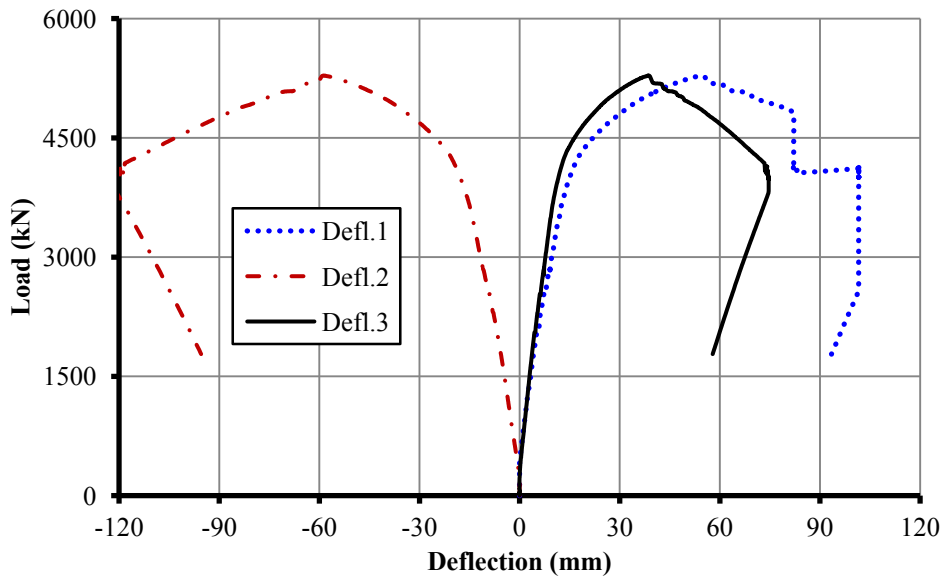


Figure 6.9: Load-deflection curves for specimen CS-6

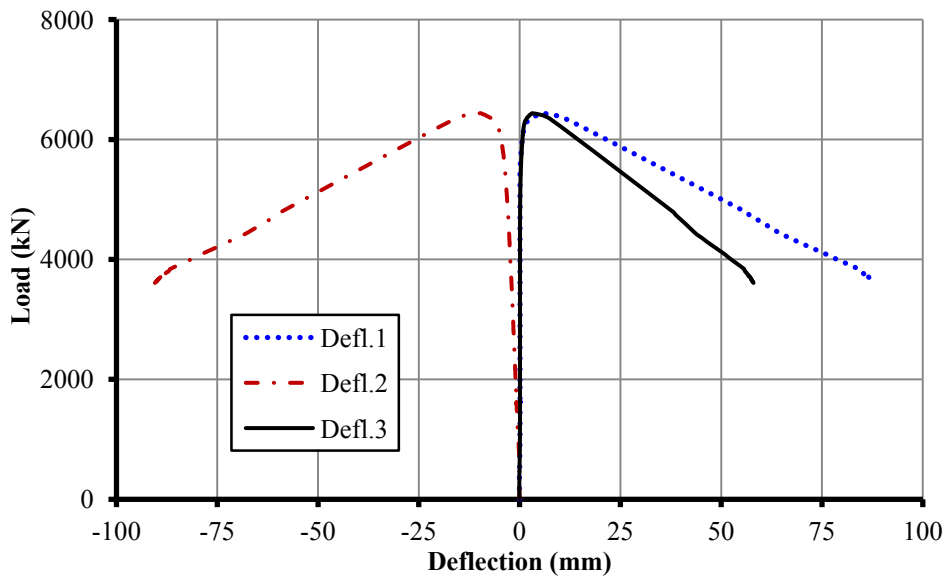


Figure 6.10: Load-deflection curves for specimen CD-1

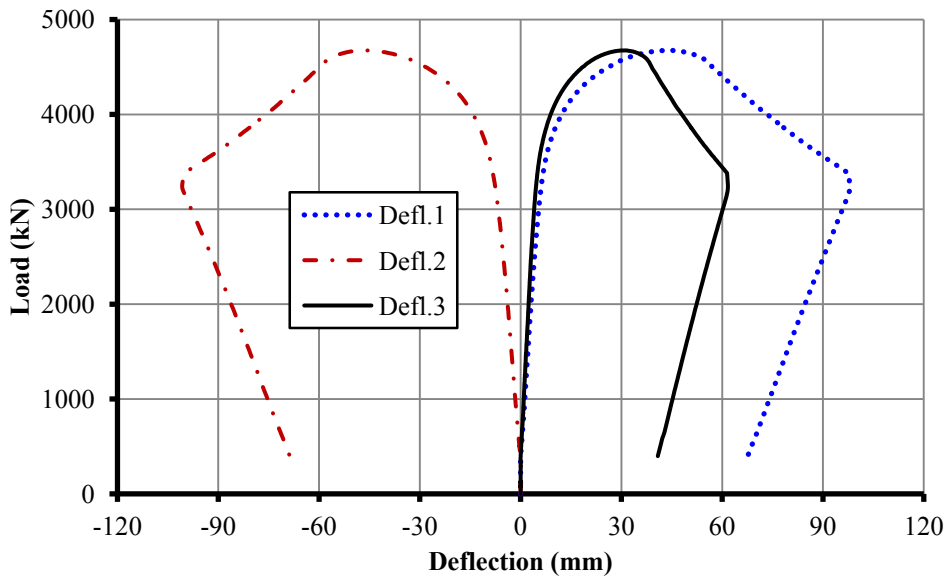


Figure 6.11: Load-deflection curves for specimen CD-2

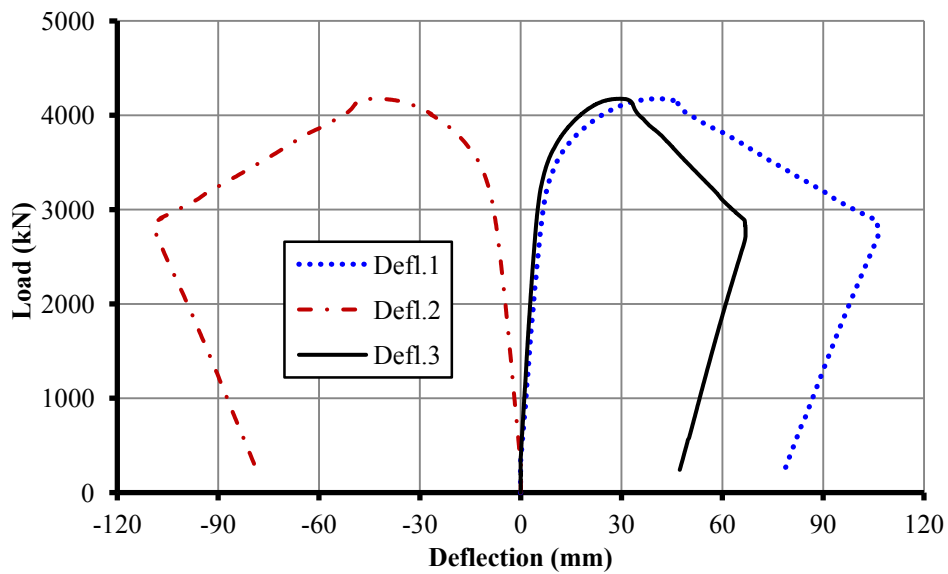


Figure 6.12: Load-deflection curves for specimen CDH-1

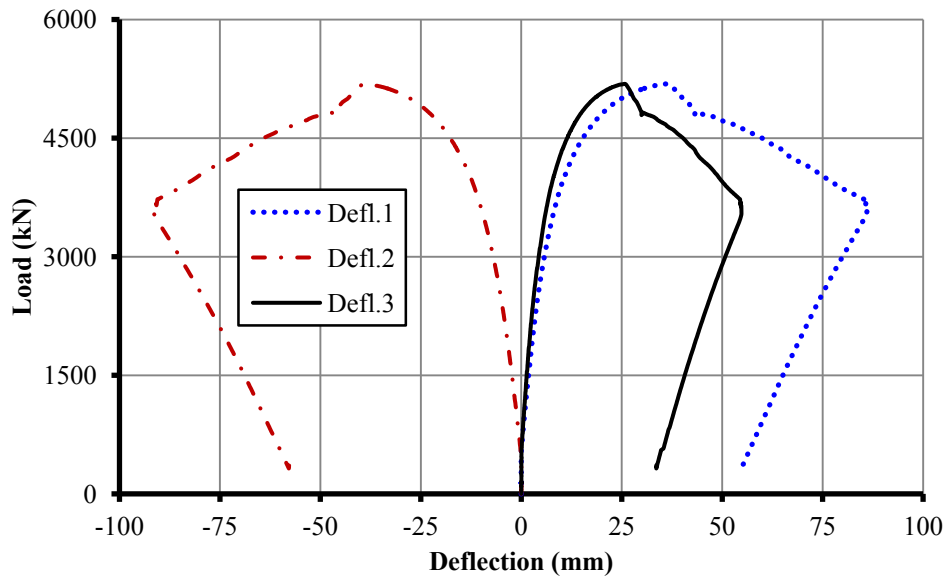


Figure 6.13: Load-deflection curves for specimen SS-1

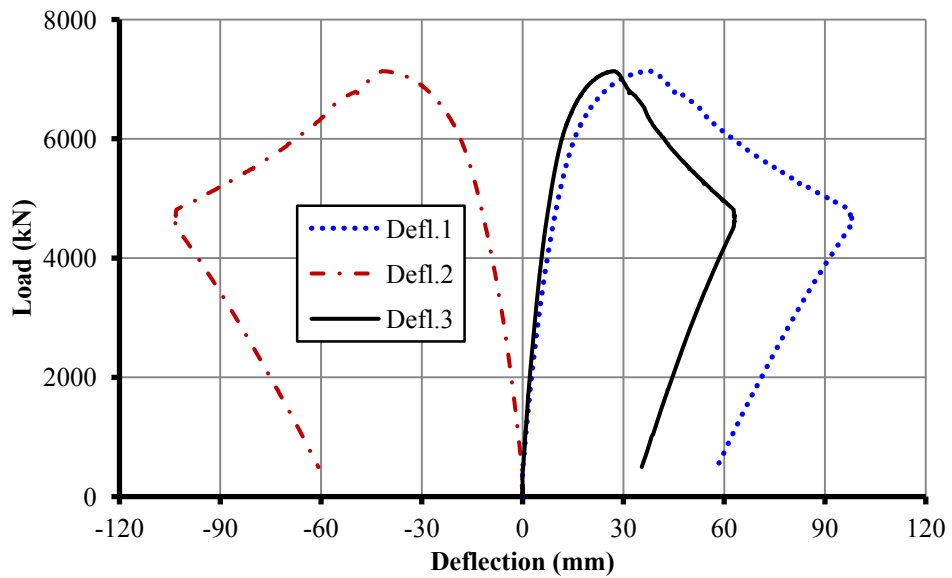


Figure 6.14: Load-deflection curves for specimen SS-2

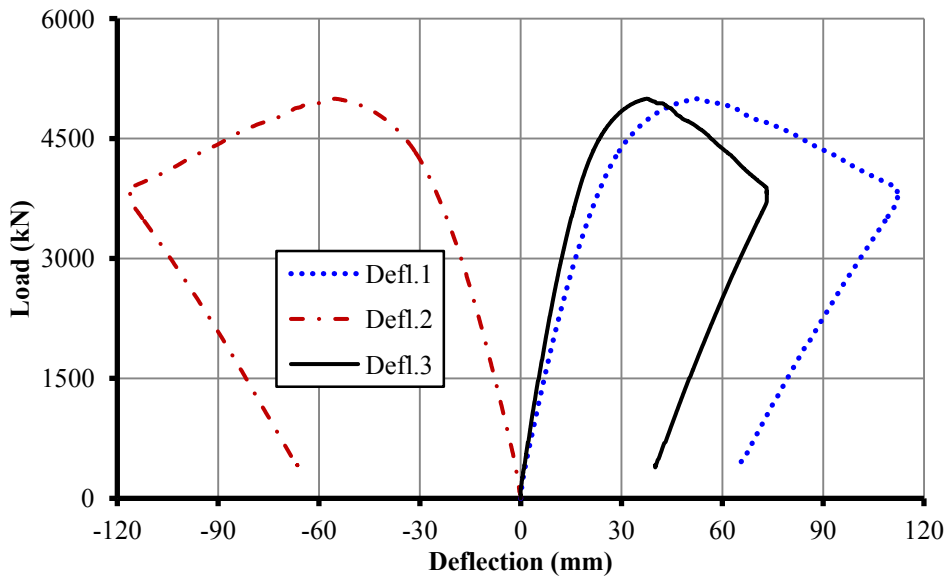


Figure 6.15: Load-deflection curves for specimen SS-3

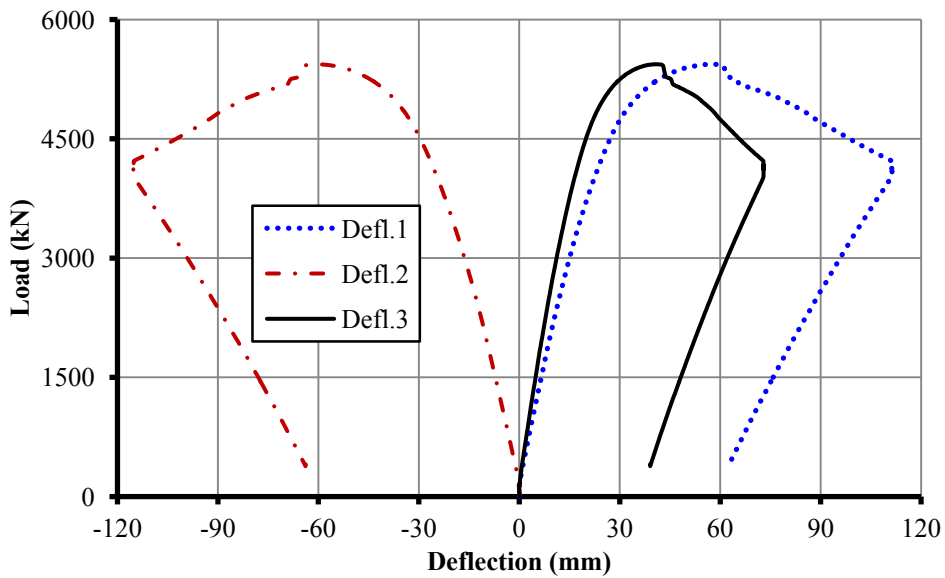


Figure 6.16: Load-deflection curves for specimen SD-1



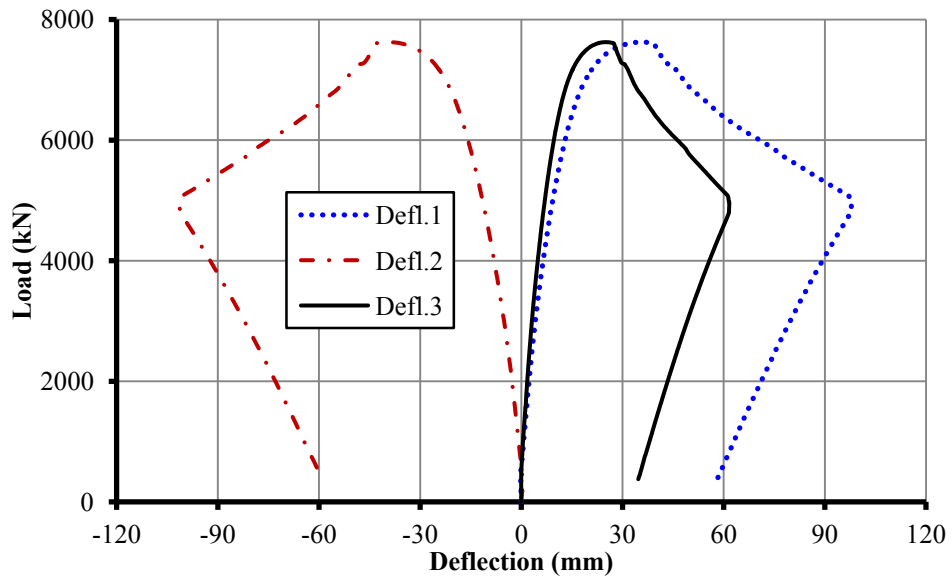


Figure 6.17: Load-deflection curves for specimen SDH-1

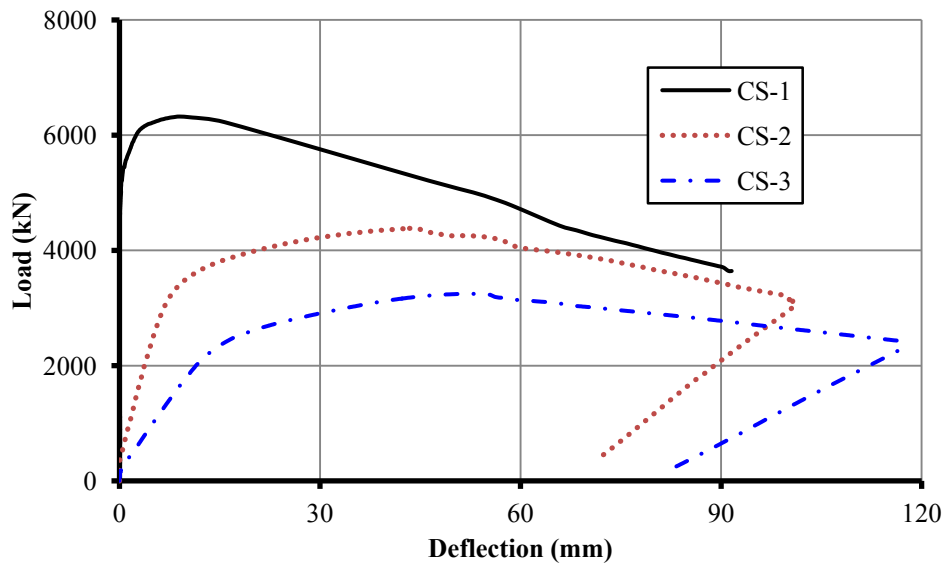


Figure 6.18: Comparison of load-deflection curves for CS-1, CS-2 and CS-3

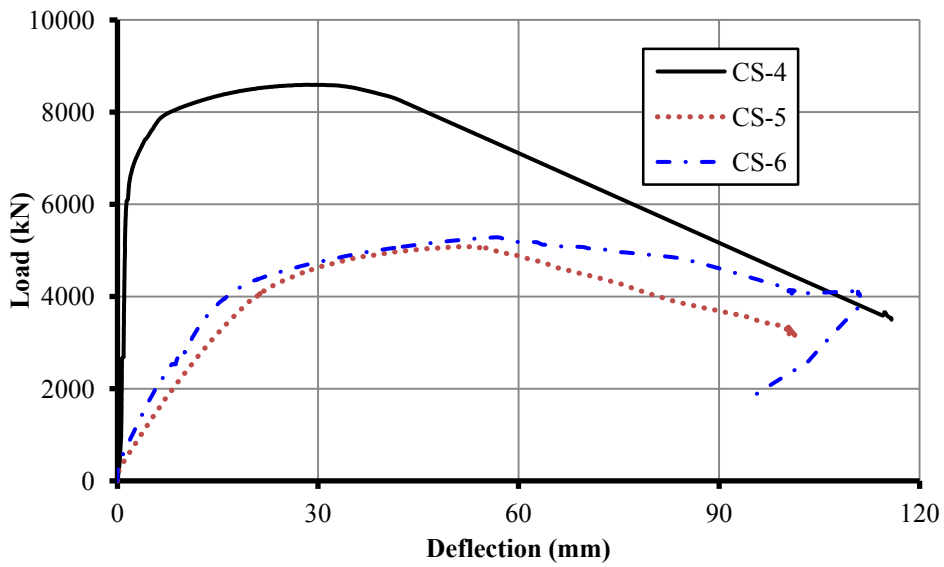


Figure 6.19: Comparison of load-deflection curves for CS-4, CS-5 and CS-6

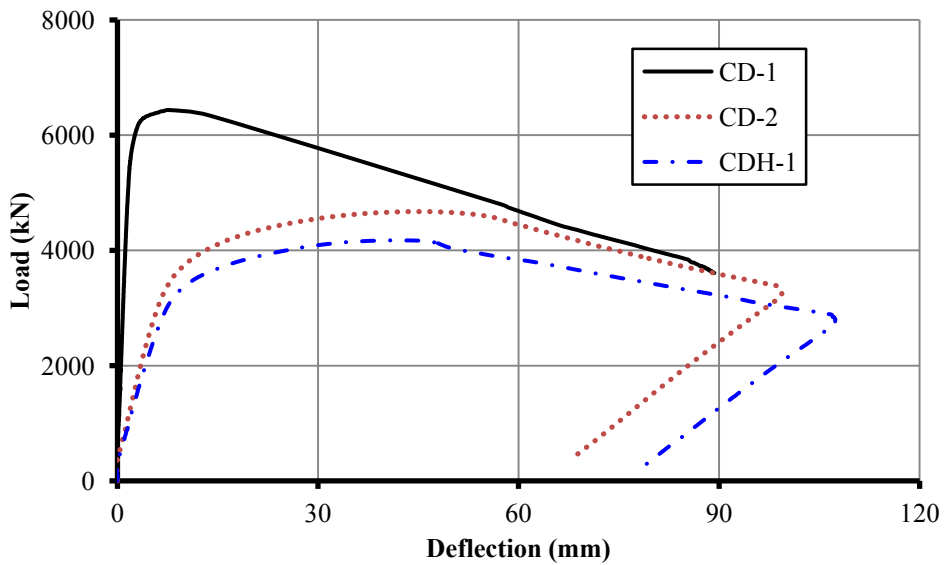


Figure 6.20: Comparison of load-deflection curves for CD-1, CD-2 and CDH-1

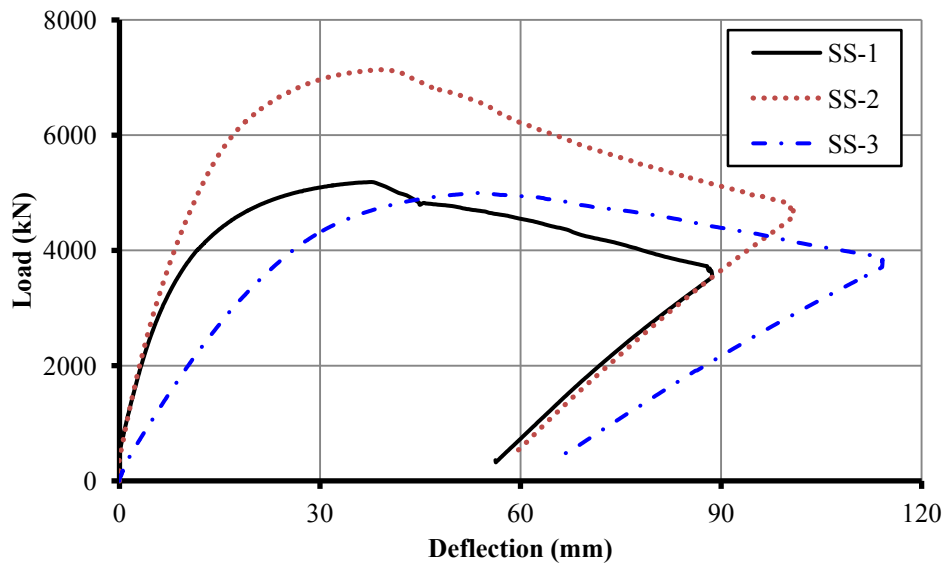


Figure 6.21: Comparison of load-deflection curves for SS-1, SS-2 and SS-3

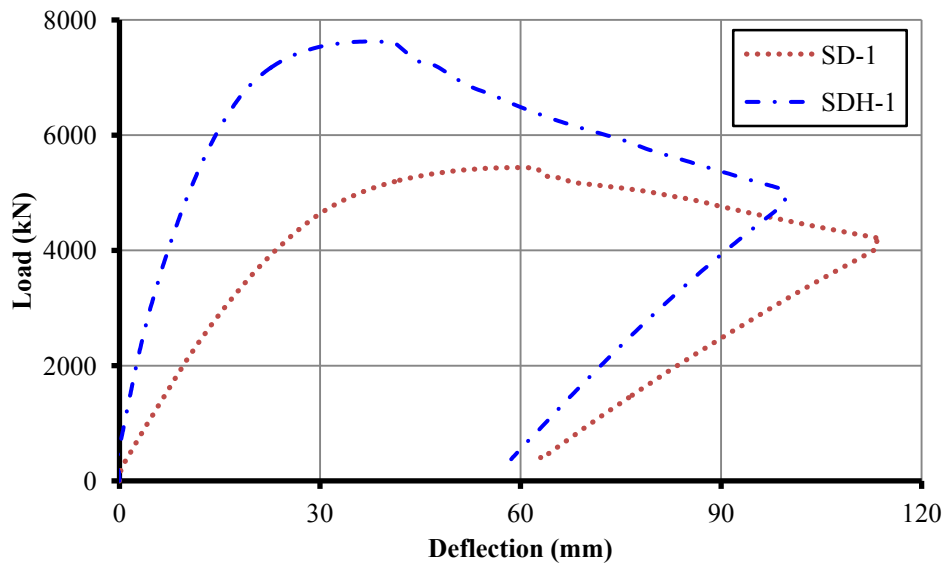


Figure 6.22: Comparison of load-deflection curves for SD-1 and SDH-1

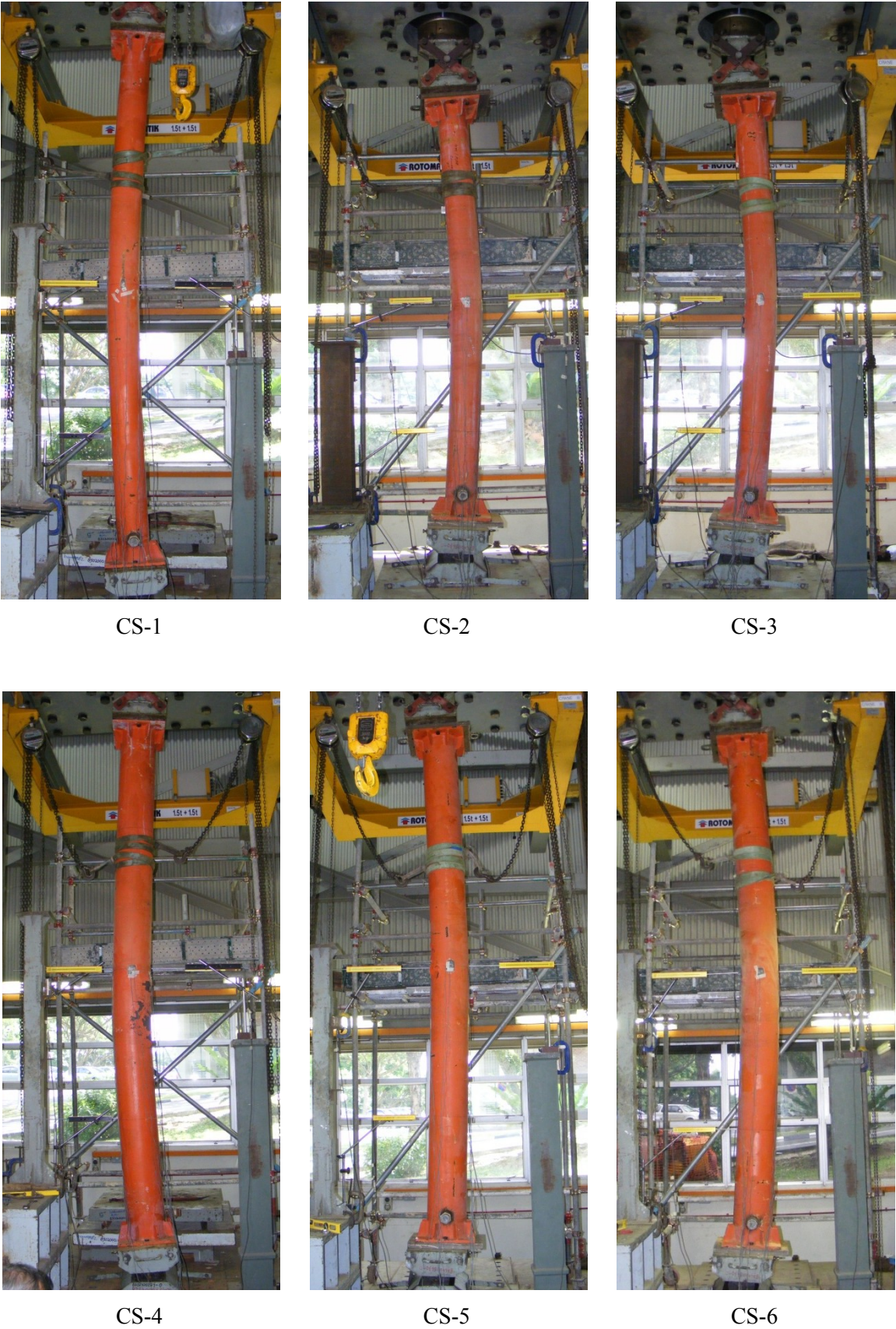


Figure 6.23: Failure modes of test specimens at the maximum deflections





CD-1



CD-2



CDH-1



SS-1



SS-2



SS-3

Figure 6.23: Failure modes of test specimens at the maximum deflections (cont'd)



SD-1



SDH-1

Figure 6.23: Failure modes of test specimens at the maximum deflections (cont'd)



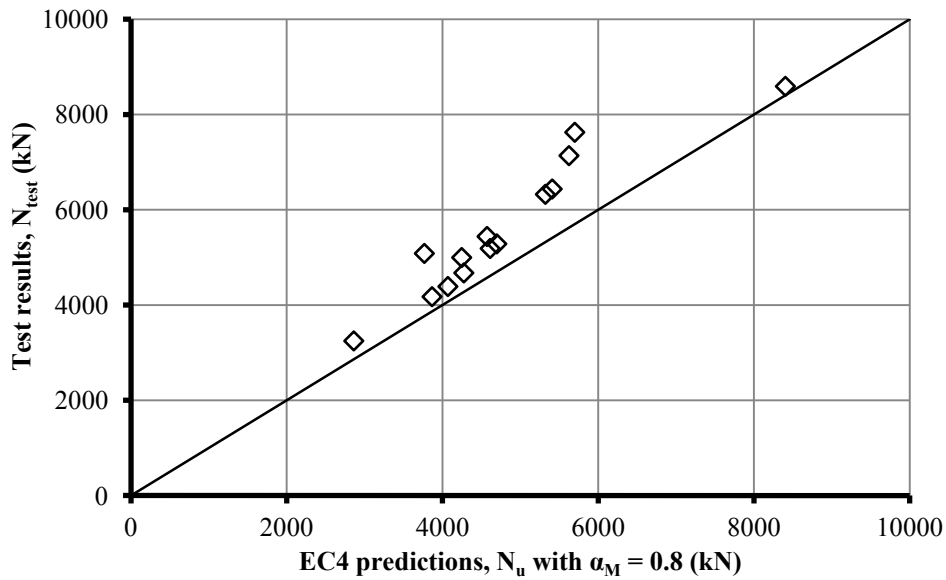


(a) CS-2

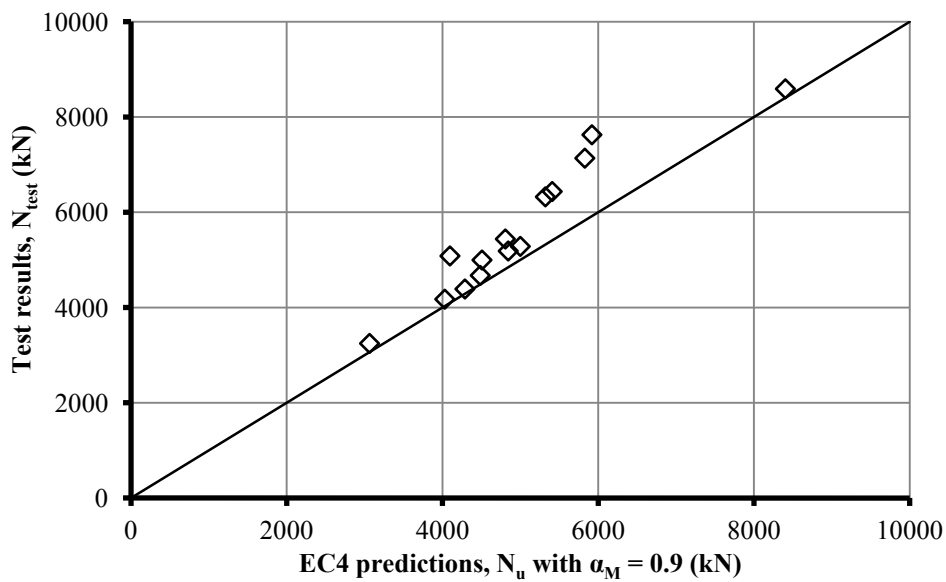


(b) SDH-1

Figure 6.24: Failure of *UHSC* infilling



(a)  $\alpha_M = 0.8$



(b)  $\alpha_M = 0.9$

Figure 6.25: Comparison of test results with Eurocode 4 predictions



## Chapter 7 Preload Effect on the axial compressive resistance of CFST columns

### 7.1 General

The structural behaviour of *CFST* members employing *UHSC* and *HSS* has been presented in previous three chapters, including stub columns under concentric compression, beams under pure bending, and slender beam-columns under concentric and eccentric compression. It has been found that ultra-high resistance can be achieved by using *UHSC* and *HSS* in *CFST* members. Therefore, they are most suitable for high-rise constructions. However, as stated in **Chapter 1**, there may be a problem of preload effect on *CFST* columns during the construction of multi-storey and high-rise structures, leading to significantly effect on the resistance of *CFST* columns.

A comprehensive investigation has been done, including analytical derivation of governing equations, experimental verifications and numerical analyses on the preload effect on the axial capacities of *CFST* columns. Theoretical analyses are conducted first and a design method is proposed based on a modified Eurocode 4 approach (2004) in which the terms and parameters used are consistent with the Eurocode 4 formulae for the design of composite columns. The proposed formulae are verified by experimental studies carried out at *National University of Singapore* on *CFST* columns with various preload ratios, material strengths and column lengths. In addition, some other published test data

are also used to validate the proposed design method. Numerical simulations are also performed for systematic verification. Finally, a step-by-step design procedure is given to illustrate application of the proposed method for the design of preloaded *CFST* columns.

## 7.2 Theoretical Analyses

In this section, the reduction factor for column overall buckling resistance is derived theoretically and compared with the approach adopted in Eurocode 4 (2004). Further modification is proposed to consider the preload effect on the overall buckling resistance of *CFST* columns.

### 7.2.1 Overall buckling resistance of steel columns

When a compressive axial force  $N$  acts on a steel column with initial out-of-straightness deflection  $\delta_0$  at the mid-height, the maximum total deflection  $\delta$  at the mid-height of the column can be approximated by (Chen & Atsuta, 1976):

$$\delta = \frac{\delta_0}{1 - \frac{N}{N_{a,cr}}} \quad (7.1)$$

where  $N_{a,cr} = \pi^2 E_a I_a / l_e^2$  is the Euler buckling load of steel column,  $E_a I_a$  is the flexural stiffness of the cross-section, and  $l_e$  is the effective column length. The maximum moment at the mid-height of the column is obtained as:

$$M = N\delta = N \frac{\delta_0}{1 - \frac{N}{N_{a,cr}}} \quad (7.2)$$

The maximum nominal stress is:

$$\sigma_{\max} = \frac{N}{A_a} + \frac{M}{S} = \frac{N}{A_a} \left[ 1 + \frac{\delta_0 y}{r^2} \frac{1}{1 - \frac{N}{N_{a,cr}}} \right] \quad (7.3)$$

where  $A_a$  is the cross-sectional area of steel column,  $S$  is the elastic section modulus,  $y$  is the maximum distance from the neutral axis to the outer edge of the section,  $r$  is the radius of gyration.

Assuming that the steel column reaches its ultimate resistance when the maximum stress reaches the yield strength  $f_y$ ,  $N$  reaches the overall buckling load  $N_{a,u}$ . From above equation, it follows:

$$N_{a,u} = \frac{f_y A_a}{1 + \frac{\delta_0 y}{r^2} \frac{1}{1 - \frac{N_{a,u}}{N_{a,cr}}}} \quad (7.4)$$

The slenderness reduction factor  $\chi'$  for overall buckling resistance can be derived as:

$$\chi' = \frac{N_{a,u}}{N_{a,pl,Rk}} = \frac{1}{\left[ \left( \frac{1 + \rho + \lambda_a^2}{2} \right) + \sqrt{\left( \frac{1 + \rho + \lambda_a^2}{2} \right)^2 - \lambda_a^2} \right]} = \frac{1}{\varphi' + \sqrt{\varphi'^2 - \lambda_a^2}} \quad (7.5)$$

where  $N_{a,pl,Rk} = f_y A_a$  is the characteristic compressive plastic resistance of the cross-section;  $\rho = \delta_0 y / r^2$ ,  $\varphi' = 0.5(1 + \rho + \lambda_a^2)$ , and  $\lambda_a$  is the relative slenderness given by:

$$\lambda_a = \sqrt{\frac{N_{a,pl,Rk}}{N_{a,cr}}} \quad (7.6)$$

### 7.2.2 Comparison with Eurocode 4 approach

The simplified method of design for composite columns in Eurocode 4 (2004) has been introduced in **Chapter 2**. Comparing Equation (7.5) with Equation (2.14), these equations are identical as long as:

$$\rho = \alpha(\lambda - 0.2) \quad (7.7)$$

### 7.2.3 Preload effect

Equation (7.7) shows that the reduction factor proposed by Equation (7.5) is consistent with that recommended in Eurocode 4 if a proper value for initial deflection is adopted. Herein, the approach to derive Equation (7.5) is further modified to consider the preload effect. When a preload  $N_{pre}$  acts on the steel tube, the maximum deflection  $\delta_1$  at the mid-height of the column is given by:

$$\delta_1 = \frac{\delta_0}{1 - \frac{N_{pre}}{N_{a,cr}}} \quad (7.8)$$

Above equation gives the initial deflection of a preloaded column before composite action is achieved. After the infilled concrete has gained sufficient strength,  $\delta_1$  can be treated as the initial out-of-straightness deflection of the composite column just like  $\delta_0$  while an equivalent Euler buckling load ( $N_{cr} - N_{pre}$ ) should be used for considering the action of existing preload. When a superimposed load  $N_{add}$  is applied to the composite column with initial deflection  $\delta_1$ , the maximum total deflection  $\delta_2$  at the mid-height of the composite column can be approximated as:

$$\delta_2 = \frac{\delta_1}{1 - \frac{N_{add}}{N_{cr} - N_{pre}}} = \frac{1 - N_{pre} / N_{cr}}{1 - N_{pre} / N_{a,cr}} \frac{\delta_0}{1 - \frac{N_{pre} + N_{add}}{N_{cr}}} \quad (7.9)$$

The term  $(1-N_{pre}/N_{cr})/(1-N_{pre}/N_{a,cr})$  in above equation is an amplification factor representing the preload influence on the initial deflection  $\delta_0$ . Since the axial compressive resistance of a practical column is normally smaller than its Euler buckling load, calibration with experimental and numerical results (to be presented in following sections) show that the Euler buckling load in the amplification factor should be replaced by the axial overall buckling load in order to capture the preload influence more accurately as:

$$\xi_{pre} = \frac{1 - N_{pre} / N_u}{1 - N_{pre} / N_{a,u}} \geq 1.0 \quad (7.10)$$

where  $\xi_{pre}$  is the preload influence factor,  $N_u$  is the overall buckling resistance of composite column without preload effect, and  $N_{a,u}$  is the overall buckling resistance of steel column.

Following the same procedure to derive Equation (7.5) and considering the preload effect with amplified initial deflection  $\xi_{pre}\delta_0$ , the slenderness reduction factor  $\chi_{pre}$  is obtained as:

$$\chi_{pre} = \frac{N_{pre,u}}{N_{pl,Rk}} = \frac{1}{\varphi_{pre} + \sqrt{\varphi_{pre}^2 - \lambda^2}} \quad (7.11)$$

where:

$$\varphi_{pre} = 0.5[1 + \alpha(\xi_{pre}\lambda - 0.2) + \lambda^2] \quad (7.12)$$

Equation (7.11) considers the fact that preload has no significant effect on stub column (i.e.  $\xi_{pre}\lambda \leq 0.2$ ). When there is no preload, i.e.,  $N_{pre} = 0$  and  $\xi_{pre} = 1$ , Equation (7.11) and Equation (7.12) are the same as those formulae recommended in Eurocode 4. However, when  $N_{pre} > 0$  and  $\xi_{pre} > 1$ , the value predicted by Equation (7.11) is smaller than that calculated from Equation (2.14) in accordance with Eurocode 4, which means that the ultimate compressive resistance is reduced due to preload effect.

#### 7.2.4 Parametric studies

Figure 7.1 shows an example of a *CFST* column comprising a square steel tube of cross-section  $600\text{mm} \times 14\text{mm}$  ( $b \times t$ ) with yield strength  $f_y = 355\text{MPa}$  and infilled concrete with cylinder strength  $f_{ck} = 40\text{MPa}$ . The design buckling curves with different values of preload ratio are compared with the Euler buckling curve and the design buckling curves “a” and “d” as defined in Eurocode 4. The preload ratio is defined as:

$$\beta_a = N_{\text{pre}} / N_{a,u} < 1.0 \quad (7.13)$$

It can be observed from Figure 7.1 that the overall buckling resistance reduces when the preload ratio increases. The reduction becomes less significant when the column relative slenderness increases beyond 2.0. For most practical applications, the preload ratio does not exceed 0.8, and then all the design buckling curves are above the curve “d” as defined in Eurocode 4. Therefore, it is conservative to adopt buckling curve “d” to design preloaded composite columns with preload ratio up to 0.8.

For non-preloaded *CFST* columns, the characteristic axial ultimate resistance is:

$$N_u = \chi N_{pl,Rk} \quad (7.14)$$

For preloaded *CFST* columns, the characteristic axial ultimate resistance is:

$$N_{pre,u} = \chi_{pre} N_{pl,Rk} \quad (7.15)$$

The preload reduction factor  $\eta_{pre}$  is defined as:

$$\eta_{\text{pre}} = \frac{N_{\text{pre,u}}}{N_{\text{u}}} = \frac{\chi_{\text{pre}}}{\chi} \leq 1.0 \quad (7.16)$$

Figure 7.2 shows the preload reduction factor curves for the composite column shown in Figure 7.1. The preload effect has little influence on stub columns (less than 5%), and it can be neglected if relative slenderness  $\xi_{\text{pre}}\lambda \leq 0.2$  or preload ratio  $\beta_{\text{a}} \leq 0.2$ . However, it has significant influence on intermediate and slender columns, and the strength reduction may exceed 15% if the preload ratio is more than 0.6.

The design value of overall buckling resistance  $N_{\text{pre,u,d}}$  with preload effect and the design plastic resistance of composite cross-section to compression  $N_{\text{pl,Rd}}$  should satisfy:

$$N_{\text{pre,u,d}} = \chi_{\text{pre}} N_{\text{pl,Rd}} > \text{design value of } (N_{\text{pre}} + N_{\text{add}}) \quad (7.17)$$

### 7.3 Verifications

A series of tests have been carried out by Jeyaraman (2003). The specimen details are shown in Table 7.1 and the test results are shown in Table 7.2, compared with the predictions.  $N_{\text{test}}$  and  $N_{\text{pre,u}}$  are respectively the test results and predictions. Compared with the test results, the predictions are mostly conservative except for CFT-S-100-30P which is overestimated by 12% and for CFT-I-30-40P which is overestimated by 3%. The mean value of  $N_{\text{pre,u}}/N_{\text{test}}$  is 0.924 and the standard deviation value is 0.092. The comparisons of predictions with the test results are also shown in Figure 7.3.

In addition, the proposed formulae are verified with the available test results from Zha (1996). The reported concrete strengths in the tests were cube strengths and hence they

are converted to cylinder strength for use in the calculation. Eight circular specimens were tested, and the test results are compared with the predictions as shown in Table 7.3 and Figure 7.4. The ratio of  $N_{pre,u}/N_{test}$  ranges from 0.863 to 1.192 with a mean value of 1.014 and a standard deviation value of 0.096.

Furthermore, the proposed formulae are verified with another available test results from Han and Yao (2003). Six square composite column specimens were tested and the comparison of results is shown in Table 7.4 and Figure 7.4. Specimens HS1-2 and HS2-2 were stub columns ( $\lambda \approx 0.1$ ), so the preload has no influence on ultimate resistance. The predictions agree very well with the experimental results with errors less than 5%. The ratio of  $N_{pre,u}/N_{test}$  ranges from 0.954 to 1.004 with a mean value of 0.988 and a standard deviation value of 0.017.

Considering all the test results shown in Table 7.2, Table 7.3 and Table 7.4, the mean value of  $N_{pre,u}/N_{test}$  is 0.968, and the standard deviation is 0.089. Therefore, the proposed design method can provide conservative and reliable predictions with preload effect.

## 7.4 Finite Element Analysis (FEA)

Finite element analysis is carried out to provide numerical results for preloaded columns to further verify the proposed design method and parametric study.

### 7.4.1 Numerical modelling and calibration with test results

The general purpose finite element package ABAQUS is adopted for the numerical simulation. The continuum solid element C3D8R, conventional shell element S4R and



continuum shell element SC8R are used to mesh the concrete core, square steel tube and circular steel tube, respectively. The material constitutive model is the conventional elastic-plastic model for steel tube while damaged plasticity model is used for concrete. The uniaxial stress-strain relationship curves adopted for concrete and steel are respectively shown in Figure 7.5 and Figure 7.6. Typical finite element meshes for the concrete core and square steel tube are shown in Figure 7.7. Only a half length ( $l_e/2$ ) of the composite column, fixed at the bottom and free at the top, is modeled. Geometrical imperfection in the form of half-sine curve with maximum initial deflection of  $\delta_0 = l_e/1000$  at the top is considered.

It is recognized that potential relative slip at the interface between the steel tube and concrete core could have some effect on the serviceability response of the columns. The bond/contact between the steel and concrete is important in analyzing local buckling failure of the steel tube. However, the present investigation focuses only on composite columns with non-slender cross section; hence the assumption of perfect bond between steel and concrete is adopted. The relative slip is limited by the fact that the column bottom end is restrained from displacement and the steel tube does not buckle locally due to its low  $d/t$  ratio. Hence the perfect bond assumption is not expected to have significant influence on the ultimate resistance prediction.

The loading process is divided into two steps: (1) the preload is firstly applied on top of the steel tube, and (2) the concrete core is added into the model and vertical displacement of the column top is applied and then the vertical reaction at the column bottom reveals the total axial load applied on the column.

To verify the accuracy of the FE model, the test specimens shown in Table 7.1 are analyzed. The numerical results obtained from the analyses are compared with the test results shown in Table 7.2. The average value of ratio  $N_{FE}/N_{test}$  is 0.967 and the standard deviation value is 0.109. Therefore, the numerical analyses provide conservative and reliable estimations, compared with the test results. The numerical results are also compared with the predictions, and the predictions are mostly conservative except in two cases which are overestimated by about 2%. The mean value of  $N_{pre,u}/N_{FE}$  is 0.958 and the standard deviation value is 0.049. Therefore, conservative and reliable predictions can be provided by the proposed formulae with preload effect.

#### 7.4.2 Numerical parametric analysis

Three groups of square cross-sectional specimens with different lengths are analyzed by considering various preload ratio values. The square cross-sectional dimension of steel tube is 600mm×14mm ( $b \times t$ ). The concrete strength is  $f_{ck} = 40\text{MPa}$ , and the steel yield strength is  $f_y = 355\text{MPa}$ . Non-dimensional column slenderness ratios of  $\lambda = 0.24, 0.59$  and 1.20 were chosen to represent a typical short, intermediate and long column.

The load-vertical displacement curves with different preload ratio values are shown in Figure 7.8. The initial axial stiffness of the load displacement curve is contributed by the steel tube alone and the composite action comes in after the load is applied to the concrete. Parametric analyses show that the preload effect has little influence on short columns. However, preload seems to have more pronounce effect on axial capacity of intermediate and slender columns. A reduction of more than 20% in axial compressive resistance is expected if the preload is high ( $\beta_a > 0.6$ ) as shown in Figure 7.8.

The values of ultimate resistance from the numerical simulation are shown in Table 7.5 and Figure 7.9, compared with predictions. According to Eurocode 4, the predicted axial resistance without preload is respectively 24541kN, 22108kN and 13063kN for the specimens in group FS, FI and FL, the same as that calculated from the proposed formulae by assuming preload ratio  $\beta_a = 0$ .

From Table 7.5 and Figure 7.9, it can be observed that the predictions are conservative in comparison with the FEM results with errors less than 20%. The mean value of  $N_{pre,u}/N_{FE}$  is 0.921 and the standard deviation value is 0.055. Therefore, the proposed method can be conveniently used for the design of preloaded *CFST* composite columns in lieu of the direct analysis method.

## 7.5 A Step-by-Step Design Procedure

The proposed modifications to Eurocode 4 equations for incorporating the preload effect are summarized in Table 7.6.

Following is a step-by-step procedure for the design of axially loaded *CFST* composite columns with preload effect:

- (1) Determine the preload  $N_{pre}$  according to the practical construction sequence and referring to relative codes for actions (EC 1, for example);
- (2) Determine  $\chi_a$  and check the resistance of steel tube subjected to the preload by
$$N_{pre} \leq \chi_a N_{a,pl,Rk};$$
- (3) Determine  $\chi$  by the formulae recommended in Eurocode 4;

- (4) Calculate the preload effect factor  $\xi_{pre}$  by Equation (7.10);
- (5) Calculate the slenderness reduction factor  $\chi_{pre}$  by Equation (7.11);
- (6) Determine the total design load acting on the composite column ( $N_{pre}+N_{add}$ ), calculate the design overall buckling resistance  $N_{pre,u,d}$  by Equation (7.17), and then check whether  $N_{pre,u,d} > (N_{pre}+N_{add})$ .

## 7.6 Summary

In this chapter, a design method based on modified Eurocode 4 approach has been developed to evaluate the axial compressive resistance of *CFST* composite columns considering the preload effect. The accuracy of the proposed method is verified with test results of 25 column specimens and numerical results obtained from finite element analyses.

The preload effect can be quantified by a non-dimensional preload effect factor  $\xi_{pre}$  which is related to preload ratio  $\beta_a$ , non-dimensional column slenderness ratio  $\lambda$ , material strengths and steel contribution ratio. Parametric analyses show that the preload effect has little influence on stub columns, and the effect can be neglected if the amplified relative column slenderness ( $\xi_{pre} \lambda$ ) is less than 0.2 or the preload ratio  $\beta_a$  is less than 0.2. However, preload is expected to have significant influence on the axial compressive resistance of intermediate and slender columns. A reduction of more than 20% in axial resistance is expected if the preload is high ( $\beta_a > 0.6$ ).

A modified EC4 method and a step-by-step design procedure are recommended for the design of preloaded *CFST* composite columns.

For *CFST* columns with slender cross-sections, the preload effect may have more pronounced effect on its compression resistance because local buckling of steel tube may occur under the preload. For this case, further investigation should be done.

Table 7.1: Test specimen details

Series	Specimens	$l_e$ mm	Circular Steel tube		$f_y$ MPa	$f_{ck}$ MPa	Preload ratio $\beta_a$
			d (mm)	t (mm)			
CS	CFT-S-40-30P	708	219	6.3	300	37	0.252
	CFT-S-100-0P	708	219	6.3	300	108	0
	CFT-S-100-30P	708	219	6.3	300	107	0.250
CI	CFT-I-40-30P	1728	219	6.3	405	44	0.299
	CFT-I-100-0P	1728	219	6.3	405	99	0
	CFT-I-100-30P	1728	219	6.3	405	113	0.305
	CFT-I-130-40P	1728	219	6.3	405	139	0.380
CL	CFT-L-40-30P	3078	219	6.3	393	49	0.306
	CFT-L-100-0P	3078	219	6.3	393	100	0
	CFT-L-100-30P	3078	219	6.3	393	111	0.310
	CFT-L-130-40P	3078	219	6.3	393	125	0.399

Table 7.2: Comparison of predictions compared with test and FEA results

Specimens	$N_{test}$ (kN)	$N_{pre,u}$ (kN)	$N_{FE}$ (kN)	$N_{pre,u}/N_{test}$	$N_{FE}/N_{test}$	$N_{pre,u}/N_{FE}$
CFT-S-40-30P	3677	3050	3502	0.829	0.952	0.871
CFT-S-100-0P	5410	5280	5692	0.976	1.052	0.928
CFT-S-100-30P	4667	5218	5661	1.118	1.213	0.922
CFT-I-40-30P	3648	3033	3378	0.831	0.926	0.898
CFT-I-100-0P	4977	4708	4853	0.946	0.975	0.970
CFT-I-100-30P	5278	4952	5078	0.938	0.962	0.975
CFT-I-130-40P	5437	5571	5700	1.025	1.048	0.977
CFT-L-40-30P	3160	2731	2868	0.864	0.908	0.952
CFT-L-100-0P	4204	3964	3987	0.943	0.948	0.994
CFT-L-100-30P	4580	3924	3843	0.857	0.839	1.021
CFT-L-130-40P	4827	4032	3937	0.835	0.816	1.024
Mean value				0.924	0.967	0.958
Standard deviation				0.092	0.109	0.049

Table 7.3: Comparison of predictions with test results from Zha (1996)

Specimen	Dimension ( $d \times t \times l_e$ ) mm	Preload ratio $\beta_a$	$f_{ck,cube}$ MPa	$f_y$ MPa	$N_{test}$ kN	$N_{pre,u}$ kN	$N_{pre,u}/N_{test}$
ZI1-1	133×4.5×1862	0	42.2	325	895	891	0.995
ZI1-2	133×4.5×1862	0	42.2	325	872	891	1.021
ZI2	133×4.5×1862	0.305	42.2	325	882	868	0.985
ZI3	133×4.5×1862	0.436	42.2	325	715	853	1.192
ZL1-1	133×4.5×2793	0	42.2	325	743	745	1.003
ZL1-2	133×4.5×2793	0	42.2	325	682	745	1.092
ZL2	133×4.5×2793	0.311	42.2	325	748	718	0.960
ZL3	133×4.5×2793	0.498	42.2	325	800	690	0.863
Mean							1.014
Standard Deviation							0.096

Table 7.4: Comparison of predictions with test results from Han and Yao (2003)

Specimen	Dimension ( $b \times t \times l_e$ ) mm	Preload ratio $\beta_a$	$f_{ck,cube}$ MPa	$f_y$ MPa	$N_{test}$ kN	$N_{pre,u}$ kN	$N_{pre,u}/N_{test}$
HS1-1	120×2.65×360	0	20.1	340	640	633	0.990
HS1-2	120×2.65×360	0.499	20.1	340	664	633	0.954
HS2-1	120×2.65×360	0	36.0	340	816	808	0.991
HS2-1	120×2.65×360	0.499	36.0	340	812	808	0.996
HI1-1	120×2.65×1400	0	36.0	340	769	764	0.994
HI1-2	120×2.65×1400	0.478	36.0	340	730	733	1.004
Mean							0.988
Standard Deviation							0.017

Table 7.5: Numerical results compared with predictions

No.	Dimension ( $b \times t \times l_e$ ) mm	Preload ratio $\beta_a$	$f_{ck}$ MPa	$f_y$ MPa	$N_{FE}$ kN	$N_{pre,u}$ kN	$N_{pre,u} / N_{FE}$
FS-0	600×14×3600	0	40	355	25355	24541	0.968
FS-2	600×14×3600	0.2	40	355	25277	24374	0.964
FS-4	600×14×3600	0.4	40	355	25225	24102	0.955
FS-6	600×14×3600	0.6	40	355	25191	23576	0.936
FS-8	600×14×3600	0.8	40	355	25174	22135	0.879
FI-0	600×14×9000	0	40	355	22705	22108	0.974
FI-2	600×14×9000	0.2	40	355	22007	21686	0.985
FI-4	600×14×9000	0.4	40	355	21295	21028	0.987
FI-6	600×14×9000	0.6	40	355	20627	19858	0.963
FI-8	600×14×9000	0.8	40	355	19994	17151	0.858
FL-0	600×14×18000	0	40	355	14589	13063	0.895
FL-2	600×14×18000	0.2	40	355	14383	12779	0.888
FL-4	600×14×18000	0.4	40	355	13958	12348	0.885
FL-6	600×14×18000	0.6	40	355	13296	11605	0.873
FL-8	600×14×18000	0.8	40	355	12348	9968	0.807
Mean value							0.921
Standard Deviation							0.055



Table 7.6: Proposed modifications to EC4 equations for incorporating preload

Strength	EC4 Approach	Proposed Method with preload $N_{pre}$
Characteristic plastic cross-sectional resistance	<p>1. Concrete filled circular tubes with <math>\lambda \leq 0.5</math>:</p> $N_{pl,Rk} = A_a \eta_a f_y + A_c f_{ck} \left(1 + \eta_c \frac{t}{d} \frac{f_y}{f_{ck}}\right) + A_s f_{sy}$ <p>2. Concrete filled circular tubes with <math>\lambda &gt; 0.5</math> and filled rectangular tubes:</p> $N_{pl,Rk} = A_a f_y + A_c f_{ck} + A_s f_{sy}$	
Design plastic cross-sectional resistance	<p>1. Concrete filled circular tubes with <math>\lambda \leq 0.5</math>:</p> $N_{pl,Rd} = A_a \eta_a f_{yd} + A_c f_{cd} \left(1 + \eta_c \frac{t}{d} \frac{f_y}{f_{ck}}\right) + A_s f_{sd}$ <p>2. Concrete filled circular tubes with <math>\lambda &gt; 0.5</math> and filled rectangular tubes:</p> $N_{pl,Rd} = A_a f_{yd} + A_c f_{cd} + A_s f_{sd}$	
Characteristic overall buckling resistance	$N_u = \chi N_{pl,Rk}$ <p>where <math>\chi = \frac{1}{\varphi + \sqrt{\varphi^2 - \lambda^2}} \leq 1.0</math></p> $\varphi = 0.5 \left[1 + \alpha(\lambda - 0.2) + \lambda^2\right]$ $\lambda = \sqrt{\frac{N_{pl,Rk}}{N_{cr}}}$ $N_{cr} = \frac{\pi^2 (EI)_{eff}}{l_e^2}$ $= \frac{\pi^2 (E_a I_a + 0.6 E_{cm} I_c + E_s I_s)}{l_e^2}$	$N_{pre,u} = \chi_{pre} N_{pl,Rk}$ <p>where <math>\chi_{pre} = \frac{1}{\varphi_{pre} + \sqrt{\varphi_{pre}^2 - \lambda^2}} \leq 1.0</math></p> $\varphi_{pre} = 0.5 \left[1 + \alpha(\xi_{pre} \lambda - 0.2) + \lambda^2\right]$ $\xi_{pre} = \frac{1 - N_{pre} / N_u}{1 - N_{pre} / N_{a,u}} \geq 1.0$ <p><math>N_{a,u}</math> is the characteristic overall buckling resistance of steel tube.</p>
Design overall buckling resistance	$N_{Ed} = \chi N_{pl,Rd}$	$N_{pre,u,d} = \chi_{pre} N_{pl,Rd}$

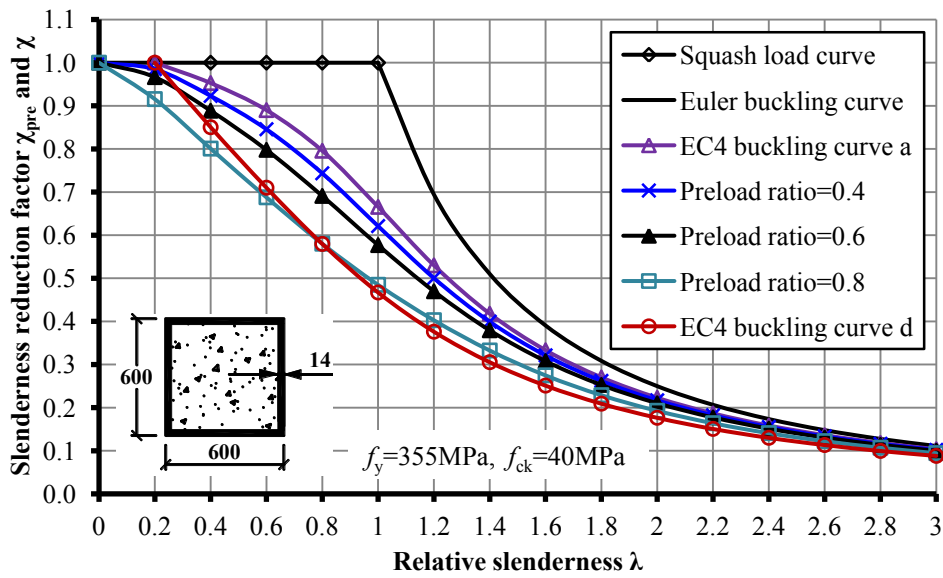


Figure 7.1: Design buckling curves of CFST columns with preload effect

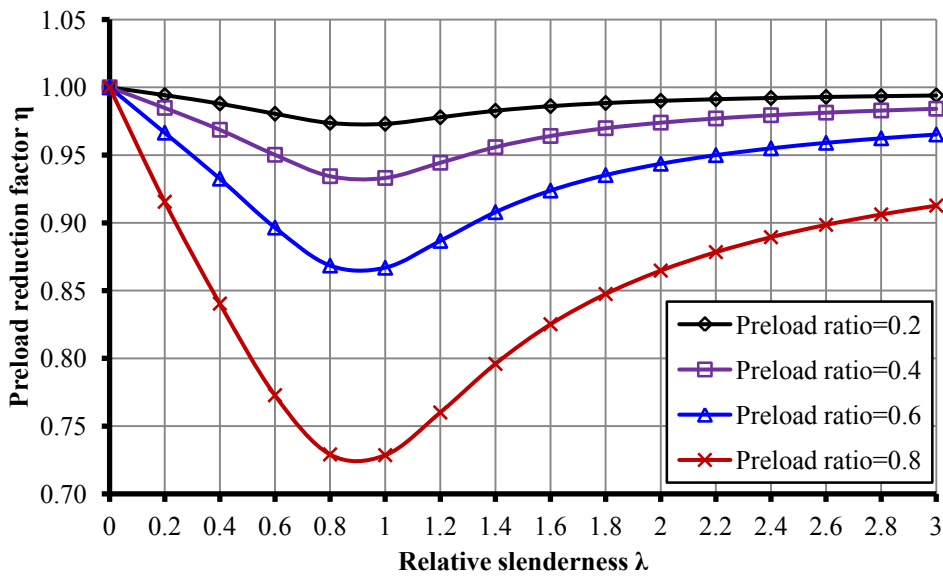


Figure 7.2: Preload reduction factor curves under different preload ratio values

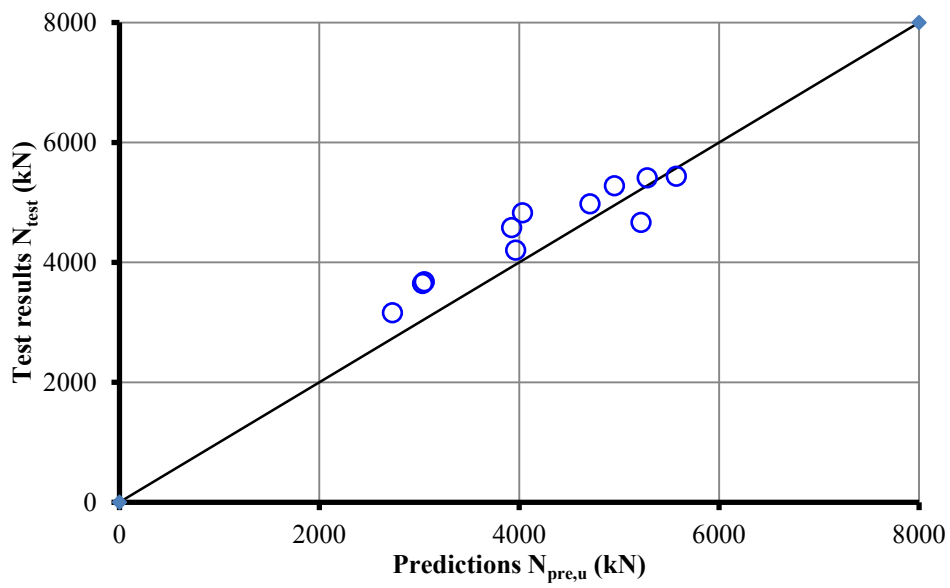


Figure 7.3: Verification of predictions with test results

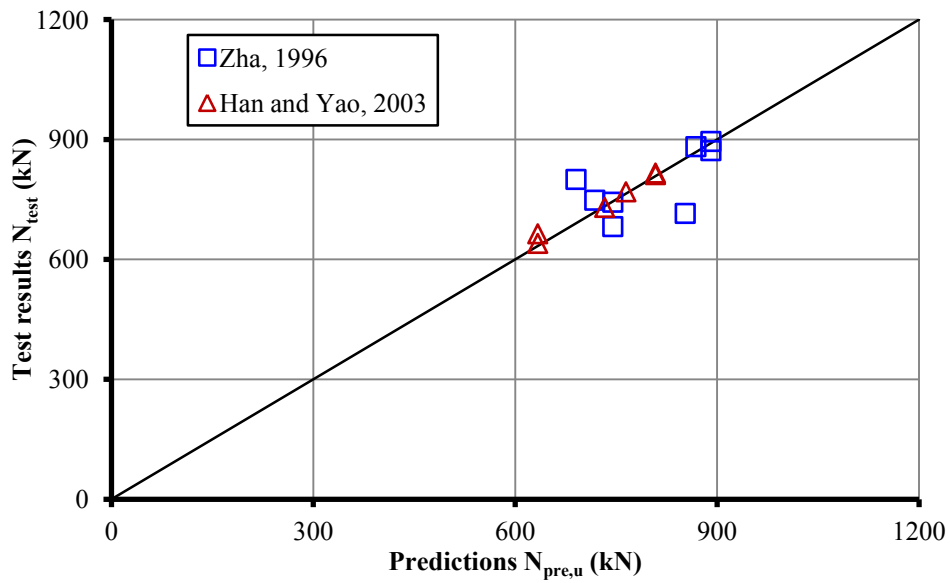


Figure 7.4: Verification of predictions with other published test results

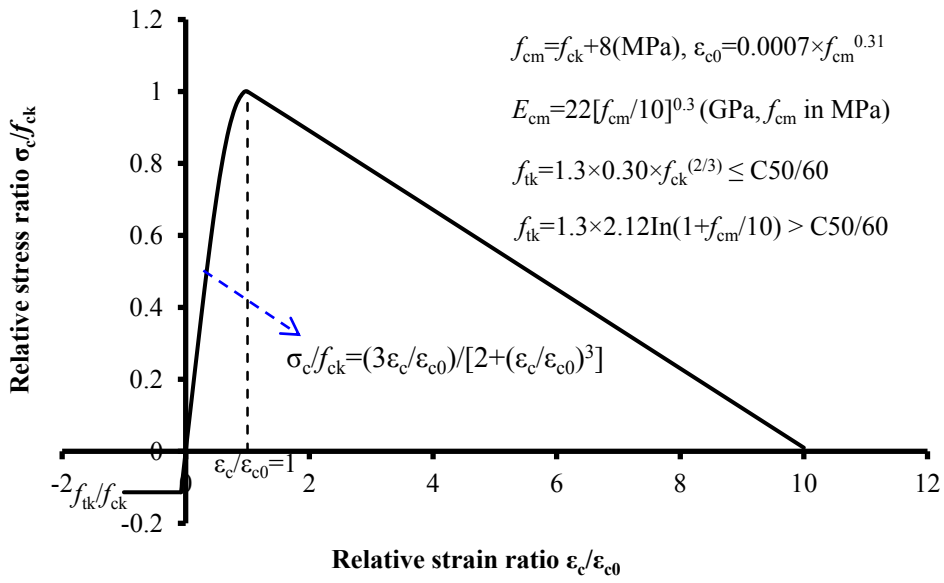


Figure 7.5: Uniaxial stress-strain relationship for concrete

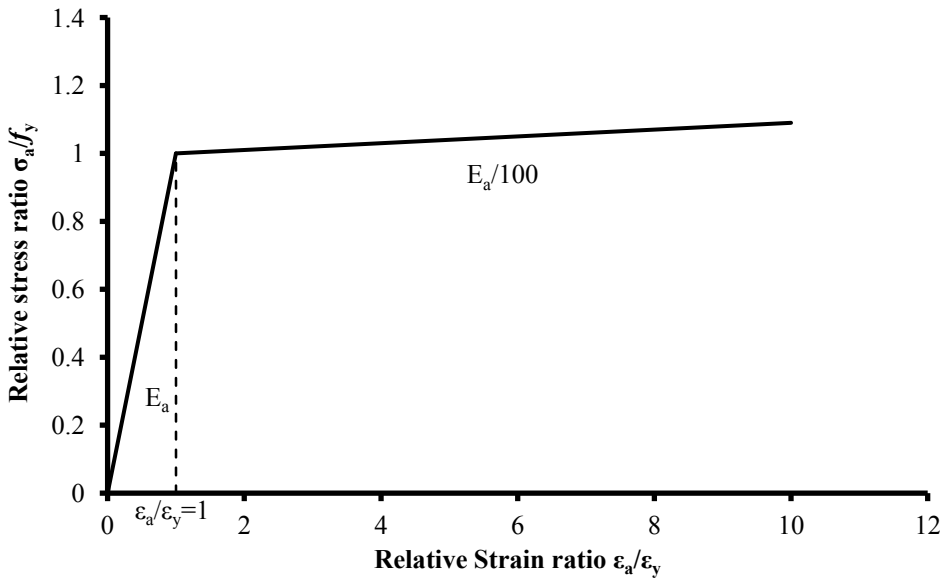


Figure 7.6: Uniaxial stress-strain relationship for steel

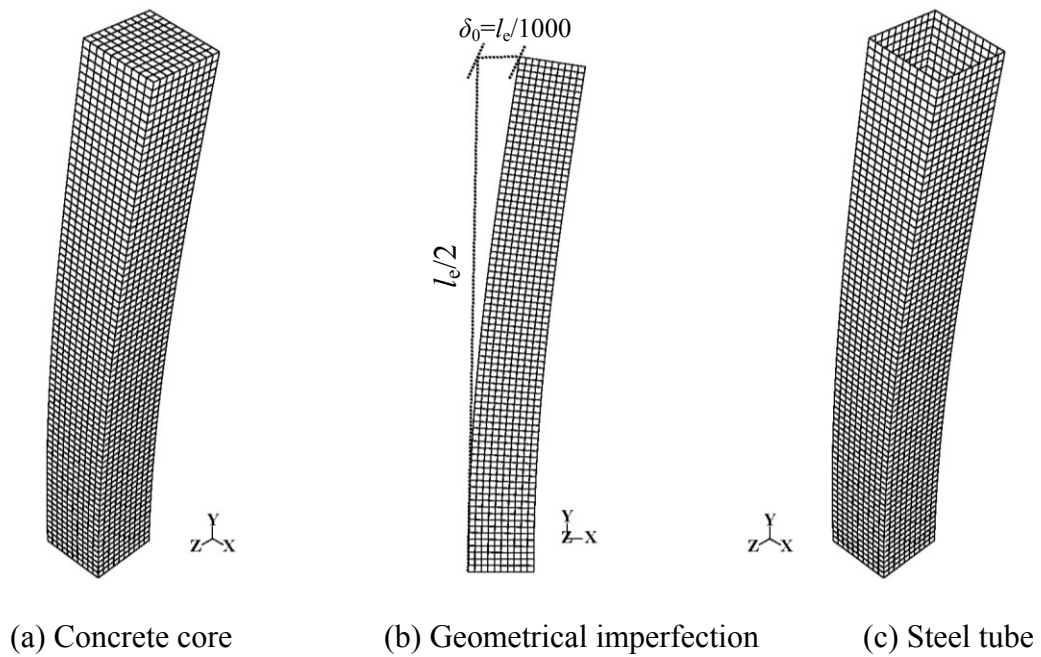


Figure 7.7: Geometrical models for steel tube and concrete core with imperfection

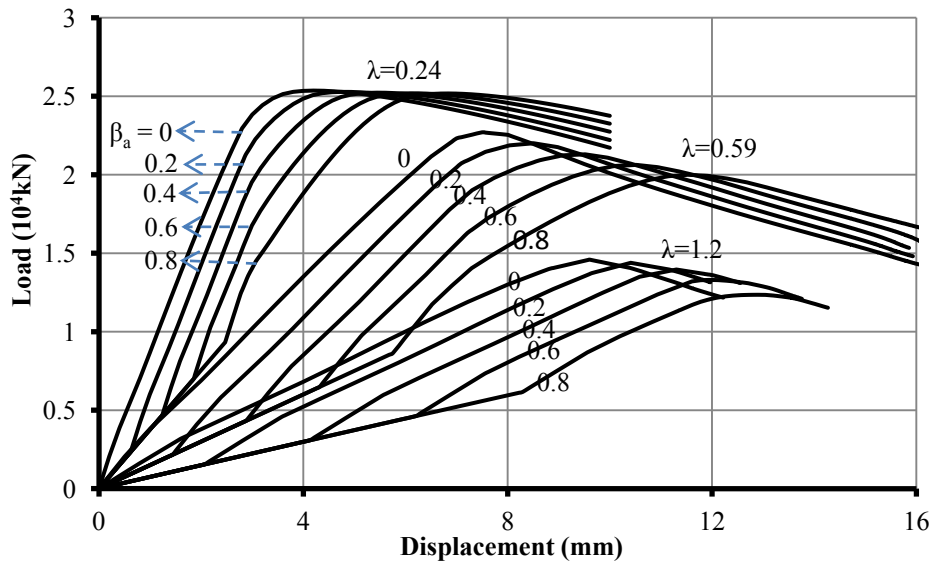


Figure 7.8: Load-displacement curves

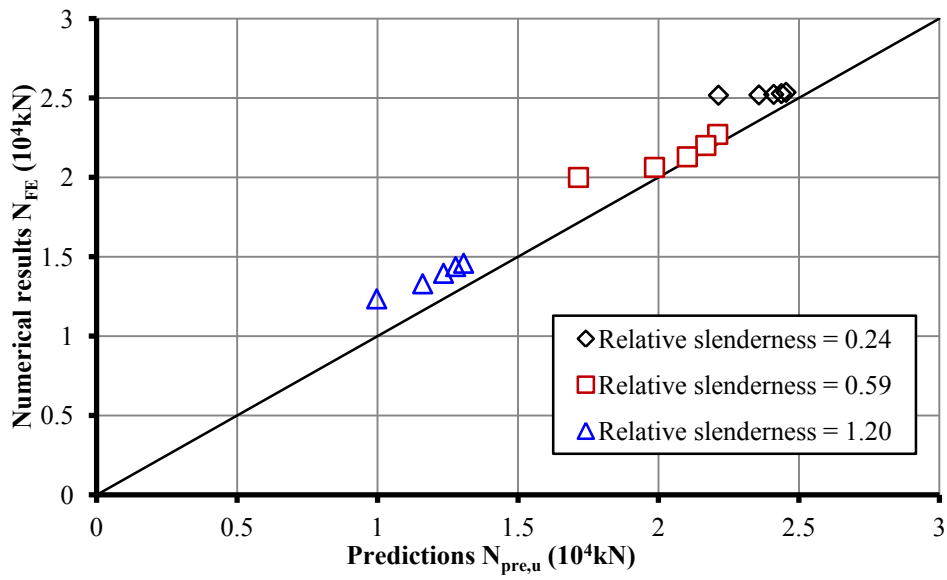


Figure 7.9: Comparison of numerical results with predictions

## Chapter 8 Conclusions

### 8.1 Conclusions

The main objective of this research was to investigate the structural behaviour of *CFST* members employing *UHSC* and *HSS*. Several series of experimental investigations were carried out on materials *UHSC* and *HSS* used in this study to examine the basic mechanical material properties, stub columns under concentric compression to assess the compressive resistance, beams under pure bending to assess the moment resistance, and slender beam-columns under concentric and eccentric compression to assess the overall buckling resistance under coupled compression and moment with second-order effect. For evaluation, the test results were compared with Eurocode 4 predictions. It is found that ultra-high resistance could be achieved by employing *UHSC* and *HSS* in *CFST* columns. Therefore, they are suitable to be applied in high-rise constructions. It is also found that Eurocode 4 limitations on materials can be extended to the *UHSC* and *HSS* materials with minor modifications. The current research has made a significant contribution to fill the gap on experimental research in *CFST* members with high strength materials as shown in Figure 8.1. Compared with Figure 1.4 and Figure 1.5 shown in **Chapter 1**, the percentage of test specimens with concrete compressive strength higher than 120MPa is increased from 1.18% to 4.46% and the percentage of test specimens with steel yield strength higher than 460MPa is increased from 7.49% to 8.42%, due to the contribution of current research. In addition, the preload effect on the overall buckling resistance of *CFST*

columns was investigated. It is found that the overall buckling compressive resistance of *CFST* columns can be reduced by more than 20% under high preload. These findings provide valuable guidelines for designers to adopt *UHSC* and *HSS* in *CFST* columns and for constructors to use fast-track construction method in *CFST* structures.

The basic mechanical material properties of *UHSC* with different mix proportion designs were firstly investigated at different curing ages as presented in **Chapter 3**. It was found the *UHSC* could achieve ultra high strength but it was very brittle under uniaxial compression. The workability is much better than *NSC*. The flow spread of fresh *UHSC* ranged from 41cm to 74cm. The 28-days compressive cylinder strength ranged from 145MPa to 177MPa, almost three times of the strength of *NSC* C50/60. The modulus of elasticity ranged from 54GPa to 62GPa, almost two times of the elastic modulus of *NSC* C50/60. High early strength of *UHSC* could be achieved. Compared with the compressive strength value at 28 days, 70% ~ 80% strength was achieved within the first 3 days and 80% ~ 90% strength was achieved within the first week. More importantly, ordinary coarse aggregates can be added to reduce the cost with slightly reduction in strength. To use 19% or 38% proportions of coarse aggregates, it only leads to a reduction of about 3.8% and 9.6% in compressive cube strength, 4.5% and 17.9% in compressive 100mm-cylinder strength. In addition, the basic mechanical material properties of *HSS* were investigated and compared with mild steel sections in **Chapter 4**, **Chapter 5** and **Chapter 6**. It was found that the yield strength of *HSS* was up to 779MPa which was almost twice as high as S355 steel, but it was less ductile with less elongation at failure and lower hardening effect. These material property results provide important information to understand the basic performance of *UHSC* and *HSS*, and they can be used to help predicting the behaviour of corresponding *CFST* columns.



**Chapter 4** presents the investigation the structural behaviour of stub *CFST* columns employing *UHSC* and *HSS* under concentric compression. It was found that ultra high compressive resistance could be achieved by employing *UHSC* and *HSS* in stub *CFST* columns. However, the ductility of *CFST* columns should be considered, due to the brittleness of *UHSC*. Based on the current investigations, it is recommended that at least 1.0% steel fiber should be added into *UHSC*, or the steel contribution ratio should be increased from 0.2 up to 0.3 when Eurocode 4 method is adopted. However, the confinement effect should be ignored for *CFST* columns with *UHSC* or Class 3 hollow steel sections. Furthermore, a reduction of 15% in compressive resistance should be considered for *UHSC* filled square *HSS* double-tube columns. With these recommendations, Eurocode 4 can be extended to the *UHSC* and *HSS* materials used in this study.

**Chapter 5** presents the investigation the flexural behaviour of *CFST* beams employing *UHSC* and *HSS* materials. It was found that the full plastic moment resistance could be achieved, provided that the brittle behaviour of *UHSC* was adequately confined by compact steel sections. The *CFST* beams with *UHSC* behaved in a ductile manner with gradual hardening at large deflections but without brittle or sudden failure as observed from stub column tests under pure compression. The full plastic moment resistance could be achieved and Eurocode 4 method provided conservative predictions of test results if the reduction coefficient  $\alpha_M$  was considered for different steel grades. Besides, no significant flexural stiffness degradation could be produced under service load. For *CFST* beams with *UHSC* and *HSS* under pure bending, it was found that the effective flexural stiffness at service load was only 80% of  $(EI)_{eff,II}$  as recommended in Eurocode 4 for beam-columns. Therefore,  $0.8(EI)_{eff,II}$  should be used to estimate the maximum deflection of

*CFST* beams under flexural load at service limit state. These findings extend the current scope of Eurocode 4 to *UHSC* and *HSS* materials to predict the moment resistance and deflection of *CFST* beams.

**Chapter 6** presents the investigation the structural behaviour of slender *CFST* beam-columns employing *UHSC* and *HSS* under concentric and eccentric compression. It was found that the behaviour of slender beam-columns was ductile with gradual load reduction from the peak load, without brittle or sudden failure as observed from stub column tests under pure compression. Compared to test results, Eurocode 4 method provided conservative prediction of the ultimate load if the reduction coefficient  $\alpha_M$  was considered. If  $\alpha_M = 1.0$  was adopted, the full plastic moment resistance could be used in the calculation and the predictions were closer to the test results. These findings extend the current scope of Eurocode 4 to *UHSC* and *HSS* materials to predict the overall buckling resistance of slender *CFST* beam-columns.

Lastly, in **Chapter 7**, design formulae were derived to predict the overall buckling resistance of *CFST* columns subjected to preload effect. The accuracy of the proposed formulae was verified against test and *FE* analysis results. It is found that the preload effect has little influence on compressive resistance if the amplified relative column slenderness ( $\zeta_{pre} \lambda$ ) is less than 0.2 or the preload ratio  $\beta_a$  is less than 0.2. However, preload is expected to have significant influence on the axial compressive resistance of intermediate and slender columns. A reduction of more than 20% in axial overall buckling resistance is expected if the preload is high ( $\beta_a > 0.6$ ). These findings are of crucial importance in terms of evaluation of preload effect on the overall buckling resistance during fast-track construction of *CFST* columns.

## 8.2 Recommendations for Future Work

Although an extensive investigation has been carried out on the structural behaviour of *CFST* members with *UHSC* and *HSS* in the current research, further investigations are necessary in following areas to provide a better understanding and more comprehensive guidelines for the design of *CFST* columns employing *UHSC* and *HSS*:

(1) More static loading tests

The current study is limited to static loading tests, and only several types of composite sections and limited specimen samples were tested. Therefore, additional types of composite sections and more specimen samples are also needed to be tested. For example, circular *HSS* single- and double-tube sections, stub double-tube sections with hollow internal tube, and polygonal sections have not been studied yet. In addition, the test results of the four stub columns with small square *HSS* double-tube sections tested in this study were much lower than Eurocode 4 predictions, but the test results of beams and slender beam-columns with bigger square *HSS* double-tube sections were much higher than Eurocode 4 predictions. Due to the capacity of the test rig used in this study, the section breadth for the stub square *HSS* double-tube specimens was limited up to 150mm, leading to a small gap between the external and internal tubes with minimum depth of 21mm as shown in Figure 8.2. As a result, it was very difficult to control the quality of the vibrating during casting of fresh concrete. Therefore, more specimen samples should be tested on stub *CFST* columns with square *HSS* double-tube sections to re-assess the ultimate compressive resistance.

(2) Dynamic loading tests

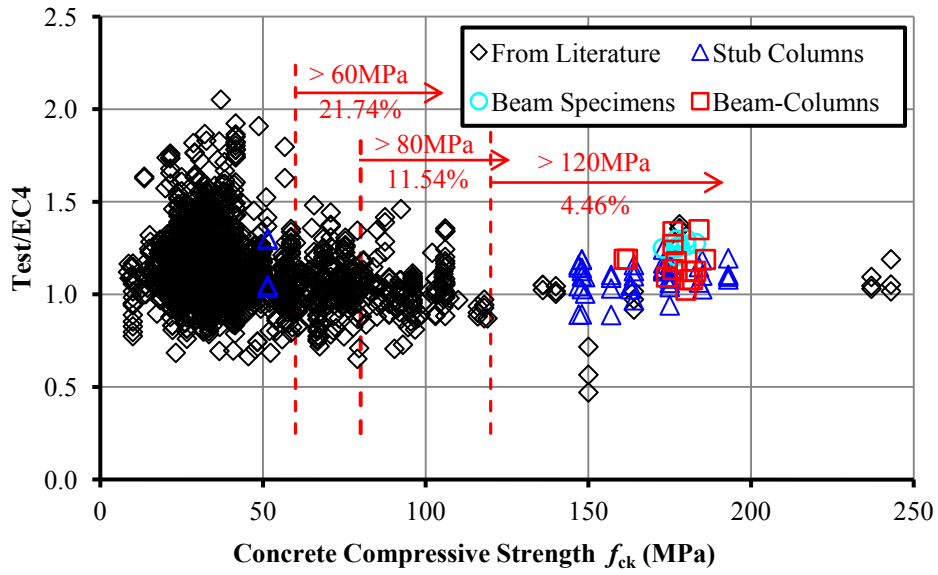
Hysteretic behavior is critical for all structure under earthquake and high-rise structure under wind load. In addition, impact and blast resistance should be considered under accidental actions. The static material properties of *UHSC* and *HSS* used in this study were very different from normal strength concrete and steel. Therefore, their properties under dynamic loading should be different, too. Therefore, the dynamic performance of *CFST* members with *UHSC* and *HSS* should be further investigated.

(3) Fire resistance tests

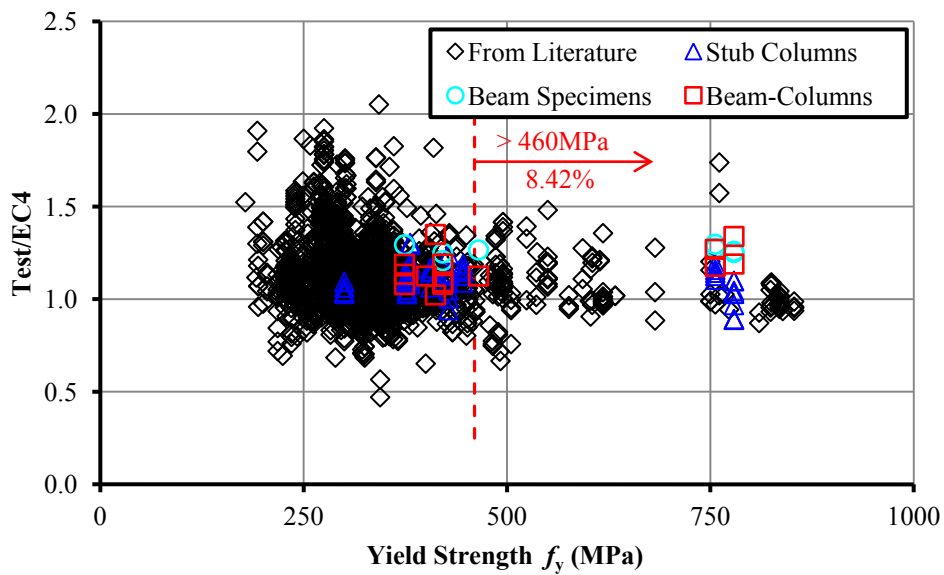
The *UHSC* used in this study was very brittle and it may be spalling and exploding at elevated temperatures. Therefore, the fire performance of *CFST* members with *UHSC* should be examined. In addition, a solution should be provided to prevent *UHSC* from exploding.

(4) Creep and shrinkage effect

Creep and shrinkage may affect the bonding strength at the interface between the steel tube and concrete core in *CFST* columns, leading to a reduction in resistance. In addition, significant redistribution of loading may be introduced between steel tube and concrete core due to the creep and shrinkage effect. As results, the proportion of loading resisted by steel tube may be increased a lot. Therefore, an equivalent effect the same as the preload effect presented in **Chapter 7** may be produced and a significant reduction in overall buckling resistance should be considered.



(a) Ratio of test/EC4 against concrete strength



(b) Ratio of test/EC4 against steel yield strength

Figure 8.1: Contribution of current research in CFST members

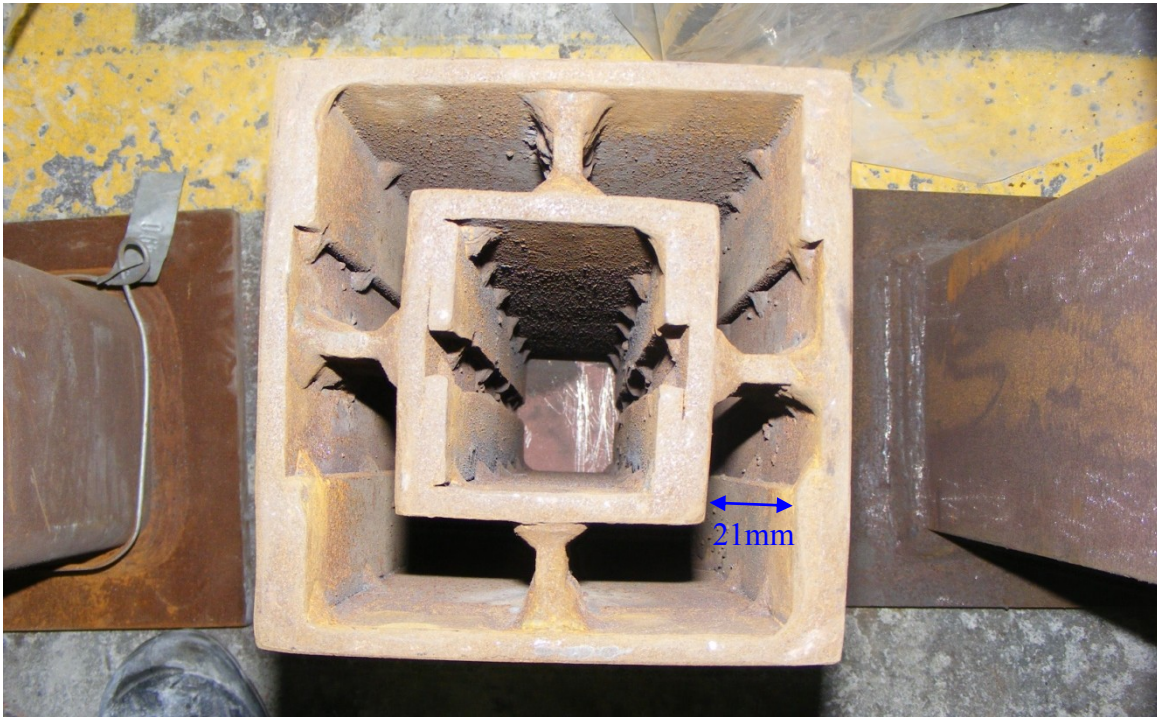


Figure 8.2: Cross-section of stub square *HSS* double-tube specimens

## References

ACI 318-08. (2008). *Building Code Requirements for Structural Concrete*. Farmington Hills, MI: American Concrete Institute.

AISC ANSI/AISC 360-10. (2010). *Specification for Structural Steel Buildings*. Chicago, IL: American Institute of Steel Construction.

AISC LRFD. (2000). *Load and Resistance Factor Design Specification for Structural Steel Buildings*. Chicago, IL: American Institute of Steel Construction.

AISC. (2011). *Steel Construction Manual Design Examples* (14.0 ed.). Chicago, IL: American Institute of Steel Construction.

ASTM C127-01. (2001). *Standard Test Method for Density, Relative Density (Specific Gravity), and Absorption of Coarse Aggregate*. West Conshohocken, PA: American Society for Testing and Materials.

ASTM C136-06. (2006). *Standard Test Method for Sieve Analysis of Fine and Coarse Aggregates*. West Conshohocken, PA: American Society for Testing and Materials.

ASTM C1611/C1611M-09a. (2009). *Standard Test Method for Slump Flow of Self-Consolidating Concrete*. West Conshohocken, PA: American Society for Testing and Materials.

ASTM C172-04. (2004). *Standard Practice for Sampling Freshly Mixed Concrete*. West Conshohocken, PA: American Society for Testing and Materials.

ASTM C192/C192M - 02. (2002). *Standard Practice for Making and Curing Concrete Test Specimens in the Laboratory*. West Conshohocken, PA: American Society for Testing and Materials.

ASTM C29/C29M-97. (2003). *Standard Test Method for Bulk Density ("Unit Weight") and Voids in Aggregate*. West Conshohocken, PA: American Society for Testing and Materials.

ASTM C33-07. (2007). *Standard Specification for Concrete Aggregates*. West Conshohocken, PA: American Society for Testing and Materials.

ASTM C39/C39M-05. (2005). *Standard Test Method for Compressive Strength of Cylindrical Concrete Specimens*. West Conshohocken, PA: American Society for Testing and Materials.

ASTM C469-02. (2002). *Standard Test Method for Static Modulus of Elasticity and Poisson's Ratio of Concrete in Compression*. West Conshohocken, PA: American Society for Testing and Materials.

ASTM C496/C496M-04. (2004). *Standard Test Method for Splitting Tensile Strength of Cylindrical Concrete Specimens*. West Conshohocken, PA: American Society for Testing and Materials.

ASTM C78-02. (2002). *Standard Test Method for Flexural Strength of Concrete (Using Simple Beam with Third-Point Loading)*. West Conshohocken, PA: American Society for Testing and Materials.

ASTM E8M - 04. (2004). *Standard Test Methods for Tension Testing of Metallic Materials*. West Conshohocken, PA: American Society for Testing and Materials.

Chen, W. F., & Atsuta, T. (1976). *Theory of beam-columns, vol. I: In-plane behavior and design*. USA: McGraw-Hill, Inc.

Cook, J. E. (1989). 10,000 psi concrete. *Concrete International* , 11 (10), 67-75.

DBJ/T13-51-2010. (2010). *Technical Specification for Concrete-filled Steel Tubular Structures*. Fuzhou, China: Department of Housing and Urban-Rural Development of Fujian Province.

European Committee for Standardization. (2002). *Eurocode 0: Basis of structural design*. Brussels.



European Committee for Standardization. (2002). *Eurocode 1: Actions on structures - Part 1-1: General actions - Densities, self-weight, imposed loads for buildings*. Brussels.

European Committee for Standardization. (2004). *Eurocode 2: Design of concrete structures - Part 1-1: General rules and rules for buildings*. Brussels.

European Committee for Standardization. (2005). *Eurocode 3: Design of steel structures - Part 1-1: General rules and rules for buildings*. Brussels.

European Committee for Standardization. (2004). *Eurocode 4: Design of composite steel and concrete structures - Part 1.1: General rules and rules for buildings*. Brussels.

Gho, W. M., & Liu, D. L. (2004). Flexural behaviour of high-strength rectangular concrete-filled steel hollow sections. *Journal of Constructional Steel Research* , 60 (11), 1681-1696.

Goode, C. D. (2008). Composite columns - 1819 tests on concrete-filled steel tube columns compared with Eurocode 4. *Structural Engineer* , 86 (16), 33-38.

Han, L. H., & Yao, G. H. (2003). Behaviour of concrete-filled hollow structural steel (HSS) columns with pre-load on the steel tubes. *Journal of Constructional Steel Research* , 59 (12), 1455-1475.

Han, L. H., Yao, G. H., & Zhao, X. L. (2005). Tests and calculations for hollow structural steel (HSS) stub columns filled with self-consolidating concrete (SCC). *Journal of Constructional Steel Research* , 61 (9), 1241-1269.

Huang, S. J., Zhong, S. T., Yan, S. Z., & Cao, H. L. (1996). Experimental research of pre-stress effect on bearing capacity of concrete filled steel tubular axial compressive members. *Journal of Harbin University of Architecture and Engineering* , 29 (6), 44-50 (in Chinese).

Jeyaraman, G. R. (2003). *Effect of preload and high strength fill material on the capacity of concrete filled tubes*. Singapore: National University of Singapore.

Liang, Q. Q., Uy, B., & Liew, J. Y. (2007). Local buckling of steel plates in concrete-filled thin-walled steel tubular beam-columns. *Journal of Constructional Steel Research* , 63 (3), 396-405.

- Liew, J. Y. (2004). Buildable design of multi-storey and large span steel structures. *J Steel Structures, Korean Society of Steel Structures* , 4 (2), 53-70.
- Liew, J. Y., & Xiong, D. X. (2009). Effect of preload on the axial capacity of concrete-filled composite columns. *Journal of Constructional Steel Research* , 65 (3), 709-722.
- Liew, J. Y., Yu, X., Wang, T. Y., & Xiong, D. X. (2012). Assessment of current design methods with test database on concrete filled steel tube columns. *Journal of Constructional Steel Research* , Submitted for publication.
- Liu, D. L. (2006). Behaviour of eccentrically loaded high-strength rectangular concrete-filled steel tubular columns. *Journal of Constructional Steel Research* , 62 (8), 839-846.
- Liu, D. L. (2004). Behaviour of high strength rectangular concrete-filled steel hollow section columns under eccentric loading. *Thin-Walled Structures* , 42 (12), 1631-1644.
- Liu, D. L. (2005). Tests on high-strength rectangular concrete-filled steel hollow section stub columns. *Journal of Constructional Steel Research* , 61 (7), 902-911.
- Liu, D. L., & Gho, W. M. (2005). Axial load behaviour of high-strength rectangular concrete-filled steel tubular stub columns. *Thin-Walled Structures* , 43 (8), 1131-1142.
- Liu, D. L., Gho, W. M., & Yuan, J. (2003). Ultimate capacity of high-strength rectangular concrete-filled steel hollow section stub columns. *Journal of Constructional Steel Research* , 59 (12), 1499-1515.
- Lue, D. M., Liu, J. L., & Yen, T. (2007). Experimental study on rectangular CFT columns with high-strength concrete. *Journal of Constructional Steel Research* , 63 (1), 37-44.
- Mursi, M., & Uy, B. (2004). Strength of slender concrete filled high strength steel box columns. *Journal of Constructional Steel Research* , 60 (12), 1825-1848.
- Patnaik, A. K., & Patnaikuni, I. (2002). Correlation of strength of 75 mm diameter and 100 mm diameter cylinders for high strength concrete. *Cement and Concrete Research* , 32 (4), 607-613.
- Popovics, S. (1998). *Strength and Related Properties of Concrete: A Quantitative Approach*. New York: John Wiley & Sons, Inc.

- Saw, H. S., & Liew, J. Y. (2000). Assessment of current methods for the design of composite columns in buildings. *Journal of Constructional Steel Research* , 53 (2), 121-147.
- Uy, B. (2008). Stability and ductility of high performance steel sections with concrete infill. *Journal of Constructional Steel Research* , 64 (7-8), 748-754.
- Uy, B. (2001). Strength of short concrete filled high strength steel box columns. *Journal of Constructional Steel Research* , 57 (2), 113-134.
- Uy, B., & Das, S. (1997). Wet concrete loading of thin-walled steel box columns during the construction of a tall building. *Journal of Constructional Steel Research* , 42 (2), 95-119.
- Varma, A. H., Ricles, J. M., Sause, R., & Lu, L. W. (2002a). Experimental behavior of high strength square concrete-filled steel tube beam-columns. *Journal of Structural Engineering - ASCE* , 128 (3), 309-318.
- Varma, A. H., Ricles, J. M., Sause, R., & Lu, L. W. (2004). Seismic behavior and design of high-strength square concrete-filled steel tube beam columns. *Journal of Structural Engineering - ASCE* , 130 (2), 169-179.
- Varma, A. H., Ricles, J. M., Sause, R., & Lu, L. W. (2002b). Seismic behavior and modeling of high-strength composite concrete-filled steel tube (CFT) beam-columns. *Journal of Constructional Steel Research* , 58 (5-8), 725-758.
- Xiong, D. X., & Zha, X. X. (2007). A numerical investigation on the behaviour of concrete-filled steel tubular columns under initial stresses. *Journal of Constructional Steel Research* , 63 (5), 599-611.
- Yu, Q., Tao, Z., & Wu, Y. X. (2008). Experimental behaviour of high performance concrete-filled steel tubular columns. *Thin-Walled Structures* , 46 (4), 362-370.
- Zha, X. X. (1996). *Investigation on the behavior of concrete filled steel tubular compression-bending-torsion members under the initial stress*. Harbin University of C.E. Architecture. (in Chinese).

Zhang, X. Q., Zhong, S. T., Yan, S. Z., Lin, W., & Cao, H. L. (1997). Experimental study about the effect of initial stress on bearing capacity of concrete filled steel tubular members under eccentric compression. *Journal of Harbin University of C.E. Architecture* , 30 (1), 50-56 (in Chinese).

## **List of Publications**

### **Journal Papers:**

Liew, J. Y. R., & **Xiong, D. X.** (2012). Ultra-high strength concrete filled composite columns for multi-storey building construction. *Advances in Structural Engineering*, 15(9), 1487-1503.

Liew, J. Y. R., & **Xiong, D. X.** (2009). Effect of preload on the axial capacity of concrete-filled composite columns. *Journal of Constructional Steel Research*, 65(3), 709-722.

### **International Conference Papers:**

Liew, J. Y. R., **Xiong, D. X.**, Xiong, M. X., & Yu, X. (2012). Design of concrete filled steel tube with high strength materials. *Proceedings of CTBUH 9<sup>th</sup> World Congress*, 19-21 September, 2012, Shanghai, China, Pages 280-287.

Liew, J. Y. R., & **Xiong, D. X.** (2012). Experimental investigation on the flexural behaviour of concrete filled steel tubes with high strength materials. *Proceedings of the 10<sup>th</sup> International Conference on Advances in Steel Concrete Composite and Hybrid Structures*, 2-4 July, 2012, Singapore, China, Pages 346-353.

Liew, J. Y. R., **Xiong, D. X.**, & Yu, X. (2012). Further investigation on composite columns with high strength steel and ultra-high strength concrete. *Proceedings of the 7<sup>th</sup> International Conference on Advances in Steel Structures*, 14-16 April, 2012, Nanjing, China, Pages 25-34.

Liew, J. Y. R., **Xiong, D. X.**, & Zhang, M. H. (2011). Experimental studies on concrete filled tubes with ultra-high strength materials. *Proceedings of the 6<sup>th</sup> International Symposium on Steel Structures*, 2-5 November, 2011, Seoul, South Korea, Pages 377-384.

Wang, Y. B., Liew, J. Y. R., & **Xiong, D. X.** (2011). Nonlinear analysis of the axial compressive behaviour of circular ultra-high strength concrete filled stub columns. *Proceedings of the 6<sup>th</sup> International Symposium on Steel Structures*, 2-5 November, 2011, Seoul, South Korea, Pages 392-399.

Liew, J. Y. R., & **Xiong, D. X.** (2010a). Experimental investigation on tubular columns infilled with ultra-high strength concrete. *Proceedings of the 13<sup>th</sup> International Symposium on Tubular Structures*, 15-17 December, 2010, Hong Kong, China, Pages 637-645.

Liew, J. Y. R., & **Xiong, D. X.** (2010b). Ultra-high strength concrete filled columns for highrise buildings. *Proceedings of the 4<sup>th</sup> International Conference on Steel & Composite Structures*, 21-23 July, 2010, Sydney, Australia, Pages 80-91.

**Xiong, D. X.**, Liew, J. Y. R., Zhang, M. H., & Chia, K. S. (2010). Effect of coarse aggregates on the performance of ultra-high strength concrete. *Proceedings of the 23<sup>rd</sup> KKCNN Symposium on Civil Engineering*, 13-15, November, 2010, Taipei, Pages 65-68.

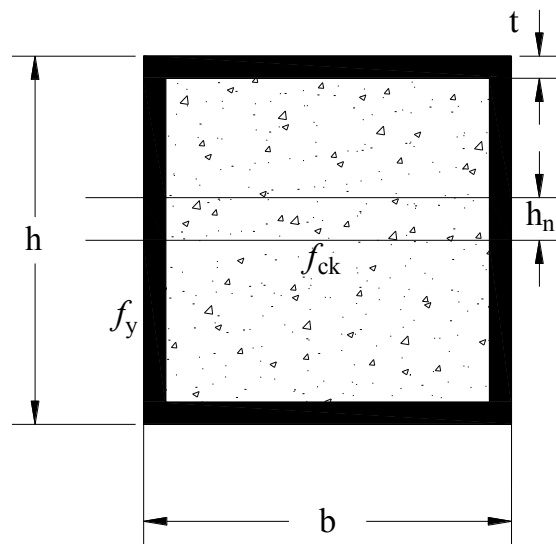
Liew, J. Y. R., Soheli, K. M. A., & **Xiong, D. X.** (2010). Design of steel-concrete composite structures with ultra-high strength and lightweight concrete. *Proceedings of the 21<sup>st</sup> Australasian Conference on the Mechanics of Structures and Materials*, 7-10 December, 2010, Melbourne, Australia, Pages 21-33.

Liew, J. Y. R., & **Xiong, D. X.** (2009). Ultra-high strength concrete-filled composite columns for multi-storey building construction. *Proceedings of the 3<sup>rd</sup> International Symposium on Advances in Steel and Composite Structures*, 3 August, 2009, Hong Kong, China, Pages 1-30.

Liew, J. Y. R., Chia, K. S., Soheli, K. M. A., & **Xiong, D. X.** (2008). Innovation in composite construction – towards the extreme of high strength and lightweight. *Proceedings of the 5<sup>th</sup> International Conference on Coupled Instabilities in Metal Structures*, 23-25 June, 2008, Sydney, Australia, Pages 19-33.

## Appendix I: Formulae for Calculation of Sectional Properties

### I.1 Concrete Filled Rectangular Single-Tube Section



External corner radius of hot finished hollow steel section for calculation:  $r_o = 1.5t$

Internal corner radius of hot finished hollow steel section for calculation:  $r_i = 1.0t$

#### (1) Cross-sectional area

$$\begin{cases} A_a = 2t(b + h - 2t) - (4 - \pi)(r_o^2 - r_i^2) \\ A_c = (b - 2t)(h - 2t) - (4 - \pi)r_i^2 \end{cases}$$

#### (2) Second moment of area

$$\begin{cases} I_a = \frac{bh^3}{12} - \frac{(b - 2t)(h - 2t)^3}{12} - 4(I_g + A_g h_g^2) + (4I_\xi + A_\xi h_\xi^2) \\ I_c = \frac{(b - 2t)(h - 2t)^3}{12} - (4I_\xi + A_\xi h_\xi^2) \end{cases}$$

where:

$$A_g = \left(1 - \frac{\pi}{4}\right)r_o^2, \quad A_\xi = \left(1 - \frac{\pi}{4}\right)r_i^2$$

$$h_g = \frac{h}{2} - \left(\frac{10-3\pi}{12-3\pi}\right)r_o, \quad h_\xi = \frac{h-2t}{2} - \left(\frac{10-3\pi}{12-3\pi}\right)r_i$$

$$I_g = \left(\frac{1}{3} - \frac{\pi}{16} - \frac{1}{3(12-3\pi)}\right)r_o^4, \quad I_\xi = \left(\frac{1}{3} - \frac{\pi}{16} - \frac{1}{3(12-3\pi)}\right)r_i^4$$

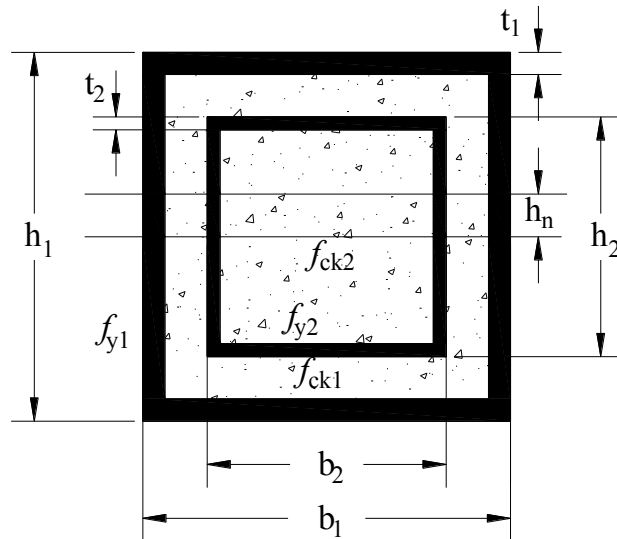
### (3) Plastic section modulus

$$\begin{cases} W_{pa} = \frac{bh^2}{4} - \frac{(b-2t)(h-2t)^2}{4} - 4A_g h_g + 4A_\xi h_\xi \\ W_{pc} = \frac{(b-2t)(h-2t)^2}{4} - 4A_\xi h_\xi \end{cases}$$

$$h_n = \frac{A_c f_{ck}}{2(b-2t)f_{ck} + 8t f_y}$$

$$W_{pan} = 2th_n^2, \quad W_{pcn} = (b-2t)h_n^2$$

## I.2 Concrete Filled Rectangular Double-Tube Section





**(1) Cross-sectional area**

$$\begin{cases} A_{a1} = 2t(b_1 + h_1 - 2t_1) - (4 - \pi)(r_{o1}^2 - r_{i1}^2) \\ A_{a2} = 2t(b_2 + h_2 - 2t_2) - (4 - \pi)(r_{o2}^2 - r_{i2}^2) \\ A_{c1} = (b_1 - 2t_1)(h_1 - 2t_1) - (4 - \pi)r_{i1}^2 - A_{a2} - A_{c2} \\ A_{c2} = (b_2 - 2t_2)(h_2 - 2t_2) - (4 - \pi)r_{i2}^2 \end{cases}$$

**(2) Second moment of area**

$$\begin{cases} I_{a1} = \frac{b_1 h_1^3}{12} - \frac{(b_1 - 2t_1)(h_1 - 2t_1)^3}{12} - 4(I_{g1} + A_{g1} h_{g1}^2) + (4I_{\xi1} + A_{\xi1} h_{\xi1}^2) \\ I_{a2} = \frac{b_2 h_2^3}{12} - \frac{(b_2 - 2t_2)(h_2 - 2t_2)^3}{12} - 4(I_{g2} + A_{g2} h_{g2}^2) + (4I_{\xi2} + A_{\xi2} h_{\xi2}^2) \\ I_{c1} = \frac{(b_1 - 2t_1)(h_1 - 2t_1)^3}{12} - (4I_{\xi1} + A_{\xi1} h_{\xi1}^2) - I_{a2} - I_{c2} \\ I_{c2} = \frac{(b_2 - 2t_2)(h_2 - 2t_2)^3}{12} - (4I_{\xi2} + A_{\xi2} h_{\xi2}^2) \end{cases}$$

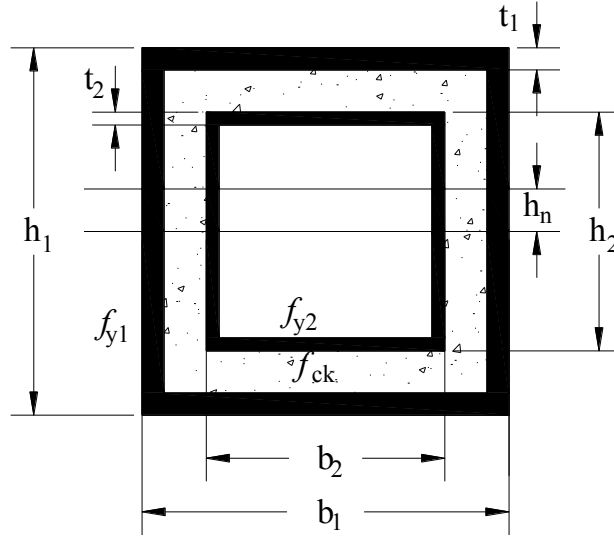
**(3) Plastic section modulus**

$$\begin{cases} W_{pa1} = \frac{b_1 h_1^2}{4} - \frac{(b_1 - 2t_1)(h_1 - 2t_1)^2}{4} - 4A_{g1} h_{g1} + 4A_{\xi1} h_{\xi1} \\ W_{pa2} = \frac{b_2 h_2^2}{4} - \frac{(b_2 - 2t_2)(h_2 - 2t_2)^2}{4} - 4A_{g2} h_{g2} + 4A_{\xi2} h_{\xi2} \\ W_{pc1} = \frac{(b_1 - 2t_1)(h_1 - 2t_1)^2}{4} - 4A_{\xi1} h_{\xi1} - W_{pa2} - W_{pc2} \\ W_{pc2} = \frac{(b_2 - 2t_2)(h_2 - 2t_2)^2}{4} - 4A_{\xi2} h_{\xi2} \end{cases}$$

$$h_n = \frac{A_{c1} f_{ck1} + A_{c2} f_{ck2}}{2(b_1 - 2t_1 - b_2) f_{ck1} + 2(b_2 - 2t_2) f_{ck2} + 8t_1 f_{y1} + 8t_2 f_{y2}}$$

$$\begin{cases} W_{pan1} = 2t_1 h_n^2, \quad W_{pan2} = 2t_2 h_n^2 \\ W_{pcn1} = (b_1 - 2t_1 - b_2) h_n^2, \quad W_{pcn2} = (b_2 - 2t_2) h_n^2 \end{cases}$$

**I.3 Concrete Filled Rectangular Double-Tube Section with Hollow Internal Tube**



**(1) Cross-sectional area**

$$\begin{cases} A_{a1} = 2t(b_1 + h_1 - 2t_1) - (4 - \pi)(r_{o1}^2 - r_{i1}^2) \\ A_{a2} = 2t(b_2 + h_2 - 2t_2) - (4 - \pi)(r_{o2}^2 - r_{i2}^2) \\ A_c = (b_1 - 2t_1)(h_1 - 2t_1) - b_2h_2 - (4 - \pi)(r_{i1}^2 - r_{o2}^2) \end{cases}$$

**(2) Second moment of area**

$$\begin{cases} I_{a1} = \frac{b_1h_1^3}{12} - \frac{(b_1 - 2t_1)(h_1 - 2t_1)^3}{12} - 4(I_{g1} + A_{g1}h_{g1}^2) + (4I_{\xi1} + A_{\xi1}h_{\xi1}^2) \\ I_{a2} = \frac{b_2h_2^3}{12} - \frac{(b_2 - 2t_2)(h_2 - 2t_2)^3}{12} - 4(I_{g2} + A_{g2}h_{g2}^2) + (4I_{\xi2} + A_{\xi2}h_{\xi2}^2) \\ I_c = \frac{(b_1 - 2t_1)(h_1 - 2t_1)^3}{12} - \frac{b_2h_2^3}{12} - (4I_{\xi1} + A_{\xi1}h_{\xi1}^2) + 4(I_{g2} + A_{g2}h_{g2}^2) \end{cases}$$

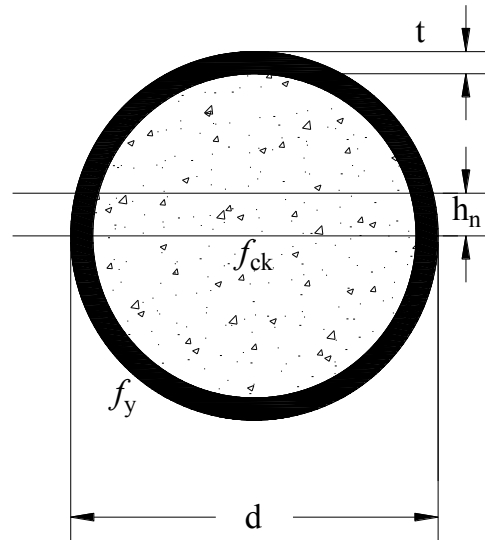
**(3) Plastic section modulus**

$$\begin{cases} W_{pa1} = \frac{b_1h_1^2}{4} - \frac{(b_1 - 2t_1)(h_1 - 2t_1)^2}{4} - 4A_{g1}h_{g1} + 4A_{\xi1}h_{\xi1} \\ W_{pa2} = \frac{b_2h_2^2}{4} - \frac{(b_2 - 2t_2)(h_2 - 2t_2)^2}{4} - 4A_{g2}h_{g2} + 4A_{\xi2}h_{\xi2} \\ W_{pc} = \frac{(b_1 - 2t_1)(h_1 - 2t_1)^2}{4} - \frac{b_2h_2^2}{4} - 4A_{\xi1}h_{\xi1} + 4A_{g2}h_{g2} \end{cases}$$

$$h_n = \frac{A_c f_{ck}}{2(b_1 - 2t_1 - b_2) f_{ck} + 8t_1 f_{y1} + 8t_2 f_{y2}}$$

$$\begin{cases} W_{pan1} = 2t_1 h_n^2, & W_{pan2} = 2t_2 h_n^2 \\ W_{pcn} = (b_1 - 2t_1 - b_2) h_n^2 \end{cases}$$

#### I.4 Concrete Filled Circular Single-Tube Section



##### (1) Cross-sectional area

$$A_a = \pi [d^2 - (d - 2t)^2], \quad A_c = \pi (d - 2t)^2$$

##### (2) Second moment of area

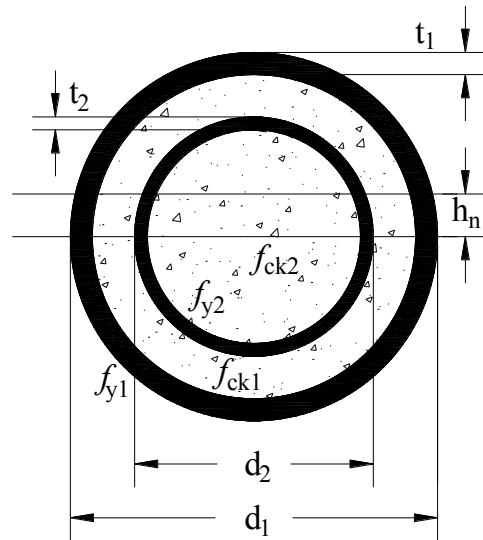
$$I_a = \frac{\pi [d^4 - (d - 2t)^4]}{64}, \quad I_c = \frac{\pi (d - 2t)^4}{64}$$

##### (3) Plastic section modulus

$$W_{pa} = \frac{d^3 - (d - 2t)^3}{6}, \quad W_{pc} = \frac{(d - 2t)^3}{6}$$

$$h_n = \frac{A_c f_{ck}}{2(d - 2t) f_{ck} + 8t f_y}, \quad W_{pan} = 2t h_n^2, \quad W_{pcn} = (d - 2t) h_n^2$$

### I.5 Concrete Filled Circular Double-Tube Section



#### (1) Cross-sectional area

$$A_{a1} = \pi \left[ d_1^2 - (d_1 - 2t_1)^2 \right], \quad A_{a2} = \pi \left[ d_2^2 - (d_2 - 2t_2)^2 \right]$$

$$A_{c1} = \pi \left[ (d_1 - 2t_1)^2 - d_2^2 \right], \quad A_{c2} = \pi (d_2 - 2t_2)^2$$

#### (2) Second moment of area

$$I_{a1} = \pi \left[ d_1^4 - (d_1 - 2t_1)^4 \right] / 64, \quad I_{a2} = \pi \left[ d_2^4 - (d_2 - 2t_2)^4 \right] / 64$$

$$I_{c1} = \pi \left[ (d_1 - 2t_1)^4 - d_2^4 \right] / 64, \quad I_{c2} = \pi (d_2 - 2t_2)^4 / 64$$

#### (3) Plastic section modulus

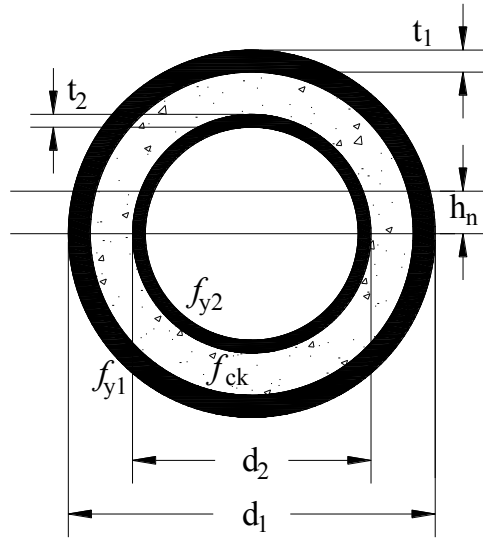
$$W_{pa1} = \left[ d_1^3 - (d_1 - 2t_1)^3 \right] / 6, \quad W_{pa2} = \left[ d_2^3 - (d_2 - 2t_2)^3 \right] / 6$$

$$W_{pc1} = \left[ (d_1 - 2t_1)^3 - d_2^3 \right] / 6, \quad W_{pc2} = (d_2 - 2t_2)^3 / 6$$

$$h_n = \frac{A_{c1}f_{ck1} + A_{c2}f_{ck2}}{2(d_1 - 2t_1 - d_2)f_{ck1} + 2(d_2 - 2t_2)f_{ck2} + 8t_1f_{y1} + 8t_2f_{y2}}$$

$$W_{pan1} = 2t_1h_n^2, \quad W_{pan2} = 2t_2h_n^2, \quad W_{pcn1} = (d_1 - 2t_1 - d_2)h_n^2, \quad W_{pcn2} = (d_2 - 2t_2)h_n^2$$

**I.6 Concrete Filled Circular Double-Tube Section with Hollow Internal Tube**



**(1) Cross-sectional area**

$$A_{a1} = \pi \left[ d_1^2 - (d_1 - 2t_1)^2 \right], \quad A_{a2} = \pi \left[ d_2^2 - (d_2 - 2t_2)^2 \right], \quad A_c = \pi \left[ (d_1 - 2t_1)^2 - d_2^2 \right]$$

**(2) Second moment of area**

$$I_{a1} = \pi \left[ d_1^4 - (d_1 - 2t_1)^4 \right] / 64, \quad I_{a2} = \pi \left[ d_2^4 - (d_2 - 2t_2)^4 \right] / 64$$

$$I_c = \pi \left[ (d_1 - 2t_1)^4 - d_2^4 \right] / 64$$

**(3) Plastic section modulus**

$$W_{pa1} = \left[ d_1^3 - (d_1 - 2t_1)^3 \right] / 6, \quad W_{pa2} = \left[ d_2^3 - (d_2 - 2t_2)^3 \right] / 6$$

$$W_{pc} = \left[ (d_1 - 2t_1)^3 - d_2^3 \right] / 6$$

$$h_n = \frac{A_c f_{ck}}{2(d_1 - 2t_1 - d_2) f_{ck} + 8t_1 f_{y1} + 8t_2 f_{y2}}$$

$$W_{pan1} = 2t_1 h_n^2, \quad W_{pan2} = 2t_2 h_n^2, \quad W_{pcn} = (d_1 - 2t_1 - d_2) h_n^2$$